State-to-State Molecular Photodissociation Dynamics

A thesis submitted for the Degree of Doctor of Philosophy

by

Stephen Richard Langford B.Sc. (hons)

Jesus College, Oxford

Michaelmas Term, 1995

Abstract

The water molecule, rotationally state selected in the third and fourth streching overtone ($|04\rangle^-$ and $|05\rangle^-$) and stretch-bend combination ($|04\rangle|2\rangle^-$) levels, has been photodissociated at $\lambda \approx 282$ nm *via* the $\tilde{A}$ state. The OH photofragment rotational distributions, determined by OH(A–X) laser-induced fluoresence (LIF), are found to differ from those reported previously by Andresen and coworkers ($H_2O|01\rangle^-$ + 193 nm), Crim and coworkers ($H_2O|04\rangle^-$ + 239.5 nm) and Rosenwaks and coworkers ($H_2O|01\rangle^+$ + 193 nm). These variations become more apparent with increasing angular momentum in the parent water molecule and with an increasing number of OH stretching quanta in the intermediate vibrational overtone. The Franck-Condon model of Balint-Kurti is able to qualitatively reproduce the observed trends, provided that dissociation at lower photolysis photon energies and *via* higher intermediate overtone states is assumed to occur preferentially from extended R_{H-OH} configurations. The calculations suggest that the variation in the photofragment rotational distributions lies in a gradual change in the inertial properties of the bound state water molecule as the H–OH bond is stretched. In a second study, the partially deuterated water molecule, rotationally state selected in the third and fourth OH stretching vibrational overtone levels have been photodissociated *via* the $\tilde{A}$ state at $\lambda \approx 288$ nm. A branching ratio betweem the H + OD and D + OH dissociation channels is estimated from OD and OH (A–X) LIF measurements to be $\Phi(OD)/\Phi(OH) > 20$; this compares well with the previous measurements of Crim and coworkers, and the theoretical work of Imre and coworkers. The small shift in the centre of mass in the water molecule arising from the substitution of of a deuterium atom for one of the hydrogen atoms is shown to have a marked effect on the rotational distributions of the OD photofragment. Calculations using a modified Franck-Condon model, which includes an approximate exit-torque, are able to reproduce qualitatively the experimental OD rotational distributions at sensible values of R_{H-OD} ($\sim$ 1.4 Å). In addition to being sensitive to the dynamics of the parent molecule on the ground state potential, the product OD state distributions are shown to be very sensitive to even the smallest exit channel torque on the excited potential surface.

Acknowledgements

There have been many people who have made me smile and kept me going over the last three years and to name them all would be impossible. To name but a few, and in no particular order, I would like to thank:

Dr. Mark Brouard, my supervisor, Prof. John Simons and Dr. David Manolopoulos for the continual help and encouragement they have given over the last three years.

Dr. Chris Morley, Dr. Kevin Hughes and Dr. Robert Lee at Thornton Research Centre for making me so welcome during the time I spent there.

My laboratory companions over the years: Andy Alexander, John Dickinson, Simon Duxon, Pedro Enríquez, Paul Joirman, Mark Lambert, Richard Mabbs, Gavin Markillie, Rob Randall, Steve Rayner, Caroline Russell and Justin Short.

The Langford clan for all of their support, spiritual and financial.

Bob Hibbins who we left with Robin.

Pete Hepworth and Ian Lane who came back for more.

Stuart MacKenzie, Russell Low and Martin Barnes for the many animated moments in the King's Arms.

Paolo Bloomfield for being such a star.

Rich, Ade, Mart., Claire, Mat, Bry, Andy and Jon for still being there after six years.

Claire for the many hours I have enjoyed her smile and spent far too long in the Philie.

John, Pat, Jo, Roger, Alex, Claire, Laura, Chris, Danny, Jase and Dixie for making those evenings what they should be.

and finally,

E.P.S.R.C. and Shell Research for providing the funding for the last three years.

Contents

Chapter 1 Introduction : State-to-state molecular photodissociation dynamics

The study of molecular photodissociation dynamics has for many decades attracted an enormous input from both experimental and theoretical research. With the ever advancing capability of laboratory techniques, the understanding and the challenges of this field have continued to become more intricate. References [1]–[28] list a number of reviews which provide a chronological guide through many of these developments. This thesis is concerned with the study of state-to-state photodissociation dynamics, preparing the parent molecule in a well defined quantum state prior to photodissociation, and the quantum state resolved detection of the photofragments; more specifically with the vibrationally mediated photodissociation (VMP) of water molecules *via* the $\tilde{A}$ state potential energy surface (PES). The aim of this chapter is to provide a brief overview of other related state specific photodissociation studies and the wealth of information that can be obtained from both experimental measurements and theoretical modelling.

From a practical point of view, photodissociation is of central importance in photochemistry [29, 30]. In most cases, the photofragments are radicals, which can then go on to play a part in the many chain reactions that take place in the atmosphere. In order to model such a system, having a detailed understanding of the possible photofragmentation pathways a molecule can have in such an environment, is of fundamental importance. The study of photodissociation also provides an ideal opportunity to study molecular dynamics on a state-to-state level. Over the past decade or so, one of the goals in reaction kinetics/dynamics has been to understand and have the ability to predict both inter- and intra-molecular reactivity on a microscopic level [31]. State selecting a molecule prior to dissociation from an excited [16, 23] or ground [8, 10, 22] electronic state can provide a much clearer picture of the processes associated with fragmentation, for example intramolecular energy transfer (electronic, rotation, vibration and translation), the interaction of different electronic states and the role different degrees of freedom may have in the breaking and making of chemical

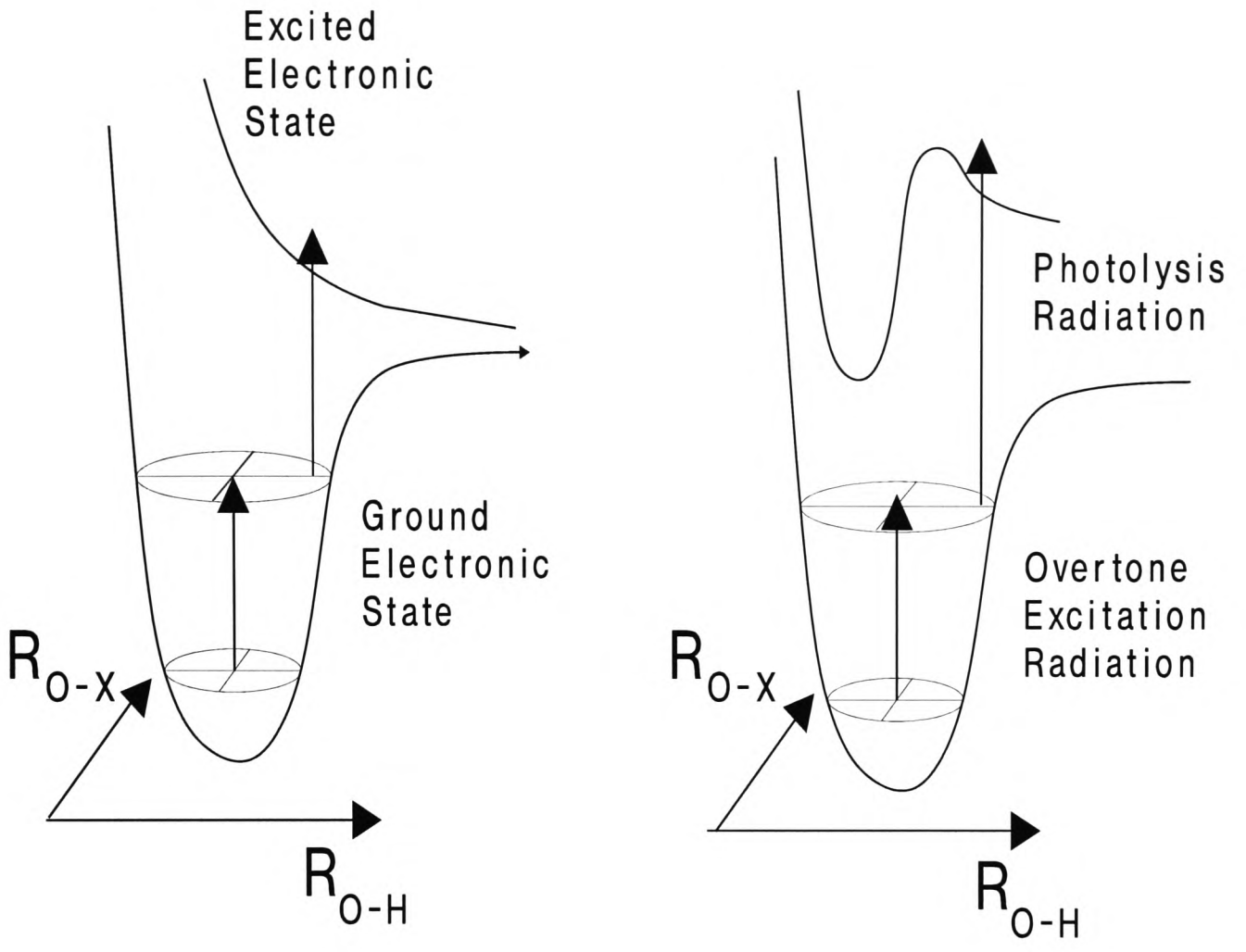

Figure 1.1 Schematic of Vibrationally Mediated Photodissociation for (a) a bound to repulsive electronic transition and (b) and bound to predissociative transition. With a low enough energy second photon, a region of the excited potential energy surface (PES) at extended bond length configurations is preferentially sampled. In the case of (b) this has the possibility of accessing the PES past the barrier or the crossing point between electronic states.

bonds.

The state-to-state dynamical study of $H_2O/HOD(\tilde{A})$ fragmentation presented in this thesis makes use of a technique pioneered by Crim and coworkers [23], **Vibrationally Mediated Photodissociation (VMP)**, which involves the preparation of a molecule in a specific rovibrational state and a subsequent UV excitation to a dissociative excited electronic state (see Figure 1.1). It has long been demonstrated that the efficiency of UV absorption up to an excited electronic state is greatly increased by the much larger overlap with the excited electronic state if excitation occurs from a vibrationally excited state [32]–[34]. Although the absorption cross-section up to the vibrational level decreases rapidly with increasing

quantum number, the enhancement in the second step makes the use of high vibrational overtones in the intermediate step experimentally viable [23]. With a careful choice of the energy of the UV photon, it is possible to restrict excitation from an intermediate stretching overtone to different ground state configurations. This is shown schematically in Figure 1.1. It is therefore possible to sample regions of both the ground and excited electronic surface(s) that normal spectroscopic and photodissociation experiments cannot.

The state-to-state fragmentation dynamics of a molecule in an excited electronic state can essentially be viewed experimentally at three different 'times':

- **Initial** - using Absorption Spectroscopy, the dynamics of the excited molecule in the Franck-Condon region above the ground electronic state can be interrogated. This is discussed in Section 1.1.
- **Intermediate** - in Section 1.2, the application of Resonance Raman Spectroscopy to explore the (nuclear) motions of the dissociating molecule just after it leaves the Franck-Condon region is discussed.
- **Final** - with a knowledge of the nuclear motion of the parent molecule prior to excitation to the excited electronic state, it is possible to study the subsequent fragmentation dynamics by probing the energy disposal in the separated photofragments. This is discussed in Section 1.3.

Of course, state selecting the parent molecule prior to dissociation can only provide a clearer picture of the photodissociation dynamics if the eigenstate(s) excited in the selection step is well characterised. In Section 1.4, the various methods that are currently used to state select a molecule and probe the excited motion(s) are discussed.

1.1 Absorption spectroscopy

The first observable in photodissociation is the UV absorption spectrum, or the total absorption cross-section, σ_{TOT},

$$\sigma_{TOT}(E) = \sum_{i,f} \sigma(i, E, f) \tag{1.1}$$

in which $\sigma(i, E, f)$ is the cross-section for electronically exciting a ground state molecule in a state i with a UV photon of energy E into a final state f. This final state may well be a set of photofragments or be another bound state and depends on the nature of the excited

electronic state or states sampled by the molecule. Although this is the most averaged of measurable quantities, it does contain the complete history of the excitation process and any subsequent fragmentation.

For direct photodissociation, one in which the molecule immediately distorts irreversibly along the dissociation coordinate, the absorption spectrum is broad and structureless *e.g.* $FNO(S_1)$ [35]. In this case, the UV photon promotes the molecule up to a region on the excited state PES directly above the ground state equilibrium geometry (the Franck-Condon region) which is purely repulsive along the dissociation coordinate. The term 'direct photodissociation' in practice has come to represent a dissociation that occurs on a time scale less than a vibrational period of the parent molecule. In the upper limit, the absorption spectrum has very diffuse structure superimposed upon the broad continuum, *e.g.* $ClNO(S_1)$ [36]–[38] and $H_2O(\tilde{A})$ [39]–[41] . The dissociation time is sufficient to allow the molecule to perform at least one stretching oscillation in a non-dissociative coordinate before the dissociating bond breaks, but not long enough for a complete oscillation of a bending motion. The Franck-Condon region on the $ClNO(S_1)$ PES is within the repulsive dissociation channel, but the slope of the potential is not steep enough for an 'immediate' fragmentation [37, 38] and at least one oscillation in the N–O stretch occurs. The Franck-Condon region of the $H_2O(\tilde{A})$ surface on the other hand accesses a saddle point above and between the two equivalent dissociation channels [40, 41]. The structure in the absorption spectrum has been assigned to motion along this saddle point perpendicular to the dissociation coordinate, corresponding to the symmetric stretch. The diffuse nature of the structure reflects the narrowness of the saddle point allowing for a (relatively) prompt dissociation.

As the dissociation time extends beyond just one vibrational period, the photodissociation process begins to be classed as indirect, where the excited state molecule has time to perform more than one stretching or bending oscillation before ultimately falling apart. The absorption spectrum now consists of increasingly resolved vibrational structure as the dissociation time, or more properly, the predissociation lifetime increases. At the extreme, in which the predissociation lifetime is of the order of tens of picoseconds or more, the absorption spectrum will consist of the various rotationally-resolved vibrational bands, which will have intensity and linewidth perturbations reflecting the predissociation mechanism(s).

There are three basic types of predissociation [42]:

1. **Predissociation by electronic transition** - This is a non-Born-Oppenheimer coupling of electronic states through either (a) vibronic interaction (internal conversion, IC), or (b) spin-orbit coupling (inter-system crossing, ISC) or (c) through electronic Coriolis coupling (both IC and ISC). These can be sub-divided into homogeneous predissociation - one in which the same electronic species are involved, and heterogeneous predissociation - in which different electronics species are involved. There are various examples of this type of predissociation in polyatomics, but two of the most notable cases involve HNO($\tilde{A}$) and $H_2O(\tilde{C})$. High resolution spectroscopic studies, coupled with theoretical modeling on ab initio calculated potential surfaces of the HNO($\tilde{A}^1A''$) ro-vibrational levels demonstrate the influence of both Coriolis induced internal conversion with the $\tilde{X}^1A'$ state [43, 44] (a J, K dependence[1] on the lineshape) and spin-orbit induced inter-system crossing with the $\tilde{a}^3A''$ state [45] (shown through an external magnetic field dependence of the lineshape)[2]. Using a 3 + 1 REMPI[3] technique, Dixon and coworkers [46, 47] and later, Kleinermanns and Kuge [48], investigated the $\tilde{C}^1B_1 \leftarrow\tilde{X}^1A_1$ transition in H_2O and showed, again through an analysis of the widths and intensities of the rotational features, three competing predissociation mechanisms, a heterogeneous *a*-inertial axis Coriolis induced predissociation *via* the $\tilde{B}^1A_1$, a homogeneous predissociation presumably involving the $\tilde{A}^1B_1$ state, and a (weak) heterogeneous Coriolis coupling with a $^1A_2$ state *via* *c*-axis rotation.
2. **Vibrational Predissociation** - This involves dissociation on the electronic state that is initially excited, which has a well at close distances bounded by a barrier into the exit channel, and is characterised by a linewidth variation within a given vibronic progression in the absorption band. Predissociation can occur either over the barrier, by intramolecular vibrational redistribution (IVR) into the reaction coordinate, or by tunnelling through the barrier. An examination of the parent vibronic state dependence of the photofragments vibrational distribution often indicates the relative contributions of IVR and tunnelling to the vibrational predissociation (*e.g.* HONO($\tilde{A}$) [49]–[53], see below, and $CH_3ONO(\tilde{A})$ [54]–[57]). For very long predissociative lifetimes (*e.g.* van der Waals molecules) the decay is dominated by the IVR mechanism,

[1] J is the total angular momentum quantum number and K is its projection onto the molecular axis.

[2] Coriolis coupling between the $\tilde{A}$ and $\tilde{X}$ states is shown to be the dominant dissociation pathway.

[3] Resonance Enhanced Multiphoton Ionization - see Figure 1.2(b).

and the absorption spectrum consists of a progression of very sharp resonances (Feshbach resonances [58, 59]).

3. **Rotational Predissociation** This is very similar to vibrational predissociation, except that it occurs through internal energy redistribution between rotation and translation. This can arise if a sufficiently high rotational state within the well on the excited potential surface can be excited and again the absorption spectrum will exhibit Feshbach resonances [4]. This type of predissociation has been observed or calculated for both closed-shell van der Waals systems *e.g.* Ne–HF [60] and He–HF [61] and open-shell van der Waals systems *e.g.* OH($\tilde{A}$)–Ar [62] and Ar–OH($\tilde{X}$) [63], and also in ionic species *e.g.* H^- [64]–[67] and PS^- [67, 68].

1.2 Resonance Raman spectroscopy

The absorption spectrum is sensitive only to the behaviour of the excited molecule within the Franck-Condon region of the excited state potential energy surface and therefore reflects the very short time dynamics of the dissociation. Once the molecule has evolved from this region into a repulsive part of the potential, the fragmenting parent and more importantly the evolving products, experience the forces inherent in this exit channel which influence the partitioning of the available energy into the separated products. To calculate an accurate potential surface for the dissociation process, it is helpful to have good idea of which degrees of freedom within the parent are involved in the dissociation dynamics. This can either be inferred from the photofragments themselves (see the following section) or measured directly using a technique pioneered by Kinsey and coworkers [69] for polyatomic molecules, resonance Raman (or spontaneous emission) spectroscopy.

When a molecule is excited up to a (rapidly) dissociative potential surface, it can evolve on this potential into photofragments or it may relax back down to the ground state potential through a radiative transition which usually occurs on a time scale of the order of tens of nanoseconds. For a reasonably direct dissociation, the molecule survives for a few tens of femtoseconds before fragmenting and dissociation will therefore be the dominant process. However, there is a tiny probability that the excited molecule will emit a photon while it

[4] If the effective potential consists of a well and a barrier, then tunnelling through the centrifugal barrier can also occur and will give rise to shape resonances [58] in the absorption spectrum.

breaks apart and return to the ground electronic state. Such an emission, known as resonance Raman scattering, into discrete ground state vibrational levels along the dissociative path is synonymous with a knowledge of the time evolution of the molecule with a sub-Angstrom resolution, in other words the dynamics on a femtosecond time scale [69, 70] [5]. Such a spectrum represents the overlap of the internal modes of the excited state parent molecule with various bound states in the lower electronic state. The overlap will be much bigger for equivalent motion in the excited and ground electronic state and the spectrum will therefore contain progression of the various vibrational modes which are 'active' during the dissociation. The relative intensity of each progression will reflect the relative importance of each mode in the dissociation dynamics[6].

Some of the illustrative examples of this technique have come from $H_2O(\tilde{A})$ [73]–[75], $H_2S(\tilde{A})$ [75]–[79] and $CH_3I(\tilde{A})$ [69, 78]. The Raman spectra for $H_2O(\tilde{A})$, for excitation wavelengths between 150 nm and 175 nm, exhibit long progressions in only the O–H stretching coordinate and do not alter significantly with photon energy. This was in agreement with the theoretical and other experimental data (see Chapter 3) which showed that only one (repulsive) electronic state was active in this absorption band and there were was no significant exit channel torque (translational to rotational energy transfer). The Raman spectrum of $H_2S(\tilde{A})$ on the other hand, as well as showing an additional weak activity in the bending mode, more importantly demonstrated a striking dependence on the excitation wavelength which was interpreted as the consequence of two overlapping electronic states [77]. This is consistent with the diffuse structure seen on the absorption spectrum [80] and the *ab initio* calculations [81]–[83].

The Raman scattering experiments of Kinsey and coworkers [69], exciting CH_3I at 266 nm found a very long progression in the C–I stretch and a very short combination progression of the C–H stretch with one quanta in the umbrella bending motion of the CH_3. This was consistent with the almost featureless absorption specrtrum [84] and the experiments of

[5] It should be noted that for an indirect dissociation, emission will primarily occur from the Franck-Condon region on the excited surface and the spectrum that is obtained will only provide the same information as the absorption spectrum.

[6] The intensity of a line in the spectrum will also reflect the vibrational dynamics in the ground electronic state which does need to be accounted for when interpreting the spectrum. This is important if calculated Raman spectrum are to be in quantitive agreement with experiment [71, 72].

Leone and coworkers [85] and Suzuki and coworkers [86], who measured the internal vibrational excitation of the CH_3 fragment and found motion predominantly in the umbrella mode. Magnetic circular dichroism (MCD) measurements [84, 87] indicated that 90 % of the intensity in the 266 nm UV absorption spectrum was due to a parallel transition to the repulsive $^3Q_0$ potential which correlates with CH_3 + $I(^2P_{\frac{1}{2}})$. A perpendicular transition would correlate with a transition to a $^1Q_1$ electronic state and the formation of $I(^2P_{\frac{3}{2}})$. At 266 nm, various experimental techniques measuring the photofragment angular distribution [87]–[94] have shown a 70:30 branching ratio between the $I(^2P_{\frac{1}{2}})$ and the $I(^2P_{\frac{3}{2}})$ channel and the velocity vector of both sets of photofragments is preferentially aligned parallel to the electric vector of the linearly polarized photolysis radiation. The initial excitation resulting in both sets of fragments is therefore solely to the $^3Q_0$ potential [1] and the $I(^2P_{\frac{3}{2}})$ channel must be opened by a non-adiabatic transition between the $^3Q_0$ and $^1Q_1$ potentials. Butler and coworkers [78] and recently Wang and Ziegler [95], using polarized emission specroscopy, were able to resolve the polarization of the emitted photons as the CH_3I molecule fragmented. At short dissociation times (corresponding to strong emission to C–H vibrational levels ≤ 4 quanta) only parallel transition photons were detected. However, further along the dissociation path, an increasing quantity of perpendicular transition photons emitted from the $^1Q_1$ potential were detected. This corresponded to a crossing between the two potentials in the exit channel and the subsequent evolution of the excited state molecule on both potentials, in agreement with the theoretical wavepacket calculations of Guo and Schatz [96] and the calculated polarized emission-spectra of Freed and coworkers [97].

1.3 Photofragment detection

The majority of photodissociation dynamics experiments concern themselves with the end product, the photofragments. With a knowledge of the parent ground state molecular motions prior to excitation into the Franck-Condon region on the excited potential energy surface, it is possible to infer from the photofragment characteristics what occurred during the dissociation. These characteristics can be measured through a variety of techniques:

- **Chemiluminescence** - When the photodissociation products are born in an excited vibrational or electronic states, analysis of the dispersed infrared and visible/ ultraviolet fluorescence respectively, can yield the fragment initial state distribution [2, 5, 16, 24, 98, 99], see Figure 1.2(a). A consideration does have to be made for the

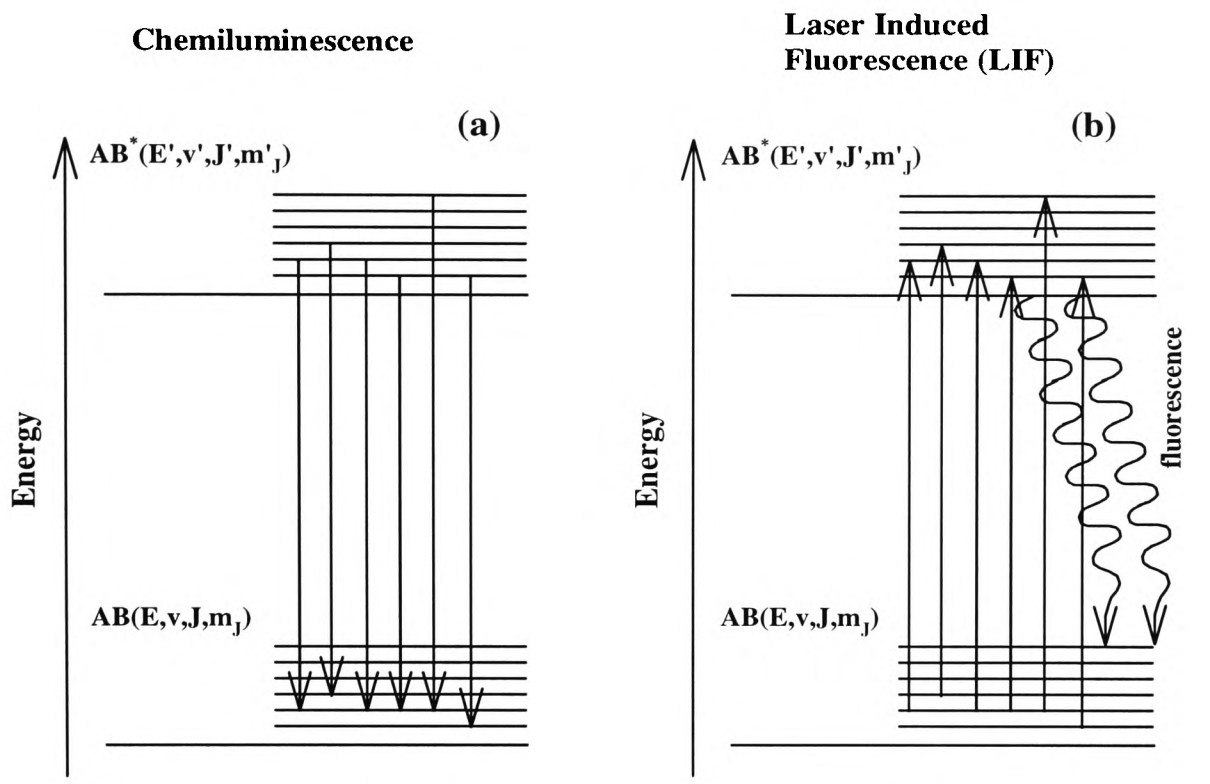

Figure 1.2 Schematic level diagram of the product detection techniques discussed in the text.

effects of long radiative lifetimes, non-radiative relaxation and predissociation, which will affect the interpretation of the relative emission intensities.

- **Laser Induced Fluorescence (LIF)** - Ground electronic state photofragments are excited from a given quantum state (the resolution of the laser radiation determines the quantum number resolution) to an intermediate electronic state from which their fluorescence is detected (see Figure 1.2(b)). Exciting the different product states by tuning the laser radiation through the correct transition frequencies, the total undispersed fluorescence intensity spectrum can be analysed to give the population distribution [98, 99]; This will be discussed in more detail in Chapter 2. If sub-Doppler laser radiation is used, it is possible to extract from the laser polarization dependence of the Doppler profile of a rotational transition, the anisotropy of the photofragment velocity and angular momentum (vector) distributions [11, 12, 18, 20, 28].
- **Fragment Ionization and Detection** - Ions can be detected with high efficiency and ionization of a photofragment, through either electron bombardment, photoionization or field ionization, is a sensitive detection technique. The simplest method is to detect the fragments with a mass-spectrometer which can be rotated with respect to the propagation direction of the photolysis radiation [14, 21, 100]. Although this method of detection is not quantum state selective, it does provide a measure of the branching ratios between the various dissociation pathways and the dissociation mechanism. Resonant absorption of m photons to an intermediate state in the photofragment from which it can be ionized by a further absorption of n photons, (Resonance Enhanced Multi-Photon Ionization, REMPI - see Figure 1.2(c)) makes the ionization process quantum state selective. Collecting the total REMPI ion yield signal as a function of m photon wavelength, this spectrum can be analysed to give fragment population distributions [98]. The mismatch of the resonant and ionization step cross sections can complicate the analysis by saturating the intermediate level and as a result the ion signal has a complex dependence on the laser power and polarization, level populations and molecular alignment [98]. If the Doppler resolved rotational line profiles of the photofragment are detected, then in a manner similar to LIF these can be used to extract the anisotopy of the velocity distribution and the velocity dependence of the angular momentum distribution [21, 101]. A more direct method of extracting the state resolved three-dimensional angular distribution of the photofragments (the differential cross section) is to use two-dimensional ion imaging

(collect the transient image of the scattered photofragment ions on a position sensitive detector) coupled with REMPI [92]–[94], [102]–[108].

With a high enough resolution of the time-of-flight ion-signal of the photofragment, it is also possible measure the rovibrational distribution of the sister photofragment, simply through conservation of energy. Until recently, this was restricted to H-atom detection, which has a sensitive enough velocity dependence on the sister quantum state to allow vibration and rotational resolution [109]–[111]. Wodtke and coworkers [112] , using the Rydberg state 'tagging' method[7] on the CO photofragment from ketene photolysis, have reported a vibrationally resolved correlated-product-state distribution[8].

- **Coherent Anti-Stokes Raman spectroscopy (CARS)** - This is a non-linear spectroscopic technique which is shown schematically in Figure 1.2(d). Anti-Stokes radiation is generated from incident radiation of frequency ω_1 and ω_2 ($\omega_1 > \omega_2$) when the frequency difference equals the frequency of a Raman active molecular transition. This Anti-Stokes radiation, which has a frequency $\omega_{AS} = 2\omega_1 - \omega_2$, is then detected [98, 99] [9]. Calculating population distributions from a CARS photofragment spectrum is not straightforward, since the relative intensities of the lines are sensitive to the relative alignment and powers of the laser and are proportional to the initial population difference between the two molecular levels connected by the CARS process. The analysis of this technique is thoroughly discussed in reference [121].

1.3.1 Rotational population distribution

The rotational population distribution of a molecular photofragment has been shown theoretically and seen experimentally to be mainly dependent on two factors

1. The rotational, bending and torsional motion of the parent molecule leaving the Franck-Condon region (from the ground state potential) on the excited state surface.

[7] Exciting the photofragment in the laser interaction region to a long-lived high Rydberg state prevents the space charge problems that accompany any tagging scheme which involves ionisation at the source [92](a), [113, 140]. The Rydberg tagged fragments are then ionized at the ion detector using weak field ionization.

[8] Product state pair correlations have also been reported using sub-Doppler LIF spectroscopy [114]–[119] and velocity-aligned Doppler LIF spectrscopy [50, 120]

[9] A Stokes wave of frequency $\omega_S = 2\omega_2 - \omega_1$ can also be generated

2. The torque generated by the anisotropy on the exited potential surface, the so called 'exit-channel effect'.

The relative contributions to the final rotational distribution made by these two factors are generally not separable. If more than one dissociation pathway produces the same photofragment (in the same electronic state) then the rotational distribution will be the weighted sum of the different contributions.

The simplest case is provided by the photodissociation of $H_2O(n = 0)$[10] in its first absorption band. This system will be discussed in greater depth along with some new experimental results [122, 123] in Chapters 3–5. Essentially, the dissociation is direct and the internal motions of the excited parent that leaves the Franck-Condon region on the excited PES are determined by the initial dynamics of the ground electronic state parent prior to photo-excitation. The exit channel torque is negligible by virtue of the similarity of the ground and excited state bending potentials and the final OH product rotational distribution can be modelled purely on the basis of the rotational (and zero-point bending vibrational) motion of the ground state parent [15, 124] - this is the so called Franck-Condon limit[11]. The angular momentum that can be generated by this motion is quite small and in the case of $H_2O(\tilde{A})$, the product rotational distribution is peaked at values of $j \leq 4$–6. However, in general the angular anisotropy on the excited state potential is not negligible and has to be included in the calculation. For a (relatively) direct photodissociation, the final product state distribution can be calculated using the rotational reflection principle [125, 126] which states that the distribution is roughly a reflection of the ground state bending wave function mediated by an excitation function above the ground state equilibrium (which directly maps the anisotropy of the excited potential at this configuration onto the distribution). The Franck-Condon model is of course the very limiting case of the rotation reflection principle when there is no exit-channel torque.

Trans-HONO($\tilde{A}$) and *trans*-DONO($\tilde{A}$) provide an example of the influence of intramolecular vibrational dynamics on state-to-state photodissociation [49]–[53], [127, 128]. The fragmentation of vibronically selected terminal NO stretching vibrations, ν_2, of *trans*-HONO($\tilde{A}$)

[10] n denoted the number of quanta of bending vibration

[11] The initially prepared distribution of fragment angular momentum states will not be altered during the fragmentation and the final distribution will reflect the bound state wave function - see Chapter 5

occurs through vibrational predissociation in which the OH(X) photofragment is produced rotationally very cold [51, 127, 128]. The OH rotational distribution is indifferent to the number of quanta of ν_2 and can be accounted for by the zero-point bending and torsional motion of the parent [52, 53], *i.e.* no final state interaction. The rotational distribution of the sister NO(X) fragment, in contrast, is strongly influenced by exit-channel torques on the excited potential surface and generates a much hotter rotational distribution ($j_{max} \sim 30$) than expected in the Franck-Condon limit [50]. State-to-state fragmentation of *trans*-DONO($\tilde{A}$) produces an OD(X) product whose rotational distribution is now dependent on the number of quanta of ν_2 vibronically selected in the parent molecule [129, 130]. This mode has been shown to be coupled to the (in plane) bending vibration which correlates with rotational excitation of the OD product [131], hence the observed correlation of increased fragment rotation with increased quanta of ν_2. This trend was reproduced by the calculated potential energy surface [52, 53] and confirms that the n$\rightarrow \pi^*$ electronic transition in the parent molecule is highly localised on the terminal N=O chromophore and has no effect on the O–H (O–D) [12].

At the other extreme to $H_2O(\tilde{A})$ is the photodissociation of $H_2O(\tilde{B})$, in which the molecular OH photofragment rotational distribution is determined by a large exit-channel torque and memory of the initial parent rotational-bending motion is essentially lost. The bending potentials of the ground and electronic state are quite different, the minimum energy configuration on the $\tilde{B}$ state being linear, compared with $\gamma_e = 104.5°$ on the ground state [132]–[135]. As a result, a large amplitude bending motion occurs upon excitation, confirmed by the emission spectra recorded by Sension and coworkers [74, 76], and produces highly rotationally excited OH($A^2\Sigma^+$) fragments [136]–[141]. Most of the available energy goes into rotation rather than translation, in contast to the dissociation of $H_2O(\tilde{A})$. As an added complication, at linear configurations, the $\tilde{B}^1A_1$ and $\tilde{A}^1B_1$ state become degenerate and the Renner-Teller pair are Coriolis coupled *via* *a*-axis rotation [143]. At extended HO–H bond lengths ($\sim$ 1.67 Å) (and linear geometry) there is also a conical intersection with the $\tilde{X}^1A_1$ state which leads to a strong vibronic $\tilde{B}$–$\tilde{X}$ coupling [134]. Both the $\tilde{X}$ and the $\tilde{A}$ state, in the bent configuration, correlate with the production of OH(X^2H). Ashfold

[12] It should be noted that the theoretical and experimental OD rotational (and vibrational) distributuions are not in quantitative agreement and indicate that the calculated potential surface is not sufficiently accurate to account for all details of the photodissociation dynamics.

and coworkers [141], using the technique of H-atom translational spectroscopy, were able to resolve the $OH(X^2\Pi)$ rotational distribution produced in the 121.6 nm photodissociation of H_2O, which is highly inverted, populating $N^{13} \approx 30$–50. The high rotational excitation is shown to be the result of the combined angular anisotropy of the two states involved in the $OH(X^2\Pi)$ production and as a consequence of the smaller torque applied on the $\tilde{A}$ state compared with the $\tilde{X}$ state, the contribution from $\tilde{B} \rightarrow \tilde{A}$ dissociation is seen as a shoulder on the distribution arising from $\tilde{B} \rightarrow \tilde{X}$ dissociation. In a recent paper, Dixon [144] has calculated the OH(X) lambda-doublet and spin-orbit population distributions produced in the photodissociation of $H_2O(\tilde{B})$, accounting for the $\tilde{B}$, $\tilde{X}$ and $\tilde{A}$ singlet states (neglecting spin-orbit coupling with the triplet states which also correlate with OH $^2\Pi$ fragments). The distributions are shown to be very sensitive functions of the initial quantum state of the parent molecule, the exit channel potentials and the value of the product rotational angular momentum quantum number.

1.3.2 Vibrational population distribution

The final vibrational state distribution of the photofragment manifests the change of its bond length along the dissociation path. The 'half collision' can be classed as either elastic, in which case there is no transfer of energy between translation and vibration, or as inelastic in which the fragment is subject to the final state interaction. For a parent molecule which has a purely elastic potential, the stretching vibrational coordinate of the diatomic fragment, R_{str} is independent of the dissociation coordinate, R_D, and as a result the mininum energy path of the exit channel will run parallel to the R_D-axis. The vibrational distribution may be cold (the Franck-Condon region lies close to the minimum energy path) or quite hot (the Franck-Condon region is displaced along R_{str}), but can be calculated using a Franck-Condon model [26, 145] (Franck-Condon mapping [146]). In the inelastic case, the excited PES exhibits a curved minimum-energy-path (the curvature increases with the coupling of R_D and R_{str}) and the fragment vibrational distribution now reflects this translational-vibrational coupling - dynamical mapping. Similar to the elastic case, the total amount of vibrational excitation still depends upon whether the Franck-Condon excitation region from the ground PES is displaced from the minimum-energy-path on the excited surface.

[13] The total OH angular momentum, excluding spin

The state-to-state photo(pre)dissociation of *trans*-HONO($\tilde{A}$) provides a good example of both Franck-Condon and dynamical mapping. The OH(X) product vibrational population distribution has been shown to be very cold [127] and the calculations of Schinke and Huber and coworkers [52, 53] showed that there is no appreciable change of the bond length of OH in going from the molecule to the free fragment (the excited parent molecule arrives on the minimum-energy-path) and there is a negligible exit channel interaction. The sister NO(X) fragment on the other hand is produced vibrationally hot [49]–[51] and is shown [52, 53] to arise from the product of an exit channel interaction and a change in the N–O bond length on the excited potential compared with the ground state equilibrium value. The actual vibrational distribution of the NO fragment has been attributed to the influence of the two competing mechanisms which are driving the vibrational predissociation of the vibronically prepared HONO($\tilde{A}$). If tunnelling through the potential barrier is the primary mechanism, then exciting a N=O stretch resonance of quantum number n^* will produce a NO fragment predominantly in the vibrational state n^* (adiabatic decay). If IVR is the dominant decay mechanism and m quanta of the excited N=O stretch need to be transferred into the dissociative N–O coordinate, then the NO fragment will be produced predominately in vibrational state n^* - m (nonadiabatic decay). The measured n^* dependence of the NO vibrational distribution shows a slight preference for a nonadiabatic decay, with a mild propensity for NO products in a final vibrational state n^* - 2.

1.3.3 Vector correlations

Absorbing linearly polarised radiation aligns a molecule with respect the electric vector $\boldsymbol{\epsilon_0}$ of the radiation, which is defined in the laboratory frame, and produces a $\cos^2\theta$ distribution of the molecule transition dipole moment $\boldsymbol{\mu}$ about $\boldsymbol{\epsilon_0}$ (θ is the angle between $\boldsymbol{\mu}$ and $\boldsymbol{\epsilon_0}$). For a direct dissociation, it has been shown that the resulting velocity, $\mathbf{v}$, and angular momentum (vector), $\mathbf{j}$, distributions of the photofragments reflect this anisotropy [147, 148]. Analysis of the correlation of $\boldsymbol{\epsilon_0}$ (*i.e* $\boldsymbol{\mu}$), $\mathbf{v}$ and $\mathbf{j}$ provides the additional 'vectorial' information which along with the 'scalar' information (internal energy distributions) creates a fuller picture of the photodissociation dynamics. The experiments presented in this thesis do not consider such vector correlations and the author refers the reader to a variety of review articles, [11, 12, 16] [19]–[21] and [28], which cover this topic.

1.4 Initial state selection and characterisation

1.4.1 Initial state selection

To differentiate between all of the contending factors which can influence how or whether an excited-state molecule can fragment, preparing the parent molecule in a well defined quantum state prior to dissociation provides a much clearer picture of the photodissociation dynamics, as well as providing a direct comparison with the detailed theoretical models of the process [8, 16, 23, 26]. The simplest case is to seed the molecules with rare gas atoms in a supersonic expansion and collapse the rotational population to a few low J states . Although this provides a degree of state selection, it is not possible to study the influence parent rotation and vibration may have in determining the final outcome of the photofragmentation. Over the past decade a variety of techniques have been developed which can provide a combination of rotational state, vibrational state and m_J state selection prior to dissociation:

- **Rovibronic Pumping** - This form of initial state selection involves pumping the ground state parent molecule up to a rotational and/or vibrational state in an excited electronic state (a rovibronic state). The excited parent can either fragment along this potential surface or absorb another photon which promotes it to an even higher dissociative electronic state. The former has been discussed earlier in the context of state-to-state predissociation on an excited electronic state. The latter is not widely used, but Brouard and coworkers [149]–[151] have carried out a resonant (one-colour) two-photon absorption on $HCO_2H(\tilde{X})$, *via* an intermediate $\tilde{A}$ rovibronic state, up to a high (repulsive) electronic state. The OH(A) photofragment fluorescence [14] was collected as a function of the laser wavelength and used to record an action spectrum of the $\tilde{A}$ state rovibronic levels (a 2-photon PhotoFragment Excitation, 2-PHOFEX, spectrum). Initially jet-cooling the ground state parent molecule can reduce the spectral congestion in the rovibronic levels and increase the level of quantum state selection of this method. Generally, rovibronic pumping does not however allow individual quantum state selection.
- **Vibrational Overtone Pumping** - This is used in the experiments presented in this thesis and is the most commonly used form of state selection [8, 23], see Figure

[14] Predissociation on $HCO_2H(\tilde{A})$ correlates with OH(X) production

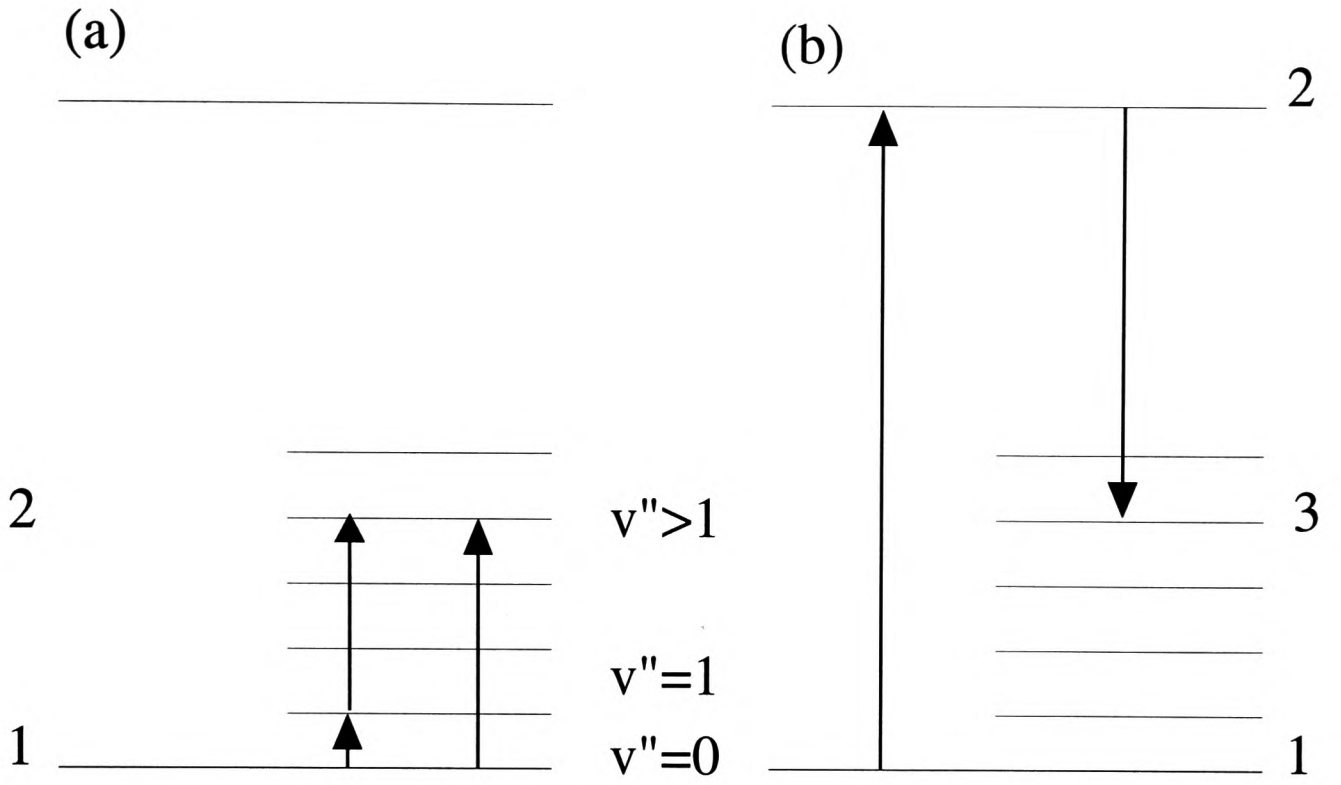

Figure 1.3 Schematic level diagram of the parent molecule rovibrational state selection techniques discussed in the text: (a) One and two-photon overtone pumping, (b) SEP and STIRAP and (c) SR pumping.

1.3(a). It has the advantage of being able to excite a molecule up to fairly high vibrational overtone levels in the ground electronic state with a reasonable efficiency. The absorption cross-section of high vibrational overtone decreases rapidly with increasing quantum number and because the strength is related to the anharmonicity of the motion, pure stretching vibrations of bonds to light atoms (*e.g.* C–H, O–H and N–H) are the strongest transitions in the near-infrared and visible region [8, 23].

- **Double-Resonance Overtone Pumping** (see Figure 1.3(a)) - For the majority of molecules, spectral conjestion does not allow individual quantum state selection, except for molecules such as H_2O which have a large enough rotational constant to give well separated rotational transitions. The usual way around this is to initially jet cool the molecule before excitation. A variation of direct overtone pumping has been developed by Rizzo and coworkers which has enabled state-to-state studies of unimolecular reactions (dissociation on the ground electronic surface - see below) [152] and some very illuminating IVR studies on high overtone levels [153]–[155]. The technique involves directly pumping a lower overtone level, usually the fundamental, and then pumping these excited molecules to the overtone level under investigation. The IR-IR double resonance transition selection rules restrict the number of final rotational states that can be populated and greatly simplifies the vibrational overtone spectrum.
- **Stimulated Emission Pumping (SEP)** - This is a variant of optical-optical double resonance in which pulsed radiation is used to prepare a molecule on an excited electronic state and a second laser then transfers the excited molecule back down to a high vibrational state in the ground electronic state [156]–[159], see Figure 1.3(b). If the lifetime of the intermediate state is long compared with the delay of the two laser pulses, then the loss of selectivity resulting from spontaneous emission during the excitation process is small. This technique, in the context of photon-induced intramolecular dynamics, has been used, for example, with great success by Houston and coworkers to probe the dissociation dynamics of metastable vibrational states above the dissociation limit in $HCO(\tilde{X})$ [160].
- **Two-Colour Laser Induced Grating Spectroscopy (TC-LIGS)** - (for a general review and a detailed description of the technique, see reference [161]). This technique has recently been applied by Chandler and coworkers [162] and Keller and coworkers [163] to the vibrationally mediated UV photolysis of H_2O and CH_3OH and by Buten-

hoff and Rohling [164] to the unimolecular dissociation of NO_2. The process involves the interaction of two phase coherent laser beams of the same frequency in the region of a vibrational overtone level. Scanning the radiation frequency, whenever the molecule absorbs (at a transition), there is a non-linear response of the medium at the point where the two beams cross and a transient diffraction grating is set up. A third laser beam, which is of enough energy to promote the vibrationally excited molecules into a dissociative state (for the VMP experiments), also crosses in the interaction region of the other beams and a small fraction of it will be diffracted by the grating in a new direction. This is then detected and can be used to study either the dynamics of the overtone level by scanning the overtone radiation or the excited state surface by scanning the UV radiation and measuring the wavelength dependence of the signal.

- **Stimulated Raman Pumping (SR)** - This is very similar to CARS (see above), where two lasers with a frequency difference that matches a Raman-allowed transition in the molecule provide a means of rovibrational state selection (see Figure 1.3(c)), pumping the molecule between the initial and final state *via* a virtual level. This has been applied by Valentini and Rosenwaks and coworkers [165]–[168] in the vibrationally mediated photodissociation of H_2O and HOD, initially exciting the fundamental OH stretching vibrational state. This method is only really efficient enough to excite the fundamental vibrations, but its potential lies in its ability to excite homonuclear vibrations, *e.g.* H_2(v) [169].
- **Stimulated Raman Scattering Involving Adiabatic Passage (STIRAP)** - (see Figure 1.3(b)) This technique is a nonlinear optical variation on SEP. It involves the coupling of the initial and final vibrational states by the radiation field of the two lasers, both tuned to be resonant with a third intermediate state. The Stokes (or dump) laser, interacts with the molecule prior to the pump laser and produces a 'trapped' state that is a combination of the initial and final state. With suitable laser intensities and optimal time delays between the two pulses, the process can have an efficiency of 100 %. To date this has only been applied to diatomic molecules [170], but may eventually prove very useful in polyatomic photodissociation studies.
- **Orienting Hexapole Electric Field** - Using an inhomogeneous electric field (*via* a hexapole rod configuration), it is possible to effect an $|JKM\rangle$ state selection for a polar symmetric top molecule, in other words orientation of the molecule's transition dipole with respect to the field vector [31]. It has been shown by Stolte and coworkers

[171] that the photodissociation of an oriented ensemble of molecules can offer more detailed dynamical information than the dissociation of an initially isotropic ensemble. In particular, it is possible to separate the contributions made to the photofragment angular distribution due to the direction of the parent transition dipole from those due to the dissociation dynamics. Very recently Kim and coworkers [172] have reported the first $|JKM\rangle$ state selected photodissociation experiment, photolysising oriented CD_3I at 266 nm and state specifically detecting the CD_3 fragment in its N,K rotational level. Although the M state of the CD_3 fragment were not resolved, this type of experiment can provide the most detailed probe of the photofragmentation process.

1.4.2 Initial state characterisation - local modes and IVR

Henry and Seibrand [173] found that X–H stretching overtone bands (X = O, C or N) of a molecule were better described in terms of local modes rather than the standard normal modes [174], and the energy levels could be defined by those of a single mode Morse oscillator (localised excitation). Localisation of vibrational excitation into specific degrees of freedom will affect the rate of both intra- and intermolecular reactions. A great deal of theoretical input has gone into understanding this topic over the years and a comprehensive review and bibliography is given in references [175]–[179]. For an AB_2 molecule, *e.g.* H_2O, the vibrational Hamiltonian can be written as

$$\hat{H} = \hat{H}_0 + \hat{H}_{coupling} + \hat{H}_{anharmonic} \tag{1.2}$$

where $\hat{H}_0$ is the zeroth order Hamiltonian of two identical harmonic oscillators, $\hat{H}_{coupling}$ is the coupling term between other vibrational states and $\hat{H}_{anaharmonic}$ is the anharmonicity term. The transition between a vibrational state being described as normal mode and local mode may be characterised by the relative magnitude of the second and third terms in equation 1.2. Quantum mechanical studies of Stannard and coworkers [180], Mortensen and coworkers [181] and Child and coworkers [182] showed that the local/normal character of the eigenstates depended upon the ratio $(\lambda/\omega x)$, where λ is the coupling parameter and ωx is the anharmonicity parameter. Local character was attributed to states that appeared in pairs split by an energy difference small compared to the energy difference to neighbouring states in the spectrum and normal character to all the other states. The splitting between the states of local character can be described as tunnelling between degenerate local modes

[183]–[185]. States of the same total quantum number v are grouped in the vth polyad, which contain the $(2v + 1)$ states whose degeneracy is lifted by the anharmonicity. Weak coupling, strong anharmonicity (*i.e.* $(\lambda/\omega x) < 1$) and high excitation favour local character states.

For the majority of molecules, the degree of localisation lies somewhere between the two limiting descriptions of purely local and normal modes and the vibrational eigenstates can be either 'described' using normal mode basis functions (including the anharmonicity) or using local mode basis functions (including the coupling terms), both methods being completely equivalent [186, 187]. As a result there is no simple physical picture of the vibrational motion excited in the molecule within a given eigenstate. In the context of state selection in photodissociation dynamics, it is obviously important to know exactly which and to what extent the different degrees of freedoms in the parent are excited during the selection process. The understanding of the specific mechanisms which control intramolcular vibrational energy redistribution (IVR) is essentially contained within a knowledge of the zeroth-order vibrational state carrying the oscillator strength of the transition from the ground level (the bright state), the nearly isoenergetic zeroth-order states that do not carry any oscillator strength (the dark states) but are coupled to the bright state, and the strength and type of the coupling [188, 189]. The author would refer the reader to references [8, 156, 157] and [188]–[191] for a thorough review of this field of research.

To conclude this section and to highlight some of the information that can be obtained experimentally on IVR, three studies which use state-to-state photodissociation to probe the IVR within the intermediate parent rovibrational state will be discussed. Rizzo and coworkers [154], studying the $4\nu_{OH}$ overtone in $HONO_2$, used subsequent excitation above the ground state dissociation threshold and monitored the OH fragment. Their results show that although the overtone consisted of a clean rotational contour, the largest collective contribution is from zeroth-order dark states that have zero quanta of O–H stretch and the zeroth-order bright state is only a minor component of the eigenstate at that energy. Brouard and Mabbs [192] alternatively, used UV excitation to an excited (dissociative) electronic state to probe the coupling to the O–O stretch in $H_2O_2(4\nu_{OH})$. Probing one of the OH photofragments, a J and K dependent (specifically about the a and b inertial axes) coupling to the dissociation coordinate was found, which was reflected in the photofragment energy distributions and relative cross-section data for σ_{00}, the photodissociation cross-

section out of the intermediate overtone state.

Crim and Rizzo and coworkers [152, 153, 193] in an extensive set of work investigated the unimolecular dissociation of $H_2O_2 \rightarrow$ OH(X) + OH(X), exciting either 'pure' O–H stretching overtones ($5\nu_{OH}$ and $6\nu_{OH}$) or in combination with other lower frequency degrees of freedom (ν_{OO} and ν_{OOH}). Comparing the OH fragment internal state distributions with the calculated distributions using a variety of statistical models which assume complete IVR within the time scale of the dissociation [194]–[196] does reveal that IVR is not complete on the timescale of the dissociation. In addition, measurement of the J–K dependent linewidths of individual eigenstates suggests an a-axis Coriolis interaction is the primary coupling mechanism.

Chapter 2 VMP of $H_2O(\tilde{A})$ and $HOD(\tilde{A})$: Experimental and data analysis

$$ABC(\tilde{X}) \xrightarrow{\lambda_1} ABC(\tilde{X}v, J) \xrightarrow{\lambda_2} ABC(\tilde{A}) \longrightarrow A + BC \overset{\lambda_3}{\rightarrow} {}^{LIF}$$

To study the vibrationally mediated photodissociation (VMP) dynamics of a molecule ABC, as indicated in the equation above, requires three tunable radiation sources, λ_1, λ_2 and λ_3. For the two experiments presented here, the VMP of $H_2O(\tilde{A})$ and $HOD(\tilde{A})$, this was accomplished with just two radiation sources, setting $\lambda_2 = \lambda_3 \approx 282$ nm (probing the (1–0) $A^2\Sigma$–$X^2\Pi$ LIF band of the OH/OD photofragments) and initially exciting the third and fourth stretch vibrational overtone with λ_1.

In Section 2.1, the laser system used to generate λ_1, λ_2 and λ_3 is outlined, with attention being made to the energy output requirements of the lasers made by the experiment. The chamber used to perform both the VMP experiments and the photoacoustic measurements of the vibrational overtones is described in Section 2.2. These acoustic measurements, which were used to tune λ_1 to a rovibrational overtone transition before attempting the VMP experiment, are described in Section 2.3. The procedure for collecting the LIF signal of the VMP photofragments, is given in Section 2.4. Finally, in Section 2.5, the effect saturation has on the calculation of the relative population distributions from the recorded photofragment LIF spectra is discussed.

2.1 Laser system

A XeCl excimer laser (Lambda Physik LPX205i) was used to pump two Lambda Physik LPD3000 dye lasers, whose output provided the two tunable radiation sources required for the experiment; one produced the infrared pulse (λ_1) and the other produced both the photolysis (λ_2) and the LIF probe (λ_3) pulses. A schematic of the experimental apparatus and setup used is shown in Figure 2.1.

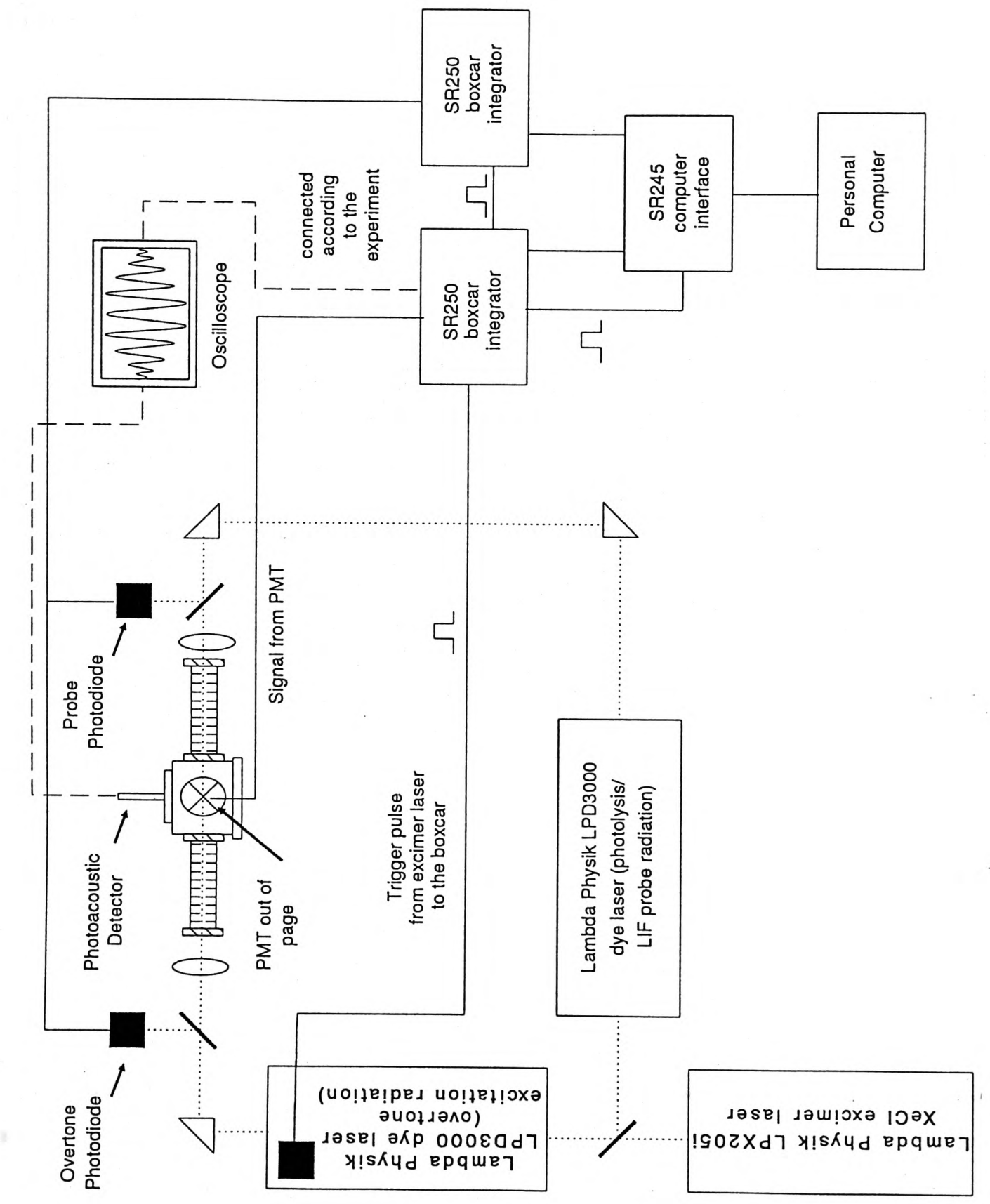

Figure 2.1 Schematic of the experimental setup and equipment used in the vibrationally mediated photodissociation (VMP) studies.

2.1.1 Excimer pump laser

The excimer laser was operated at or close to its peak energy of 400 mJ/pulse, with a 15Hz reprate. The beam was split into two with a 50:50 beam splitter to provide $\approx$ 200 mJ/pulse of the 308 nm radiation to each of the dye lasers. As will be mentioned later in the text, ensuring maximum efficiency and power output from the dye lasers, especially for the overtone excitation radiation, was critical in producing data of good enough quality to allow accurate analysis of the raw data. Regular monitoring and maintenance of the excimer laser throughout the study was therefore of great importance to the success of the experiments. Gas mixtures were changed every 2-3 weeks to keep the energy output always above 350 mJ/pulse. The high repetition rate the excimer was fired at (15Hz) reduced the operating lifetime of the gas mixture considerably, but was found to produce the best results, giving good signal-to-noise ratios and shorter scanning times.

Triggering of the excimer laser during the experiments was controlled by one of the dye laser controllers. The high laser power needed for the photolysis photon (λ_2) meant that the photofragment LIF probe, which used the same radiation source, produced a very saturated signal (see Section 2.5.3). In order to guarantee this was always the case throughout each experiment, the triggering stability of the excimer laser (*i.e.* its power output) was continually monitered. No fluctuations were ever seen and the LIF raw data could be analysed using the same procedure.

2.1.2 Overtone excitation dye laser

One of the two dye lasers used during these experiments produced the near-infrared/visible tunable radiation neccessary for pumping the vibrational overtone rotational transitions in the molecules studied. The dye laser itself was a standard Littrow-type laser, with a high grating efficiency and a radiation output bandwidth of ≈ 0.2 cm^{-1}. A typical beam diameter of 2.5 mm and good collimation ensured little radiation loss before entering the reaction chamber. Throughout the VMP experiments the laser beam was focussed down into the centre of the chamber using a quatrz lens (f $\approx$ 500 mm); this increased the signal-to-noise levels of the LIF signal by at least by a factor of four due to the increase the flux of the laser radiation pulse, enhancing the number of molecules within the detection region that are excited into the vibrational overtone. In addition, it was found necessary to focus

Vibrational transition	Rotational transition	Absorption Cross-Section σ / cm^2 molecule^{-1}	Excitation efficiency
$\|04\rangle^- \leftarrow (0,0,0)$	$0_{00} \leftarrow 1_{01}$	$6.54\text{x}10^{-24}$ (a)	0.15 %
	$4_{04} \leftarrow 3_{03}$	$33.78\text{x}10^{-24}$ (a)	0.78 %
$\|05\rangle^- \leftarrow (0,0,0)$	$0_{00} \leftarrow 1_{01}$	$1.87\text{x}10^{-24}$ (b)	0.04 %
	$4_{04} \leftarrow 3_{03}$	$1.42\text{x}10^{-24}$ (b)	0.03 %

(a) Taken from reference [197]

(b) Taken from reference [198]

Table 2.1 Absorption cross sections for some of the strong lines in the $H_2O|04\rangle^-$ [197] and $H_2O|05\rangle^-$ [198] spectra. Also shown are the corresponding estimated excitation efficiencies with the experimental setup presented in this chapter.

the photolysis radiation for similar reasons and having both laser beam diameters the same within the centre of the cell increased the overall efficiency of the double-resonance scheme. The very weak absorption cross-sections of the vibrational overtone states investigated ensured that the rotational transitions would not be saturated even when the radiation was focussed down. The absorption cross-section for some of the strong $H_2O|04\rangle^-$ and $|05\rangle^-$ rotational transitions are given in Table 2.1 [197, 198], along with the estimated excitation efficiencies with this experimental setup[1].

The laser dyes used to produce the tunable infrared/visible radiation needed in these experiments are listed in Table 2.2 along with the average energy output during the experiment and the tuning ranges used to excite the different bands.

2.1.3 Photolyis/LIF probe dye laser

The second dye laser, in conjunction with a β-Barium Borate (BBO-1) frequency doubling crystal was used to produce both the photolysis (λ_2) and the LIF probe (λ_3) laser radiation. The nature of the molecular systems studied was such that the photon energy required to interrogate the VMP photofragments was also the energy needed to photolyse the state-

[1]The beam area at the focus of the 500 mm focal length lens is calculated as being 0.0267 mm^2

Vibrational Overtone Level	Lambda Physik Dye	Average Energy Output	Band Tuning Range
$H_2O(\tilde{X})$ $\|04\rangle^-$	Rhodamin 700 (LC7000)	17 mJ/pulse	716–730 nm
$H_2O(\tilde{X})$ $\|05\rangle^-$	Rhodamin 6G (LC5900)	25 mJ/pulse	588–595 nm
$H_2O(\tilde{X})$ $\|04\rangle\|2\rangle^-$	Rhodamin 6G	–	590.5–595 nm [a]
$HOD(\tilde{X})$ (4,0,0)	Rhodamin 700	–	716–730 nm
$HOD(\tilde{X})$ (5,0,0)	Rhodamin 6G	–	587–597 nm

(a) This only covered the R-branch transitions, to the band origin.

Table 2.2 The laser dyes used to produce the tunable radiation needed to excite the rotational transitions of the vibrational overtone levels studied in these experiments. Also shown are the average energy output maintained throughout the work and the tuning ranges used the record the P,Q and R-branch transitions of each band.

LIF band	Lambda Physik Laser Dye	Average Energy Output	Band Tuning Range
$OH(A^2\Sigma–X^2\Pi)$ (1–0)	Coumarin 153 (LC5400)	23 mJ/pulse	562.2–569.0 nm
$OD(A^2\Sigma–X^2\Pi)$ (1–0)	Coumarin 153	–	574.3–579.6 nm

Table 2.3 The laser dyes used to produce the tunable UV radiation needed to monitor the LIF bands of the photofragments produced in the VMP process. Also shown are the average power output maintained throughout the work and the tuning ranges used.

selected parent molecules. Scaning across the small OH(D) A←X(1-0) LIF spectral range, the change in the total supplied energy in the VMP process (from the change in the energy of λ_2) is $\sim$ 420 cm^{-1} for OH and $\sim$ 320 cm^{-1} for OD. This is a very small change compared with the total supplied energy ($\sim$ 49300 cm^{-1} for the VMP of $H_2O/HOD(4\nu_{OH})$ and $\sim$ 52400 cm^{-1} for the VMP of $H_2O/HOD(5\nu_{OH})$) and will therefore not effect the interpretion of the data.

To produce the ultraviolet tunable radiation needed to monitor the photofragments, the fundamental output from the laser dyes listed in Table 2.3, were frequency doubled using a BBO-1 doubling crytal, suitable for the energy ranges used. To separate out the funda-

mental from the doubled radiation either a UG5 broad-band filter or Pellin-Broca prism was used. The dye laser produced a well collimated laser beam, minimizing the radiation loss before it entered the reaction chamber, even though the path length was greater for the probe radiation. The beam was focussed down with a quartz lens (f $\approx$ 25 cm) to the centre of the chamber for the VMP experiments.

2.2 Experimental chamber

A schematic of the experimental chamber used for the VMP experimental work is shown in Figure 2.2. This stainless steel chamber was setup for a collinear arrangement of the incoming laser beams and each side arm was fitted with a spectrosil-B window. Interference from scattered light in the viewing region of the photomultiplier was minimized by having baffled side arms and a matt black surface on the inside. An aperture at the side of the chamber allowed the laser-induced fluorescence to be collected at right-angles to the propagation of the laser beams. An iris was placed in front of both side arms to aid the alignment of the two laser beams straight through the centre of the chamber. This was critical for the VMP experiments as the LIF signal-to-noise ratios were only acceptable when both beams were fully overlapped within the viewing region of the photomultiplier at the centre of the cell.

A microphone (Knowles CF Series), attached to the top of the chamber by a stainless steel rod, was used to photoacoustically record the rovibrational spectra of the overtone transitions studied (see Section 2.3 for details). The distance between the microphone and the laser beams could be adjusted and during the VMP experiments the microphone was raised to the top of the chamber to reduce scattered light.

The chamber was evactuated with an oil diffusion pump (Edwards E09) backed by a two-stage rotary pump (Edwards 40), which provided a static pressure of $\ll 10^{-3}$ Torr (determined by a MKS baratron attached to the cell). The H_2O / HOD gas was flowed into the cell *via* a bulb attached to the chamber and a needle valve was used to maintain a steady pressure in the cell. The HOD was made with a 5:1 mixture of H_2O and D_2O (99.95 % pure, Aldrich Chemical Ltd). To ensure collision free conditions and still have a large enough molecular density to give good signal-to-noise levels, an optimum pressure of 100 mTorr was used throughout the VMP experiments. During the photoacoustic measurements, the chamber

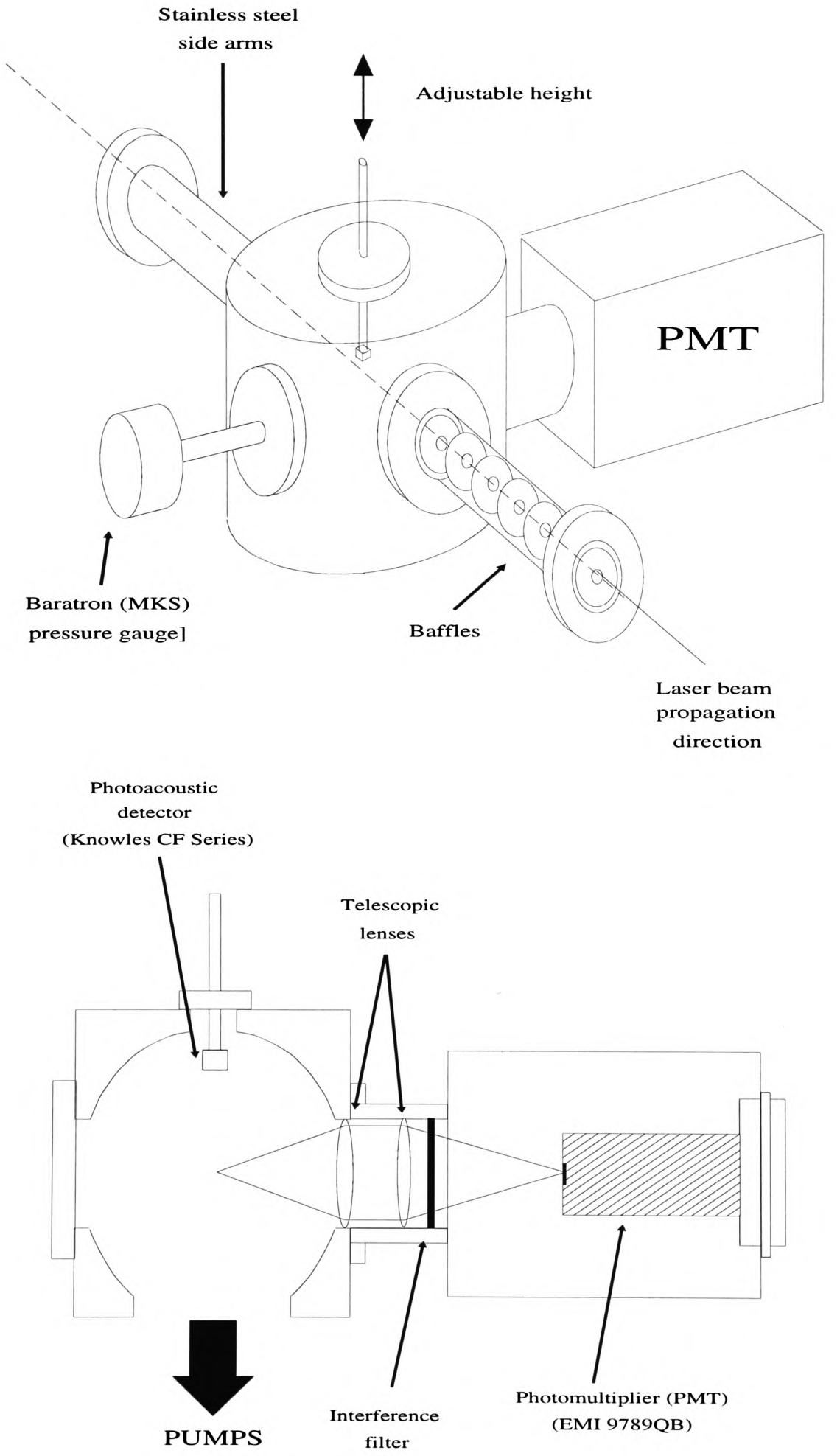

Figure 2.2 Schematic of the experimental chamber used during the VMP experiments. Also shown is the position of the photoacoustic microphone and the telescopic lens arrangement used for LIF fluorescence collection at the photomultiplier.

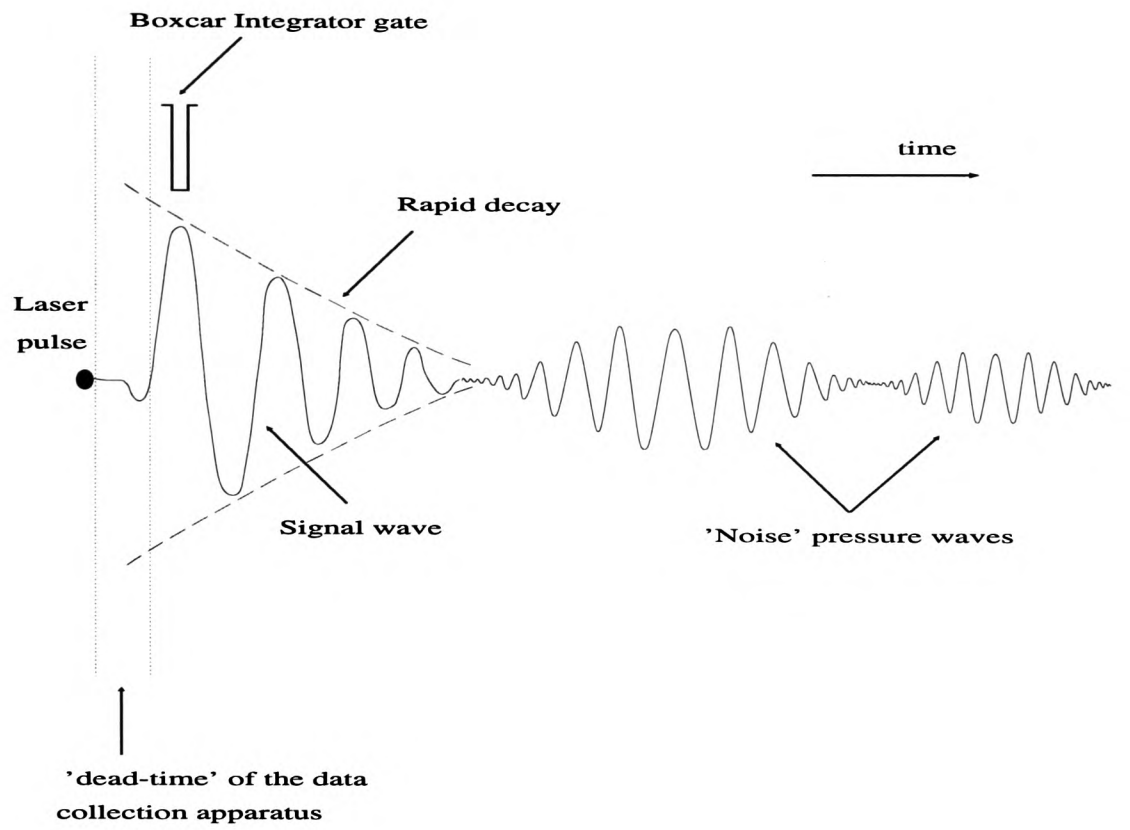

Figure 2.3 Schematic representation of the photoacoustic signal and the 'position' of the detector and boxcar integrator gate. Note the width of the gate with respect to the signal wave.

was isolated from the vacuum pumps and filled upto the vapour pressure ($\approx$ 17 Torr) of H_2O or HOD.

2.3 Photoacoustic spectroscopy

Pulsed laser photoacoustic spectroscopy was used as a means of accurately measuring the line positions of the rotational transitions of the vibrational overtone and combination bands employed in the study before attempting the VMP experiments. This was a very sensitive and accurate method of recording these very weak transitions. The technique involves the formation of thermal pressure waves in the gas due to absorption of the laser radiation by the molecules, which are then detected with a microphone; the intensity of the wave reflects the extent of the absorption. Unlike the conventional use of cw laser radiation, pulsed laser excitation provided a more sensitive experimental approach to photoacoustic spectroscopy and detection [199, 200]. Pulsed excitation provides temporal resolution of the photoacoutic signal (*vs.* phase resolution in the cw technique), which makes it possible to separate the

molecular absorption signal from backround cell wall and window signal waves (see figure 2.3). The sensitivity of photoacoustic detection is primarily limited by the magnitude of the background signal, and rejection of a large portion of it by temporal resolution leads to higher signal-to-noise ratios. This made detection of the high vibrational overtone and combination levels utilised in this study much easier.

The photoacoustic detector (a Knowles CF Series microphone) was positioned $\approx$ 5–6 mm from the overtone excitation laser beam at the centre of the chamber. As is shown in figure 2.3, the signal wave hits at the detector first, followed by pressure waves caused by reflections off cell walls and windows. The boxcar integrator gate (see below) needed to be positioned (in time) where the signal wave was at its maximum for optimal sensitivity. To prevent any damage to the microphone, it could not be placed any closer to the laser beam than $\sim$ 3 mm. Including the 'dead time' of the data acquisition equipment (the time between signal detection and arrival for collection), the best signal was found by placing the detector $\sim$ 5–6 mm away from the laser beam. The signal from the microphone was fed through a fast pre-amplifier before being transferred to a gated boxcar integrator (Stanford Research System SRS250). The unaveraged and integrated signal was then sent to a PC, *via* an computer A$\rightarrow$D interface (Stanford Research System SRS245), for shot-by-shot collection and averaging (typically over 30–50 laser shots) on a home-made data acquisition program.

The boxcar gate delay and width were set at the peak of the pressure wave and although a gate width of 15 μs was employed, only a few percent of the signal could be collected. A better detection efficiency could be obtained with a longer boxcar gate width, but even with this reduction in sensitivity, the signal-to-noise ratios were good.

2.4 LIF data acquisition

With the aid of the photoacoustic detection of the vibrational overtone levels monitored in this study, the overtone dye laser was tuned to particular rotational transitions. LIF spectra of the resulting VMP OH/OD photofragment were then be recorded, scanning the probe dye laser across the ranges given in Table 2.3. To improve the signal-to-noise level of the data collected, each LIF spectra was recorded at least three times and then averaged.

The collected fluorescence was focussed onto the photocathode of a UV sensitive photomul-

tiplier (PM) tube (EMI 9789QB) using two quartz lenses in a telescopic arrangment. To reduce the amount of laser light seen by the PM tube, a 310 nm-centered, 10 nm fwhm interference filter was placed in front of the detector (Figure 2.2). This was centered on the (1–1) $A^2\Sigma$–$X^2\Pi$ band of the OH/OD photofragments whose fluorescence was collected after pumping the (1–0) band at $\lambda_3 \approx 282$ nm. To record all of the populated rotational levels in the OH and OD photofragment, fluorescence had to be collected between $\approx$ 306.3 – 312.2 nm and $\approx$ 306.6 – 309.6 nm respectively. The transmittance of the interference filter, centered at 310 nm, drops by 5 % (of the peak transmittance) at the two extreme wavelengths of the fluorescence. Corrections were made to the LIF spectrum to account for this drop-off, but in practice, this actually made little difference to the resulting population distributions.

The output from the PM tube was either fed directly into a gated boxcar integrator and amplifier (Stanford Research System SR250) or *via* a high gain (x100) fast amplifier, depending on the signal level of the experiment. The photomultiplier was operated between 1.2 and 1.4 kV (the fast amplifier reducing this by 0.2 kV). An identical boxcar integrator (SR250) was used to simultaneously collect the output from a photodiode which monitored the pulse energy of the probe laser during the data collection. The photodiode was calibrated before the experiment to ensure a linear response to the laser pulse energy throughout the experiment. The unaveraged, integrated LIF and power signals were sent to a PC *via* a computer A→D interface (Stanford Research System SR245) for shot-by-shot collection and averaging (typically over 30–50 laser shots).

2.5 OH/OD LIF spectral analysis

The photofragments produced in the vibrationally mediated 282 nm ($\tilde{A}$←$\tilde{X}$) photolysis of H_2O and HOD, $OH(X^2\Pi)$ and $OD(X^2\Pi)$ respectively, are produced primarily in their ground vibrational state. Although no measurements of any v=1 photofragments were made[2], this conclusion can be drawn from work of Crim and coworkers [201]–[203]. Photolysing the third stretching vibration overtone of H_2O with 218, 240 and 266 nm radiation, decreasing the photolysis energy reduced the percentage of OH in v=1 from $\approx$ 5 %, at 218 nm, to $<$ 2 % at 266 nm; an identical result was obtained for the VMP of HOD. It can be expected

[2]None of the LIF bands which probe the population of $v = 1$ in OH or OD are within an energy range that could also be used to provide a photolysis photon sufficient to excite the state-selected parent molecules up to the $\tilde{A}$ electronic state.

that photolysis with 282 nm radiation will produce > 99 % of the VMP photofragments in v=0.

The LIF (1–0) vibrational bands of the OH and OD $A^2\Sigma$–$X^2\Pi$ system that are used to determine the photofragment rotational energy distribution, are well characterised and assigned [204, 205]. Predissociation can occur from the upper state of OH and OD, competing with the fluorescence and this has to be taken into account in the interpretation of the LIF spectra. For $OH(^2\Sigma)$, predissociation into a repulsive $^4\Sigma^-$ electronic state, has been shown to occur for $N \geq 23$ in $v = 0$ and $N \geq 14$ for $v = 1$ [206, 207]. Similarly, for $OD(^2\Sigma)$, predissociation into the repulsive state occurs for $N \geq 35$ in $v = 0$ and $N \geq 28$ in $v = 1$ [207, 208]. The hydroxyl photofragments produced in the photodissociation of H_2O and HOD *via* the $\tilde{A}$ state, are produced rotationally cold (see Chapters 3 and 4). The LIF radiation will therefore only excite the OH/OD fragments into $A(^2\Sigma)$ rovibrational levels that are well below the onset of predissociation and no correction had be made to the recorded LIF spectra in this study.

2.5.1 Spin-orbit and Λ-doublet ratios

The spectroscopy of ground state OH and OD is very well understood, as is the importance Λ–doubling in helping the interpretation of the dynamics of a molecular process [209]–[214]. The spin-orbit coupling at low rotational numbers in the ground electronic state of both OH and OD is large and well descibed by Hund's case (a). Through the interaction of the nuclear rotation and orbital angular momentum, each of the resulting spin-orbit states ($^2\Pi_{\frac{1}{2}}$ and $^2\Pi_{\frac{3}{2}}$), are further split into Λ-doublets, A′ and A″. As the nuclear rotation increases, the OH(OD) quantum states become increasingly better characterised by Hund's case (b). With regards to data analysis, this is highly significant, as the electron density in both the Λ-doublets, intially both cylindrically symmetric, become either completely symmetric (A′) or antisymmetric (A″) with respect to reflection in the rotational plane in the high J limit. The pΠ lobe of the unpaired valence electron is then either aligned along J (A″) or perpendicular to J (A′), and become chemically distinct. Dynamical preferential population of a particular Λ-doublet is possible, reflecting the dynamics of the molecular process. This can be measured through analysis of the main branch Q (probing Π(A″)), P and R (probing Π(A′)) lines for the OH(OD) $^2\Sigma^+ \leftarrow ^2\Pi$ transition.

2.5.2 Determination of saturation levels in the LIF measurements

As a result of the laser powers needed to produce acceptable LIF signal-to-noise levels in the VMP experiments (see section 2.1.3), the OH and OD rotational transitions were found to be saturated. The effect this has on population measurements has been discussed by various authors for both partial and full saturation. In the limit of full saturation, modified expressions (much simpler than those for no saturation) for extracting the population from LIF spectra have been formulated by Altkorn and Zare [215]. For partial saturation extraction of populations is rather more complex. However, Kinsey and coworkers [216] have developed a model which can correct, with reasonable accuracy, for any degree of saturation on LIF measurements. The determination of the photofragment relative population distributions was the main undertaking in this study and no attempt to measure the rotational alignments of the OH or OD were made. Although this is relatively straightforward for full saturation (see below), extraction of the rotational alignment from measurements with partial saturation is much more involved.

To determine which regime was applicable to these experiments, ratios of intensities of main branch lines to those of the corresponding satellite branch lines were measured (*e.g.*, Q_{11} and Q_{21}, R_{22} and R_{21} [3]). Such pairs of lines probe the same lower $X^2\Pi$ state but with substantially different transition strengths [217, 218], especially for high rotational states.

The intensity ratio of the main branch transitions and their corresponding satellites for N=7 (where N is the OH(OD) total angular momentum quantum number excluding spin) for all of the OD and OH LIF spectra were measured at least three times. The fragment rotational distributions from both the VMP of $H_2O(\tilde{A})$ and $HOD(\tilde{A})$ are very cold, only populating as far as $N \approx 10$, but predominantly $N \leq 5$. Choosing N=7 gave a large enough difference between the line strengths of the main and satellite transitions and a good signal-to-noise ratio. The values obtained, using either peak heights or integrated areas ranged from between 0.9 and 1.0 ± 0.05. Considering the transition strengths of the satellites were between 10–20 times smaller than their main branch lines, the LIF spectra were certainly close to the fully saturated regime.

[3] The notation used here is that of Dieke and Crosswhite [204], $\Delta N_{f'f''}$, where N is the total angular momentum excluding spin and f′ and f″ label the spin orbit manifolds involved in the transition

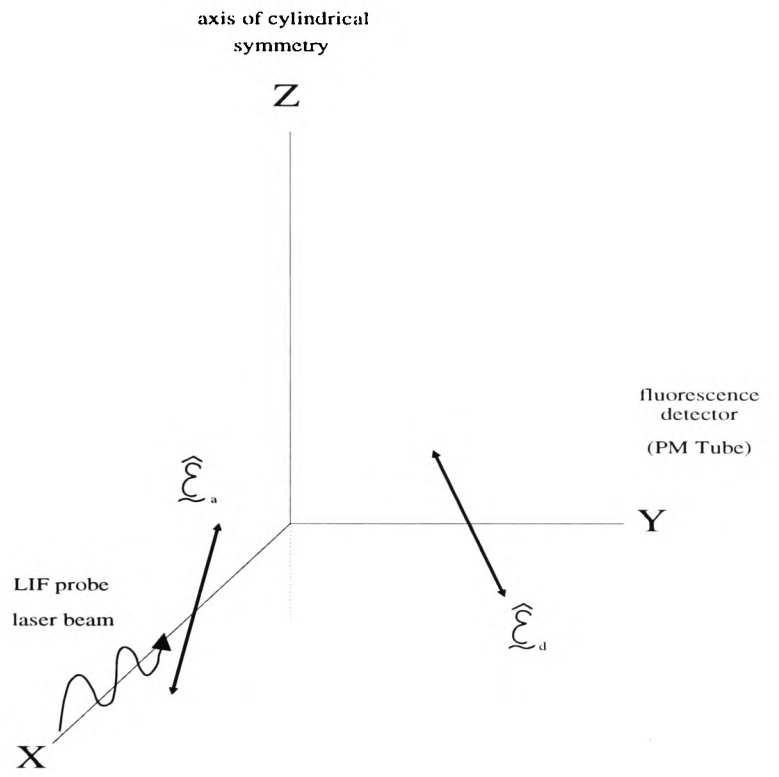

Figure 2.4 Right angled LIF excitation-detection geometry. Molecules are excited by a linear polarized laser $\hat{\varepsilon}_a$ incident along the X axis. Fluorescence is detected along the Y axis and the Z axis is chosen to lie along the axis of cylindrical symmetry.

2.5.3 The effect of full saturation on population measurements

The experimental arrangement used in this study is the traditional right angle excitation-detection geometry in which the laser is incident along the X axis with linearly polarization $\hat{\boldsymbol{\varepsilon}}_{\boldsymbol{a}}$, and fluorescence detected along the Y axis (see Figure 2.4). Although the detector used in these experiments is not sensitive to the polarization of the fluorescence, the expressions outlined below are developed for polarized fluorescence detection. The correct averaging over the two geometries is carried out to derive the final expression used to extract the relative populations from the LIF spectra.

The LIF intensity in the limit of no saturation can be expressed as [215]:

$$I = Kn \int \frac{(\sum_{l=0}^{\infty} a_l P_l(\cos\theta))\, a_{21} b_{12} \rho}{2b_{12}\rho + A_{21}} \{1 - \exp[-(2b_{12}\rho + A_{21})\Delta t_L]\} d\Omega \qquad (2.1)$$

in which

K is a constant depending on the details of the detection system

n represents the total concentration of molecules in the state of interest

a_{21} and b_{12} are directional (or differential) Einstein coefficients

A_{21} is the integrated Einstein A coefficient

ρ is the radiation density (energy/unit volume/unit frequency interval)

Δt_L is the laser pulse duration

for an angular momentum distribution $n(\theta)$ expressed as an expansion of Legendre polynomials:

$$n(\theta) = n \sum_{l=0}^{\infty} a_l P_l(\cos\theta)$$

l is restricted to even integers for a cylindrically symmetric distribution of **J**, as is produced in photodissociation; θ is the angle between the **J** vector of the molecule and the Z axis.

In the limit of very strong saturation, $b_{12}\rho\Delta t_L \gg 1$ (and $b_{12}\rho \gg A_{21}$) and equation 2.1 reduces to

$$I = \frac{Kn}{2} \int [1 + a_2 P_2(\cos\theta)] a_{21} d\Omega \tag{2.2}$$

The fluorescence intensity is therefore independent of the Einstein B coefficient and the laser power because half of the molecules in the probed state are excited regardless of their line strengths. From equation 2.2, Altkorn and Zare have calculated expressions for the saturated fluorescence signal for different fluorescence branches and detection polarizations. These are given Table 2 of Ref. [215]. It is important to note that the fragment rotational alignment term, a_2, can still be determined even under these conditions, but only with fluorescence polarization and branch resolved detection. However, with the experimental setup used in this study, detecting unpolarized and unresolved branch fluorescence, integrating equation 2.2 and performing the correct averaging over the fluorescence branches and polarization [219, 220] gives for the fluorescence intensity in these experiments:

$$I = K'n \tag{2.3}$$

K′ is a constant dependent only on the detection system and not on the rotational transition or alignment.

This expression for the LIF intensity is valid for peak height measurements under fully saturated conditions. As well as affecting the fluorescence intensity, full (and partial) saturation also alters the linewidth (and hence the integrated area) of the transitions in the LIF spectra. Power or saturation broadening causes a change in the linewidth which is

proportional to $(\rho B_{12})^{\frac{1}{2}}$, ρ being the laser power and B the line strength [99]. Relative populations were calculated from the LIF raw data, either directly with peak height or integrated area measurements (making no corrections for line strength or laser power), or by integrated area measurements, normalising with $(\rho B_{12})^{\frac{1}{2}}$. The photofragment population distributions calculated from peak heights or integrated areas, with or without line strength or power normalisation, were found to be identical within the experimental error. The effect of power broadening seems therefore to be small, either because the LIF lineshape is dominated by Doppler broadening [99] or because of the fact that the line strengths in OH(1–0) and OD(1–0) do not vary much between the the six main branch transitions [217, 218]. To further substantiate the choice of analysis of the LIF data, the OH photofragment rotational distributions produced in the H_2O VMP study are compared with those obtained from the previous experimental studies of Crim and coworkers [201] (see Chapter 3). Wherever the theoretical calculations predict that the product distributions from this study should be indistinguishable with those of Crim, the agreement is consistently good [122].

Chapter 3 The VMP of $H_2O(\tilde{A})$: Experimental results

$$H_2O(\tilde{X}^1A_1) \xrightarrow{\lambda_1} H_2O(\tilde{X}^1A_1; v, J) \xrightarrow{\lambda_2} H_2O(\tilde{A}^1B_1) \rightarrow H(^2S) + OH(X^2\Pi_\Omega; N'') \xrightarrow{\lambda_3, LIF}$$

Presented in this chapter are the experimental results of the 282 nm photodissociation of the water molecule excited into the third and fourth stretching vibrational overtone and a stretch-bend combination band of the same energy as the fourth stretch overtone. The OH($^2\Pi$;v=0) photofragment rotational distributions for all three intermediate parent states are presented in Section 3.3, arising from a range of initial parent angular momentum states and a comparison is made with the corresponding distributions from previous experimental studies. A preferential population in both of the OH fragment spin-orbit and lambda-doublet states is considered in Sections 3.4 and 3.5 respectively. To begin the chapter however, a brief outline of the previous studies into the photodissociation dynamics of $H_2O(\tilde{A})$ is presented.

3.1 Previous studies

The photodissociation of water in its first absorption band has become a model system for studying direct photodissociation processes over the last ten years. As mentioned in Chapter 1, the molecule fragments on only one excited (repulsive) potential surface which has a negligible angular (γ) and bond-length (r) dependence in the exit-channel. As a result, most of the energy available for the photofragments ($\sim$ 80 %) is channeled into translational energy, and the OH product is produced rotationally cold. The OH product is also produced with a reasonable amount of vibrational excitation, which is a result of the instantaneous motion of the parent along the saddle point (symmetric stretching motion) in the Franck-Condon region of the excited PES. Decreasing the photolysis energy moves the Franck-Condon region away from the saddle point and creates a strong photon-energy dependence in the OH vibrational distribution.

Many elegant and pioneering experiments have investigated both the direct photolysis [34, 212], [221]–[223] and the state-to-state photodissociation dynamics [34, 122, 165, 166, 201, 224, 225]. In addition, resonance Raman studies [73, 74] and measured state-to-state vector correlations [166, 221] have added to the vast amount of information available on this system. The water molecule is also small enough for full *ab initio* calculations to be reliable. Precise semiempirical [226]–[229] and *ab initio* [40, 228, 230, 231] calculated potential energy surfaces (PES) for the two electronic states and the $\tilde{A}$–$\tilde{X}$ dipole function [40, 230] have provided a detailed knowledge of the bound-state energy levels [175, 182] and an interpretation of the photodissociation dynamics induced upon $\tilde{A}$–$\tilde{X}$ excitation [40, 41, 122, 224, 232, 234, 235].

Schinke and coworkers [40], calculating the state-to-state photodissociation cross-sections and the total absorption spectrum, were able to replicate the measured spectrum [236] and assign the diffuse structure in the spectrum. From the same study, predictions were made about the effects of different photolysis photon wavelengths (for direct photodissociation) on the vibrational distribution of the OH(X) photofragment. At the time, the only experimental work available for comparison was that of Andresen and coworkers [15, 34, 212], using 157 nm and 193 nm radiation; the results were consistent with those of Andresen. Decreasing the photolysis energy progressively removed any vibrational excitation in the fragment OH. Comes *et al.* [222] recently remeasured the 157 nm photodissociation and also photolysed water *via* a two-photon excitation at 354.6 nm (corresponding to 177.3 nm). They found much less vibrational excitation in the OH fragment than Andresen had earlier measured and than the calculations had predicted. Rosenwaks and coworkers [223] have since repeated the 354.6 nm two-photon photodissociation and obtained the same results. This discrepancy has so far been associated with an error in the excited-state potential used in the calculations [222]. Engel *et al.* [124] commented that shifting the barrier energy to correct the calculated vibrational distributions, as was suggested initially, would completely destroy the agreement of the calculated with the experimental absorption spectrum. This puzzle will be discussed further in chapter 5.

The vibrationally mediated photodissociation experiments of Crim and coworkers [201], initially exciting $H_2O|04\rangle^-$, considered the effects of three different photolysis wavelengths (218, 239.5 and 266 nm) on the OH fragment vibrational distribution. With a total supplied energy equivalent to a single photon with a wavelength of $\geq$ 170 nm, their findings are in

accord with those of Comes *et al.* and Rosenwaks *et al.* and again in disagreement with the *ab initio* calculations.

The calculation of the fragment rotational distributions have met with greater success through the satisfactory modelling of the experimental distributions [34, 201, 232] using the Franck-Condon model of Balint-Kurti [233]. This implies that final-state interactions in the exit channel are of minor importance, at least at supplied energies less than that required for excitation above the H + OH → OH + H reaction barrier on the $\tilde{A}$-state surface. This is reinforced by the resonance Raman studies of Sension *et al.* [73, 74], who found motion purely in the dissociation coordinate R_{H-OH} during the fragmentation, consistent with a negigible angular dependence of the $\tilde{A}$ state potential surface.

The OH lambda-doublet population distributions, from the state-to-state experiments of Andresen *et al.* [15, 34] ($H_2O|01\rangle^-$ [1] + 193 nm), Rosenwaks *et al.* [165] ($H_2O|01\rangle^+$ [2] + 193 nm), Crim *et al.* [201] ($|04\rangle^-$ and $|13\rangle^-$ [3]+ 239.5 nm) and Nesbitt *et al.* [225] ($|03\rangle^-$ + 248 nm), were found to be highly structured, non-statistical, and depended sensitively on the initial parent rotation state $J_{Ka,Kc}$ [4]. Further work by Crim and Schinke and coworkers [224], through initial excitation of the stretch-bend combination bands $|03^-1\rangle$ and $|03^-2\rangle$, looked at the effect of bending vibration on the photofragment rotation. The calculated distributions using the Franck-Condon model were in reasonable accord with the experimental measurements, although exit channel effects were believed to be responsible for the slight cooling of the rotational distributions compared with those expected from the Franck-Condon limit. The similarity between these experimental studies, for population distributions derived from the same parent initial rotational state, led to the conclusion that the photofragment rotational excitation is insensitive to both the intermediate OH stretching state selected in the ground state water molecule and to the dissociation photon energy [124]. No account of the OH stretching motion was taken in the calculations, which

[1] This can also be written as (0,0,1) in the normal-mode vibration notation, (ν_1, ν_2, ν_3), for the water quantum states [237].

[2] This can be written as (1,0,0) in the normal-mode notation.

[3] For higher vibrational quantum states in the water molecule, the local-mode notation, $|mn^{\pm}k\rangle$, where m and n refer to the number of quanta in the OH local mode stretches and k to the number in the bend, gives a better desciption than normal-mode vibrations [175, 182].

[4] J is the parent total angular momentum and K_a and K_c refer to the quantum number K, the projection of J along the internuclear axis, in the prolate and oblate symmetric rotor limit respectively.

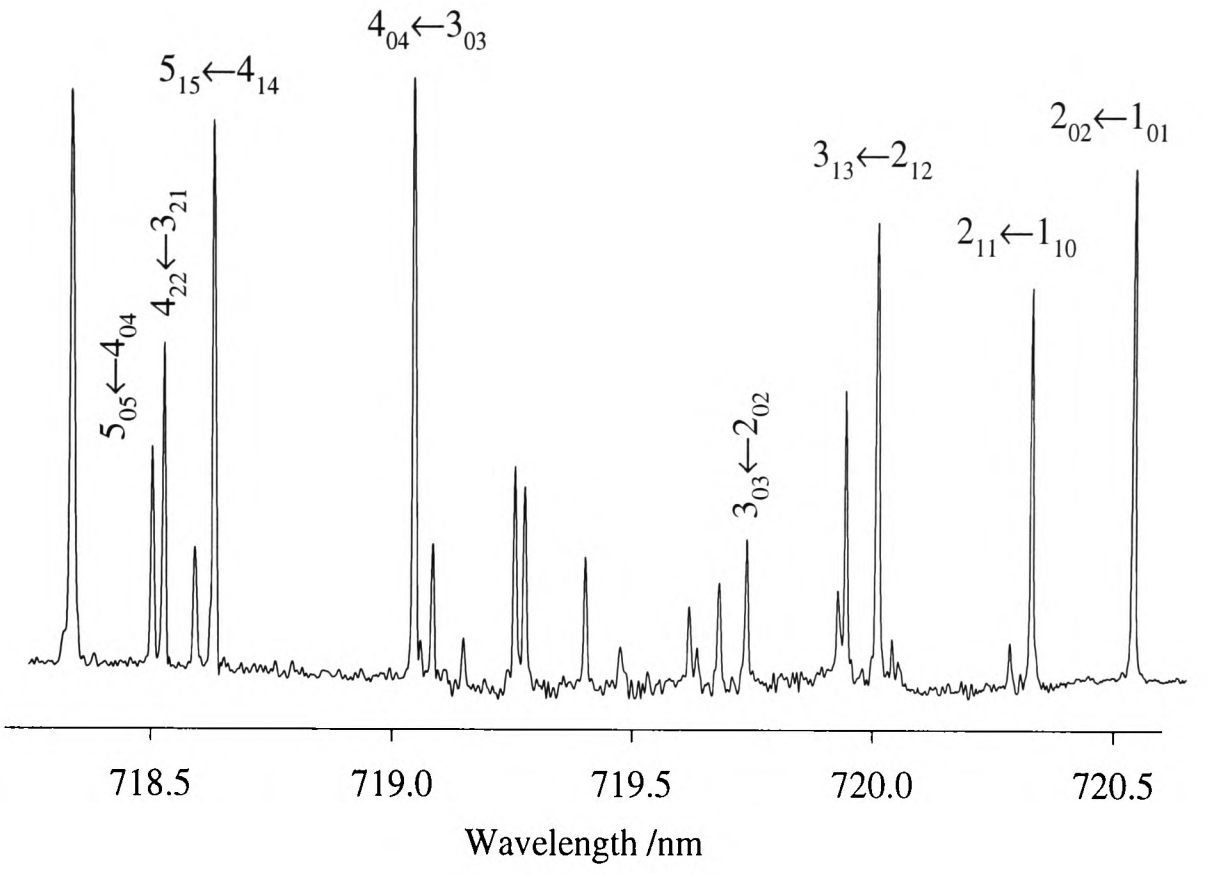

Figure 3.1 Segment of the third stretching vibrational overtone spectrum of water in the region of the $|04\rangle^-$ local mode eigenstate. Assignment of the rotational transitions was made using the papers of Mecke [238] and Mandin and coworkers [197].

implied a rather weak stretch-bend coupling in the ground (and excited) state(s) of water [124, 224], a conclusion that is consistent with the vibrational energy structure of $H_2O(\tilde{X})$ [175, 182].

The state-to-state experiments of Crim [201] also focussed upon the effect of the initial parent vibrational motion upon the OH photofragment vibrational distribution. For the $|04\rangle^-$ vibrational state, the OH is produced predominantly in its lowest vibrational state v=0 ($\approx$ 98 %), with very little in v=1 ($\approx$ 2 %). For the $|13\rangle^-$ vibrational state, although very similar in energy to $|04\rangle^-$, only $\approx$ 16 % of the OH is produced in v=0, with $\approx$ 84 % born in v=1. The vibrational distribution is shown to reflect the nodal character of the ground state parent vibrational wavenfunction along the nondissociative bond coordinate. This indicated that the vibrationally mediated photodissociation process preserves the initial excitation in the undissociated bond because it accesses regions of the excited electronic

potential surface where the interaction between the two bonds is small [124, 201].

3.2 Intermediate H_2O rovibrational states

3.2.1 $H_2O|04\rangle^-$ overtone spectrum

A segment of the third stretching vibrational overtone spectrum of water in the region of the $|04\rangle^-$ local mode eigenstate is shown in Figure 3.1. This nomenclature refers to the symmetry-adapted local mode contribution to the molecular eigenstate made by the pure local mode states $|04\rangle$ and $|40\rangle$ ($|nm\rangle$ refers to the number of quanta of stretching vibration in the two bond oscillators m and n),

$$|04\rangle^- = \frac{1}{\sqrt{2}}(|04\rangle - |40\rangle) \ .$$

It has previously been shown through both classical, semiclassical and quantum mechanical studies [175] that the high vibrational states in water are very well described by the local mode picture. In the nomenclature of Child and Lawton [182], the parameter ξ indicates whether a normal [174] or local mode description is more suited to a particular molecule. This is given by

$$\xi = \tfrac{2}{\Pi} \arctan\left(\tfrac{\lambda}{\omega x}\right)$$

$$\xi \longrightarrow 0 \quad - \quad \textit{Local Mode Limit}$$

$$\xi \longrightarrow \pm 1 \quad - \quad \textit{Normal Mode Limit}$$

in which

λ is an interbond coupling parameter for the molecule and

ωx is the anharmonicity parameter for the vibrational motion.

For the water molecule, Child and Lawton reported a value of ξ=-0.34, which is sufficient to separate the $|04\rangle^-$ and $|05\rangle^-$ overtone (see the following section) from the other vibrational states in their vibrational manifolds [175, 182]. Another 'measure' of the local mode character in H_2O is given by Reimers and Watts [227], who, using symmetry-adapted linear combinations of (local-mode) basis functions (SALCBF) to describe the vibrational eigenstates of H_2O, quote the percentage contribution to each eigenstate attributable to the SALCBF used to label it. For $H_2O|04\rangle^-$, a value of 97 % is quoted, clearly indicating that

Transition	Wavelength
$0_{00} \leftarrow 1_{01}$	723.897 nm
$2_{02} \leftarrow 1_{01}$	720.488 nm
$2_{11} \leftarrow 1_{10}$	720.274 nm
$3_{13} \leftarrow 2_{12}$	719.965 nm

$3_{03} \leftarrow 2_{02}$	719.692 nm
$4_{04} \leftarrow 3_{03}$	719.006 nm
$4_{22} \leftarrow 3_{21}$	718.477 nm
$5_{15} \leftarrow 4_{14}$	718.583 nm

$5_{05} \leftarrow 4_{04}$	718.455 nm
$2_{11} \leftarrow 2_{12}$	722.203 nm
$3_{13} \leftarrow 3_{12}$	724.863 nm
$4_{22} \leftarrow 4_{23}$	723.073 nm

Table 3.1 Rotational transitions excited in the $H_2O|04\rangle^-$ overtone state during the 282 nm VMP experiments. Assignments are taken from the papers of Mecke [238] and Mandin and coworkers [197].

the description, of four quanta of stretching vibration localised in one bond and none in the other, is very good. This is of course very useful in the analysis and interpretation of the data from this study and from the previous work.

A full list of all the rotational transitions excited in this overtone is given in Table 3.1. The large rotational constant of water separates the transitions enough to allow excitation of a single rotational state with only modest resolution. The nomenclature used in this thesis for the parent rotational states refers to J_{K_a,K_c}, where J is the parent total angular momentum and K_a and K_c refer to the quantum number K (the projection of J along the internuclear axis) in the prolate and oblate symmetric rotor limit respectively. As is shown in Table 3.1, the OH LIF spectra were recorded by pumping R↑ transitions in the parent molecule. Figure 3.2 shows the $OH(X^2\Pi_{\frac{3}{2}})$ rotational distributions arising from the 282 nm photodissociation of $H_2O|04\rangle^-$ $J_{J_a,K_c} = 2_{11}(R\uparrow)$ and $2_{11}(Q\uparrow)$. Apart from a difference in the signal-to-noise level of the LIF data, the photofragment spectra were found to be insensitive to the choice of the branch employed. A similar result is seen for $J_{H_2O} = 3_{13}$ and 4_{22}. As was discussed in Section 2.5.3, the LIF spectra were taken to be fully saturated, and as a result, were insensitive to rotational alignment of the photofragment OH with respect to the electric vector of the photolysis laser radiation (*i.e.* the H_2O $\tilde{A}$–$\tilde{X}$ transition dipole moment). Similarly, any information on the effect of the alignment of the parent molecule with respect to the electric vector of the overtone excitation laser radiation, seen through a $\mu_{H_2O(\tilde{A})} - J_{OH}$ vector correlation measurement, will also be lost.

In the same spectral region of the $|04\rangle^-$ overtone are seven other local mode eigenstates, three belonging to the same vibrational manifold (four quanta of stretching vibration), $|13\rangle^{\pm}$

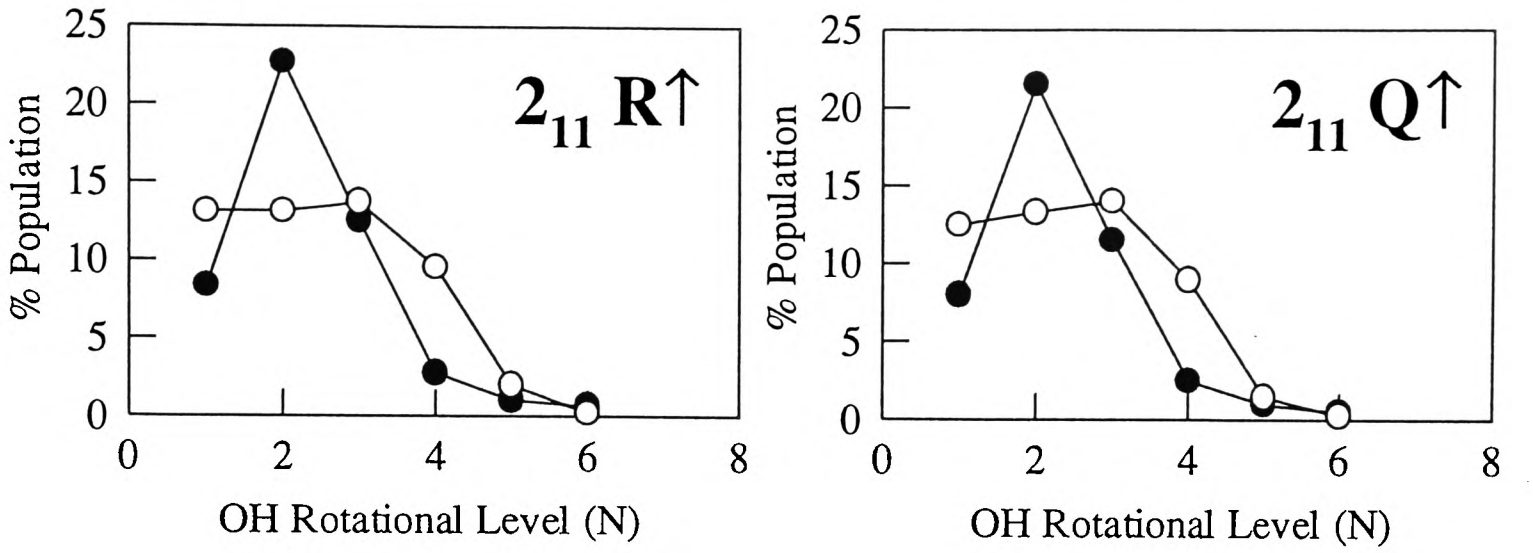

Figure 3.2 The photofragment $OH(X^2\Pi_{3/2})$ population distributions (plotted against N, the total angular momentum quantum number excluding spin) within the A′ (•) and A″ (○) lambda doublet levels arising from the photodissociation of $H_2O|04\rangle^-$ ($J=2_{11}$ R↑ and Q↑).

and $|04\rangle^+$, and the rest to another manifold, $|12\rangle|2\rangle^\pm$ and $|03\rangle|2\rangle^\pm$ (here $|mn\rangle|k\rangle^\pm$ is used to denote excitation of k quanta of bending vibration in addition to the stretching vibration [5]). Characteristic of good local mode states, the band origin energy gap between $|04\rangle^-$ and its sister state, $|04\rangle^+$, is very small (2.6 cm^{-1}) and is well separated from the rest of the eigenstates within the $4\nu_{OH}$ manifold, the closest, $|13\rangle^+$, being 390.2 cm^{-1} higher in energy [183, 238, 239]. The band origins of the stretch-bend combination bands are ≈170 cm^{-1} higher ($|12\rangle|2\rangle^\pm$) and lower ($|03\rangle|2\rangle^\pm$) in energy with respect to $|04\rangle^-$. Examination of the overtone spectrum around the rotational transitions used in this study [238, 239] shows no obvious indication of any resonant rotational states or transitions from the other local mode bands. Using the spectroscopic data available, only rotational states that belong to the $|04\rangle^-$ overtone are excited in these experiments, allowing a complete characterisation of the rotational and vibrational motion of the ground state water molecule prior to photolysis.

3.2.2 $H_2O|05\rangle^-$ overtone spectrum

[5] Throughout this thesis, whenever a local mode eigenstate is referred to without specifying bending vibration excitation, the k quantum number is dropped from the nomenclature.

Transition	Wavelength
$0_{00} \leftarrow 1_{01}$	592.333 nm
$2_{02} \leftarrow 1_{01}$	590.048 nm
$2_{11} \leftarrow 1_{10}$	589.907 nm
$3_{13} \leftarrow 2_{12}$	589.720 nm
$4_{04} \leftarrow 3_{03}$	589.144 nm
$4_{23} \leftarrow 3_{22}$	589.017 nm
$4_{22} \leftarrow 3_{21}$	588.669 nm
$5_{15} \leftarrow 4_{14}$	588.886 nm
$5_{05} \leftarrow 4_{04}$	588.771 nm
$6_{06} \leftarrow 5_{05}$	588.323 nm
$7_{17} \leftarrow 6_{16}$	588.295 nm
$2_{11} \leftarrow 2_{12}$	591.206 nm
$3_{13} \leftarrow 3_{12}$	593.004 nm
$4_{22} \leftarrow 4_{23}$	591.397 nm

Table 3.2 Rotational transitions excited in the $H_2O|05\rangle^-$ overtone state during the 282 nm VMP experiments. Assignments are taken from the papers of Mecke [239] and Camy-Peyret and coworkers [198].

3.2.2 $H_2O|05\rangle^-$ overtone spectrum

A segment of the fourth stretch overtone in the region of the $|05\rangle^-$ local mode eigenstate is shown in Figure 3.3. The upper half shows the photoacoustic spectrum and the lower half of the figure shows the VMP action spectrum, recorded by fixing the photolysis radiation on the OH photofragment LIF $A^2\Sigma$–$X^2\Pi$ (1–0) $Q_{11}(2)$ transition and scanning the overtone excitation radiation. The excellent signal-to-noise ratios observed is a characteristic of the large enhancement of the total photodissociation cross-section when using the VMP scheme [23].

The energy splitting between $|05\rangle^-$ and $|05\rangle^+$ is 0.4 cm^{-1} [175, 227, 198], compared with 2.6 cm^{-1} for the $|04\rangle^\pm$ local mode doublet. This pattern of increasingly close local mode doublets at higher energies, is characteristic of good local mode character in a molecular vibration. Reimers and Watt [227] quote a value of 98 % local character for this overtone level and it is well described by the excitation of five quanta of stretching vibration in one of the O–H bonds and none in the other.

In the spectral region of the $|05\rangle^-$ state, there are three other local mode eigenstates, one belonging to the same vibrational manifold, $|05\rangle^+$ (*c.f.* three for $|04\rangle^-$), and two to another manifold, $|04\rangle|2\rangle^\pm$ (*c.f.* four for $|04\rangle^-$). An examination of the overtone spectrum around the rotational transitions listed in Table 3.2 reveals no obvious signs of coincidental resonances with rotational states or transitions of the other local mode bands [239, 198] and only rotational states corresponding to the $|05\rangle^-$ overtone are excited up to the $\tilde{A}$ electronic

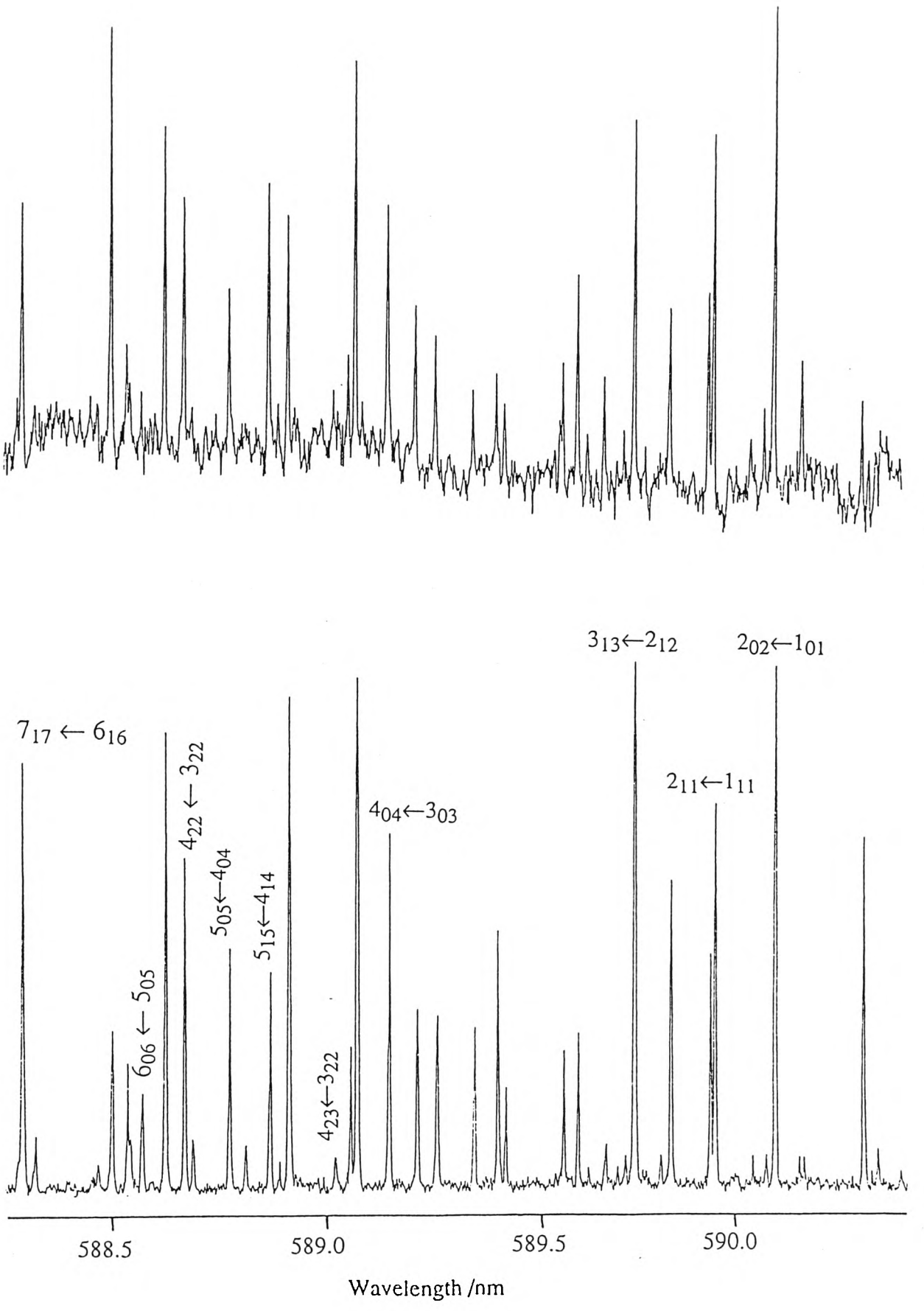

Figure 3.3 Segment of the fourth stretching vibrational overtone spectrum of water in the region of the $|05\rangle^-$ local mode eigenstate. The top spectrum is recorded using photoacoutic spectroscopy and the bottom is the VMP action spectrum, recorded by fixing the photolysis radiation on the OH photofragment LIF $A^2\Sigma$–$X^2\Pi$ (1–0) $Q_{11}(2)$ transition and scanning the overtone excitation radiation.

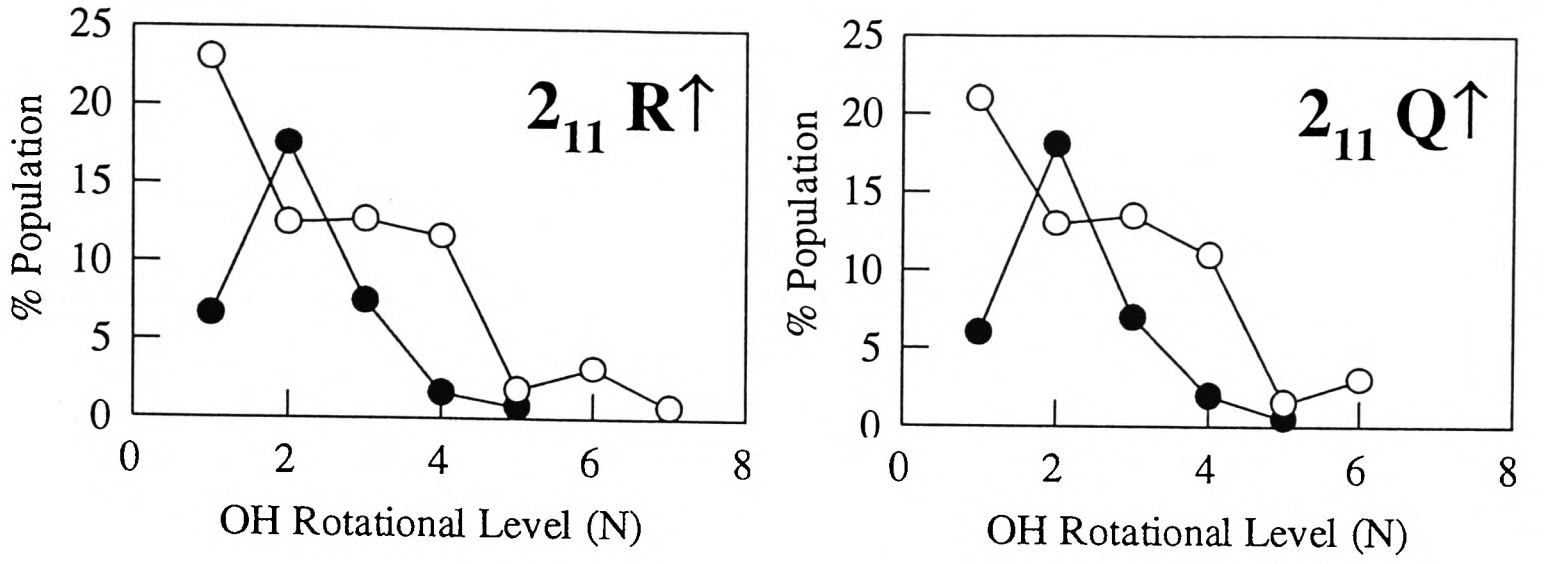

Figure 3.4 The photofragment $OH(X^2\Pi_{3/2})$ population distributions (plotted against N, the total angular momentum quantum number apart from spin) within the A′ (•) and A″ (○) lambda doublet levels arising from the photodissociation of $H_2O|05\rangle^-$(J=2_{11} R↑ and Q↑).

and coworkers [241]. Figure 3.4 shows the OH $^2\Pi_{\frac{3}{2}}$ population distribution arising from the photodissociation of $H_2O|05\rangle^-$ $J = 2_{11}$ R↑ & Q ↑. The photofragment spectra were again found to be insensitive to the choice of the overtone rotational branch employed.

3.2.3 $H_2O|04\rangle|2\rangle^-$ overtone spectrum

The band origin of the $|04\rangle|2\rangle^-$ combination state is only ≈ 77.2 cm^{-1} lower in energy than the $|05\rangle^-$ overtone, but much weaker in intensity [176, 241]. A segment of the VMP action spectrum within the region of these two levels is shown in Figure 3.5, recorded by fixing the LIF probe radiation on the OH(A–X) $Q_{11}(2)$ transition and scanning the overtone excitation radiation. The two strongest rotational transitions in the $|04\rangle|2\rangle^-$ state are labelled and may be compared with the $|05\rangle^-$ $0_{00} \leftarrow 1_{01}$ line (∗) which is also labelled. A full list of the transitions that were excited in this study is given in Table 3.3. The obvious reduction in the absorption cross-section of the combination level meant that OH photofragment rotational distributions could be obtained with a reasonable degree of precision from only a few intermediate parent rotational states. The $0_{00} \leftarrow 1_{01}$ transition was unfortunately too weak to provide a comparison with the earlier work of Crim and coworkers [224] on the

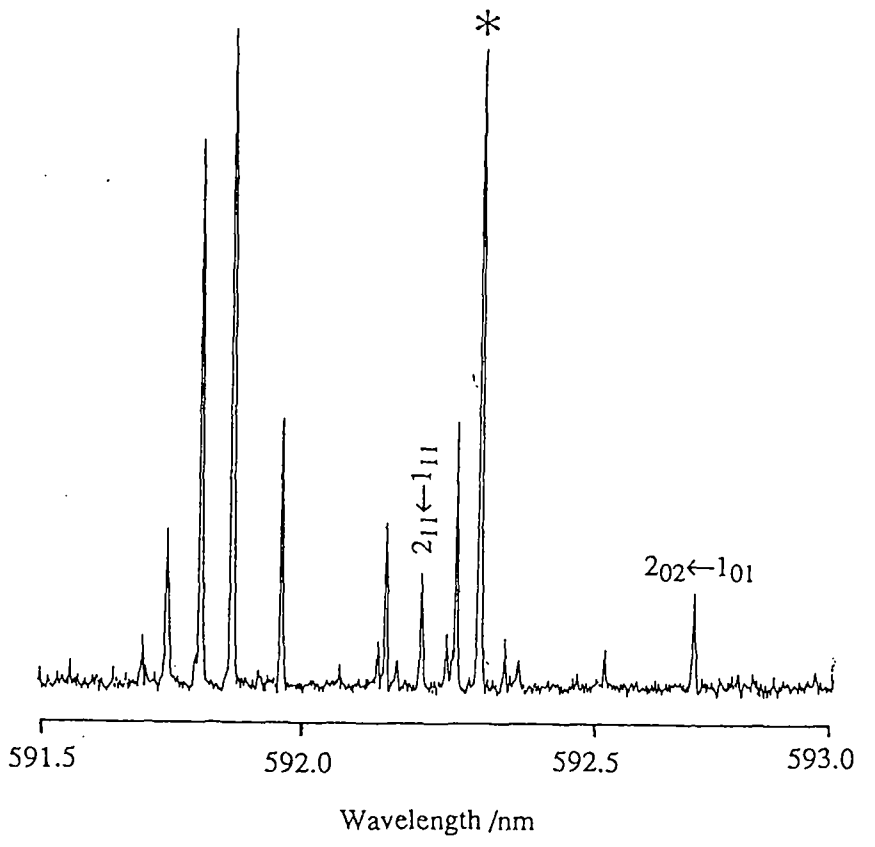

Figure 3.5 Segment of the VMP action spectrum in the region of the $|04\rangle|2\rangle^-$ and $|05\rangle^-$ overtone levels in the water molecule. The J=0 transition of the $|05\rangle^-$ state (*) and the two strongest $|04\rangle|2\rangle^-$ transitions are labelled.

Transition	Wavelength
$2_{02} \leftarrow 1_{01}$	592.745 nm
$2_{11} \leftarrow 1_{10}$	592.412 nm
$4_{13} \leftarrow 3_{12}$	590.985 nm

$4_{22} \leftarrow 3_{21}$	590.807 nm
$5_{15} \leftarrow 4_{14}$	591.326 nm

Table 3.3 Rotational transitions excited in the $H_2O|04\rangle|2\rangle^-$ overtone state during the 282 nm VMP experiments. Assignments are taken from the papers of Mecke [240] and Camy-Peyret and coworkers [241].

a few intermediate parent rotational states. The $0_{00} \leftarrow 1_{01}$ transition was unfortunately too weak to provide a comparison with the earlier work of Crim and coworkers [224] on the $|03\rangle|2\rangle^-$ level.

3.3 OH photofragment rotational state distributions

3.3.1 The 282 nm VMP of H_2O $|04\rangle^-$ *via* the $\tilde{A}$-state

The 282 nm photodissociation of water, initially selected in the third stretch overtone level, generates an excess energy of $E_{AVL} \approx 8000$ cm^{-1} for disposal in the photofragments, some 6000 cm^{-1} less than in the experiments of Crim and coworkers [201], Andresen and coworkers [34] and Rosenwaks and coworkers [165]. From simple Franck-Condon and energy conservation arguments, these experiments should preferentially sample the bound state wavefunction at larger internuclear separations, as demonstrated in Figure 3.6. The ground state potential of Jensen and coworkers [229] and the excited state potential of Steammler and Palma [40, 230] are plotted as a function of the dissociation coordinate, R_{HO-H}, fixing R_{H-OH} at its equilibrium value of 0.970 $\AA$. The significance of the apparent preferential excitation from a classically forbidden region of the ground state potential for the 282 nm photodissociation of the $H_2O|04\rangle^-$ will be discussed in chapter 5.

The OH photofragment $A^2\Sigma$–$X^2\Pi$ (1–0) LIF spectrum arising from the 282 nm photodissociation of $H_2O|04\rangle^-$ $J_{K_a,K_c} = 5_{15}$. is shown in Figure 3.7. The signal-to-noise ratio seen here is typical of the LIF spectra recorded in this experiment. Inspection of the R_{11} branch profile (probing OH $^2\Pi_{\frac{3}{2}}A'$) and the Q_{11} branch (OH $^2\Pi_{\frac{3}{2}}A''$) clearly shows that the population distributions for the two lambda-doublet OH states are very different. The OH LIF spectrum, arising from each rotational state excited in the parent $|04\rangle^-$ vibrational state, is recorded at least 3–4 times, and the rotational distributions are calculated from an average of these spectra. The difference between this and the distributions calculated from the individual spectra provides an estimate of the experimental error, which is calculated to be $\pm$ 5 % for the least populated OH levels.

It is also noteworthy that there is an unfortunate overlap of the $Q_{22}(1)$ and $Q_{22}(3)$ rotational transitions [204]. The OH $^2\Pi_{\frac{1}{2}}(A'')$ level is probed by only one LIF main branch line (Q_{22}), unlike its sister lambda-doublet state which is probed by both the P_{22} and R_{22} transitions.

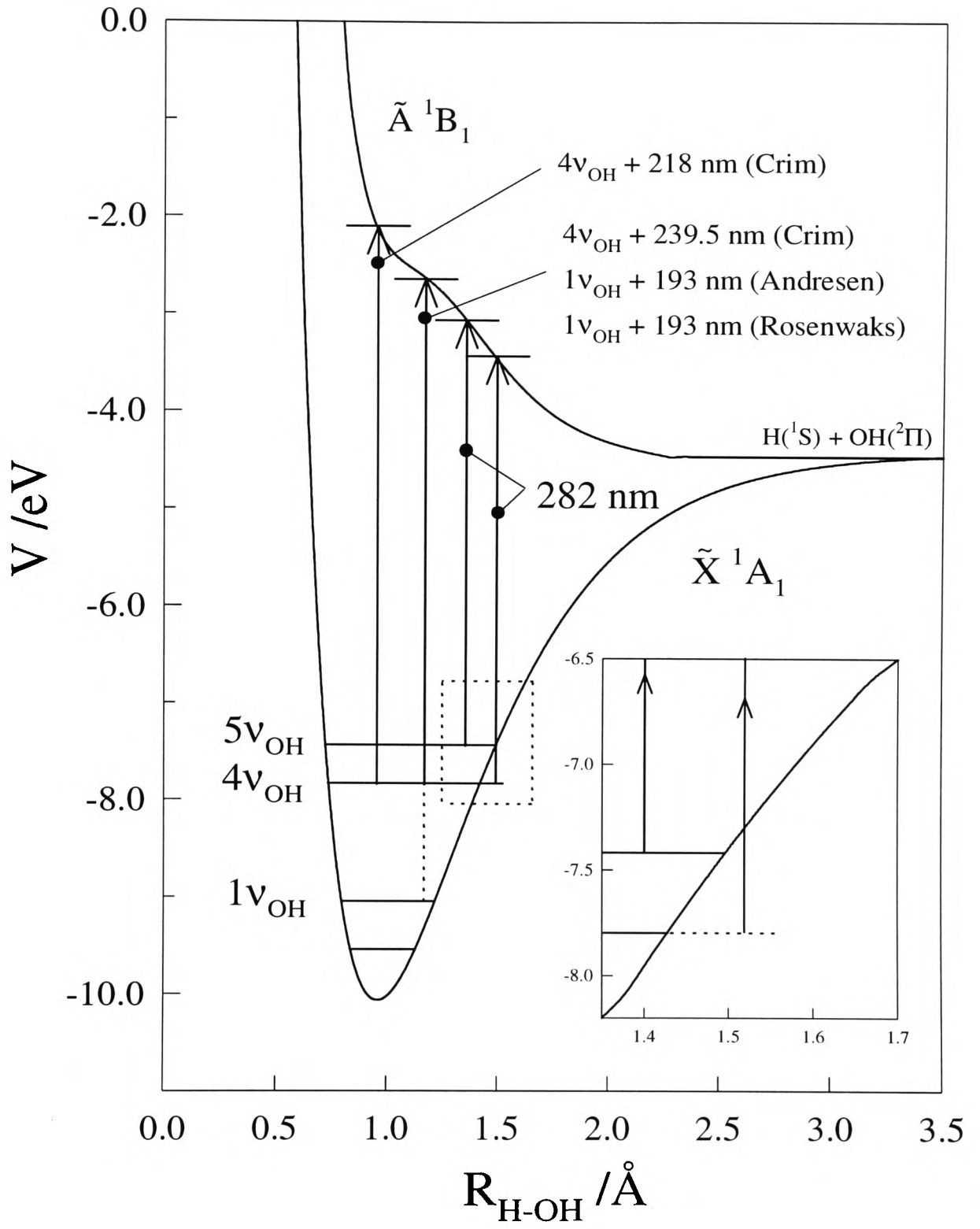

Figure 3.6 Plot of the water ground state potential of Jensen and coworkers [229] and the Ã-state potential of Steammler and Palma [230] against R_{HO-H}, the dissociation coordinate. Note that on purely energetic grounds, excitation from the $04\rangle^-$ overtone state with a 282 nm photon should occur preferentially from a classically forbidden region on the ground state potential.

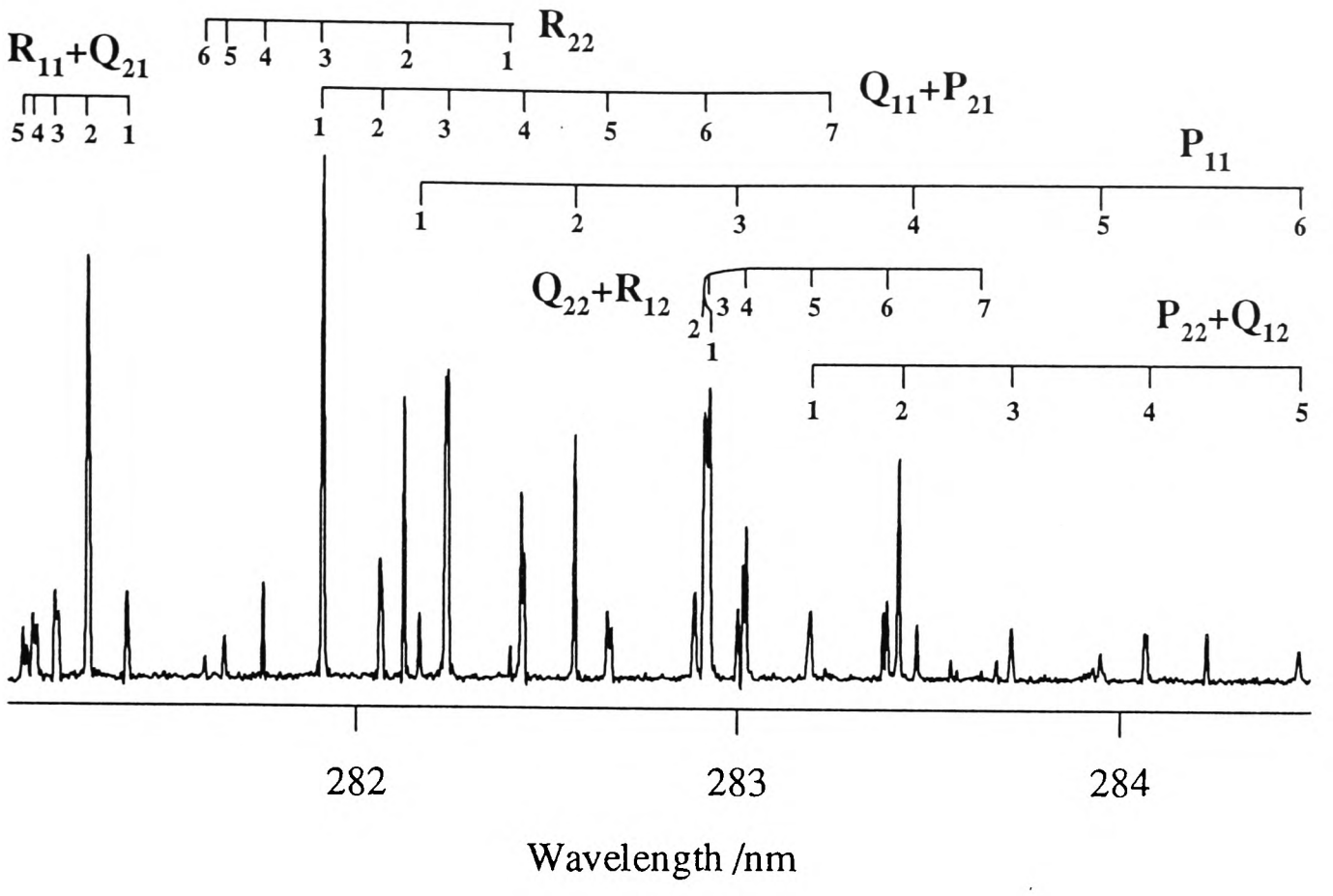

Figure 3.7 The OH photofragment $A^2\Sigma$–$X^2\Pi$ (1,0) LIF spectrum arising from the 282 nm photodissociation of $H_2O|04\rangle^-$ $J_{K_a,K_c} = 5_{15}$. The notation used to label the main and satellite branches refers to Δj, where j is the total angular momentum of the OH product [203].

different main branch. It is possible to use the OH $^2\Pi_{\frac{3}{2}}$ state distribution for a comparison but this would assume that the two spin-orbit states were populated according to their statistical weightings. As a result, no such a comparison can be made, and the OH $^2\Pi_{\frac{1}{2}}(A'')$ population distribution unfortunately remains incomplete.

Shown in figure 3.8 is the rotational distribution (plotted as a function of N, the total angular momentum quantum number j, apart from spin) within the A′ and A″ lambda-doublet levels of the OH $^2\Pi_{\frac{3}{2}}$ state arising from the 282 nm photodissociation of $H_2O|04\rangle^-$ J=0 and, for comparison, the analogous distribution obtained by Andresen and coworkers in the 193 nm photodissociation of $H_2O|01\rangle^-$ [34]. Clearly, the two distributions are very similar, the only difference being a change in the relative population of N=2 in the A″ lambda-doublet. Within the experimental error of both experiments ($\approx \pm 1$ on the scale plotted in the figure) however, this is probably not significant.

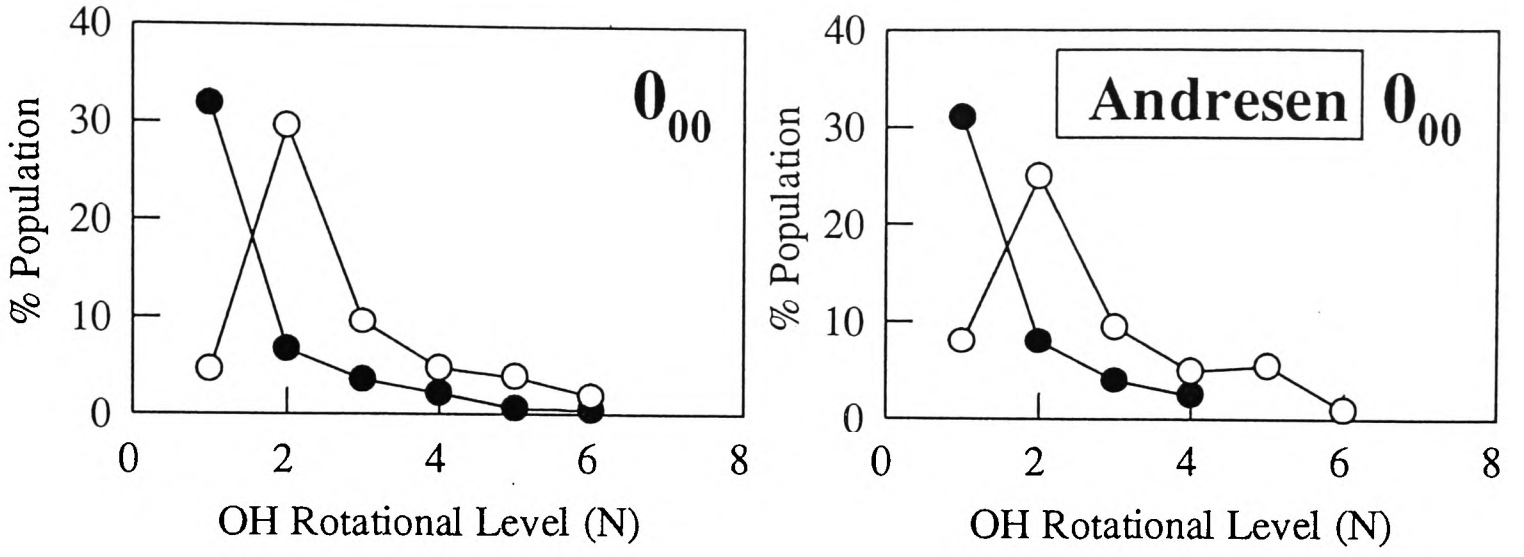

Figure 3.8 The $OH(X^2\Pi_{\frac{3}{2}})$ product population distribution, for both of the lambda doublet levels A′ (•) and A″ (○), arising from the 282 nm photodissociation of $H_2O|04\rangle^-(J = 0_{00})$. Shown on the right is the analogous distribution obtained by Andresen and coworkers [34] in the 193 nm photodissociation of $H_2O|01\rangle^-$.

Although there is a difference of ≈ 6000 cm^{-1} in the total supplied energy between this and Andresen's experiments, this close agreement is in accord with the conclusions drawn from previous work on $H_2O(\tilde{A})$ photodissociation. The OH product distributions for $J_{H_2O} \geq 0$ obtained by Andresen and coworkers [34], and the isoenergetic studies of Crim and coworkers [200] ($|04\rangle^-$ + 239.5 nm) and Rosenwaks and coworkers [166] ($|01\rangle^+$ + 193 nm), also show very close agreement.

Presented in Figures 3.9 and 3.10 are the OH $^2\Pi_{\frac{3}{2}}$(A′) & (A″) rotational state distributions obtained in this study upon selection of parent molecular states with $J_{K_a,K_c} > 0$, and the analogous distributions from the experiments of Andresen, Crim, Rosenwaks, and coworkers. The lambda-doublet populations are presented in separate figures for clarity and each distribution is normalised to unity, the relative lambda-doublet distributions not being presented in these figures. The errors in the relative populations of the OH fragment are well represented by the symbols used to plot out the distributions. It is clear from Figures 3.9 and 3.10 that there are significant differences between the OH rotational distributions obtained in this and in previous studies. The phase of the j-dependent oscillatory structure of the OH lambda-doublet populations [34, 232] is essentially the same for all of the

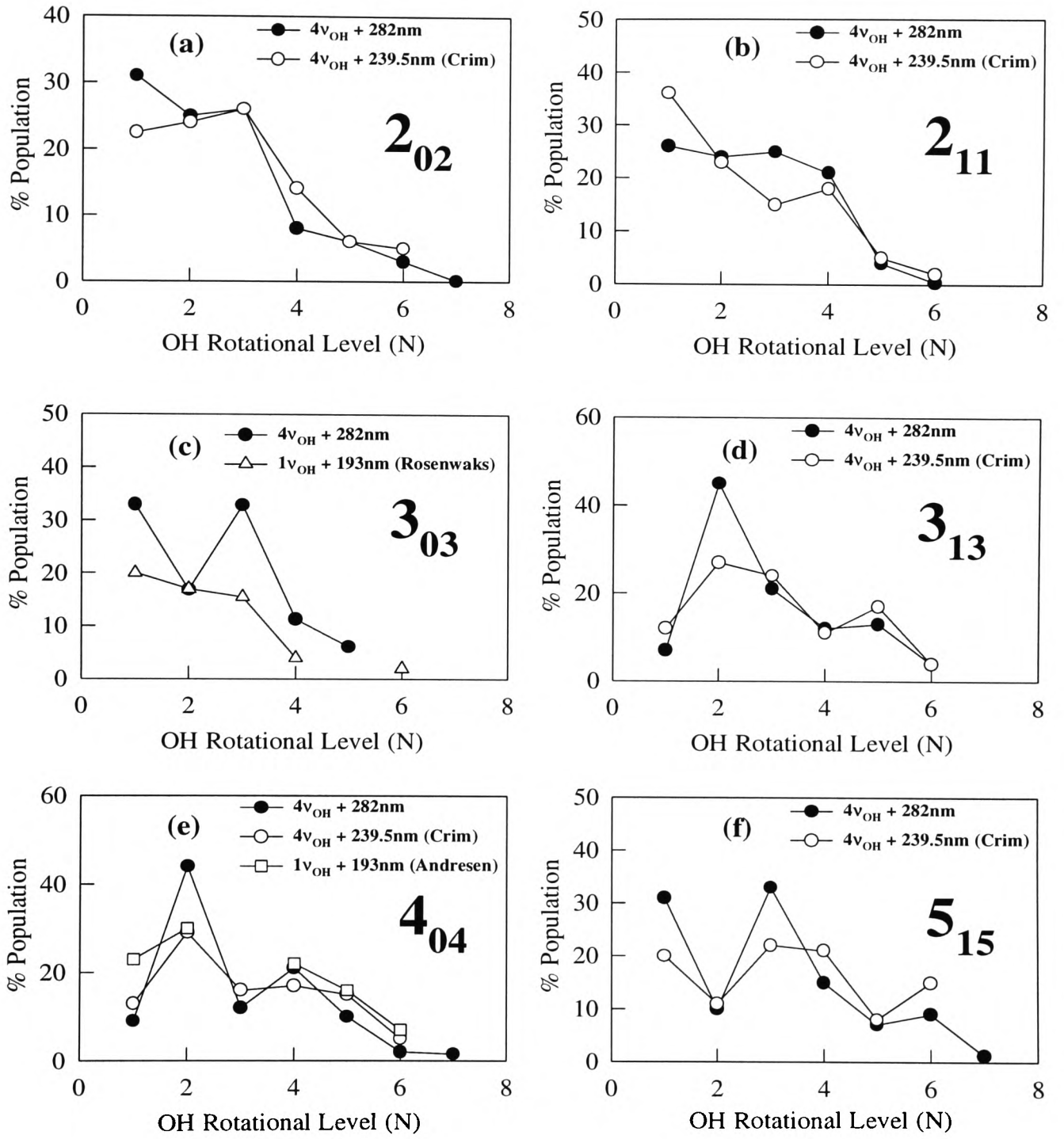

Figure 3.9 The OH $^2\Pi_{\frac{3}{2}}(A'')$ population distribution generated *via* the 282 nm photodissociation (•) of the $J_{K_a,K_c} = 2_{02}$ (a), 2_{11} (b), 3_{03} (c), 3_{13} (d), 4_{04} (e) and 5_{15} (e) rotational states of $H_2O|04\rangle^-$. The data is compared with the distributions obtained by Andresen and coworkers (⊓) [34], Crim and coworkers (∘) [201, 224], and Rosenwaks and coworkers (△) [165].

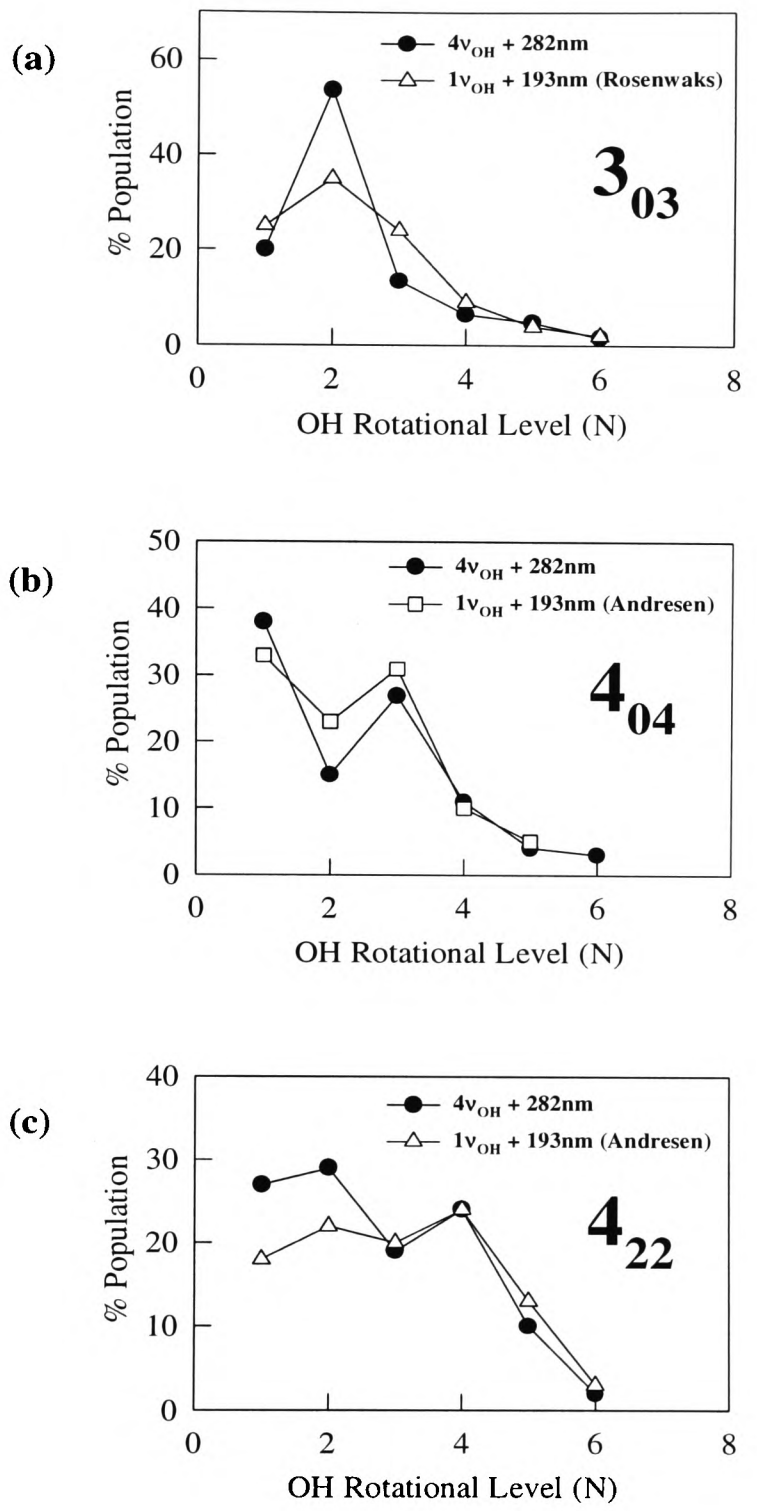

Figure 3.10 The OH $^2\Pi_{\frac{3}{2}}(A')$ population distribution generated *via* the 282 nm photodissociation (•) of the $J_{K_a,K_c} = 3_{03}$ (a), 4_{04} (b) and 4_{22} (c) rotational states of $H_2O|04\rangle^-$. The data is compared with the distributions obtained by Andresen and coworkers (⊓) [34] and Rosenwaks and coworkers (△) [165]. These are the only OH $^2\Pi_{\frac{3}{2}}(A')$ distributions presented in the previous experimental studies.

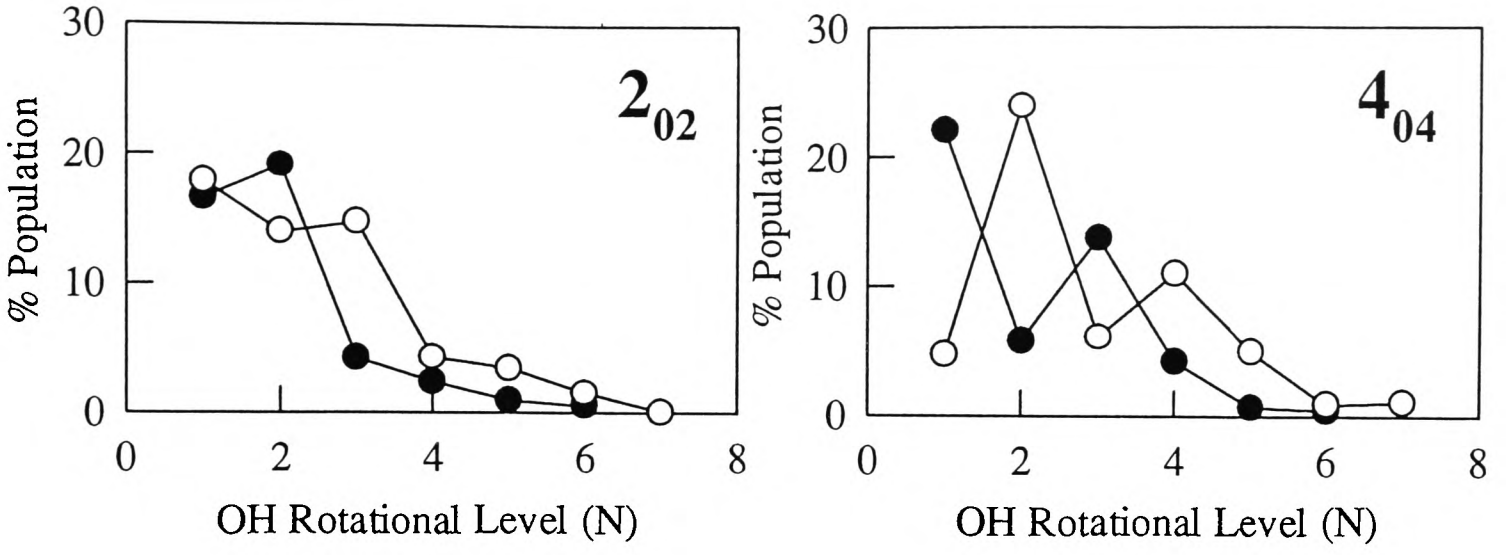

Figure 3.11 The relative OH $^2\Pi_{\frac{3}{2}}$ lambda-doublet population distributions (A′ = •, A″ = ○) arising from the 282 nm photodissociation of $J_{K_a,K_c} = 2_{02}$ (left)and 4_{04} (right). The total population in the spin orbit state has been normalised to unity.

J_{K_a,K_c} intermediate parent rotational states; the differences are primarily evident through changes in the amplitude of these oscillations, and become more pronounced with selection of higher values of J in the intermediate state. As N increases, this oscillatory structure gradually vanishes, and the population distributions from this and previous studies become very similar. It is only at low values of N, where the fluctuations in the lambda-doublet populations are prominent, that the differences can be seen.

The relative lambda-doublet populations for the OH $^2\Pi_{\frac{3}{2}}$ state arising from the 282 nm photodissociation of $H_2O|04\rangle^-$ $J_{K_a,K_c} = 2_{02}$ and 4_{04} are shown in figure 3.11. Comparing this with the distribution arising from $J_{K_a,K_c} = 0$ shown in Figure 3.8, it is clear that the oscillations between the populations in the two lambda-doublet states extends to higher N values as J in the intermediate parent state is increased. More pronounced differences are therefore seen in the OH fragment distributions for higher values of J_{H_2O}, because the structure in the distribution seems to be a sensitive indicator of the disparity of this and the previous experiments.

A similar picture emerges for the other OH product spin-orbit state, $^2\Pi_{\frac{1}{2}}$. Although very little data has been presented for this state in the previous studies, the comparisons that

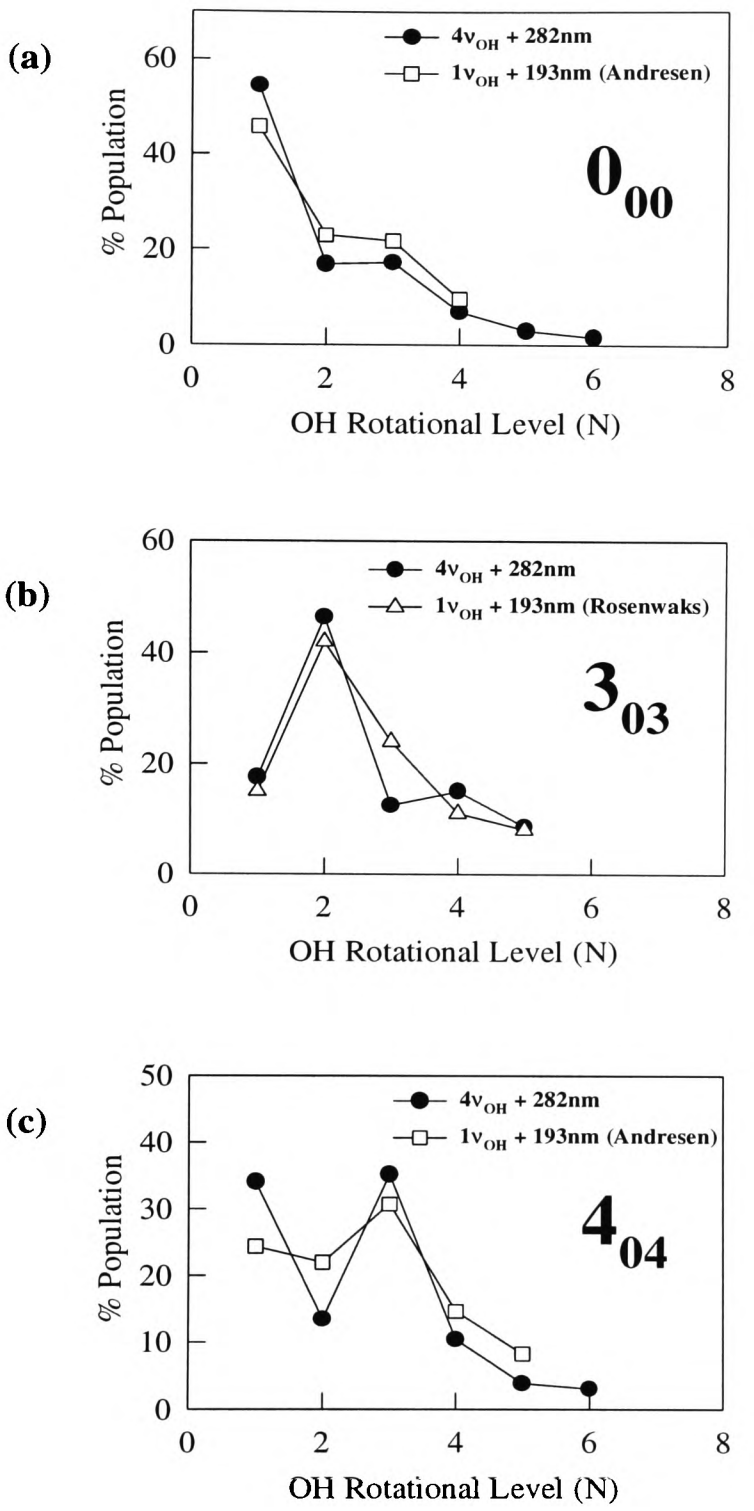

Figure 3.12 The OH $^2\Pi_{\frac{1}{2}}(A')$ population distribution generated *via* the 282 nm photodissociation (•) of the $J_{K_a,K_c} = 0_{00}$ (a), 3_{03} (b) and 4_{04} (c) rotational states of $H_2O|04\rangle^-$. The data is compared with the distributions obtained by Andresen and coworkers (⊓) [34] and Rosenwaks and coworkers (△) [165].

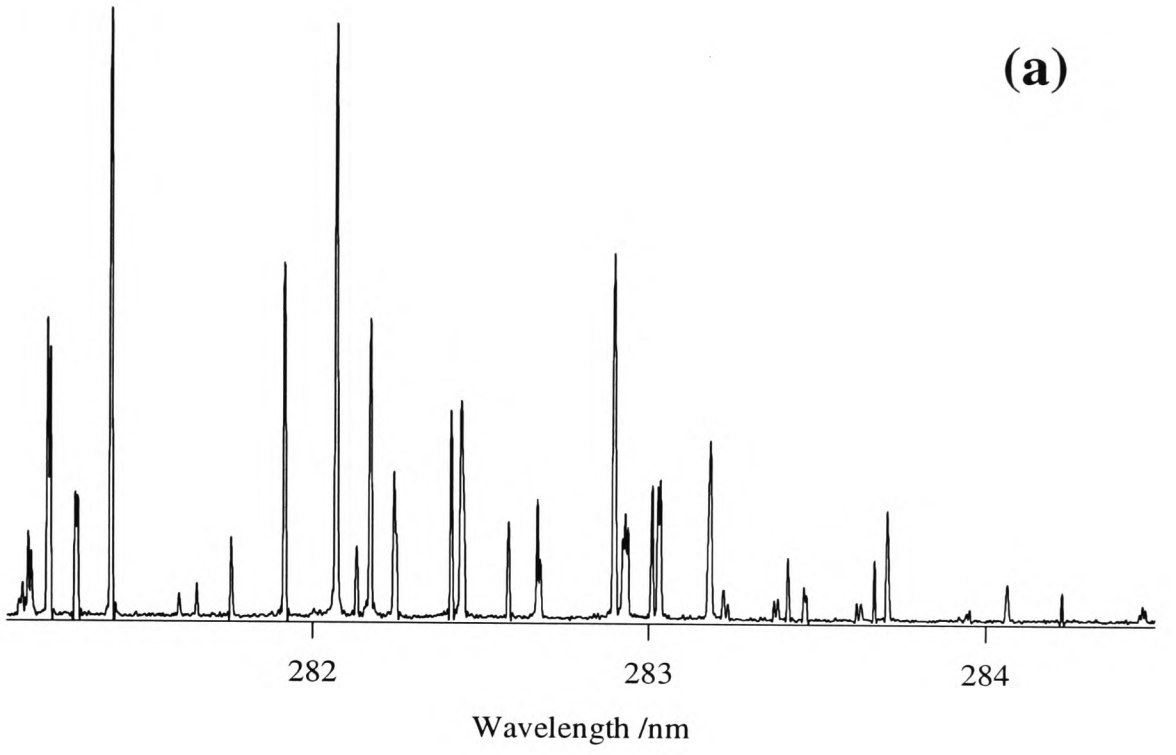

Figure 3.13 OH photofragment $A^2\Sigma$–$X^2\Pi$ (1–0) LIF spectra arising from the 282 nm photodissociation of (a) $H_2O|04\rangle^-$ and (b) $H_2O|05\rangle^-$. The intermediate rotational state selected in the water molecule was $J_{K_a,K_c} = 4_{04}$. The assignments of the rotational transitions are shown in Figure 3.7.

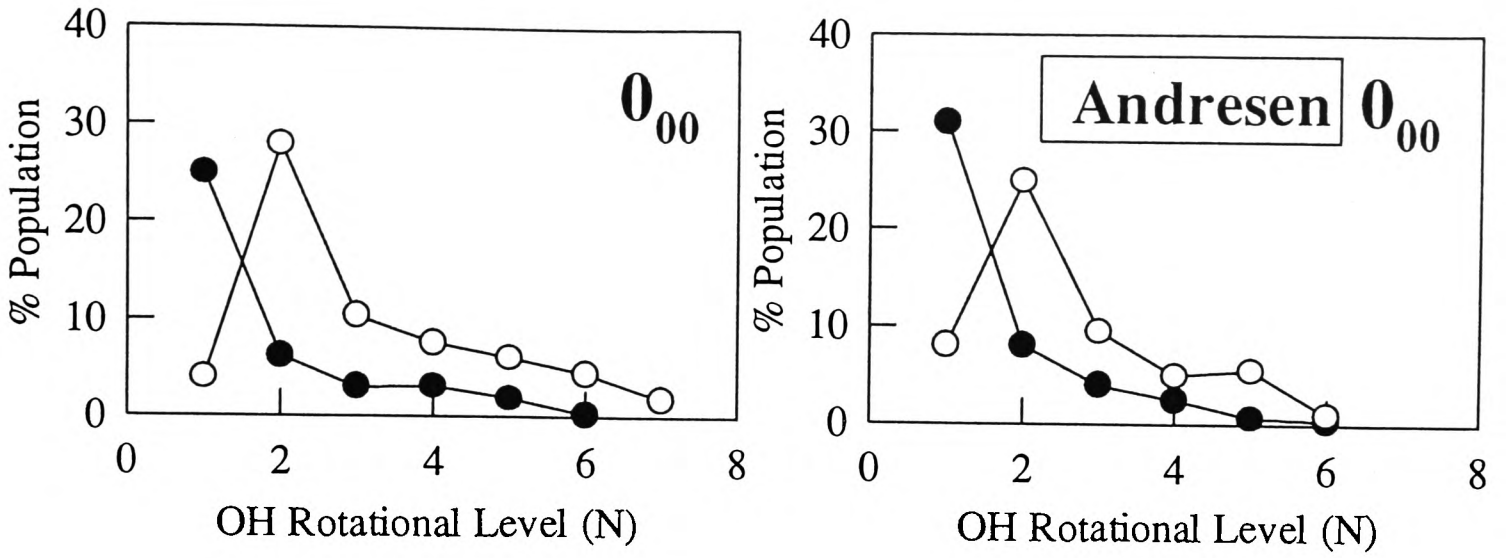

Figure 3.14 The photofragment $OH(X^2\Pi_{\frac{3}{2}})$ population distributions within the A′ (•) and A″ (○) lambda doublet levels arising from the 282 nm photodissociation of $H_2O|05\rangle^-(J = 0_{00})$. Also shown on the right is the analogous distribution obtained by Andresen and coworkers [34] in the 193 nm photodissociation of $H_2O|01\rangle^-$. Within the experimental error of both studies, the small differences between these two distributions are virtually inconsequential.

could be made with this study are presented in figure 3.12. Only the A′ lambda-doublet is shown, for reasons mentioned earlier regarding the calculation of the population in the A″ state. In line with the OH $^2\Pi_{\frac{3}{2}}$ state, the differences between the OH $^2\Pi_{\frac{1}{2}}$ population distributions obtained from this and the previous work can only be seen for $J_{H_2O} > 0$. Similiarly, only changes in the amplitude and not the phase of the j-dependent oscillatory structure are observed.

3.3.2 The 282 nm VMP of $H_2O|05\rangle^-$ *via* the $\tilde{A}$-State

The 282 nm photodissociation of H_2O initially selected in the fourth stretching vibrational overtone level, generates an excess energy of $E_{AVL} \approx 11000$ cm^{-1} for disposal in the photofragments, some 3000 cm^{-1} less than was supplied the studies of Andresen and coworkers [15, 34], Crim and coworkers [125, 200] and Rosenwaks and coworkers [166]. This experiment should preferentially sample the bound state wavefunction at larger internuclear separations than the previous experimental work, as was shown in Figure 3.6.

experiment should preferentially sample the bound state wavefunction at larger internuclear separations than the previous experimental work, as was shown in Figure 3.6.

Shown in Figure 3.13 are the OH photofragment LIF spectra arising from the 282nm photodissociation, *via* the $\tilde{A}$-state, of $H_2O|04\rangle^-$ and $H_2O|05\rangle^-$ for one intermediate rotational state, $J_{K_a,K_c} = 4_{04}$. Apart from illustrating the excellent signal-to-noise ratio achievable in the fourth overtone experiment, it is clear that there is a dramatic difference in the OH product rotational distributions obtained from the two experiments. Using the same procedure as in Section 3.3.1, the error in the distributions is calculated as being $\pm$ 5 % for the least populated OH fragment rotational states.

Photolysing $H_2O|05\rangle^-$ J = 0 results in an OH rotational distribution similar to that found in the $H_2O|04\rangle^-$ experiment, which appears to be insensitive both to the photolysis energy and to the intermediate stretching vibrational overtone; this is shown in Figure 3.14 for the OH $^2\Pi_{\frac{3}{2}}$ A′ and A″ lambda-doublet population distribution. Also shown is the corresponding distribution obtained by Andresen and coworkers [34, 15] ($H_2O|01\rangle^-$ + 193nm).

The OH $^2\Pi_{\frac{3}{2}}$ population distributions arising from the selection of parent molecular states with $J_{K_a,K_c} > 0$ are presented in Figures 3.15 and 3.16 for the A″ and A′ lambda-doublets respectively ($J_{K_a,K_c} = 2_{02}$ [Fig. 3.15(a), 3.16(a)]; $J_{K_a,K_c} = 2_{11}$ [Fig. 3.15(b), 3.16(b)]; $J_{K_a,K_c} = 3_{13}$ [Fig. 3.15(c), 3.16(c)]; $J_{K_a,K_c} = 4_{04}$ [Fig. 3.15(d), 3.16(d)]; $J_{K_a,K_c} = 5_{05}$ [Fig. 3.15(e), 3.16(e)]; $J_{K_a,K_c} = 5_{15}$ [Fig. 3.15(f), 3.16(f)]). A comparison is also made with the corresponding distributions of Crim and coworkers [201] ($H_2O|04\rangle^-$ + 239.5nm) and Andresen and coworkers [15, 34] in Figure 3.15, and with the data for $H_2O|04\rangle^-$ from this study in Figure 3.16. It is evident that the differences in the OH rotational distributions become increasingly marked as the angular momentum in the intermediate state of the parent molecule is increased. The appearance of these differences is also seen to be additionally dependent on the amount of *a*-axis rotation in the reagent state.

There is a difference in the total supplied energy of ≈ 3000 cm^{-1} between the work of Crim and Andresen and the 282 nm photodissociation of $H_2O|05\rangle^-$; for parent rotational states with $K_a > 0$ (Fig. 3.15(b), (c) & (f)), these differences are primarily evident as changes in the amplitude of the oscillatory structure in the OH lambda-doublet populations at low values of N. At higher values of N, changes in the phase of the oscillations become apparent with increasing values of J in the intermediate state. For reagent rotational states

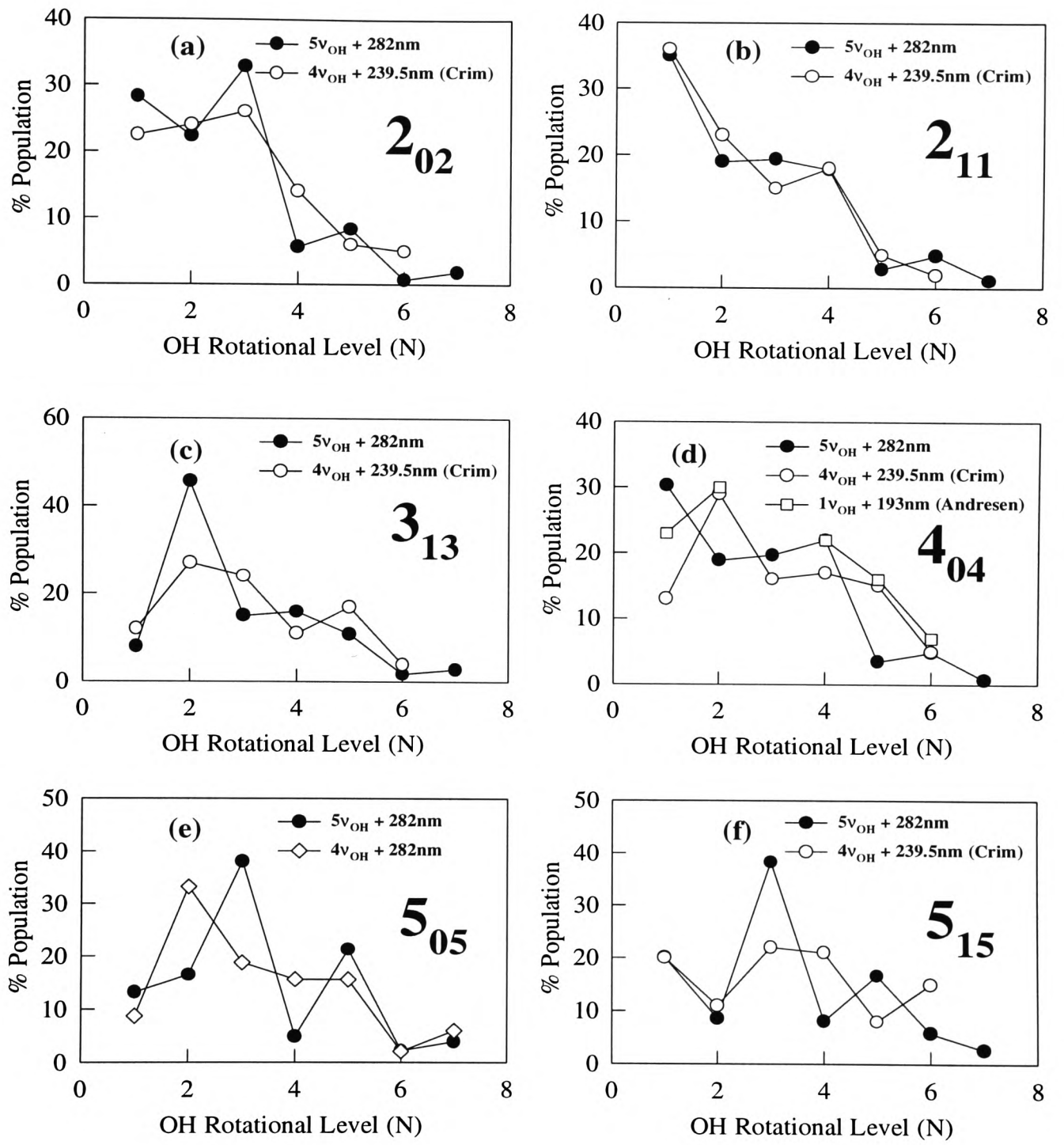

Figure 3.15 The OH $^2\Pi_{\frac{3}{2}}(A'')$ population distribution generated *via* the 282 nm photodissociation (•) of the $J_{K_a,K_c} = 2_{02}$ (a), 2_{11} (b), 3_{13} (c), 4_{04} (d), 5_{05} (e) and 5_{15} (e) rotational states of $H_2O|05\rangle^-$. The data is compared with the distributions obtained by Andresen and coworkers ⊓) [34], Crim and coworkers (∘) [201, 224], and the $H_2O|04\rangle^-$ data from this study (◇).

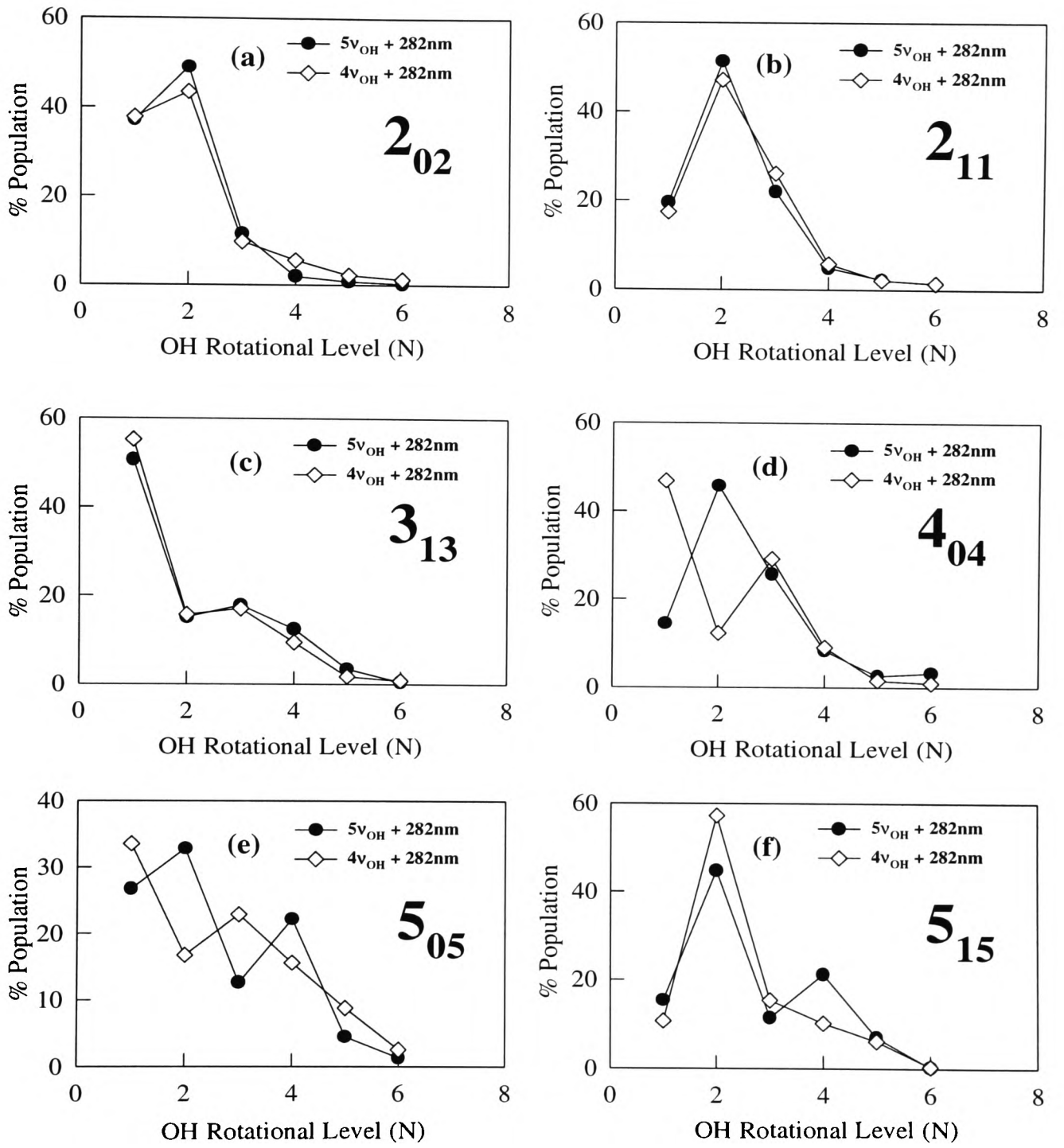

Figure 3.16 The OH $^2\Pi_{\frac{3}{2}}(A')$ population distribution generated *via* the 282 nm photodissociation (•) of the $J_{K_a,K_c} = 2_{02}$ (a), 2_{11} (b), 3_{13} (c), 4_{04} (d), 5_{05} (e) and 5_{15} (e) rotational states of $H_2O|05\rangle^-$. The data is compared with the distributions obtained in the 282 nm photodissociation of $H_2O|04\rangle^-$ (◇).

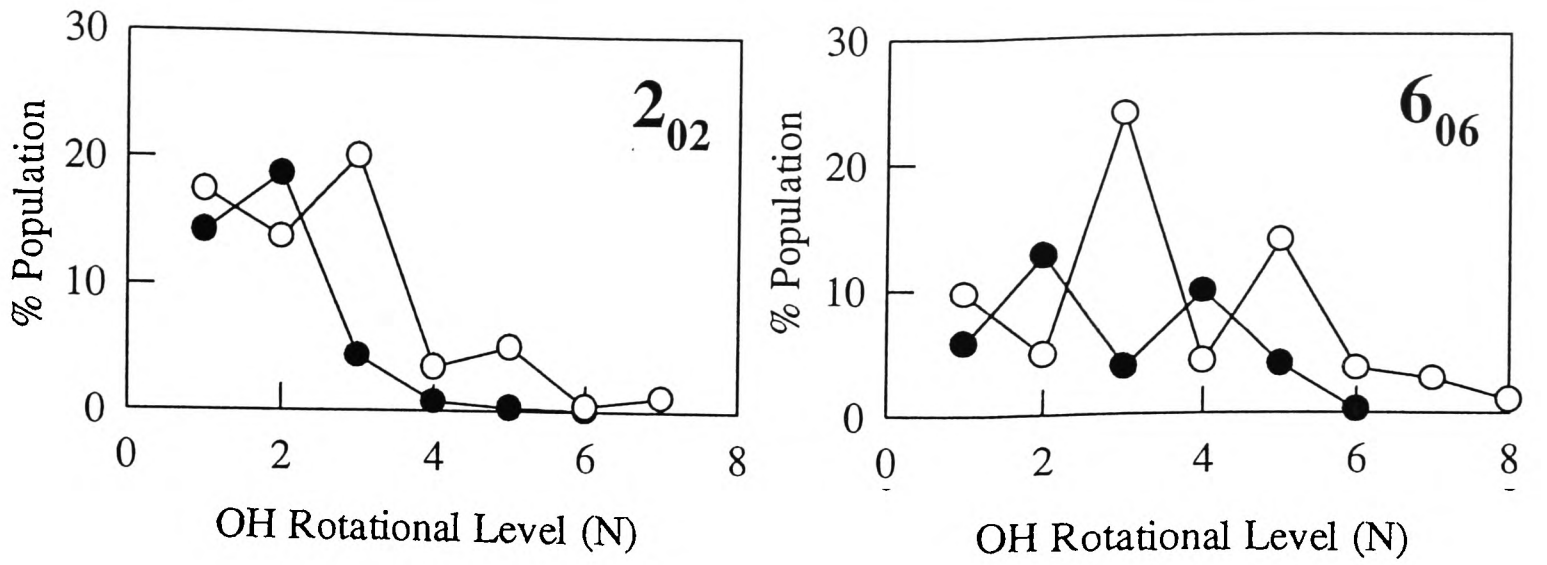

Figure 3.17 The relative OH $^2\Pi_{\frac{3}{2}}$ lambda-doublet population distributions (A′ = •, A″ = ○) arising from the 282 nm photodissociation of $J_{K_a,K_c} = 2_{02}$ (left) and 6_{06} (right). The total population in the spin orbit state has been normalised to unity.

Comparing the 282 nm photodissociation of $H_2O|05\rangle^-$ and $H_2O|04\rangle^-$ (an increase in the total supplied energy of ≈ 3000 cm^{-1}) in Figure 3.16 reveals a similar result, the change in the OH population distributuions being greatest for reagent states with high J and low K_a values. However, the overall magnitude of the changes are much smaller than those seen when the data of Crim and Andresen is used as a comparison . The differences in the oscillatory structure only become apparent for high parent rotational states $J \geq 4$ and at low values of N, where the oscillations are more prominent. Similar to the data for $H_2O|04\rangle^-$, the structure in the OH distributions increases and extends to higher values of N as the value of J in the parent intermediate state increases (see Figure 3.17).

The OH $^2\Pi_{\frac{1}{2}}$ (A′) population distributions obtained upon selection of $J_{K_a,K_c} = 0_{00}$ and 4_{04} in $H_2O|05\rangle^-$ are shown in Figure 3.18. The corresponding distributions from the experiments of Andresen and coworkers are also shown. Similar to the OH $^2\Pi_{\frac{3}{2}}$ data, the differences in the OH $^2\Pi_{\frac{1}{2}}$ lambda-doublet distributions when compared to data from other experiments can only be seen for $J_{K_a,K_c} > 0$. These trends are highlighted in Table 3.4 which shows the sums of the squared differences between the OH distributions obtained subsequent to 282 nm dissociation *via* the third and fourth overtone states.

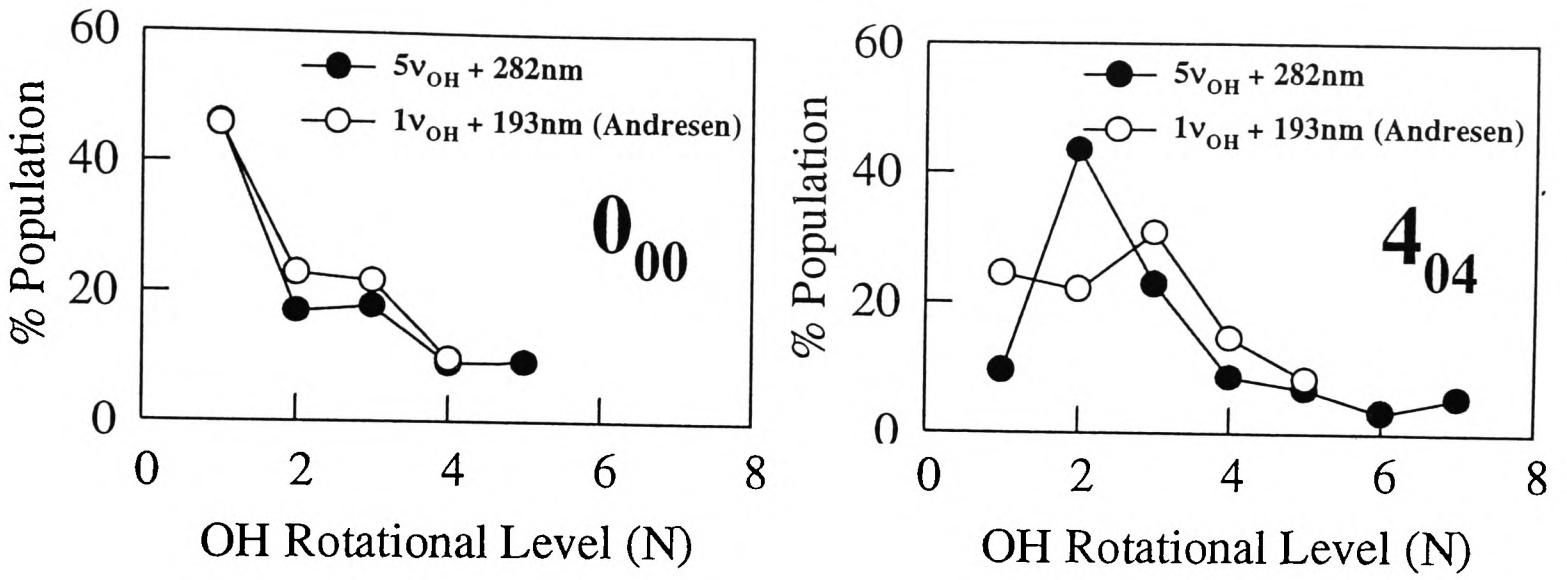

Figure 3.18 The OH $^2\Pi_{\frac{1}{2}}(A')$ population distribution generated *via* the 282 nm photodissociation (•) of the $J_{K_a,K_c} = 0_{00}$ (left) and 4_{04} (right) rotational states of $H_2O|05\rangle^-$. The data is compared with the distributions obtained by Andresen and coworkers (⊓) [34].

0_{00}	2_{02}	2_{11}	3_{13}	4_{04}	4_{22}	5_{05}	5_{15}
0.007	0.025	0.024	0.026	0.678	0.078	0.134	0.060

Table 3.4 Comparison of the OH populations generated subsequent to the 282 nm photolysis of H_2O selected initially in the third and fourth OH stretching overtone levels. The numbers presented are the sums of the squared differences in the OH populations arising from the photodissociation of the two vibrational levels for each J_{K_a,K_c} state selected in the parent water molecule.

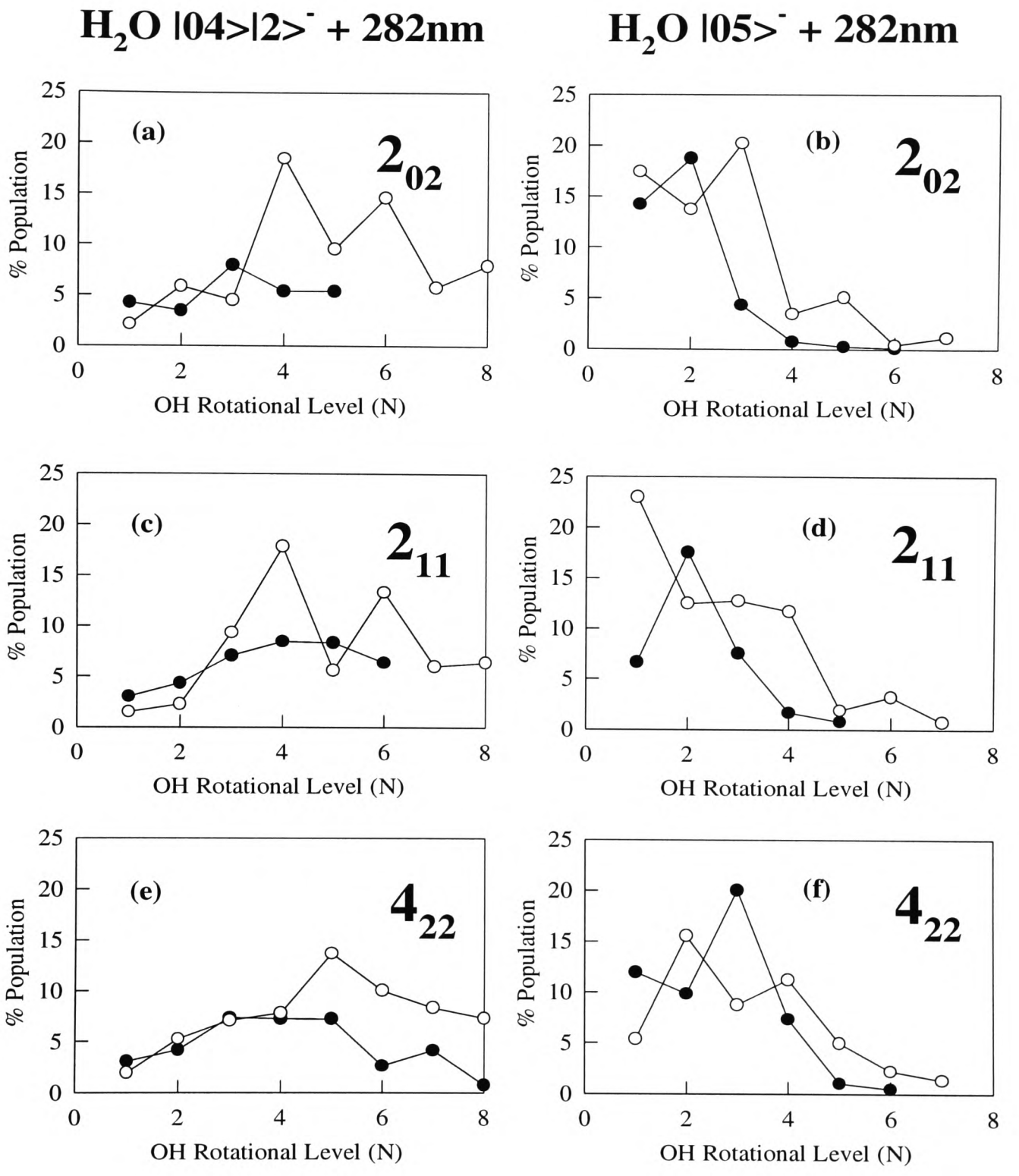

Figure 3.19 OH $^2\Pi_{\frac{3}{2}}$ rotational population distributions in the A′ (•) and A″ (◦) lambda-doublet levels generated *via* the 282 nm photodissociation of the $J_{K_a,K_c} = 2_{02}$ (a), 2_{11} (c) and 4_{22} (e) rotational states of $H_2O|04\rangle|2\rangle^-$. Also shown are the corresponding distributions obtained from the 282 nm photolysis of $H_2O|05\rangle^-$, [right (b), (d) and (f)].

0_{00}	2_{02}	2_{11}	3_{13}	4_{04}	4_{22}	5_{05}	5_{15}
0.007	0.025	0.024	0.026	0.678	0.078	0.134	0.060

Table 3.4 Comparison of the OH populations generated subsequent to the 282 nm photolysis of H_2O selected initially in the third and fourth OH stretching overtone levels. The numbers presented are the sums of the squared differences in the OH populations arising from the photodissociation of the two vibrational levels for each J_{K_a,K_c} state selected in the parent water molecule.

bending mode, broadly consistent with the previous findings of Crim and Schinke [224]. This is again borne out with the population distributions for the other OH fragment spin-orbit state, OH $^2\Pi_{\frac{1}{2}}$. Figure 3.20 shows the OH $^2\Pi_{\frac{1}{2}}$ lambda-doublet distribution arising from the photolysis of $|04\rangle|2\rangle^-$ (left) and $|05\rangle^-$ (right) for $J_{K_a,K_c} = 2_{02}$.

It is also worth noting that, although the excited bending motion of the bound state parent and the exit channel torque on the A state primarily determines the resultant OH fragment rotational distributions, there is a residual memory of the bound parent rotational state (and the zero-point bending motion) induced rotational distributions. The oscillatory structure of the $|04\rangle|2\rangle^-$ distributions in Figure 3.19 for $N \geq 4$ is reminicent of the structure in the corresponding (J_{K_a,K_c}) $|05\rangle^-$ distributions ($N \geq 1$), particularly for the OH(A″) lambda-doublet, which are also shown in the figure.

3.4 Relative OH spin-orbit state distributions

The question of a selective OH fragment spin-orbit state population in the dissociation of $H_2O(\tilde{A})$ is considered in Figures 3.21 and 3.22 for the $H_2O|04\rangle^-$ and $|05\rangle^-$ respectively. The ratio of the population of rotation states in $^2\Pi_{\frac{1}{2}}(N)$ and $^2\Pi_{\frac{3}{2}}(N)$ is plotted as a function of N in each figure. The degeneracy of the spin states is taken into account by the factor $\frac{N}{N+1}$. A value of 1 corresponds to an equal probability of populating both spin-orbit states (a 'statistical' distribution).

Using the A″ lambda-doublet data, a mean distribution very close to 'statistical' is obtained for both intermediate parent stretching overtones. Although there may be a very slight preference for the $^2\Pi_{\frac{3}{2}}$ state, this is not certain within the experimental error margin.

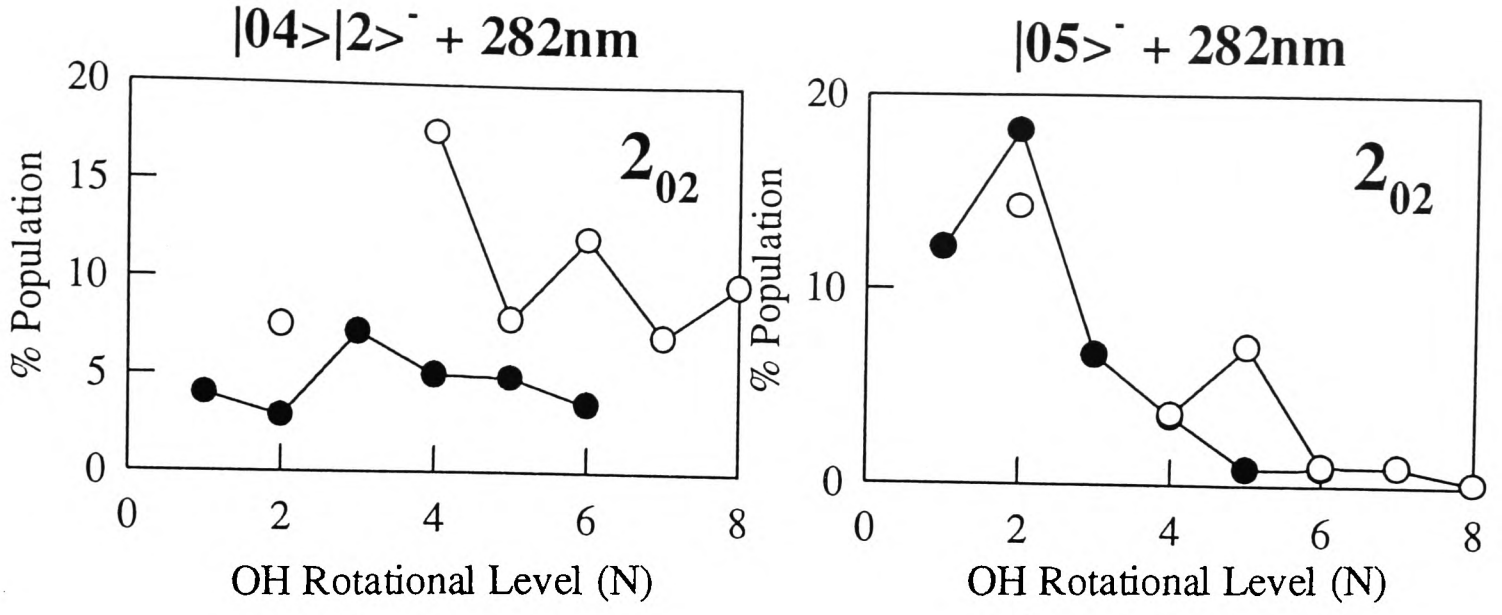

Figure 3.20 The relative OH $^2\Pi_{\frac{1}{2}}$ lambda-doublet population distribution (A′ = •, A″ = ○) arising from the 282 nm photodissociation of $H_2O|04\rangle|2\rangle^-$ (left) and $|05\rangle^-$ (right), $J_{K_a,K_c} = 2_{02}$. The total population in the spin orbit state has been normalised to unity.

of N in each figure. The degeneracy of the spin states is taken into account by the factor $\frac{N}{N+1}$. A value of 1 corresponds to an equal probability of populating both spin-orbit states (a 'statistical' distribution).

Using the A″ lambda-doublet data, a mean distribution very close to 'statistical' is obtained for both intermediate parent stretching overtones. Although there may be a very slight preference for the $^2\Pi_{\frac{3}{2}}$ state, this is not certain within the experimental error margin. Using the data for the A′ lambda-doublet, however produces a radically different answer: Even within the ± 20 % error[6], there is a small but clear preference for the $^2\Pi_{\frac{1}{2}}$ spin orbit state. Interestingly, the OH fragment spin-orbit population distributions arising from the photodissociation of $H_2O|04\rangle|2\rangle^-$, shown in Figure 3.23, are 'statistical' within the experimental error, for both OH lambda-doublet states.

The OH $^2\Pi_{\frac{1}{2}}(A')$ and OH $^2\Pi_{\frac{3}{2}}(A')$ population distributions obtained from the selection of $|04\rangle^-$, J=0 in the parent intermediate state, are shown in Figures 3.8 and 3.12(a) respectively. Although they are similar, there is a small but noticable change in the relative intensities of N = 2 & 3, the population in N = 3 becoming greater than N = 2 for the

[6]This is the accumulative error in the ratio taken from the 5 % error in the population distributions.

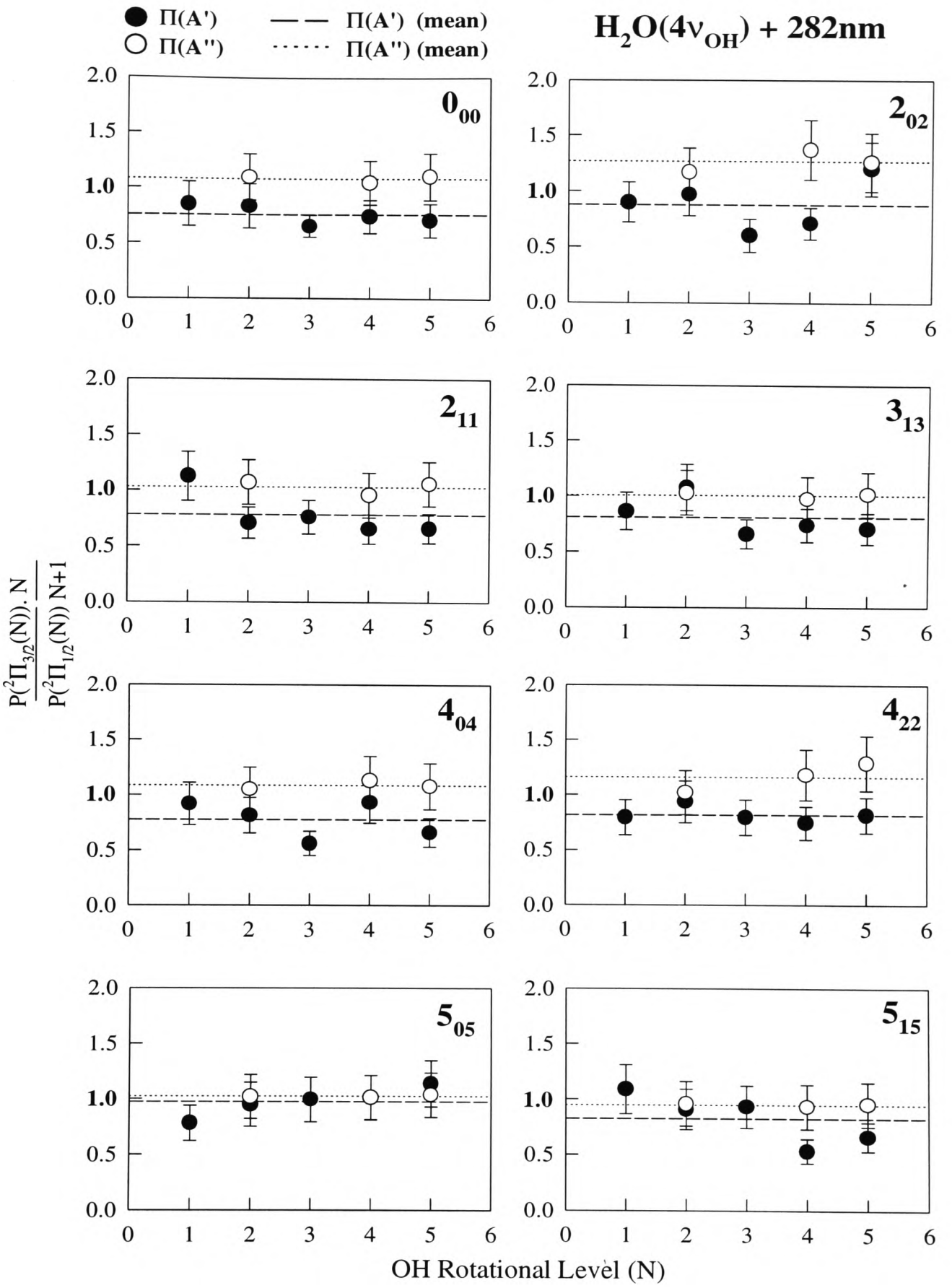

Figure 3.21 The ratio of the population of rotational states in $^2\Pi_{\frac{1}{2}}(N)$ and $^2\Pi_{\frac{3}{2}}(N)$ arising from $H_2O|04\rangle^-$, plotted as a function of N. The degeneracy is taken into account by the factor $\frac{N}{N+1}$. The spin populations for the A′ (•) and the A″ (○) levels are shown, as are the corresponding mean distribution.

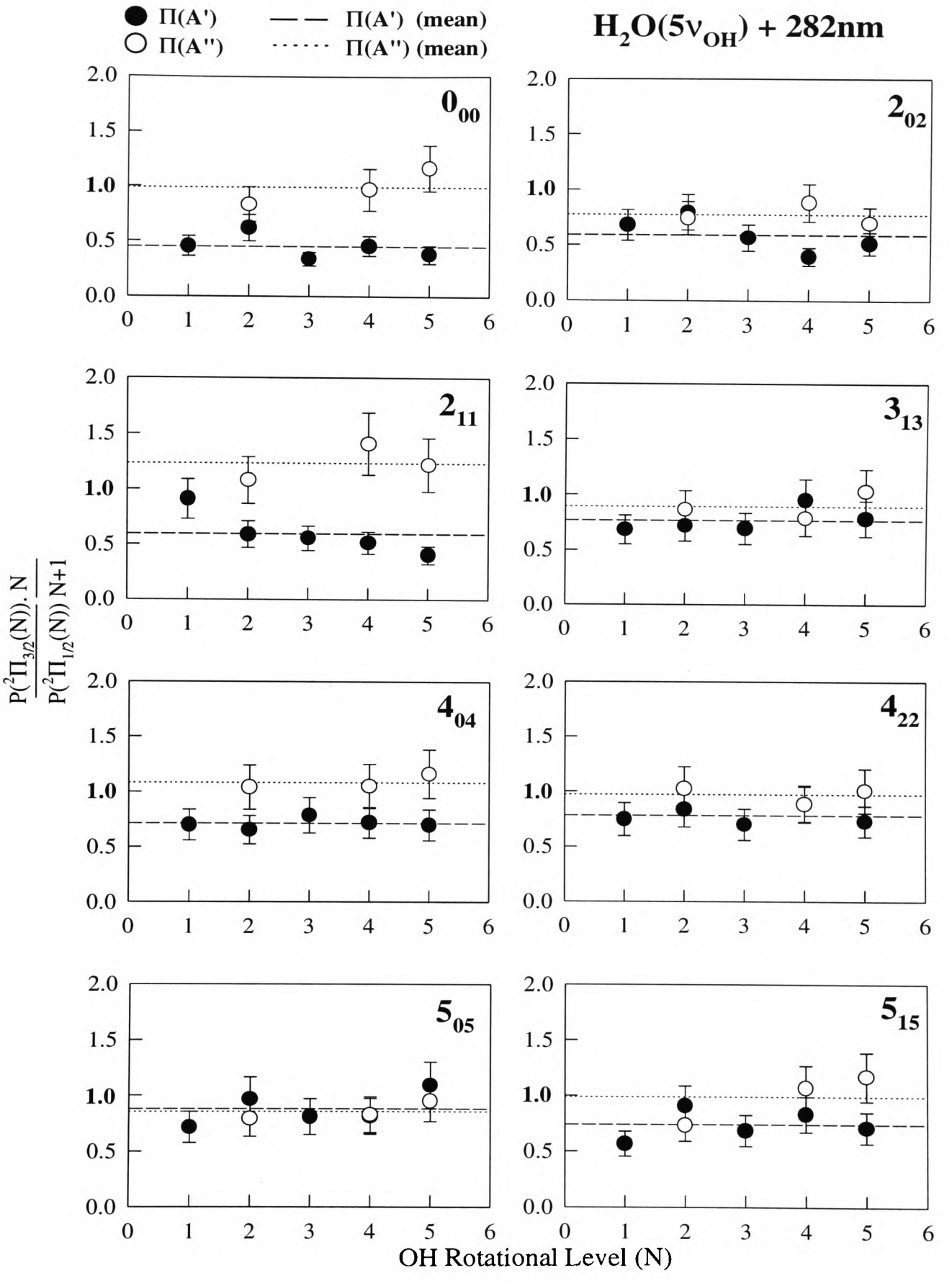

Figure 3.22 The ratio of the population of rotational states in $^2\Pi_{\frac{1}{2}}(N)$ and $^2\Pi_{\frac{3}{2}}(N)$ arising from $H_2O|05\rangle^-$, plotted as a function of N. The spin populations for the A′ (•) and the A″ (○) levels are shown, as ared the corresponding mean distribution.

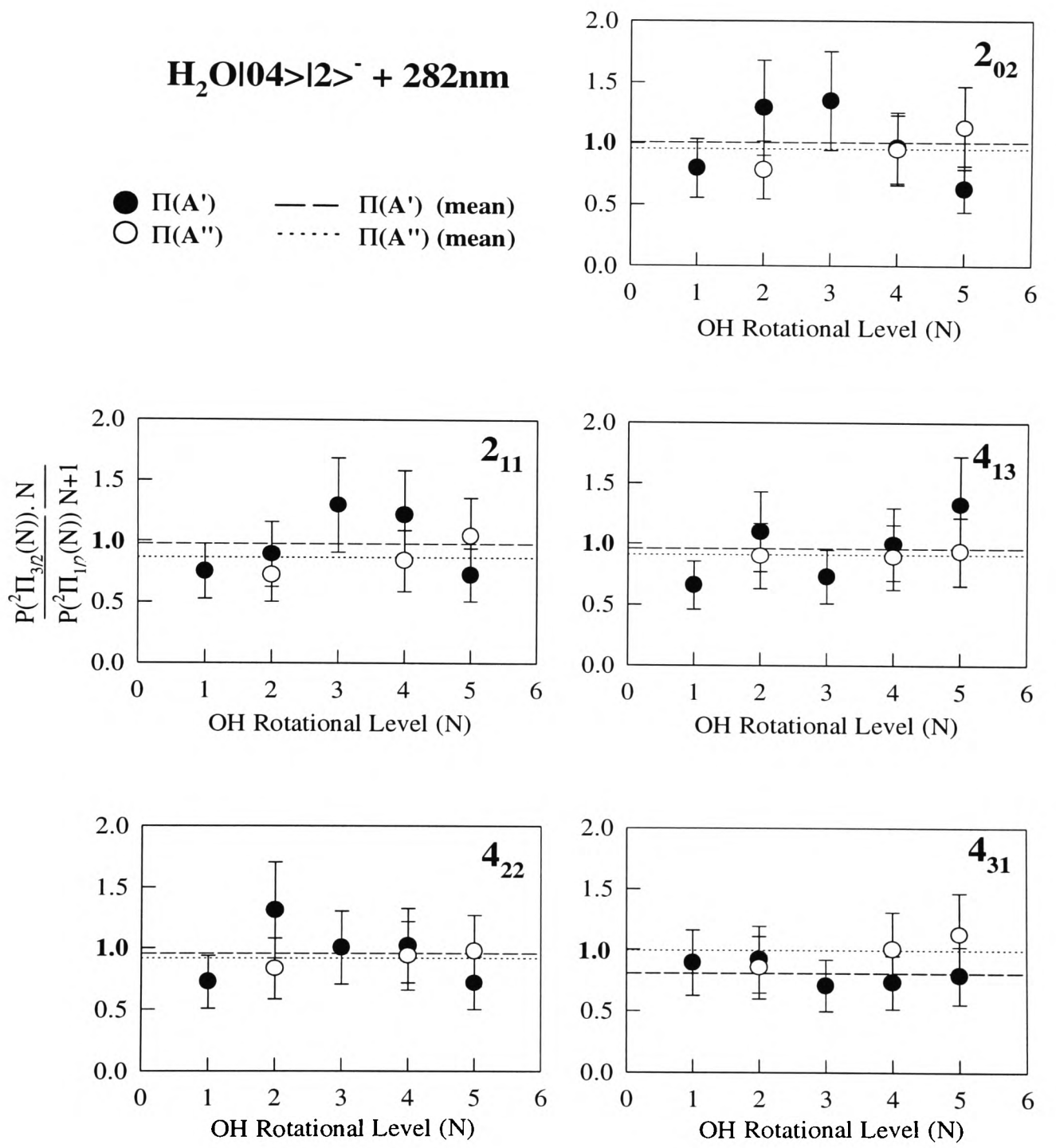

Figure 3.23 The ratio of the population of rotational states in $^2\Pi_{\frac{1}{2}}(N)$ and $^2\Pi_{\frac{3}{2}}(N)$ arising from $H_2O|04\rangle|2\rangle^-$, plotted as a function of N, for both lambda-doublet levels A′ (•) and A″ (○). Also shown are the corresponding mean distribution.

small, but clear differences between the A′ lambda-doublet distributions of the two spin-orbit states. Although no realistic comparison can be made for the A″ lambda-doublet state, from what can be seen of the population distributions in figures 3.24 and 3.25, the $^2\Pi_{\frac{3}{2}}(A'')$ and $^2\Pi_{\frac{1}{2}}(A'')$ data appears to be very similar. These lambda-doublet-specific differences between the population distributions of the two spin orbit states may be correlated to the observed trend in the spin-orbit state population distributions towards a slight preference for the $^2\Pi_{\frac{1}{2}}$ state for the A′ lambda-doublet and towards a 'statistical' population for the A″ state.

The relative lambda-doublet population distributions for both OH spin-orbit states, OH $^2\Pi_{\frac{1}{2}}$ and OH $^2\Pi_{\frac{3}{2}}$, are shown in Figure 3.26 for the intermediate $|04\rangle|2\rangle^-$ rotational states $J_{K_a,K_c} = 4_{13}$ [(a) & (b)], 4_{22} [(c) & (d)], and 4_{31} [(e) & (f)]. Although the OH $^2\Pi_{\frac{1}{2}}(A'')$ distribution is again incomplete, there is no clear difference between the population distributions of both spin-orbit states, for both lambda-doublet states. A statistical population of the spin-orbit states is also observed for both lambda-doublets.

3.5 Preferential OH product Λ-doublet population

The lambda-doublet-averaged OH $^2H_{\frac{3}{2}}$ population distribution for each of the intermediate rotational states selected in $H_2O|04\rangle^-$ and $H_2O|05\rangle^-$ has been fitted to a Boltzmann plot, and a rotational temperature for each distribution has been calculated from the gradient of the line fitted through each plot. Some of the Boltzmann plots for four parent $|04\rangle^-$ and $|05\rangle^-$ rotational states ($J_{K_a,K_c} = 0_{00}$, 2_{02}, 4_{04} and 5_{05}) are shown in Figures 3.27 and 3.28, respectively. With increasing angular momentum, j, in the photofragment OH, there are modest deviations from the Boltzmann plot line. Examining the lambda-doublet population distributions shown in Figures 3.8, 3.11, 3.24, 3.14, 3.17 and 3.25, this deviation is reflected in a preferential population of the A″ lambda-doublet level.

An examination of the relative lambda-doublet population distributions arising from the photodissociation of $H_2O|04\rangle|2\rangle^-$ for both OH $^2\Pi_{\frac{1}{2}}$ and OH $^2\Pi_{\frac{3}{2}}$ (shown in Figures 3.19, 3.20 and 3.26), also shows a clear preference for the A″ level, especially at the higher values of N where the OH fragments are primarily populated. The j-averaged distributions could not be fitted to a Boltzmann plot to provide a single rotational temperature.

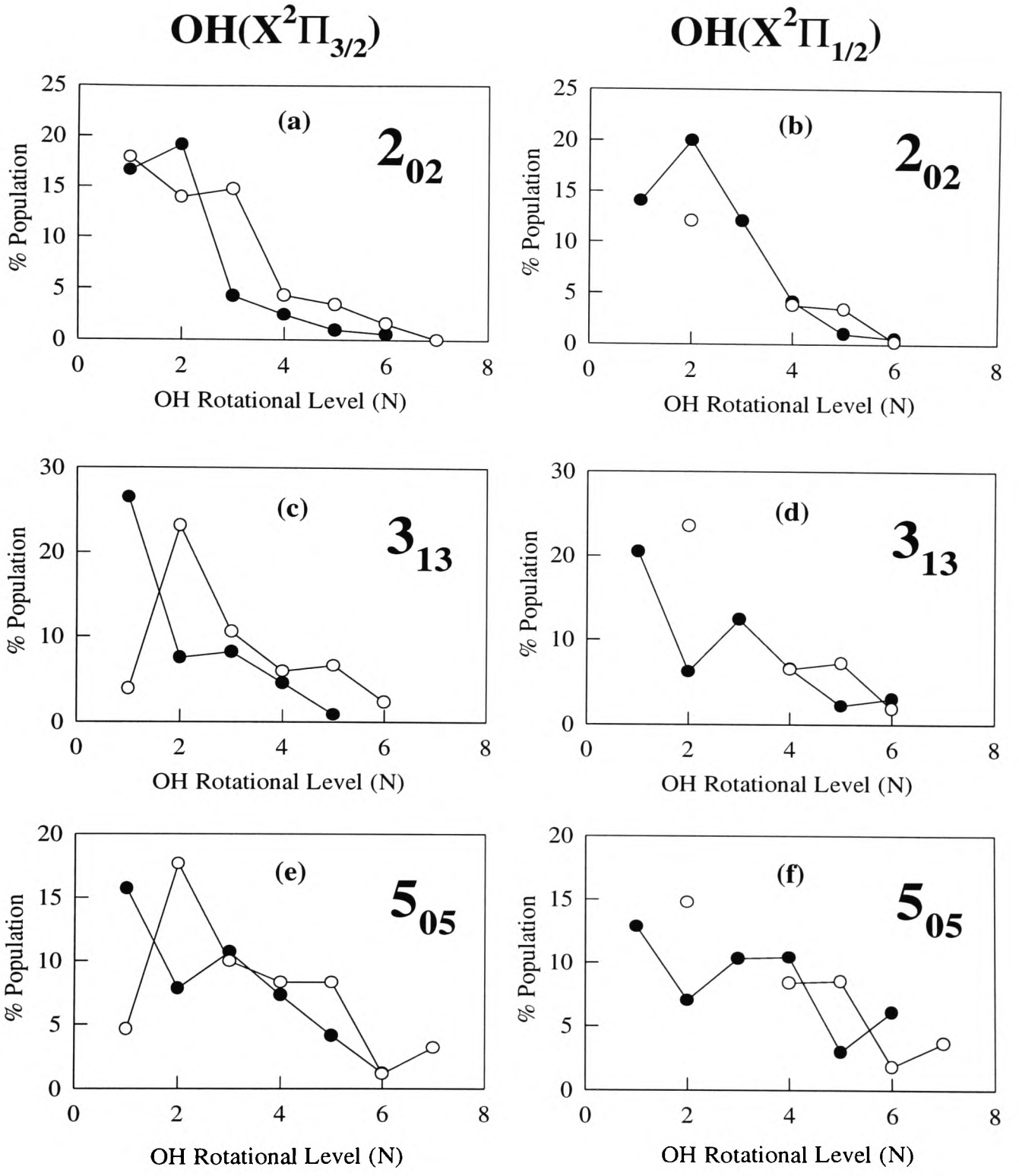

Figure 3.24 The relative OH $^2\Pi_{\frac{3}{2}}$ and OH $^2\Pi_{\frac{1}{2}}$ lambda-doublet population distributions ($A' = \bullet$, $A'' = \circ$) arising from the 282 nm photodissociation of $J_{K_a,K_c} = 2_{02}$ (a), 3_{13} (b) and 5_{05}. The total population in each spin orbit state has been normalised to unity.

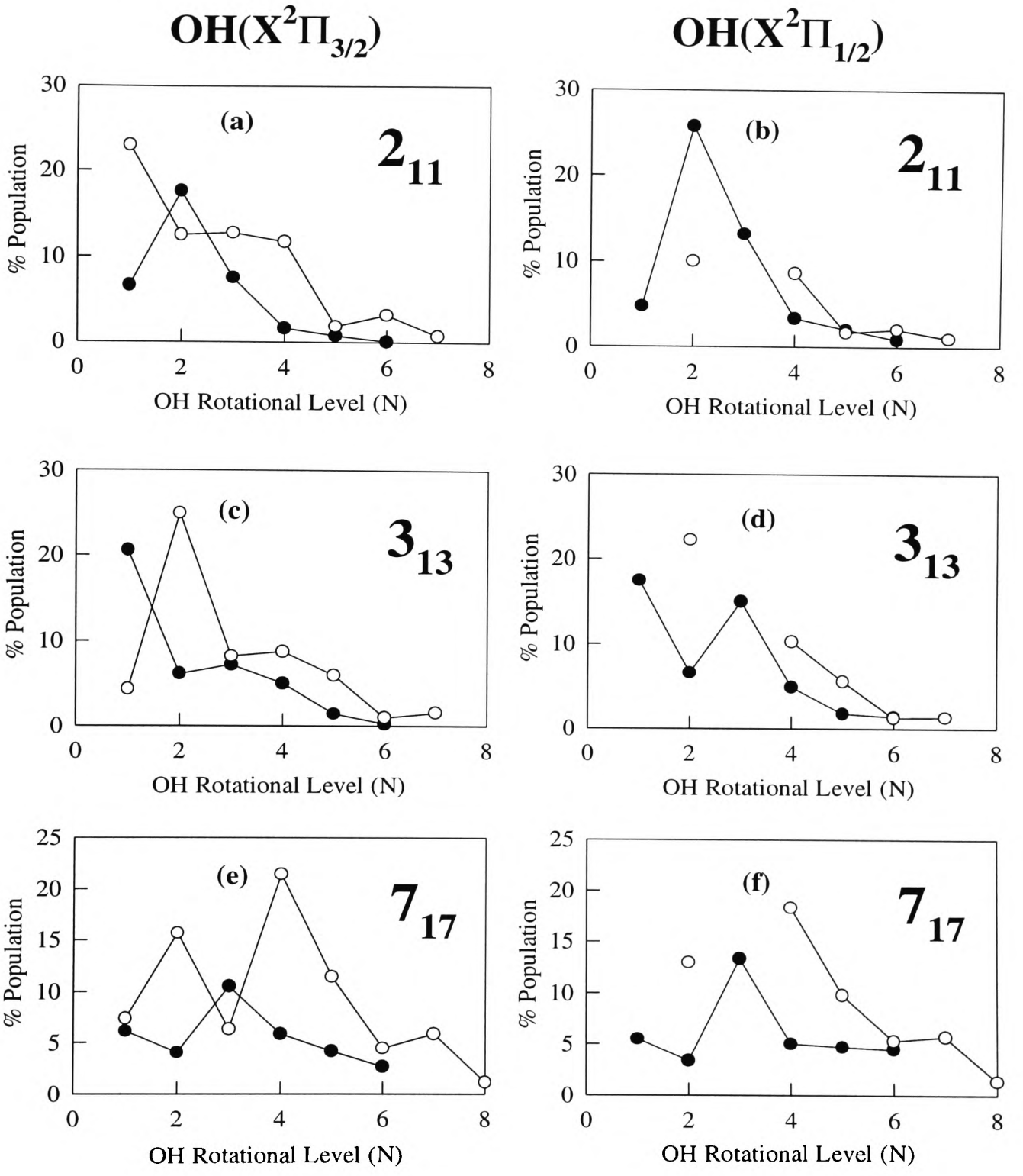

Figure 3.25 The relative OH $^2\Pi_{\frac{3}{2}}$ and OH $^2\Pi_{\frac{1}{2}}$ lambda-doublet population distributions ($A' = \bullet$, $A'' = \circ$) arising from the 282 nm photodissociation of $J_{K_a,K_c} = 2_{02}$ (a), 3_{13} (b) and 5_{05}. The total population in each spin orbit state has been normalised to unity.

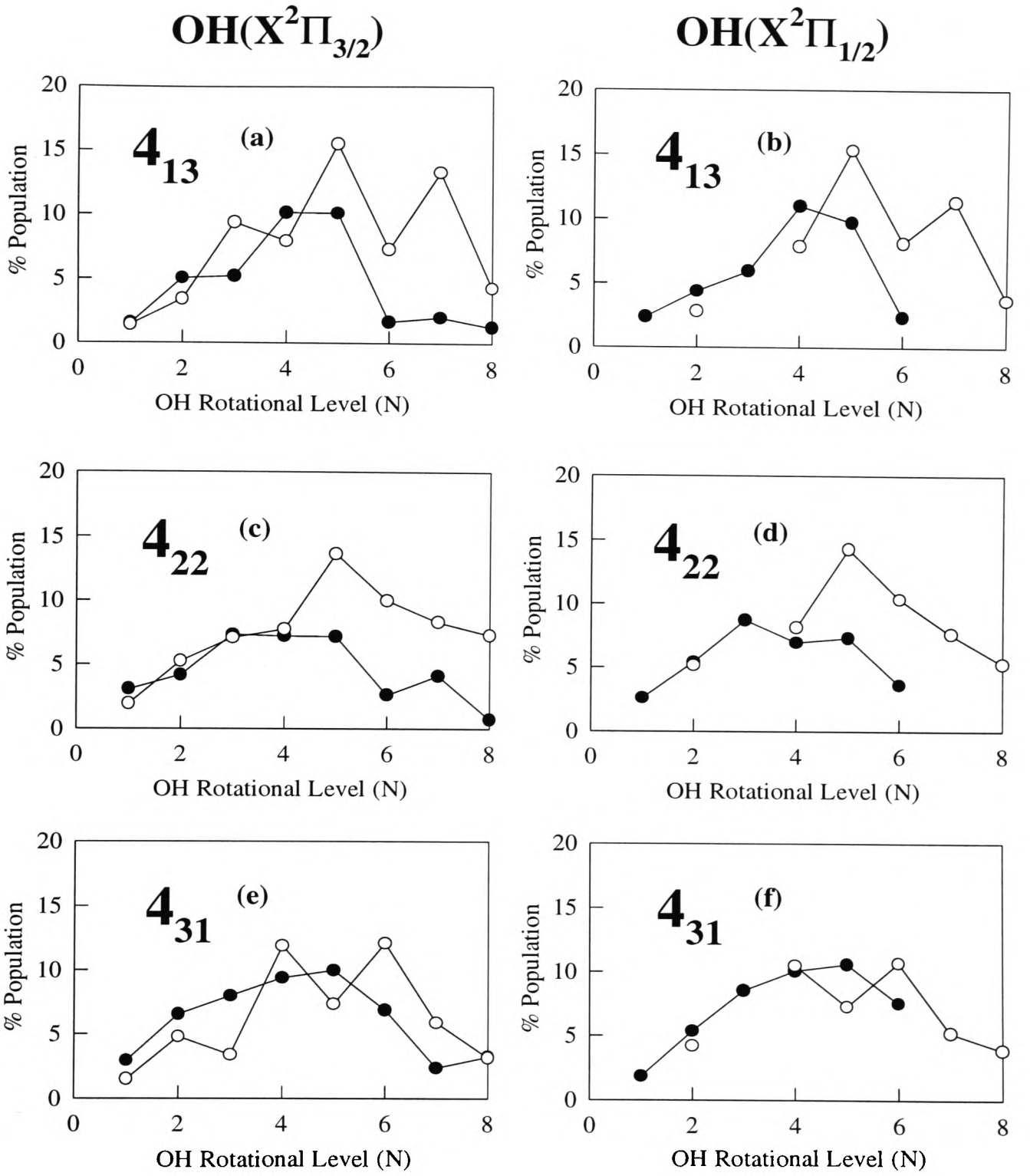

Figure 3.26 The relative OH $^2\Pi_{\frac{3}{2}}$ and OH $^2\Pi_{\frac{1}{2}}$ lambda-doublet population distributions (A′ = •, A″ = ∘) arising from the 282 nm photodissociation of $H_2O|04\rangle|2\rangle^-$ $J_{K_a,K_c} = 4_{13}$ [(a) & (b)], 4_{22} [(c) & (d)] and 4_{31} [(e) & (f)]. The total population in each spin orbit state has been normalised to unity.

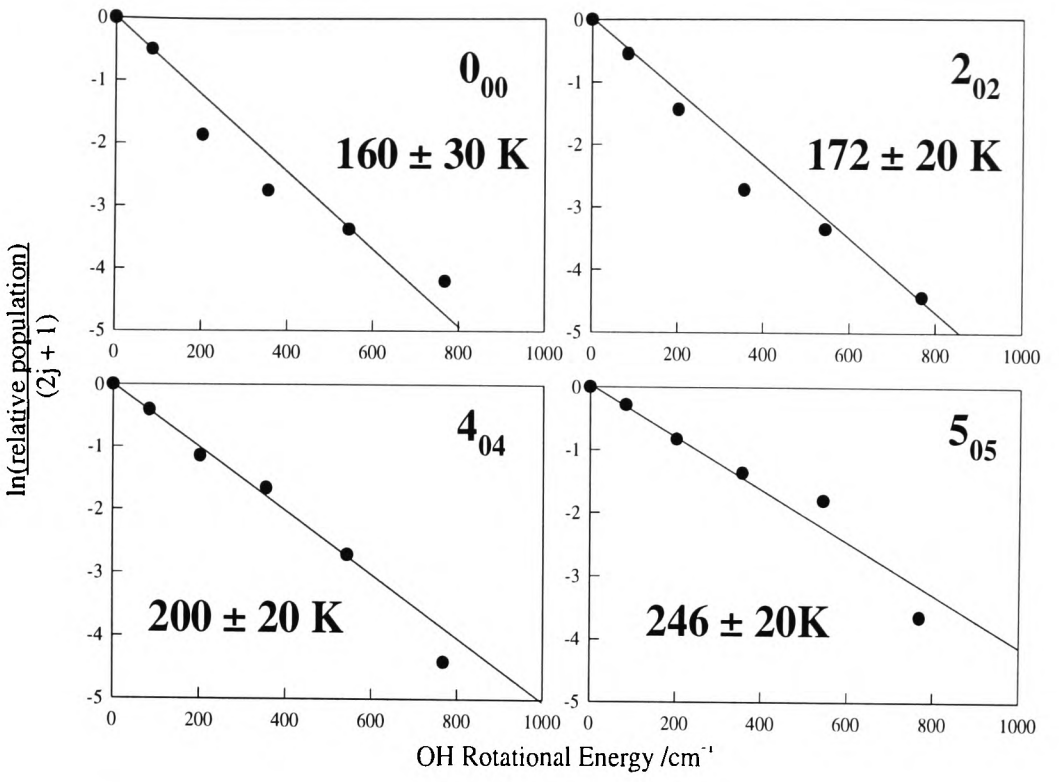

Figure 3.27 Boltzmann plots of the lambda-doublet avaraged OH $^2\Pi_{\frac{3}{2}}$ population distribution for various $H_2O|04\rangle^-$ rotational states, 0_{00}, 2_{02}, 4_{04} and 5_{05}. Also shown are the corresponding OH photofragment rotational temperatures calculated from the gradient of the lines drawn through the experimental points.

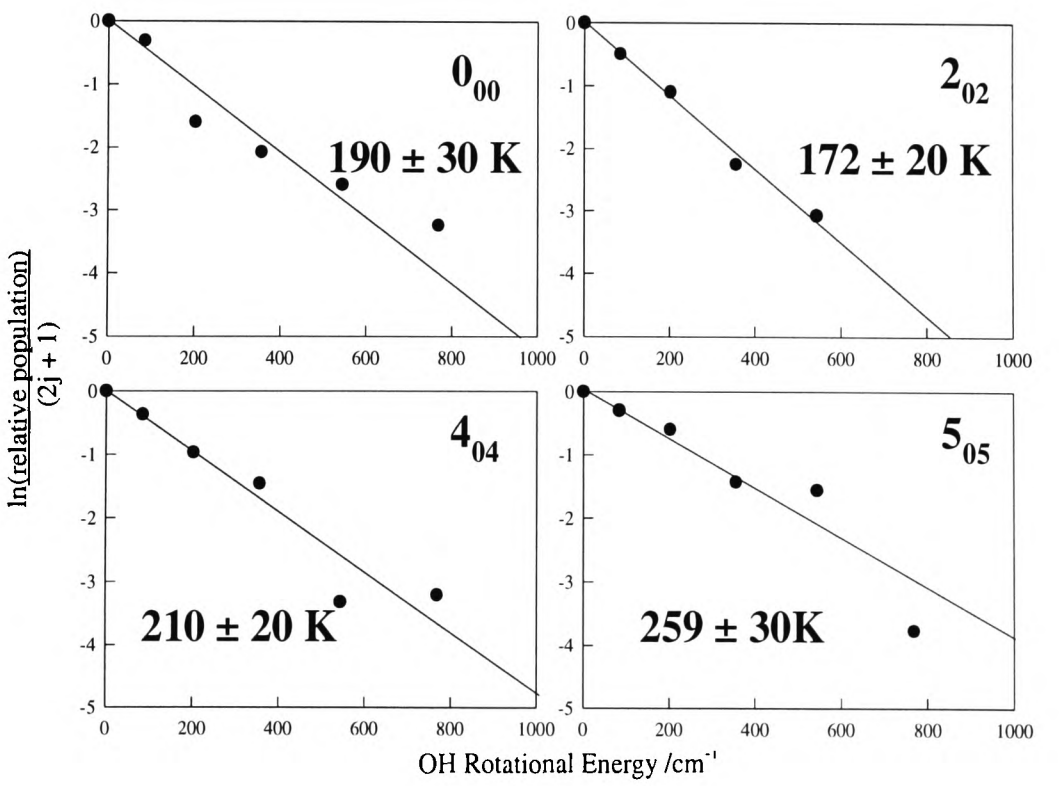

Figure 3.28 As in Figure 3.27 but from the photolysis of $H_2O|05\rangle^-$.

	E_{AVL} /cm^{-1}	0_{00}	2_{02}	2_{11}	3_{13}
$\|04\rangle^-$ + 282 nm	≈ 8000	160±30 K	172±20 K	176±20 K	192±20 K
$\|05\rangle^-$ + 282 nm	≈ 11000	190±30 K	172±20 K	170±20 K	208±20 K
$\|01\rangle^-$ + 193 nm[a]	≈ 14000	193 K[b]			

4_{04}	4_{23}	4_{22}	5_{05}	5_{15}	6_{06}	7_{17}
200±20 K	-	270±30 K	244±30 K	246±20 K	-	-
210±20 K	285±30 K	267±20 K	263±40 K	259±30 K	392±20 K	455±20 K
377 K[b]						

(a) From Reference [34].

(b) No error is quoted for these values [34].

Table 3.5 The OH photofragment rotational temperatures, calculated from Boltzmann plots of the lambda-doublet averaged rotational distributions, generated *via* the 282 nm photodissociation of rotational states J_{K_a,K_c} (J = 2–7) of $H_2O|04\rangle^-$ and $|05\rangle^-$. Also shown are two values arising from the experiments of Andresen and coworkers, photolysing $H_2O|01\rangle^-$ at 193nm, and the energy available in each study for disposal in the photofragments, E_{AVL}.

The OH product rotational temperatures obtained from the photolysis of $H_2O|05\rangle^-$ and $|04\rangle^-$ are summarised in Table 3.5; also shown are two values arising from the experiments of Andresen and coworkers, photolysing $H_2O|01\rangle^-$ at 193nm, for $J_{K_a,K_c} = 0_{00}$ and 4_{04}. It can be seen that there is a small increase in the OH photofragment rotational temperature with increasing J and K_a in the reagant rotational state. In addition, increasing the total supplied energy for a given intermediate rotational state, J_{K_a,K_c}, has virtually no effect on the product rotational temperature, within the given errors.

3.6 Summary

3.6.1 The VMP of $H_2O|04\rangle^-$ and $H_2O|05\rangle^-$

- The OH $^2\Pi_{\frac{1}{2}}$ and $^2\Pi_{\frac{3}{2}}$ fragment lambda doublet population distributions arising from the photodissociation of $H_2O(J = 0)$ from this and the previous study of Andresen and coworkers [34], are found to be insensitive to the amount of energy available for disposal in the photofragments.

- The OH $^2\Pi_{\frac{1}{2}}$ and $^2\Pi_{\frac{3}{2}}$ fragment lambda doublet population distributions arising from the photodissociation of $H_2O(J > 0)$ are found to depend sensitively on the number of quanta in the intermediate parent vibrational overtone and the energy of the photolysis photon.
- For a given initial parent rovibrational state and photolysis energy, there are small differences in the oscillatory structure of the product OH $^2\Pi_{\frac{1}{2}}(A')$ and OH $^2\Pi_{\frac{3}{2}}(A')$ lambda-doublet population distibutions. No differences are seen for the other lambda-doublet state A'' within the experimental error.
- A small preferential population of the OH $^2\Pi_{\frac{1}{2}}$ spin-orbit state is found for the A' population distributions, but a near-'statistical' distribution is observed for the A'' data.

3.6.2 The VMP of $H_2O|04\rangle|2\rangle^-$

- Much hotter OH fragment rotational distributions than those obtained in the isoenergetic VMP of $H_2O|05\rangle^-$ are observed, in accord with the previous work of Crim and coworkers [224].
- The $OH^2\Pi_{\frac{3}{2}}$ and $OH^2\Pi_{\frac{1}{2}}$ lambda-doublet population distributions are found to be identical within the experimental error.
- No preferential population of an OH photofragment spin-orbit state is observed for both the A'' and A' population distributions, within the experimental error.

Chapter 4 The VMP of HOD($\tilde{A}$): Experimental results

$$HOD(\tilde{X}^1A_1) \xrightarrow{\lambda_1} HOD(\tilde{X}^1A_1; v, J) \xrightarrow{\lambda_2} HOD(\tilde{A}^1B_1) \rightarrow H(^2S) + OD(X^2\Pi_\Omega; N'') \xrightarrow{\lambda_3, LIF}$$
$$\rightarrow D(^2S) + OH(X^2\Pi_\Omega; N'') \xrightarrow{\lambda_3, LIF}$$

Presented in this chapter are the experimental results of the 288 nm photodissociation of the partially deuterated water molecule, excited into the third and fourth O–H stretching vibrational overtone. In Section 4.2 the rotational assignment of the two parent overtone spectra is discussed. In Section 4.3, an estimate of the branching ratio, $\frac{\phi(OD)}{\phi(OH)}$, between the two dissociation channels is presented and the OD($^2\Pi_\Omega$;v=0) photofragment rotational distributions arising from a range of initial parent angular momentum states are presented in Section 4.4. A preferential population of either of the OD photofragment spin-orbit or lambda doublet states is considered in Sections 4.5 and 4.6 respectively. To introduce the chapter, a brief outline of the previous studies into the photodissociation dynamics of HOD($\tilde{A}$) is presented.

4.1 Previous studies

Following the success of modelling the photodissociation of H_2O in its first absorption band, a decade ago two groups transferred their attention to the partially deuterated isotopomer, HOD. With the introduction of a deuterium atom, the symmetry of the molecule is broken and the two dissociation channels, equivalent in HOH, are now distinct, producing either OH + D or OD + H. Schinke and coworkers [240] carried out full quantum-mechanical and classical time-independent calculations on the photodissociation HOD(0,0,0),(1,0,0) and (0,0,1)[1], J = 0 at a variety of energies, calculating the dissociation cross-section and the branching ratio into the two dissociation channels. Although no experimental data were present at the time of the study, the calculations showed that the HOD absorption

[1]The nomenclature refers to (ν_{OH},ν_{bend},ν_{OD}), the number of quanta in the three vibrational modes of HOD

spectrum was very similar in detail to that of H_2O, but slightly shifted to higher energies. The branching ratio, $\frac{\phi(OD)}{\phi(OH)}$, was more importantly found to be very dependent both on the total supplied energy and on the initial vibrational excitation of the parent. In addition, pre-excitation of the vibration in a particular bond was shown to enhance the dissociation of that bond, especially for H–OD. The classical and quantum mechanical results are in very good agreement, and classical intuition could to a large extent be used to explain this aspect of the dynamics.

Running in parallel to this work was that of Imre and coworkers [241], who were using a time-dependent wavepacket appproach [185] to model the photodissociation dynamics of HOD. As well as reproducing the findings of the time-independent study, a calculated resonance Raman spectrum and a two-photon scheme capable of controlling the bond breaking process in HOD were presented. The interpretation and success of these two results rested on the dynamics of the parent in its ground state. Due to the loss of symmetry, the stretching vibration local mode states $|nm\rangle$ and $|mn\rangle$ are not equivalent, and the dynamical tunnelling effect [185, 183, 184], which produces the local mode doublets $|nm\rangle^{\pm}$ in H_2O, is destroyed [242]. This means that a wave packet initially displaced only along the O–D bond will move along the R_{OD} coordinate and will not develop any appreciable amplitude along the R_{OH} coordinate; in other words, initially localised excitation will remain localised. As well as greatly simplifying the interpretation of the emission spectrum, the use of a UV photon should also allow the selective dissociation of a locally excited HOD molecule into a particular set of products. In practice, the calculations showed that a complete preference for H + OD production was possible over a significant UV photon energy range from $\nu_{OH} = 1$ and higher. However, a clear preference for the D + OH channel could be achieved only if the double resonance photolysis went through a high OD stretching overtone ($\nu_{OD} \geq 3$).

In the light of these predictions, an experimental demonstration of this isotope effect in HOD($\tilde{A}$–$\tilde{X}$) photodissociation was achieved by several laboratories. Bersohn and coworkers [243] photodissociated HOD in a 50/50 mixture of H_2O and D_2O by a single-photon at 157.5 nm and produced $\approx$ 4.2 times more H + OD than D + OH, consistent with Imre's calculated data [241].

Resonance Raman spectra of HOD were obtained by Sension and coworkers [244], with excitation at 174.6, 171.4, 160.0 and 150.0 nm (all resonant with the $\tilde{A}$ state). These

spectra were consistent with the corresponding spectra for H_2O and D_2O, showing only a progression in the symmetric stretch, and were relatively insensitive to the photon energy. A comparison with the calculated spectra of Imre and coworkers [241, 244] provided an altogether satisfactory agreement between theory and experiment.

In a series of papers, Rosenwaks and coworkers [167] were able to show that compared with unexcited parent molecules, the preparation of HOD with one quantum of O–H stretching vibrational excitation prior to 193 nm photolysis, lead to an enhancement of $\sim$ 300 in the decomposition. However, the excitation of one quantum into the O–D stretch produced an enhancement of only $\sim$ 6; in addition, the photodissociation of the (1,0,0) state produced at least 2.5 $\pm$ 0.5 times more OD than OH. These enhancements are explained in terms of an increasing Franck-Condon overlap of the vibrational wave function of the ground electronic state with the upper PES, and are in qualitative agreement with the theoretical predictions [240, 241].

The photodissociation of HOD, excited into the third OH stretching overtone (4,0,0) at three different wavelengths (218.5, 239.5 and 266.0 nm) has been carried out by Crim and coworkers [202, 203]. Dissociation at the two longer wavelengths resulted in the production of at least 15 times more OD than OH, but comparable amounts were produced when the 218.5 nm UV photon was used. The large selectivity and the strong dependence on the photodissociation wavelength are consistent with the theoretical results [203, 240, 241] and are not simple energetic differences. The photolysis at 239.5 nm is isoenergetic (same total supplied energy) with the experiments of Rosenwaks, who found very different relative yields of OH and OD. The results reflect the crucial role of the vibrationally excited intermediate state in accessing different regions of the excited potential surface.

Rosenwaks and coworkers [168] have recently demonstrated the preferential production of D + OH (unlike all of the previous studies) by photodissociating HOD($\nu_{OD} = 3$) at 193 nm, obtaining a branching ratio OD/OH of $\approx$ 0.38. This is in agreement with the earlier predictions of Imre and coworkers [241] on the enhancement of $\nu_{OD} \geq 3$ photodissociation, but differs in the branching ratio obtained at the specific wavelength. Imre calculated that a preference would be seen for $\lambda_2 \geq 210$ nm, with aproximately equal amounts of OH and OD being produced by 193 nm excitation.

To date, no group has considered the vibrational or rotational distributions of the OH or

Vibrational Level	Band Origin	Rotational Constants cm^{-1}		
$(\nu_{OH},\nu_{bend},\nu_{OD})$	Energies cm^{-1}	A	B	C
(0,0,0) [a]	0	23.4139	9.1034	6.4063
(1,0,0) [b]	3707	22.3549	9.0864	6.3183
(4,0,0)	13844.8	19.465	9.042	6.092
(5,0,0)	16911.8	18.467	9.022	6.020

(a) From ref. [245] (b) From ref. [246]

Table 4.1 The band origin energies and equilibrium rotational constants with increasing quanta in the O–H stretch of HOD. The zero point energy of HOD is 4000.26 cm^{-1}. The rotational constants quoted for $4\nu_{OH}$ and $5\nu_{OH}$ were calculated for J $\geq$ 4 to an accuracy of $\pm$ 0.2 cm^{-1} on the calculated rotational line positions.

OD photofragments and the full effect the ground-state parent rovibrational motion has on ensuing photofragment dynamics on the $\tilde{A}$ state potential.

4.2 HOD($4\nu_{OH}$) and ($5\nu_{OH}$) overtone spectrum

No spectroscopic study of the O–H (or O–D) high stretching vibrational overtone states has yet been carried out; only the ground and fundamental stretching rovibrational spectra have been recorded and assigned [245]–[248]. Crim and coworkers [202], in their HOD VMP experiments were only concerned with measuring the branching ratios between the two dissociation channels on the $\tilde{A}$ state, and the assignment of the three rotational transitions that were excited in the (4,0,0) state was not required.

Shown in Figure 4.1(b) is a segment of the photoacoustic spectrum in the region of the (4,0,0) overtone of HOD, recorded with a mixture of H_2O and D_2O. There are no D_2O transitions in this region and the transitions that are present can be assigned to $H_2O|04\rangle^-$ and HOD. Figure 4.1(a) shows the photoacoustic spectrum recorded with just H_2O present and a comparison of the two clearly shows which transitions in Figures 4.1(b) belong to HOD. Figure 4.1(c) shows the HOD($\rightarrow$OD) VMP action spectrum in the same region.

Similar to H_2O, the rotational contant in HOD is large enough for the individual rotational transitions to be resolved with only modest resolution. To assign the transitions, a simula-

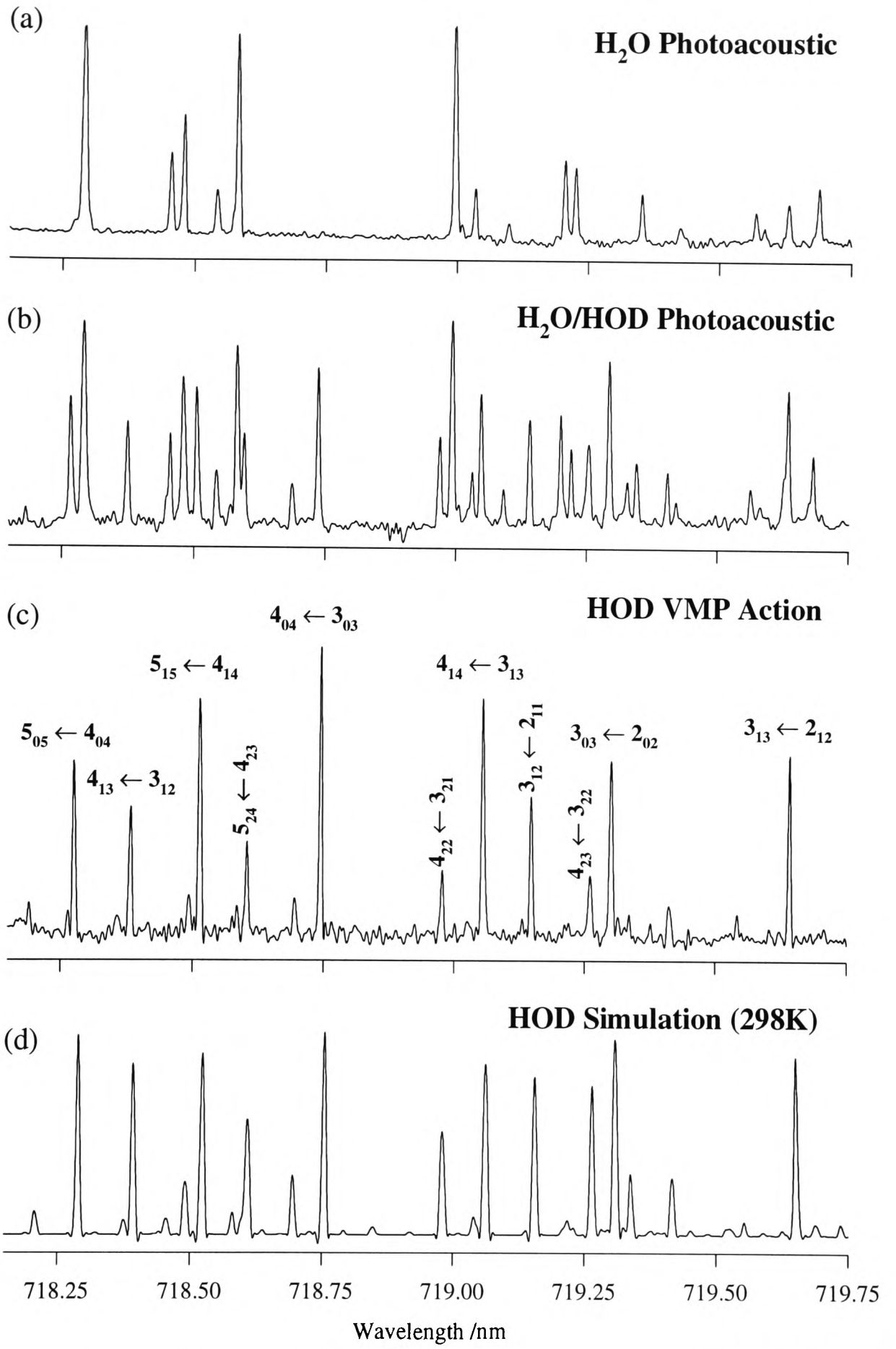

Figure 4.1 A segment of the rovibrational spectrum in the region of the third O–H stretch overtone of HOD using (b) photoacoustic spectroscopy and (c) recording a VMP action spectrum, fixing the probe radiation on the $A^2\Sigma$–$X^2\Pi$ (1–0) $Q_{22}(1)$ LIF transition of OD and scanning the overtone excitation radiation. Also shown are (a) the photoacoustic spectrum of just H_2O in the same region and (d) a simulation of the HOD($4\nu_{OH}$) band at 298K.

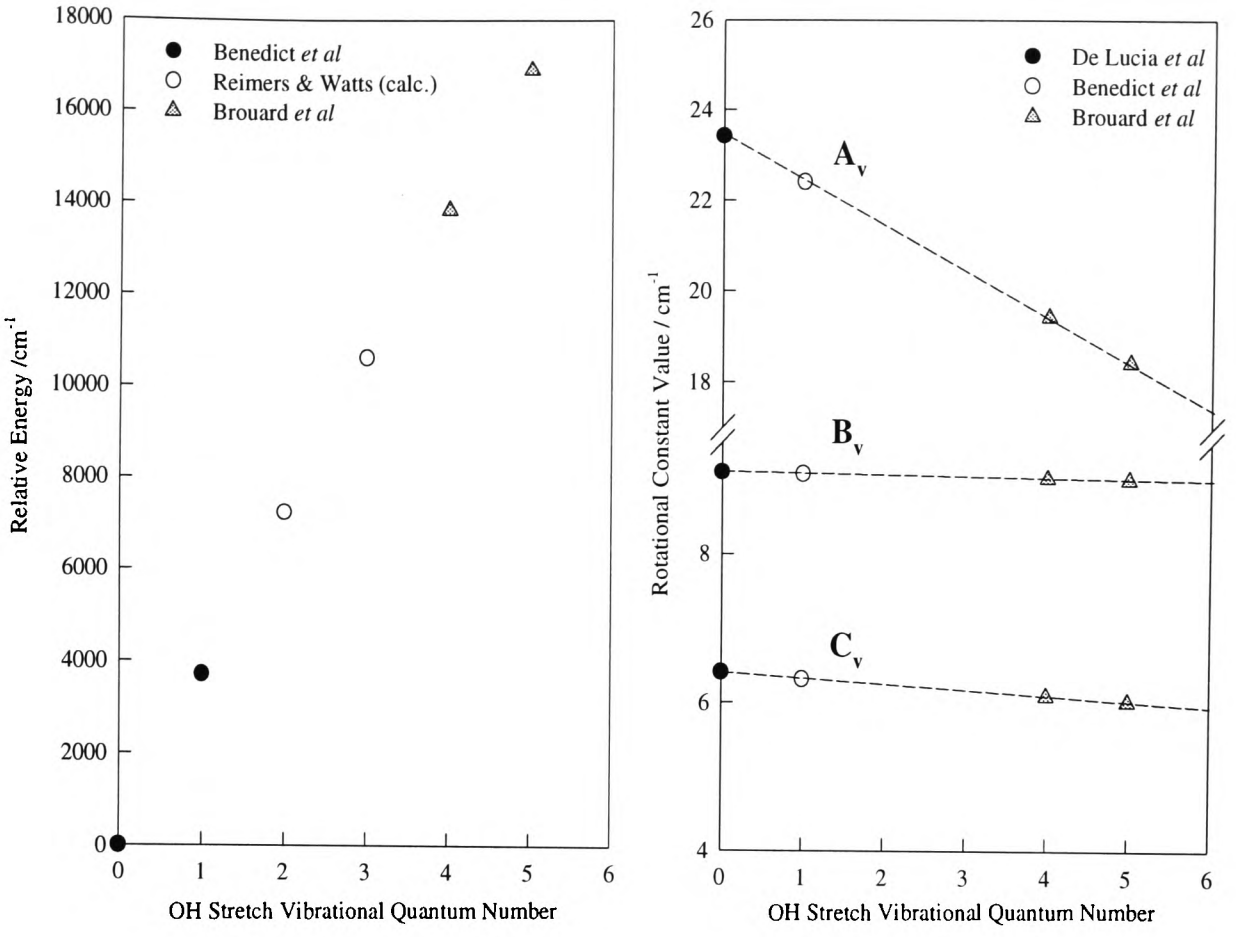

Figure 4.2 A plot of the experimental (Benedict *et al* [246]) and calculated (Reimers *et al* [227]) band origin relative energies (left) and A, B and C rotational constant values [245, 246] (right) as a function of the O–H stretch quantum number in HOD. Also shown are the experimentally measured band origins and calculated equilibrium rotational constants for the (4,0,0) and (5,0,0) overtone states, arising from a simulation of the respective rovibrational spectrum.

tion of the rovibrational spectrum was carried out (see Figure 4.1), assuming it to be that of a near-prolate asymmetric rotor [249, 174, 250] with predominantly A-type rather than B-type transitions ($\approx$ 0.7:0.3) [245]–[248].

Shown in Figure 4.2 is a plot of the HOD($n\nu_{OH}$) n = 1–5 overtone band origin energy and the A, B and C equilibrium rotational constant values (right) as a function of O–H stretch vibrational quantum number. An estimate of the (4,0,0) band origin and rotational constants was initially taken from an extrapolation of the data of Benedict *at al* [246], De Lucia *et al* [245] and Reimers and Watts [227]. These values were then refined using standard techniques [249, 250] until the calculated line positions agreed with the experimentally observed

transitions within $\pm$ 0.2 cm^{-1}, which was more than adequate for these experiments.

The measured band origin and calculated equilibrium rotational constants for the (4,0,0) band of HOD are shown in Figure 4.2 and in Table 4.1. As a comparison, the data for the ground and fundamental vibrational level [246, 245] and the values obtained from the measurement of the (5,0,0) band are also given (see below). It is very clear, from the large change in the equilibrium A rotational constant with increasing O–H vibration, that the vibrational motion is predominantly perpendicular to the a inertial axis. In addition, the equilibrium rotational motion becomes less near-prolate top with increasing quanta in the OH stetch. A segment of the simulated HOD(4,0,0) rotational spectrum is shown in Figure 4.1(d).

HOD(4,0,0) rotational transitions (P↑, Q↑ and R↑), up to J=8, were unambiguously assigned to the observed transitions in the VMP action spectrum recorded between 716.6 nm and 729.6 nm. Within the signal-to-noise ratio, no transitions from any other HOD vibrational level could be seen. As is mentioned earlier, the break in symmetry caused by the introduction of a deuterium atom into the water molecule produces two very localised oscillators, H–OD and HO–D. Reimers and Watts [227] calculated a percentage measure of the local mode character of the HOD($n\nu_{OH}$) states as they did for H_2O, up to $n = 3$. Values between 100 and 97 % were quoted which compared very well with those obtained for H_2O. It can therefore be expected that the $4\nu_{OH}$ (and $5\nu_{OH}$) overtone is very well described within the local mode picture and is well separated from the other vibrational levels.

To determine whether there are any isotope effects in the $\tilde{A}$ state photodissociation dynamics of the water molecule, it was desirable to excite the same rotational states in the intermediate overtone level as the isoenergetic 282 nm photolysis of $H_2O|04\rangle^-$ (and $H_2O|05\rangle^-$). In addition, the slightly lower rotational constants of HOD compared with those of H_2O meant that higher J states (upto J = 6-7) could also be excited. According to the simulations the J = 0 transition, $0_{00} \leftarrow 1_{01}$, was spectrally overlapped with another transition, $2_{20} \leftarrow 2_{21}$, within the resolution of the laser radiation ($\approx$ 0.2 cm^{-1}). The calculated line positions were 13844.87 cm^{-1} and 13844.76 cm^{-1} respectively and the experimentally observed line was at 13844.8 cm^{-1}. As the rotational distribution of the resulting photofragment depends so much on the intermediate parent rotational state, no data could be obtained for J = 0 with any degree of confidence.

Rotational Transition	$3_{13} \leftarrow 2_{12}$	$4_{04} \leftarrow 3_{03}$	$5_{05} \leftarrow 4_{04}$
Line Position / nm	719.639	718.741	718.270

Table 4.2 Rotational transitions and line positions excited in the HOD(4,0,0) overtone level. The assignments were calculated from a prolate asymmetric rotor fit to the measured spectrum.

For transitions with J > 0, a similar scenario was encountered for 6_{16}(R↑), 5_{15}(R↑), 3_{03}(R↑) and 2_{02}(R↑). From the remaining strong R-branch transitions, data of good enough quality could only be obtained for the three transitions listed in Table 4.2: 5_{05}(R↑), 4_{04}(R↑) and 3_{13}(R↑). No alternative transition (Q and P branch lines) to the desired rotational states could provide suitable LIF photofragment data.

Shown in Figure 4.3(a) is a segment of the VMP action spectrum recorded in the region of the HOD(5,0,0) vibrational overtone; also shown is a simulation of the band using the equilibrium rotational constants and band origin taken from Table 4.1. The (5,0,0) rotational spectrum was again assumed to be that of a near-prolate asymmetric rotor with 70 % A type transitions, in accordance with the lower overtone levels. It is clear from the Figure that the fit of the calculation to experiment is very good, with an error of ± 0.2 cm^{-1} between the calculated and experimental line positions for J ≥ 5. The differences observed in the relative intensities of the transitions in the action spectrum and simulation are to be expected, as they reflect the dependence of the photofragment rotational distribution on the parent rotational state, not the rotational temperature of the reagent molecule. All of the transitions in the experimental VMP action spectrum between 587.7 nm and 597.7 nm could be assigned to the HOD(5,0,0) overtone, and no transitions from other vibrational levels are observed.

The rotational states excited in this experiment are listed in Table 4.3, along with the line positions and the type of transition (R↑, P↑ or Q↑). The transition accessing the J = 0 state is overlapped with another transition within the spectral resolution of the laser radiation (0.2 cm^{-1}). In the simulation of the overtone spectrum, $0_{00} \leftarrow 1_{11}$ occurs at 16911.66 cm^{-1}, and the $4_{22} \leftarrow 4_{23}$ transition occurs at 16911.81 cm^{-1}; the experimentally observed line was at 16911.7 cm^{-1}. The 4_{22}(Q↑) transition is much weaker than 0_{00}(P↑)

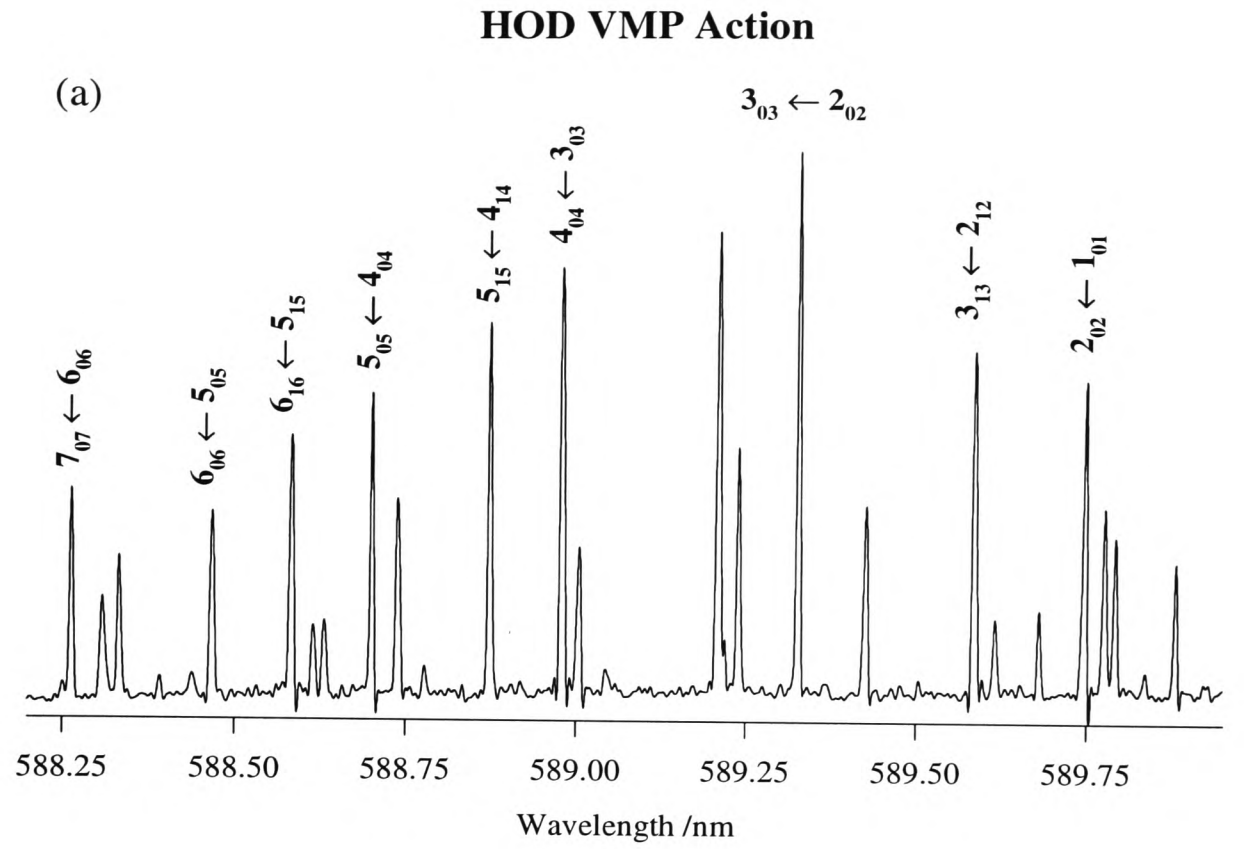

Figure 4.3 A section of the (a) VMP action spectrum in the region of the HOD(5,0,0) vibrational overtone, recorded by fixing the LIF probe radiation on the OD photofragment $Q_{22}(2)$ transition and scanning the overtone excitation radiation. Shown in (b) is a near-prolate asymmetric rotor simulation of the HOD(5,0,0) state in the same spectral region. The assigments shown in (a) are from the simulation.

$J''_{K_a,K_c} \leftarrow J'_{K_a,K_c}$	Line Position		
$3_{13} \leftarrow 2_{12}$	589.589 nm	$6_{16} \leftarrow 5_{15}$	588.577 nm
$3_{03} \leftarrow 2_{02}$	589.329 nm	$6_{06} \leftarrow 5_{05}$	588.464 nm
$4_{04} \leftarrow 3_{03}$	588.980 nm	$7_{07} \leftarrow 6_{06}$	588.289 nm
$5_{15} \leftarrow 4_{14}$	588.875 nm	$1_{11} \leftarrow 2_{12}$	591.847 nm
$5_{05} \leftarrow 4_{04}$	588.700 nm	$1_{11} \leftarrow 1_{10}$	591.044 nm

Table 4.3 Rotational transitions excited in the HOD(5,0,0) stretching overtone during the 288 nm VMP experiments. All of the rotational states are selected using R-branch transitions, except for 1_{11} where a P↑ and a Q↑ line were used.

and will therefore make only a small contribution to the rovibrational excitation of HOD at 16911.7 cm^{-1}. However, as the photofragment rotational distributions are very sensitive to the intermediate parent rotational state, no data for HOD(5,0,0) J = 0 could be recorded with complete confidence.

To confirm that the photofragment rotational state distributions in this study were insensitive to the parent rotational branch chosen to excite the intermediate rovibrational state, distributions were obtained arising from $J_{K_a,K_c} = 1_{11}$(P↑ and Q↑). These are shown for the OD $^2\Pi_{\frac{3}{2}}$ photofragment in Figure 4.4. The close similarity of the two lambda-doublet distributions reaffirms the observation made during the H_2O experiments in Chapter 3 that any effect due to parent alignment (with respect to the overtone excitation radiation) on the photodissociation dynamics is lost in the very saturated LIF regime.

4.3 (OH + D)/(OD + H) branching ratio

The partially deuterated water molecule, excited into its third and fourth O–H stretch vibrational overtone, has been photodissociated at 288 nm *via* the $\tilde{A}$ state. These studies provide $\sim$ 8000 cm^{-1} and $\sim$ 11000 cm^{-1} excess energy respectively for partitioning into the photofragments. This is considerably lower than that provided in the experiments of Crim and coworkers [202, 203] photolysing HOD($4\nu_{OH}$) at 218.5, 239.5 and 266.0 nm respectively. This is shown in Figure 4.5 in which the ground and electronic state potentials of HOD are plotted against the dissociation coordinate R_{H-OD}. Two of the possible dissociation

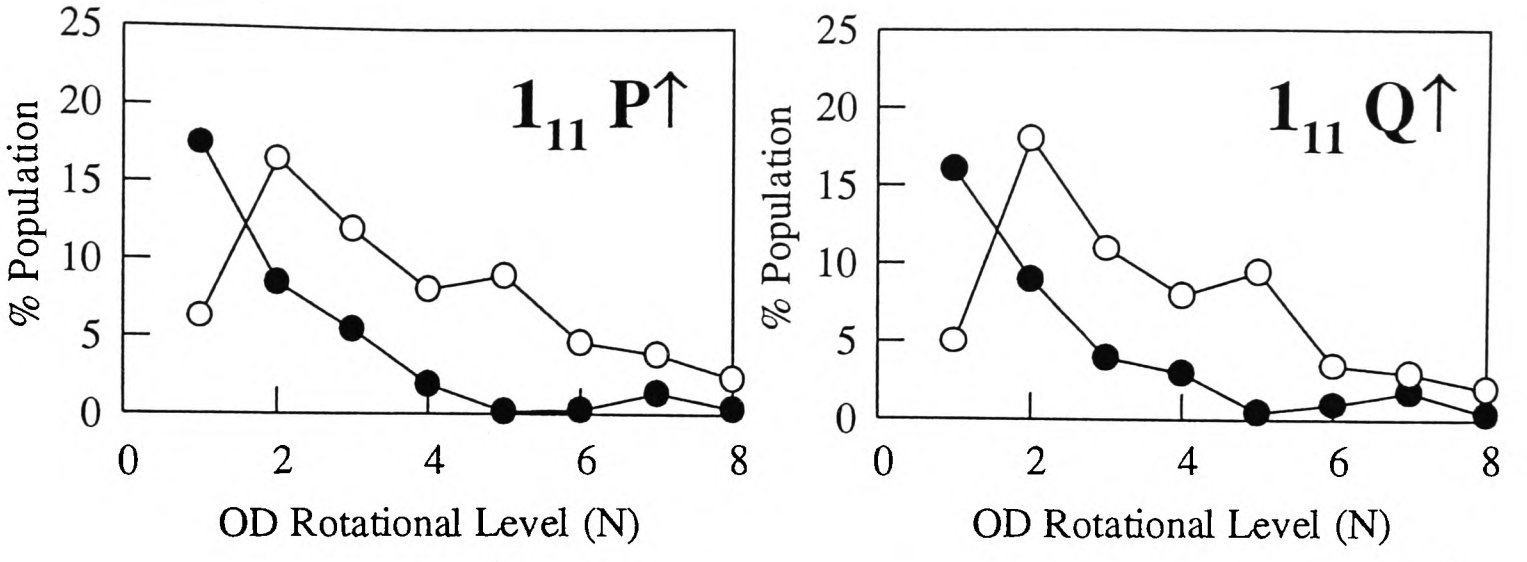

Figure 4.4 The photofragment OD($X^2\Pi_{3/2}$) population distributions (plotted against N, the total angular momentum quantum number, j, apart from spin) within the A′ (•) and A″ (○) lambda doublet levels arising from the 288 nm photodissociation of HOD(5,0,0); J=1_{11} P↑ and Q↑.

channels, producing OH($X^2\Pi$) and OD($^2\Pi$) in their ground vibrational state, have been probed using laser-induced fluorescence.

Shown in Figure 4.6(a) is the OD $A^2\Sigma$–$X^2\Pi$ (1–0) LIF spectrum arising from the 288 nm photodissociation of HOD(4,0,0);$J_{K_a,K_c} = 4_{04}$. It can be seen that the overall signal-to-noise level obtained in this experiment was much lower than in the H_2O experiments. This is likely to be primarily due to the reduced number of HOD molecules present in the laser interaction region in the experimental cell for an H_2O/D_2O mixture compared with pure H_2O. Effects due to a reduction in the overtone absorption cross-section and to the Franck-Condon overlap of the intermediate state with the excited electronic state will be discussed below.

As was expected from the reduced rotational constant of OD compared with OH, higher angular momentum states in the photofragment (up to N = 10) are observed in the LIF spectrum. In addition, a problem similar to that encountered for the OH (1–0) LIF spectrum is an unfortunate overlap of the $Q_{22}(1)$ & (4) and (2) & (3) transitions within the laser resolution; this makes it impossible to extract the relative population of the $^2\Pi_{\frac{1}{2}}(A'')$

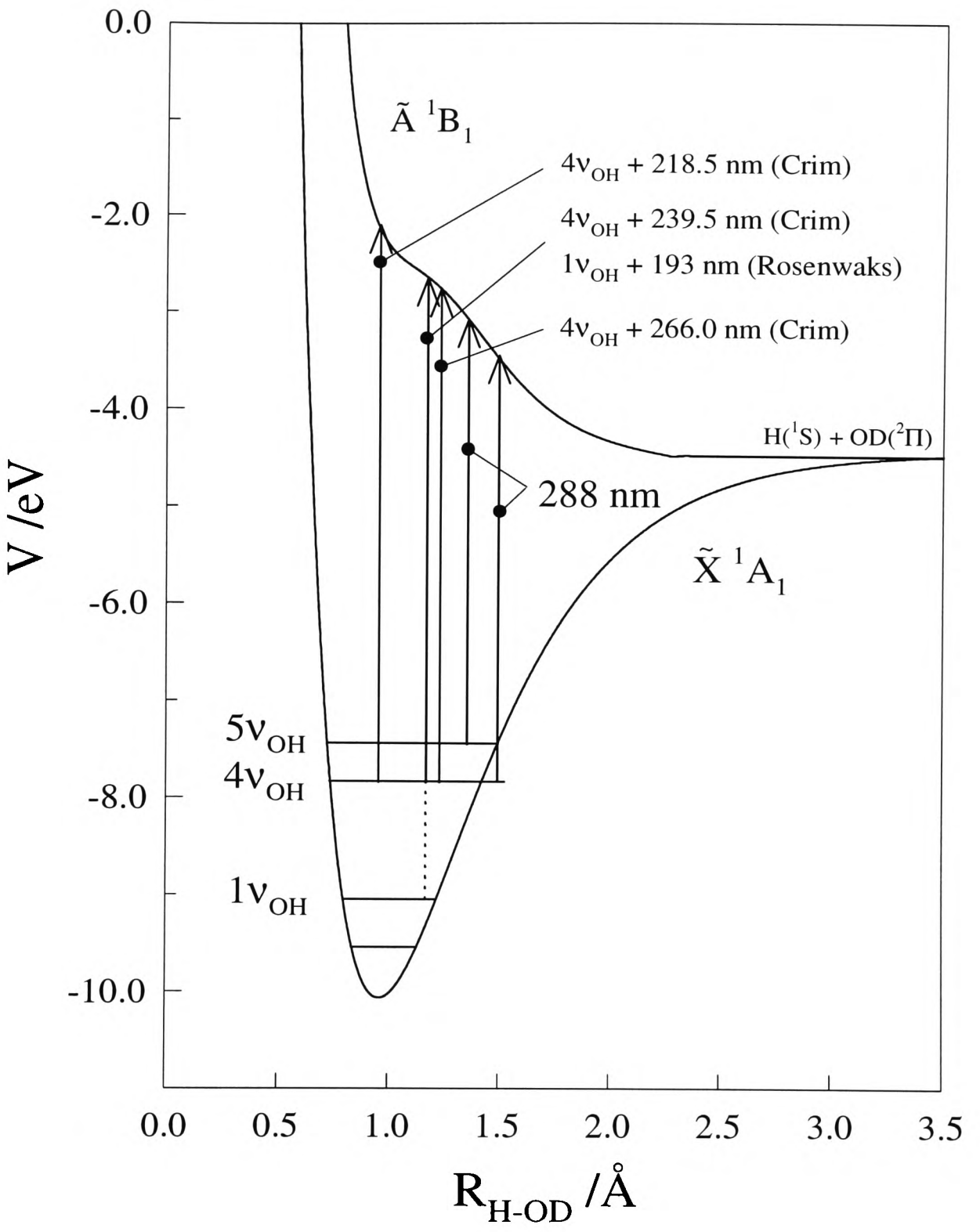

Figure 4.5 A plot of the water ground state potential of Jensen and coworkers [229] and the $\tilde{A}$-state potential of Steammler and Palma [230] against the dissociation coordinate, R_{H-OD}. Excitation to the $\tilde{A}$ state potential should preferentially occur from more extended H–OD configurations than in the previous studies of Crim and coworkers [202, 203] and Rosenwaks and coworkers [167].

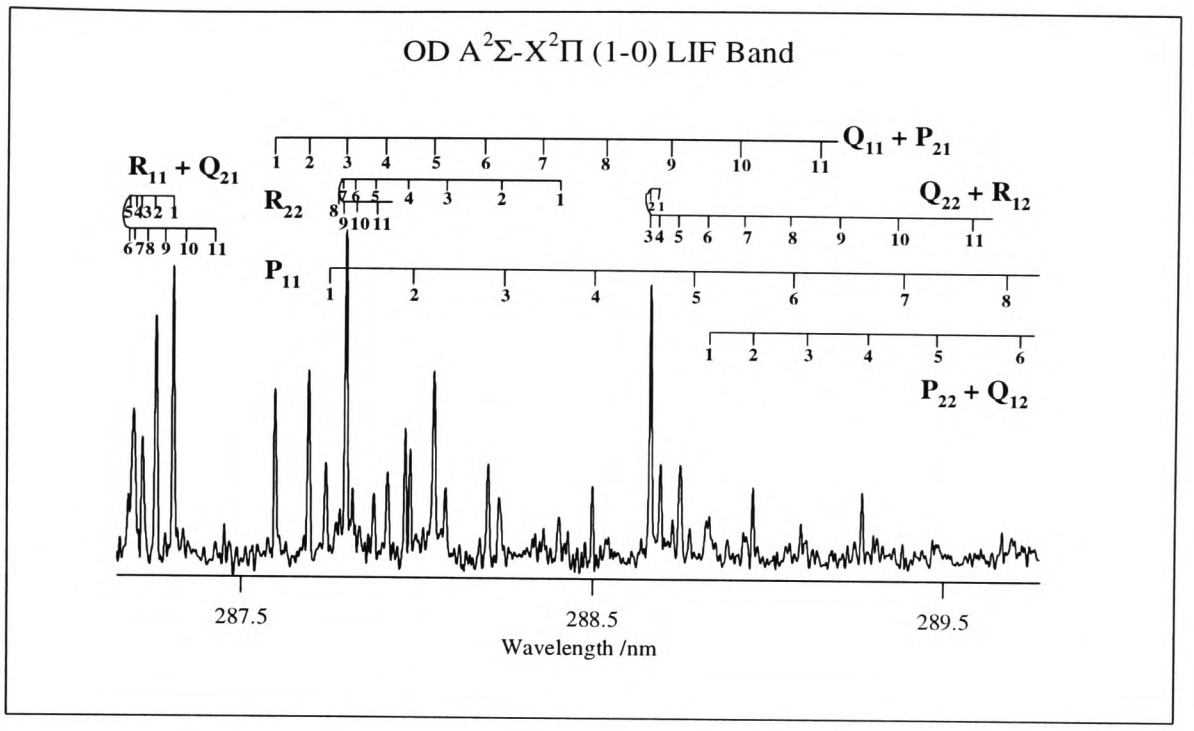

Figure 4.6 (a) OD $A^2\Sigma$–$X^2\Pi$ (1–0) and (b) OH $A^2\Sigma$–$X^2\Pi$ (1–0) LIF spectra arising from the 288 nm photodissociation of HOD(4,0,0);$J_{K_a,K_c} = 4_{04}$

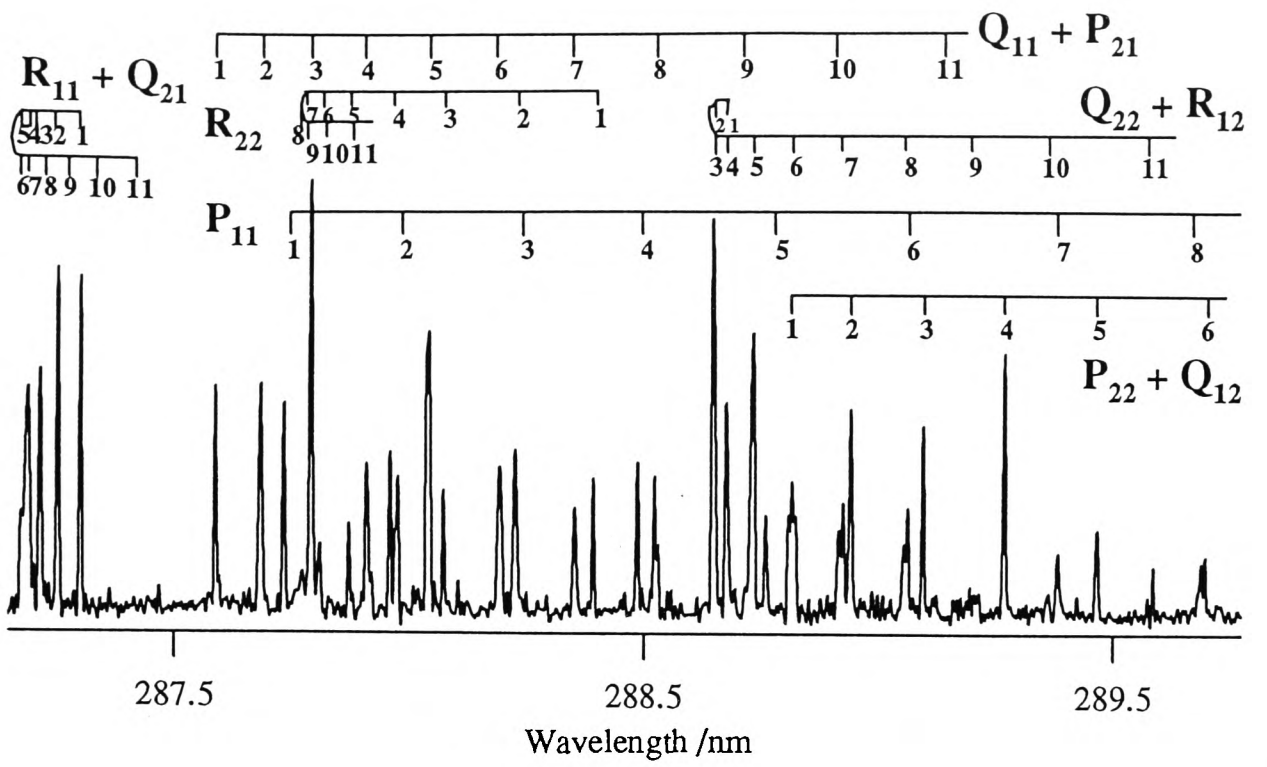

Figure 4.7 OD photofragment $A^2\Sigma$–$X^2\Pi$ (1–0) LIF spectrum arising from the 288 nm photodissociation of HOD(5,0,0) $J_{K_a,K_c} = 4_{04}$. The assignments are taken from reference [204](a).

lambda-doublet state for $N \leq 4$.

Shown in Figure 4.6(b) is a scan across the OH $A^2\Sigma$–$X^2\Pi$ (1–0) LIF band, again exciting HOD(4,0,0);$J_{K_a,K_c} = 4_{04}$ in the parent intermediate state. There are no H_2O transitions near this HOD transition and, in line with the measurements of Crim and coworkers [201, 202], very little OH was detected. Within the signal-to-noise levels, an estimate of the branching ratio from the total LIF signal gave $\frac{\phi(OD,v=0)}{\phi(OH,v=0)} > 12$.

Shown in Figure 4.7 is the OD photofragment $A^2\Sigma$–$X^2\Pi$ (1–0) LIF spectrum arising from the 288 nm photodissociation of HOD(5,0,0) $J_{K_a,K_c} = 4_{04}$. Although the signal-to-noise levels are not quite as good as those obtained from the 282 nm photodissociation of $H_2O|05\rangle^-$, there is a clear improvement on the data for HOD(4,0,0), shown in Figure 4.6 for the same rotational state $J_{K_a,K_c} = 4_{04}$.

The absorption cross-section for the (5,0,0) band is approximately an order of magnitude

lower than that of (4,0,0)[2]. The overall VMP cross-section, which is a product of $\sigma_{(5,0,0)}$ and $\sigma_{Elec.}$ [3] taken from the total LIF signals or an estimate based on the signal to noise ratios, is however approximately twice as large as that for the VMP of HOD(4,0,0). This would suggest that at 288 nm the overlap between the $\tilde{A}$ state potential and the $5\nu_{OH}$ state is approximately 20 times larger than that with the $4\nu_{OH}$ state. As is shown in Figure 4.5, on purely energetic grounds excitation to the $\tilde{A}$ state at 288 nm from the (4,0,0) overtone should occur preferentially in a classically forbidden region of the ground state potential surface where the vibrational wavefunction drops off exponentially from a peak close to the classical turning point. In contrast, excitation from (5,0,0) should occur close to the peak of the vibrational wavefunction at the turning point. This may well be the primary cause for the differing VMP cross-sections, and will be discussed further in Chapter 5.

Fixing the overtone radiation upon (5,0,0) $4_{04} \leftarrow 3_{03}$ transition, the LIF probe radiation was scanned across the OH (1–0) LIF band as well as the OD (1–0) band; similar to the 288 nm photolysis of HOD(4,0,0), no OH(X, v = 0) photofragments were detected within the signal-to-noise. From an examination of the photoacoustic spectrum of a mixture of H_2O/D_2O and the VMP action spectrum of HOD(5,0,0), it is clear that there are no H_2O transitions overlapped with this transition. From the total LIF signals collected, the branching ratio for the 288 nm photodissociation of HOD(5,0,0) was estimated as $\frac{\phi(OD,v=0)}{\phi(OH,v=0)} > 21$. This is larger than the value arising from the 288 nm photolysis of HOD(4,0,0) ($\frac{\phi(OD,v=0)}{\phi(OH,v=0)} > 12$), but the better signal-to-noise levels obtained in this experiment should have provided a much more accurate estimate of the ratio, and the differences between the two data sets are probably not significant. Compared with the value obtained by Crim and coworkers [202, 203] for the 218.5, 239.5 and 266.0 nm photolysis of HOD(4,0,0)[4] (≈ 1, > 15 and > 15 respectively), the current data are consistent with an increasingly preferential dissociation into the OD + H channel with increasing photolysis wavelength, which is also consistent with excitation up to the excited electronic state occuring further into the OD + H exit channel.

---

[2]No absorption cross-sections have been measured for these two overtone levels, but measured values for $H_2O|04\rangle^-$ and $|05\rangle^-$ do provide a good estimate of their relative magnitudes.

[3]$\sigma_{(5,0,0)}$ is the absorption cross-section from the ground vibrational state to the (5,0,0) vibrational overtone and $\sigma_{Elec.}$ is the cross-section from the intermediate overtone state to the excited electronic state

[4]According to the line positions quoted by Crim, using the asmmetric rotor simulation the three transitions that were used in this study were $1_{11} \leftarrow 1_{10}$, $1_{10} \leftarrow 2_{11}$ and $2_{02} \leftarrow 3_{03}$

4.4 OD X($^2\Pi$) photofragment rotational state distributions

4.4.1 The 288 nm VMP of HOD($4\nu_{OH}$) *via* the $\tilde{A}$ State

Shown in Figure 4.8 are the OD $X^2\Pi_{\frac{3}{2}}$ photofragment rotational distributions, for both of the lambda-doublet states A′ and A″, arising from the 288 nm photodissociation of HOD(4,0,0) $J_{K_a,K_c} = 3_{13}$ (a), 4_{04} (b), and 5_{05} (c). The population in each distribution has been normalised to unity to show the relative lambda-doublet populations. Again, the distributions are very structured and depend sensitively on the rotational state of the ground state parent molecule in the intermediate overtone level. A comparison can be made with the corresponding data arising from the isoenergetic 282 nm photolysis of $H_2O|04\rangle^-$ shown in Figures 3.9(d) & (e) and 3.24(e). The j-dependent oscillatory structure is very similar in both experiments (allowing for the increased experimental error for the HOD data), except that the distributions arising from HOD photolysis appear to be shifted along by one unit of angular momentum N.

Figure 4.9 shows the OD photofragment distributions for the $^2\Pi_{\frac{1}{2}}$ spin-orbit state. The low signal-to-noise levels prevented any reasonable data from being obtained for the A″ lambda-doublet for both $J_{K_a,K_c} = 3_{13}$ and 4_{04}. Only the A′ distribution is therefore shown, and the percentage population values shown do not reflect the relative lambda-doublet populations. However, data for both lambda-doublet states were obtained for $J_{K_a,K_c} = 5_{05}$, and the relative population distributions are shown in Figure 4.9(c). The photofragment distributions depend sensitively upon the intermediate parent rotational state; the structure in the lambda-doublet population distributions is similar to the corresponding distributions from the 282 nm VMP of $H_2O|04\rangle^-$ if it is shifted along by one unit of angular momentum N.

4.4.2 The 288 nnm VMP of HOD($5\nu_{OH}$) *via* the $\tilde{A}$ State

Shown in Figure 4.10 are the relative OD $X^2\Pi_{\frac{3}{2}}$ photofragment lambda-doublet distributions obtained from the 288 nm photodissociation of HOD(5,0,0) [Fig. (a), (c) & (e)] and HOD(4,0,0) [Fig. (b), (d) & (f)] $J_{K_a,K_c} = 3_{13}$, 4_{04} and 5_{05}. Comparing the two sets of data, there are small but noticable differences in parts of the oscillatory structure, although the general shape of each lambda-doublet distribution remains very much the same. This is

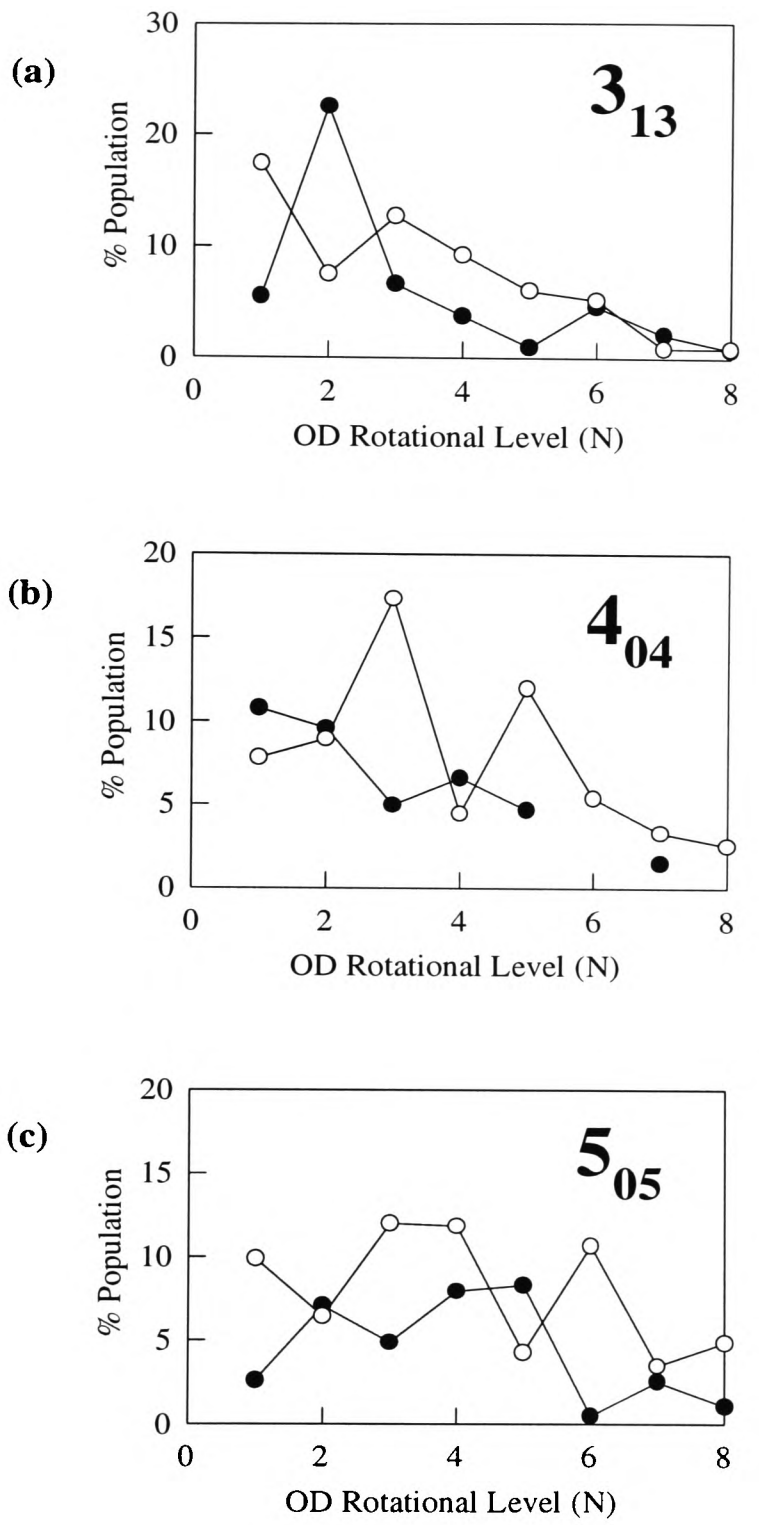

Figure 4.8 The OD $X^2\Pi_{\frac{3}{2}}$ photofragment rotational distributions, for both lambda-doublet states, A′ (•) and A″ (○), arising from the 288 nm photodissociation of HOD(4,0,0) J_{K_a,K_c} = 3_{13} (a), 4_{04} (b) and 5_{05} (c). Each distribution has been normalised to unity.

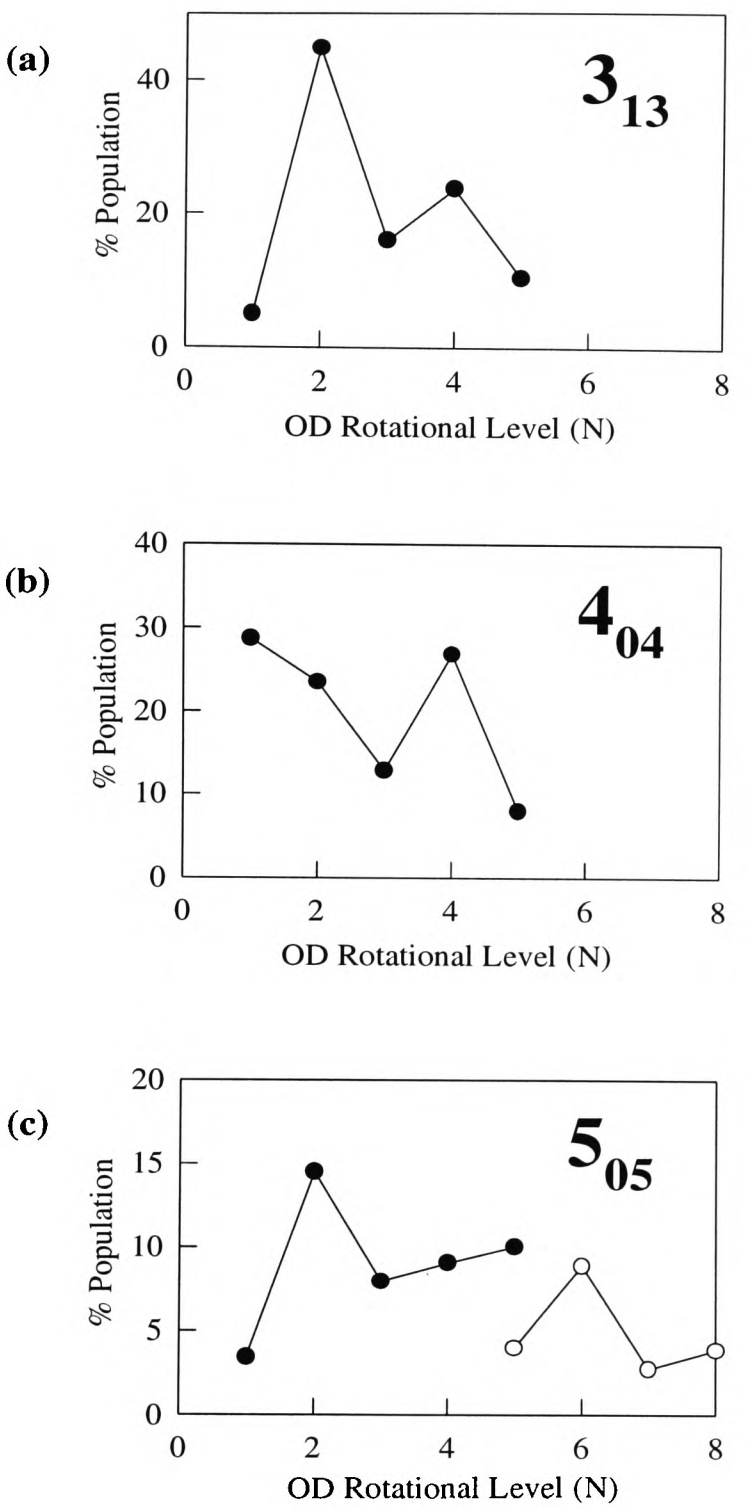

Figure 4.9 OD $X^2\Pi_{\frac{1}{2}}$ photofragment rotational distributions, arising from the 288 nm photodissociation of HOD(4,0,0) $J_{K_a,K_c} = 3_{13}$ (a), 4_{04} (b) and 5_{05} (c). The A′ population (•) is shown in each distribution, but only the A″ distribution (○) is shown for $J_{K_a,K_c} = 5_{05}$.

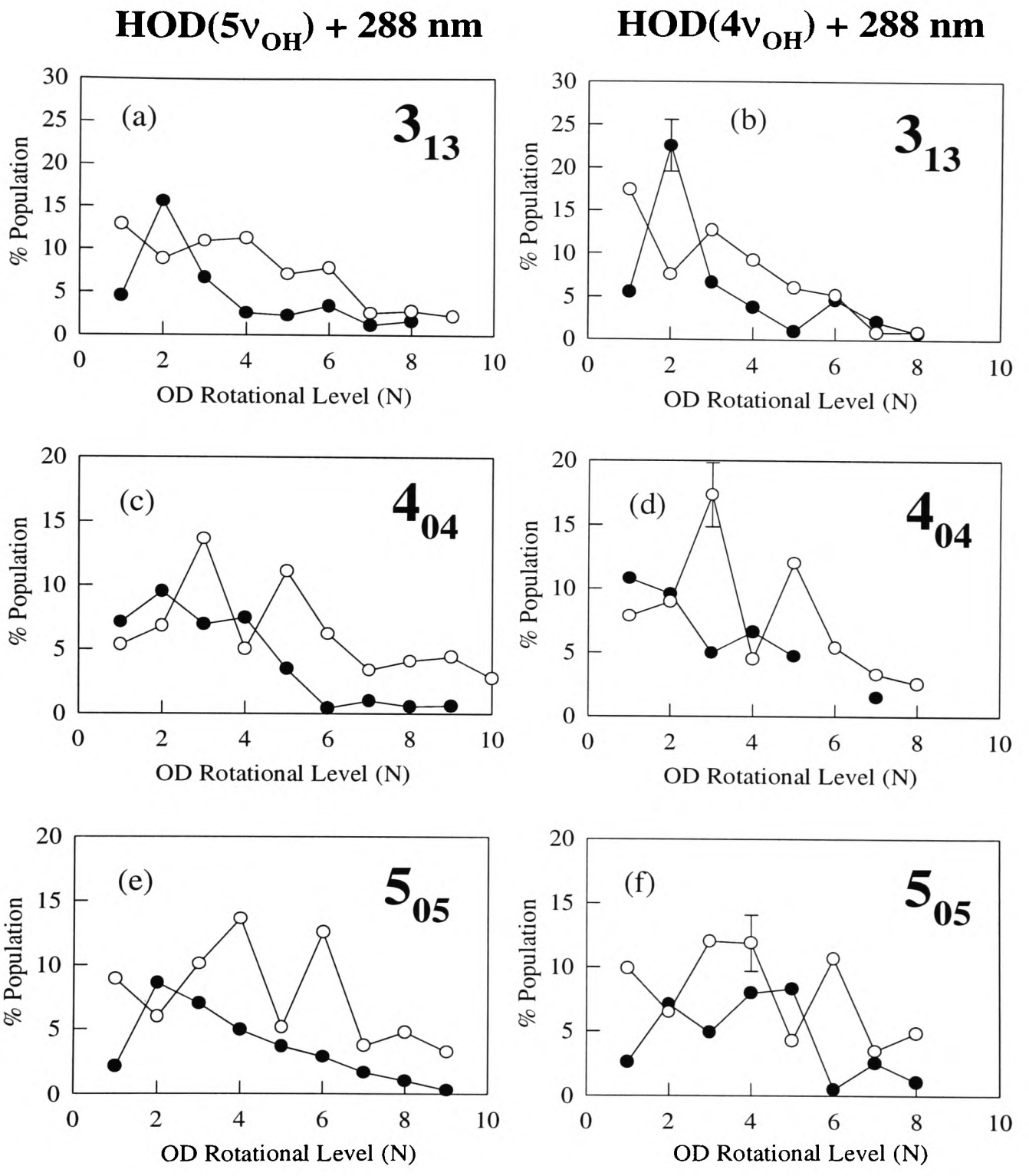

Figure 4.10 The OD $X^2\Pi_{\frac{3}{2}}$ photofragment lambda-doublet population distributions A′ (•) and A″ (○), obtained from the 288 nm photodissociation of HOD(5,0,0) $J_{K_a,K_c} = 3_{13}$ (a), 4_{04} (c) and 5_{05} (e). Also shown are the corresponding distributions arising from the 288 nm photodissociation of HOD(4,0,0) [(b), (d) & (f)]. Each distribution has been normalised to unity.

unlike the 282 nm VMP of H_2O in which dramatic changes in the phase and intensity of the structure in the OH photofragment lambda-doublet distributions were seen between those arising from the excitation of the $|04\rangle^-$ and $|05\rangle^-$ overtone levels. Energetically, there is little difference between the 288 nm VMP of HOD(4,0,0) & (5,0,0) and the 282 nm VMP of $H_2O|04\rangle^-$ & $|05\rangle^-$ respectively. Any differences between the two experiments must be attributed to the effect of the isotopic substitution on the ground- and excited-state motion of the parent during the VMP process.

The remaining OD $X^2\Pi_{\frac{3}{2}}$ photofragment lambda-doublet distribution are summarised in Figure 4.11 for HOD(5,0,0) $J_{K_a,K_c} = 1_{11}$ [Fig. 4.11(a)], 3_{03} [Fig. 4.11(b)], 5_{15} [Fig. 4.11(c)], 6_{06} [Fig. 4.11(d)], 6_{16} [Fig. 4.11(e)], 7_{07} [Fig. 4.11(f)]. It is clear from this figure that increasing the value of J in the ground state parent has two effects on the OD photofragment rotational distributions: As well as changing and increasing the oscillatory structure, the peak in the resulting OD photofragment distribution spreads to higher values of N. This would suggest that there is still a good correlation between the OD photofragment rotational excitation and ground state parent rotational motion, but it is perhaps not as strong as that seen in the H_2O experiments (see Chapter 3).

The OD $X^2\Pi_{\frac{1}{2}}(A')$ photofragment distributions, obtained from the 288 nm photolysis of HOD(5,0,0) are shown in Figure 4.12 for $J_{K_a,K_c} = 3_{13}$ (a), 4_{04} (c) and 5_{05} (e), as well as the corresponding data for HOD(4,0,0). Each distribution has been normalised to unity and therefore does not reflect the relative lambda-doublet populations. As with the OD $X^2\Pi_{\frac{3}{2}}$ data, only small differences between the two sets of distributions are evident within the experimental errors.

The remaining OD $X^2\Pi_{\frac{1}{2}}(A')$ photofragment lambda-doublet distributions arising from the photolysis of HOD(5,0,0) $J_{K_a,K_c} = 1_{11}$ [Fig. 4.13(a)], 3_{03} [Fig. 4.13(b)], 5_{15} [Fig. 4.13(c)], 6_{06} [Fig. 4.13(d)], 6_{16} [Fig. 4.13(e)], 7_{07} [Fig. 4.13(f)] are presented in Figure 4.13. Again, only the A′ lambda-doublet data have been shown. Very little information can be gained from the 2 or 3 data points obtained for the $^2\Pi_{\frac{1}{2}}(A'')$ population distributions . In line with the corresponding data for the $^2\Pi_{\frac{3}{2}}$ state shown in Figure 4.11, the change in the oscillatory structure and peak of the overall distribution with parent angular momentum J is again evident.

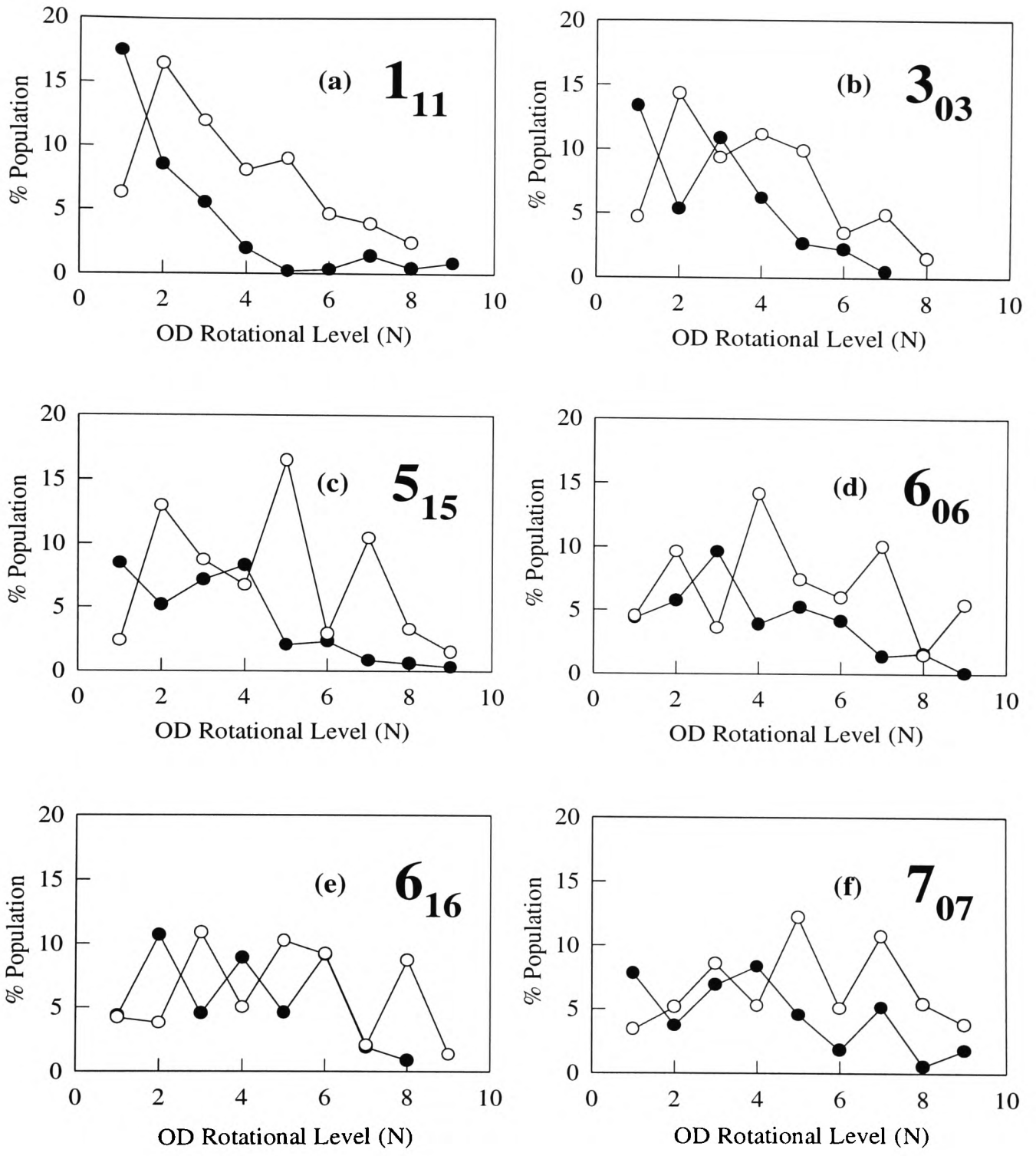

Figure 4.11 The OD $X^2\Pi_{\frac{3}{2}}$ photofragment rotational distributions, for both the A′ (•) and A″ (○) lambda-doublet states, arising from the 288 nm photodissociation of HOD(5,0,0) $J_{K_a,K_c} = 1_{11}$ (a), 3_{03} (b), 5_{15} (c), 6_{06} (d), 6_{16} (e) and 7_{07} (f). Each distribution has been normalised to unity.

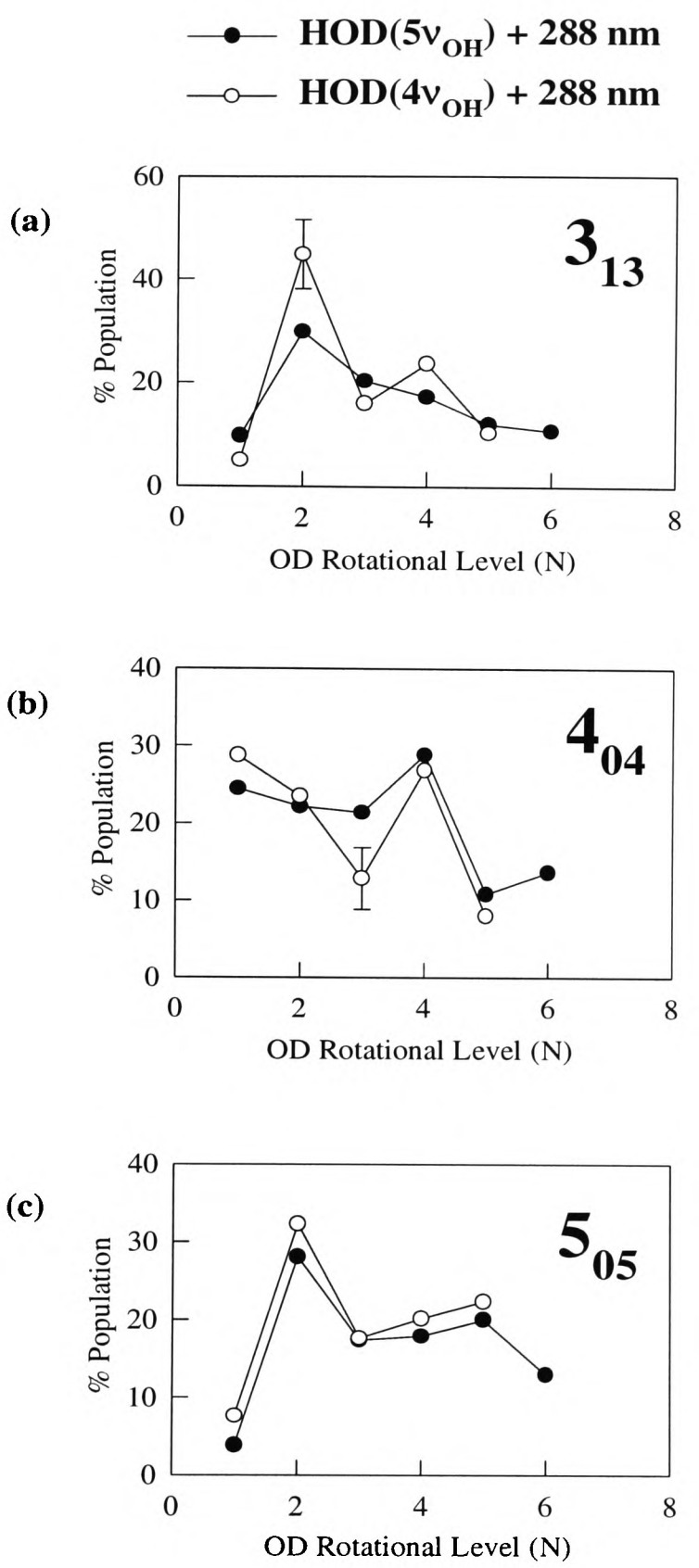

Figure 4.12 The OD $X^2\Pi_{\frac{1}{2}}$ photofragment rotational distributions, in the A′ lambda doublet state arising from the 288 nm photodissociation of HOD(5,0,0) (•) and HOD(4,0,0) (○) for $J_{K_a,K_c} = 3_{13}$ (a), 4_{04} (b) and 5_{05} (c). Each distribution has been normalised to unity and therefore does not reflect the relative lambda-doublet populations within the spin-orbit state.

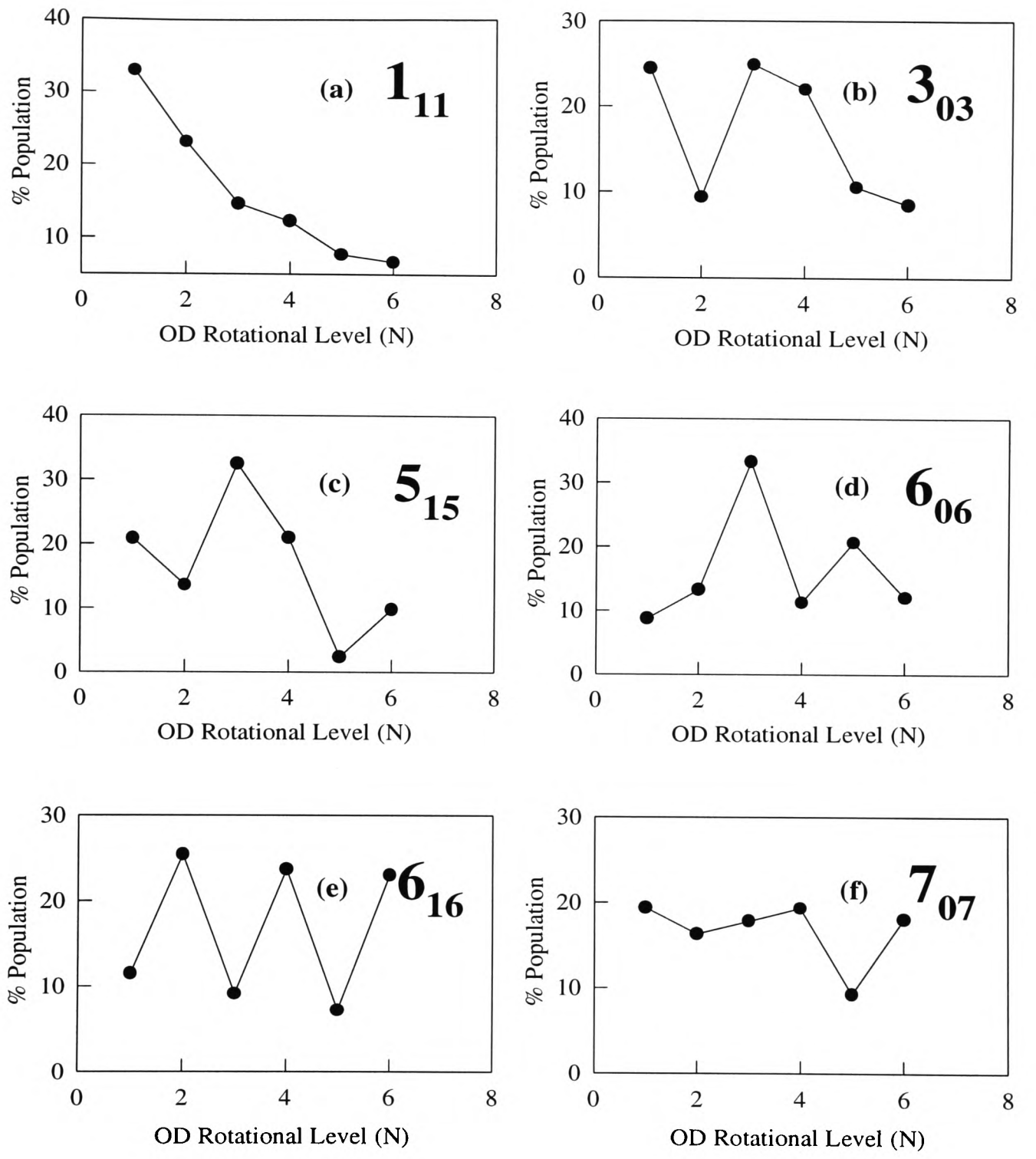

Figure 4.13 The OD $X^2\Pi_{\frac{1}{2}}(A')$ photofragment population distributions arising from the 288 nm photodissociation of HOD(5,0,0) $J_{K_a,K_c} = 1_{11}$ (a), 3_{03} (b), 5_{15} (c), 6_{06} (d), 6_{16} (e) and 7_{07} (f). Each distribution has been normalised to unity.

4.5 Relative OD spin-orbit state distributions

Comparing the lambda-doublet population distributions arising from the photodissociation of HOD(4,0,0) for both of the OD product spin-orbit states (shown in Figures 4.8 and 4.9), the two sets of data are very similar within the experimental error, although there may be small changes in the relative intensities of the peaks on the structure. Making a similar comparison with the HOD(5,0,0) data, there are perhaps small differences in the oscillatory structure of the lambda-doublet distributions of the two spin-orbit states of the OD photofragment, $^2\Pi_{\frac{3}{2}}$ (Figures 4.10(a), (c) & (e) and 4.11) and $^2\Pi_{\frac{1}{2}}$ (Figures 4.10(•) and 4.13) within the experimental error margin. This is primarily seen in changes in the relative intensities of the population in N = 3 and 4 of the fragment. More importantly, it appears that as J in the ground state parent increases, these changes appear to diminish to a negligible level.

The possibility of a selective population of the OD product spin-orbit states obtained on selection of (4,0,0) and (5,0,0) in the HOD intermediate state, is considered in Figures 4.14 and 4.15, respectively. The ratio of the population of rotational states in $^2\Pi_{\frac{1}{2}}$(N) and $^2\Pi_{\frac{3}{2}}$(N) is plotted as a function of N for a range of parent rotational states. Using the data for the A′ lambda-doublet state produces a ratio very close to 1 within the experimental error, for both intermediate overtone states. Whether there is a slight preference for either of the spin states is not certain. Although there are only a few data points for the A″ lambda-doublet state, using this data set produces the same result, a near-'statistical' distribution. This is unlike the 282 nm photodissociation of $H_2O|04\rangle^-$ and $|05\rangle^-$, where a small, but clear preference is seen for the OH fragment $^2\Pi_{\frac{1}{2}}$ spin state, using the A′ data, within the experimental error margin.

4.6 Preferential OD product Λ-doublet population

Averaging over the lambda-doublet populations within either of the OD fragment spin-orbit state distributions for any given initial parent rotational state removes the oscillatory structure; this could be fitted to a rotational temperature with the aid of a Boltzmann plot as is shown in Figures 4.16 and 4.17 for the lambda-doublet averaged OD $^2\Pi_{\frac{3}{2}}$ distributions arising from the 288 nm photodissociation of HOD(4,0,0) and (5,0,0) respectively. At higher values of N there are some deviations from the Boltzmann plot, and an examination of the

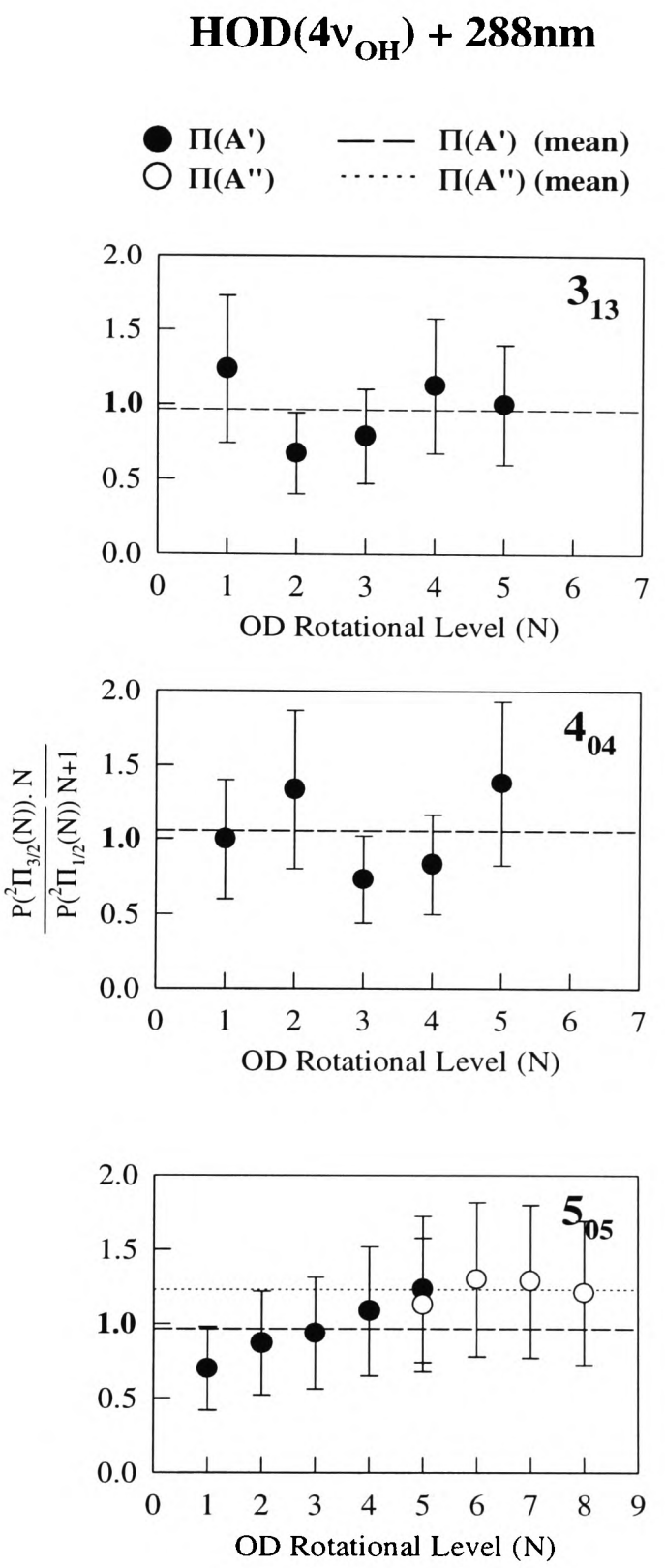

Figure 4.14 The ratio of the population in rotational states in $^2\Pi_{\frac{1}{2}}(N)$ and $^2\Pi_{\frac{3}{2}}(N)$ plotted as a function of N arising from the excitation of $J_{K_a,K_c} = 3_{13}$, 4_{04} and 5_{05} into the intermediate overtone (4,0,0). Shown are the spin state populations for the A′ (•) and the A″ (○) lambda-doublet levels and the corresponding mean distribution.

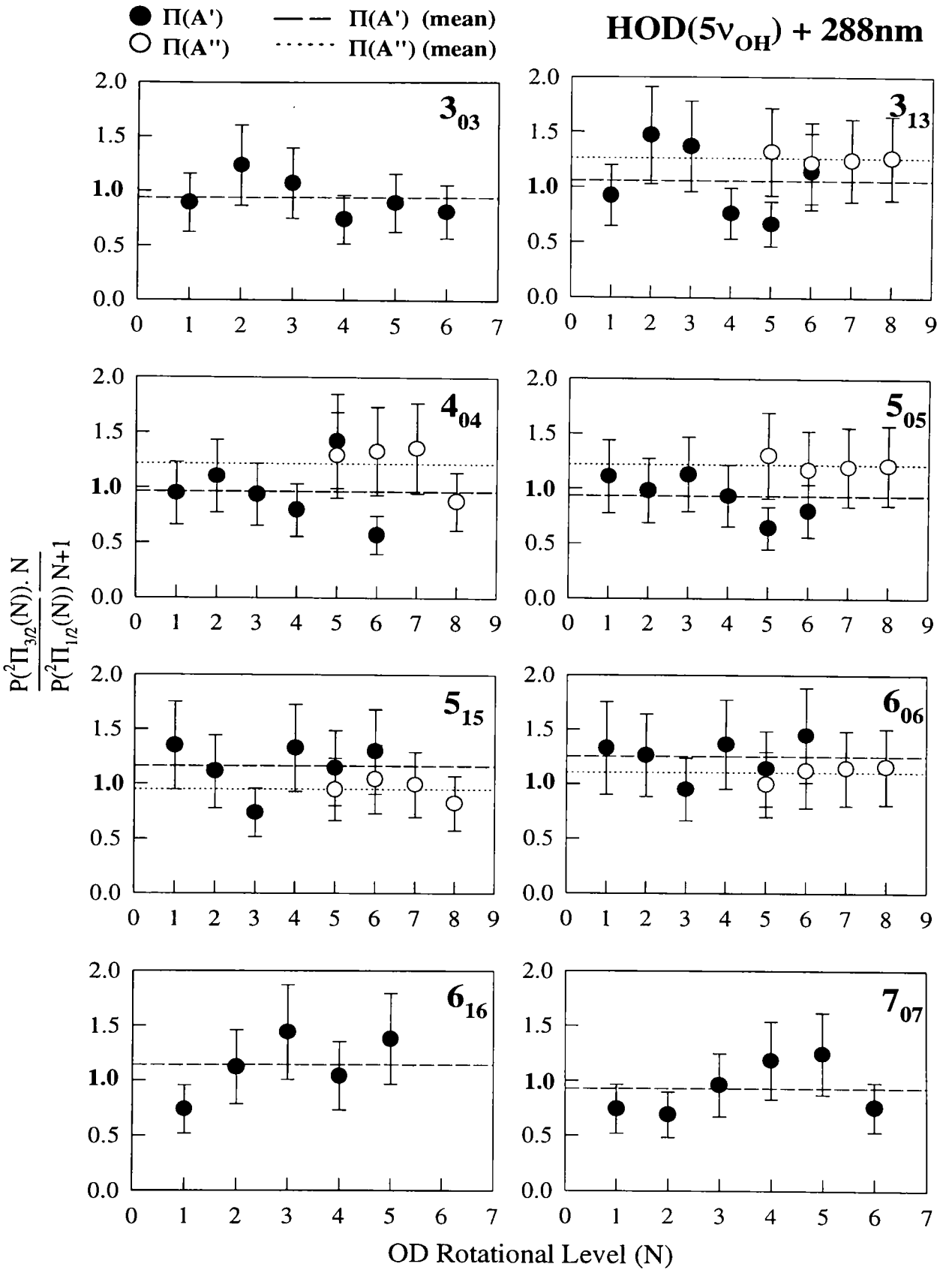

Figure 4.15 The ratio of the population in rotational states in $^2\Pi_{\frac{1}{2}}(N)$ and $^2\Pi_{\frac{3}{2}}(N)$ plotted as a function of N arising from the excitation of $J_{K_a,K_c} = 3_{03}$, 3_{13}, 4_{04}, 5_{05}, 5_{15}, 6_{06}, 6_{16} and 7_{07} into the intermediate HOD overtone (5,0,0). Shown are the spin state populations for the A′ (•) and the A″ (○) lambda-doublet levels and the corresponding mean distribution.

	3_{03}	3_{13}	4_{04}	5_{05}
HOD($4\nu_{OH}$) + 288 nm[a]	-	135±30 K	160±40 K	222±40 K
HOD($5\nu_{OH}$) + 288 nm[b]	162±40 K	173±40 K	200±30 K	241±50 K
$H_2O(4\nu_{OH})$ + 282 nm[a],[c]	-	192±20 K	200±20 K	244±30 K
$H_2O(5\nu_{OH})$ + 282 nm[b],[c]		208±20 K	210±20 K	259±30 K

5_{15}	6_{06}	6_{16}	7_{07}
-	-	-	-
233±50 K	250±40 K	280±60 K	292±60 K
246±20 K	-	-	-
259±30 K	392±20 K	-	455±20 K

(a) Available energy for the photofragments $\approx$ 8000 cm^{-1} (b) Available energy $\approx$ 11000 cm^{-1} (c) Taken from Table 3.5 in Section 3.5

Table 4.4 OD photofragment rotational temperatures, calculated from Boltzmann plots of the lambda-doublet averaged rotational distributions, generated *via.* the 288 nm photodissociation of HOD(4,0,0) and (5,0,0);J_{K_a,K_c} (J = 3–7). Also shown are the corresponding OH product temperatures arising from the 282 nm photolysis of $H_2O|04\rangle^-$ and $|05\rangle^-$.

relative lambda doublet distributions discussed Section 4.4 clearly shows a preference for the A″ lambda doublet state. These result are consistent with the results of the 282 nm VMP of H_2O presented in Chapter 3.

Table 4.4 summarises the OD fragment rotational temperatures obtained in this study. The same small increase in the overall rotation of the molecular photofragment with increasing parent initial angular momentum, seen for the VMP of H_2O, is again evident. Comparing the values resulting from the initial selection of HOD(4,0,0) and (5,0,0), there is perhaps only a very small increase in the OD fragment rotational excitation with increasing total supplied energy, although there is a difference of $\sim$ 3000 cm^{-1} in the available energy.

These trends are consistent with the analogous data presented in Section 3.5 for the VMP of H_2O. However, comparing the values in Table 4.4 for the isoenergetic[5] pairs HOD($4\nu_{OH}$)

[5]The energy available for disposal in the photofragments

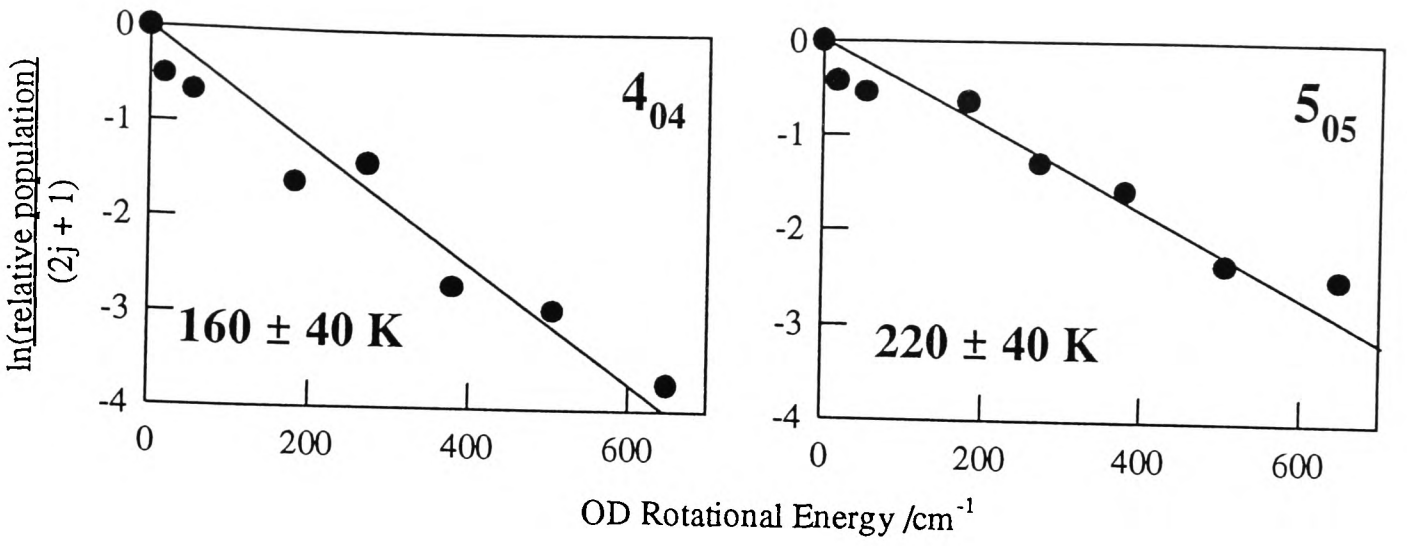

Figure 4.16 Bolzmann plot of the lambda-doublet averaged OD $^2\Pi_{\frac{3}{2}}$ product population distribution arising from the excitation of $J_{K_a,K_c} = 4_{04}$ and 5_{05} in HOD(4,0,0). Also shown are the rotational temperatures and errors calculated from the gradient of the line fitted to the data points.

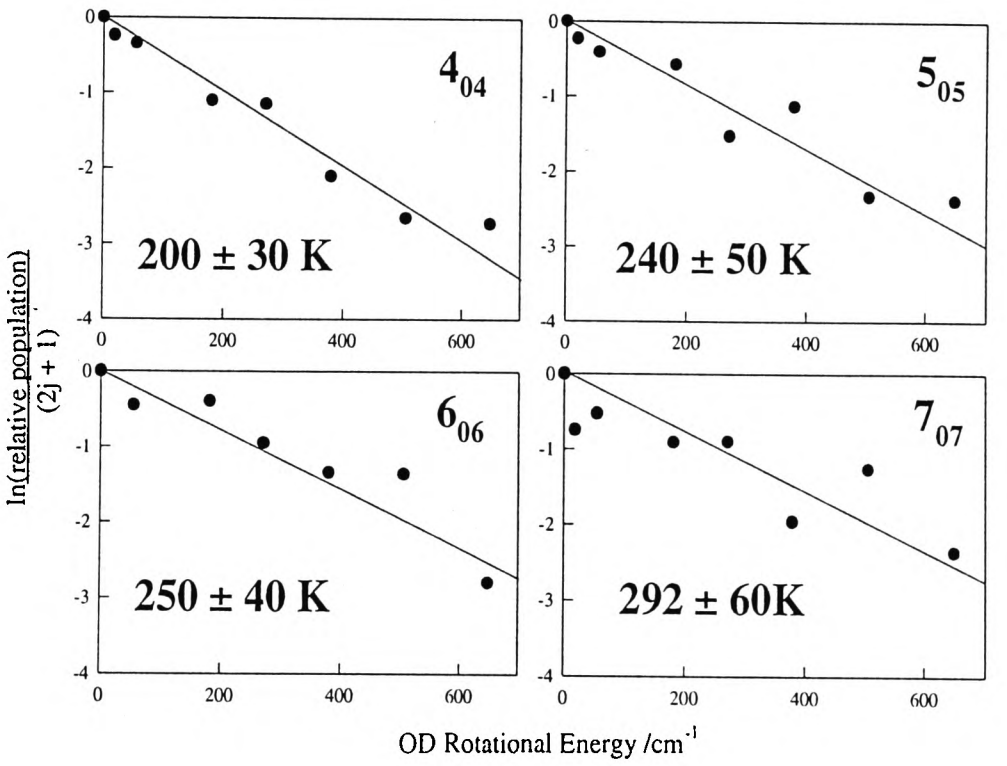

Figure 4.17 Bolzmann plot of the lambda-doublet averaged OD $^2\Pi_{\frac{3}{2}}$ product population distribution arising from the excitation of $J_{K_a,K_c} = 4_{04}$, 5_{05}, 6_{06} and 7_{07} in HOD(5,0,0). Also shown are the rotational temperatures and errors calculated from the gradient of the line fitted to the data points.

+ 288 nm & $H_2O(4\nu_{OH})$ + 282 nm and $HOD(5\nu_{OH})$ + 288 nm & $H_2O(5\nu_{OH})$ + 282 nm clearly shows a slight cooling of the HOD photolysis photofragment rotational distribution compared with H_2O photodissociation.

4.7 Summary

- The branching ratio between the two possible dissociation channels is estimated as $\frac{\phi(OD)}{\phi(OH)} > 20$, consistent with the previous work of Crim and coworkers [202, 203].
- The photodissociation cross-section for the 288 nm VMP of HOD(5,0,0) is estimated to be $\sim$ 20 times greater than the cross-section for the 288 nm VMP of HOD(4,0,0).
- Consistent with the VMP of H_2O, the OD($^2\Pi$) photofragment rotational population distributions produced in the state-to-state photolysis of HOD are highly structured and depend sensitively upon the intermediate parent rotational state.
- The OD($^2\Pi$) product distributions appear to be relatively insensitive to the number of O–H vibrational quanta excited in the intermediate ground state HOD overtone.
- No selective formation of the OD photofragment in particular a spin-orbit state is found within the experimental error.
- The measured rotational temperature of the HOD VMP fragment, for a given intermediate rovibrational state, are noticeably lower than the corresonding fragment rotational temperature produced in the VMP of H_2O.

Chapter 5 Franck-Condon calculations and discussion

5.1 Introduction

At the time of the state-to-state experiments of Andresen and coworkers [34], Balint-Kurti [232, 233] derived a simple and elegant Franck-Condon model for the photodissociation of water *via* the $\tilde{A}$ state, extending the earlier work of Beswick and Gelbart [251], Morse and Freed [145, 252] and Kaplan and Shapiro [253], by taking into account the open shell electronic character of the OH and H products. Using this model, Schinke and coworkers [15, 34] were then able to qualitatively predict the OH lambda-doublet population distributions arising from Andresen's experiments, photolysing $H_2O|01\rangle^-$ at 193 nm. The same Balint-Kurti model has been applied to the present problem, the 282 nm VMP of $H_2O|04\rangle^-$ & $|05\rangle^-$ and 288 nm VMP of HOD(4,0,0) & (5,0,0).

5.2 General theory

Balint-Kurti and Shapiro [254] derived explict expressions for the quantal theory of the photodissociation of a triatomic molecule,

$$ABC(i, E_i) + \hbar\omega \longrightarrow A + BC(nj)$$

which is in a well defined initial state i prior to dissociation. This formulism was then generalised by Balint-Kurti [233] to apply to processes which produce photofragments having both electronic orbital and spin angular momentum, *e.g.*

$$H_2O(\tilde{X}^1A_1) \xrightarrow{\hbar\omega} H_2O(\tilde{A}^1B_1) \longrightarrow OH(^2\Pi) + H(^2S)$$

The photodissociation cross-section in the weak electromagnetic field limit of an ABC($\tilde{X}$) molecule, *via* a single dissociative electronic state, initially in a state of energy E_i and defined by the quantum numbers $J_iM_iP_i$ (the total angular momentum, its space-fixed z component and the total parity respectively) and producing fragments BC and A with

quantum numbers vjm$_j$i and sm$_s$ respectively, scattered into a solid angle $d\Omega$ about a direction $\hat{\mathbf{k}}$ can be written as, [254, 233]

$$\sigma(\hat{k}Evjm_ji, m_s|E_iJ_iM_iP_i)\frac{\rho(\epsilon)}{h\nu}d\nu d\Omega = \left(\frac{8\pi^3}{h^2c}\right)\rho(\epsilon)|\langle\Psi_f^-(\hat{k}vjm_ji, m_s)|\hat{\epsilon}\cdot\hat{\mu}|\Psi_i(E_iJ_iM_iP_i)\rangle|^2 d\nu d\Omega \quad (5.1)$$

$\left(\frac{\rho(\epsilon)}{h\nu}\right)d\nu$ is the flux of polarised photons of the electric field (in the direction $\hat{\epsilon}$) and $\hat{\mu}$ is the dipole moment operator. Ψ_f^- corresponds to the outgoing scattering wave function in the dissociative electronic state, which evolves to a well defined state of the fragments, $|vjm_ji, m_s\rangle$ [255]. The quantum numbers vjm$_j$i refer to the vibrational and rotational state of the BC fragment and i enumerates the Λ-doublet state [1]. m$_s$ is the space-fixed z component of the spin quantum number s of the atomic fragment, which is assumed to be in its ground electron state. Ψ_i refers to the initial bound state wave function of the parent molecule, within the Born-Oppenheimer approximation, in the quantum level $|E_iJ_iM_iP_i\rangle$.

5.2.1 Bound and continuum wave functions

To evaluate the integral in equation 5.1, it is convenient to employ the same set of coordinates to describe both the bound state and continuum wave functions, which are chosen to be the Jacobi or body-fixed coordinates. These are shown pictorially in Figure 5.1, **R**, the A to BC(cm) displacement vector, **r** the B–C displacement vector and γ, the angle separating **R** and **r**. Also indicated in the figure are the three Euler angles, $\Phi, \Theta, \Xi(=0)$, through which the space-fixed axis system is rotated to obtain the body fixed axes, following the convention of Edmonds [256]. The advantages of using these variables and a body-fixed axis system within the context of this problem has been thoroughly discussed in references [257] and [258].

The bound state triatomic has an Hamiltonian [34, 233, 252, 254, 258]

$$\hat{H} = -\frac{\hbar^2}{2\mu}\left[\frac{1}{R^2}\frac{\partial}{\partial R}\left(R^2\frac{\partial}{\partial R}\right)\right] + \frac{\hat{l}^2}{2\mu R^2} + \frac{\hat{j}^2}{2\mu_{BC}r^2} - \frac{\hbar^2}{2\mu}\left[\frac{1}{r^2}\frac{\partial}{\partial r}\left(r^2\frac{\partial}{\partial r}\right)\right] + V(R, r, \gamma) \quad (5.2)$$

where $\hat{\mathbf{l}}^2$ is the orbital angular momentum operator for the relative motion of A and BC, $\hat{\mathbf{j}}^2$ is the rotational angular momentum operator of the BC fragment, μ is the reduced mass of ABC, μ_{BC} is the reduced mass of BC and V(**R**, **r**, γ) is the full potential energy function.

[1] This theory was developed with a $^2\Pi$ photofragment in mind, and the lambda doublet states $^2\Pi_{\frac{3}{2}}$ (A′), (A″), $^2\Pi_{\frac{1}{2}}$ (A′) and (A″) are labelled 1 to 4 respectively

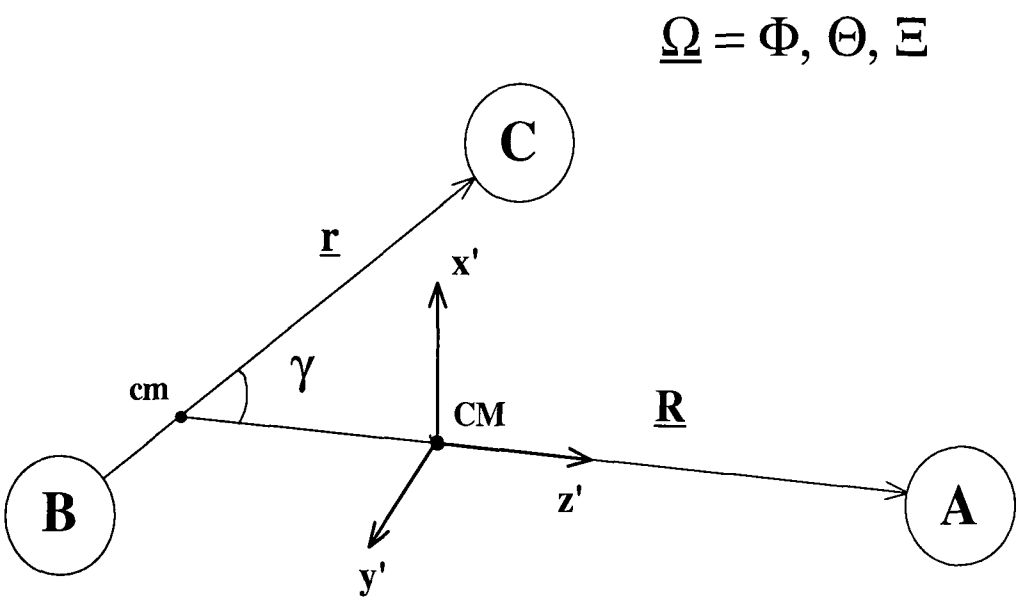

Figure 5.1 Centre of mass body-fixed coordinate system for the photodissociation of a triatomic molecule. CM is the location of the total centre of mass of the ABC system and cm is centre of mass of the BC fragment. $\Phi, \Theta, \Xi(= 0)$ are the Euler angles defined in the text.

The bound state wave function can be expanded in the form: [258]

$$\Psi^{J_i M_i}(R, r, E_i) = \sum_{vj\lambda} \frac{1}{R}\, Y_{j\lambda}^{J_i M_i P_i}(\gamma, \underline{\Omega})\; \chi_{vj}(r)\; \Phi_{vj\lambda}^{J_i P_i}(R) \tag{5.3}$$

$Y_{j\lambda}^{J_i M_i P_i}(\gamma, \underline{\Omega})$ are a complete, orthonormal set (in the variables defined) of parity adapted angular basis functions, defined as

$$Y_{j\lambda}^{J_i M_i P_i}(\gamma, \underline{\Omega}) = \frac{1}{\sqrt{2(1+\delta_{\lambda 0})}} \left[Y_{j\lambda}^{J_i M_i}(\gamma, \underline{\Omega}) + (-)^{J_i + P_i} Y_{j-\lambda}^{J_i M_i}(\gamma, \underline{\Omega})\right] \tag{5.4}$$

in which

$$Y_{j\lambda}^{J_i M_i}(\gamma, \underline{\Omega}) = \left(\frac{2J_i + 1}{4\pi}\right)^{\frac{1}{2}} Y_{j\lambda}(\gamma, 0)\; D_{\lambda M_i}^{J_i}(\underline{\Omega}) \tag{5.5}$$

λ refers to the helicity quantum number, the projection of J and j onto the body fixed z axis, **R**, and takes on the values min(J,j) $\geq \lambda \geq 0$ (P = +1) or 1 (P = -1). $\chi_{vj}(r)$ are the radial part of the rotational-vibrational eigenfunctions of the diatomic BC fragment and $\Phi_{vj\lambda}^{J_i P_i}(R)$ are body-fixed radial wave functions which are the solutions of the set of coupled differential

equations obtained upon the inserting equation 5.3 into the Schrödinger equation (taken from equation 5.2) and have the standard bound state boundary conditions:

$$\Phi_{vj\lambda}^{J_i P_i}(R) = 0 \quad \begin{cases} R \to 0 \\ R \to \infty \end{cases} \tag{5.6}$$

The continuum wave function, $\Psi_f^-(\mathbf{R}, \mathbf{r}, \mathrm{E})$, asymptotically has the form of a plane wave in the direction $\hat{\mathbf{k}}$ (in the space-fixed axes) into which the fragments are expelled. Taking this into account, a similar expansion to that of the bound state wave function can also be made in terms of $\chi_{vj}(\mathbf{r})$, the BC rovibrational eigenfunctions, $\Phi_{vk\lambda ji}^{-\ (Jvk\lambda jiP)}(R)$, the body-fixed radial wave functions and $|JMP; klji\rangle$, a set of photofragment basis functions. These basis functions, derived in reference [233] are given by an expression

$$|JMP, jlki\rangle = \sum_{\lambda} (-)^{k-\lambda} \frac{2}{\sqrt{2(1+\delta_{\lambda 0})}} \ (Jkl0|J\lambda k-\lambda) \ G_{k\lambda ji}^{JMP}(\gamma, \underline{\Omega}) \tag{5.7}$$

where (.....|.....) are Clebsch-Gordon coefficients[2] and $G_{k\lambda ji}^{JMP}(\gamma, \underline{\Omega})$ are body-fixed channel functions which are analogous to the angular functions $Y_{j\lambda}^{J_i M_i P_i}(\gamma, \underline{\Omega})$ defined in equations 5.4 and 5.5. The final state asymptotic wavefunction (for photofragments with an electronic structure of $^2\Pi$ and ^{2}S) requires a proper consideration of the symmetry properties and the coupling of the electronic spin, s, and orbital angular momentum, l, to the rotational angular momentum, j, when forming the basis function. The quantum numbers k[3] and J in the equation are the resultants of the coupling of s & j and k & l respectively. To treat the coupling correctly, Balint-Kurti [233] developed a valence bond model to connect the continuum wavefunction to the electronic orbitals of the $^2\Pi$ + ^{2}S fragments. The inclusion of the electronic and spin degrees of freedom in the expansion of the continuum wave function is the major difference between this and previous photodissociation theories. It does however lead to an added complexity of the resulting expression for $\Psi_f^-(\mathbf{R}, \mathbf{r}, \mathrm{E})$ (see equations 20 & 21 and Section 5 of reference [233]), but is essential for a proper comparison with the experimental measurements. The reader is referred to reference [233] for a detailed discussion of the construction and specific form of the continuum wave functions.

[2]Edmonds [256] is used throughout this formalism for the notation and properties of Clebsch-Gordon coefficients and rotational matrices

[3]not be confused with anything to do with $\hat{\mathbf{k}}$ previously employed

5.2.2 Integral cross-section and photofragmention T matrix

In the experiments presented in this thesis, the projection quantum number of neither the parent or diatomic photofragment molecules are resolved and the detector cannot distinguish between photofragments expelled into different directions. Using the expansions of the bound and scattering wave function, equation 5.1, summing over all initial and final magnetic quantum numbers and integrating over all solid angles, an expression for the integral photodissociation cross section of a triatomic molecule can be derived. Writing it in terms of a photofragmentation **T** matrix $t(EJvk\lambda ji|E_iJ_iP_i)$ [6, 9, 254] gives,

$$\bar{\sigma}(Evji|E_iJ_iP_i) = \frac{1}{2J_i+1}\ \frac{16\pi^2\nu\mu k_{vji}}{3\hbar^2}\ \sum_{Jk\lambda}\ \delta(J_iJ1)\ |t(EJvk\lambda ji|E_iJ_iP_i)|^2 \tag{5.8}$$

in which $\delta(J_iJ1)$ is non-zero for

$$J_i \geq J \geq 1$$

and, by definition,

$$\begin{aligned} t(EJvk\lambda ji|E_iJ_iP_i) &= \sum_{v'k'\lambda'j'i'}\ \sum_{v''j''\lambda''}\ \langle \frac{1}{R}\ G^{JMP}_{k'\lambda'j'i'}(\gamma,\underline{\Omega})\ \chi_{v'j'}(r)\ \Phi^{-\ (Jvk\lambda jiP)}_{v'k'\lambda'j'i'}(R)| \\ &\times\ \hat{\epsilon}\cdot\hat{\mu}|\frac{1}{R}\ Y^{J_iM_iP_i}_{j''\lambda''}(\gamma,\underline{\Omega})\ \chi_{v''j''}(r)\ \Phi^{J_iP_i}_{v''j''\lambda''}(R)\rangle \\ &\times\ (-)^{M_i}\begin{pmatrix} J & 1 & J_i \\ -M_i & 0 & M_i \end{pmatrix}^{-1} \end{aligned} \tag{5.9}$$

There are basically three different techniques used to evaluate the **T** matrix elements, the artificial channel, driven equation and direct methods. These have all been discussed in detail in reference [9]. The integral in equation 5.9 can be analytically solved for all of the variables except the radial coordinate, **R**. Each method primarily involves the separate computation (solving the Schrödinger equation) of the radial components of the continuum wave function, $\Phi^{-\ (Jvk\lambda jiP)}_{v'k'\lambda'j'i'}(R)$, and the bound state wave function, $\Phi^{J_iP_i}_{v''j''\lambda''}(R)$. These can then be used to evaluate the remaining integral in the **T** matrix

$$\langle\frac{1}{R}\Phi^{-\ (Jvk\lambda jiP)}_{v'k'\lambda'j'i'}(R)|\mu_y(v'j'k'\nu\lambda'|vj\lambda)|\frac{1}{R}\Phi^{J_iP_i}_{v''j''\lambda''}(R)\rangle \tag{5.10}$$

$\mu_y(v'j'k'\nu\lambda'|vj\lambda)$, the non-zero dipole matrix elements for a 'perpendicular' transition (H_2O $\tilde{A}\leftarrow\tilde{X}$) are defined as ([233], Eqn. (69))

$$\mu_y(v'j'k'\nu\lambda'|vj\lambda) = \int \chi_{v'j'}(r)\ \mu_y(k'\nu\lambda'|j\lambda)\chi_{vj}(r)\ r^2\ dr \tag{5.11}$$

$$\mu_y(k'\nu\lambda'|j\lambda) = \int_0^\pi d^{k'}_{\nu\lambda'}(\gamma)\ \mu_y(R,r,\gamma)\ Y_{j\lambda}(\gamma,0)\ \sin\gamma\ d\gamma \tag{5.12}$$

5.3 The Franck-Condon model

The Franck-Condon model of Balint-Kurti [232, 233] for calculating the rotational state distribution of a BC($^2\Pi$) photofragment makes the same basic assumptions as the earlier models of Beswick and Gelbart [251] and Morse and Freed [145, 252]. These are listed below along with a justification of their validity in the context of the $H_2O(\tilde{A}\leftarrow\tilde{X})$ transition:

1. The $\tilde{A}$–$\tilde{X}$ transition dipole moment μ is a constant, independent of **R** and **r**.
   - Schinke and coworkers [40] have calculated the $H_2O(\tilde{A}\leftarrow\tilde{X})$ transition moment using a SCF method. Their results indicate that μ has a weak coordinate dependence within the transition state region around $R_{H-OH} = 0.957$Å. This is shown in Figure 5.2(a) where a contour plot of the dipole moment is plotted against the two O–H bond lengths. The long wavelength ($\lambda_2 \geq 239.5$ nm) vibrationally mediated photodissociation of H_2O will access the excited state surface at extended values of R. It is clear that μ does have has a slight R dependence between $R_{OH} \approx 1.0$–1.3 Å. Plotted in Figure 5.2(b) is the angular dependence of the dipole function as a function of increasing R and for reference, the ground state total bending wavefunction, $|\Psi(\gamma)|^2$. It is clear that within the region sampled by the wave function, the angular dependence of μ is rather isotropic.
2. Vibration-rotation coupling in the OH($X^2\Pi$) photofragments is ignored, removing the j-dependence of the vibrational wave functions $\chi_{vj}(r)$.
   - Only the ground vibrational state OH (and OD) rotational distributions are measured in this work. The same is also true for the previous studies [34, 224, 165].

   Combining these two aproximations reduces the dipole matrix elements to a simple integral:

$$\mu_y(v'j'k'\nu\lambda'|vj\lambda) \approx \mu_y\ \delta_{v'v''}\ \int_0^\pi d^{k'}_{\nu\lambda'}(\gamma)\ Y_{j\lambda}(\gamma,0)\ \sin\gamma\ d\gamma \tag{5.13}$$

3. There is no inelastic scattering in the final electronic state and all the final state (now elastic) radial channel functions $\Phi^{-}_{v'k'\lambda'j'i'}{}^{(Jvk\lambda jiP)}(R)$ are identical. This removes the the summations over v′k′λ′j′i′, the final state quantum numbers, in equation 5.9 and reduces the channel functions to just an **R** dependent function, $\Phi^-(\mathbf{R})$.

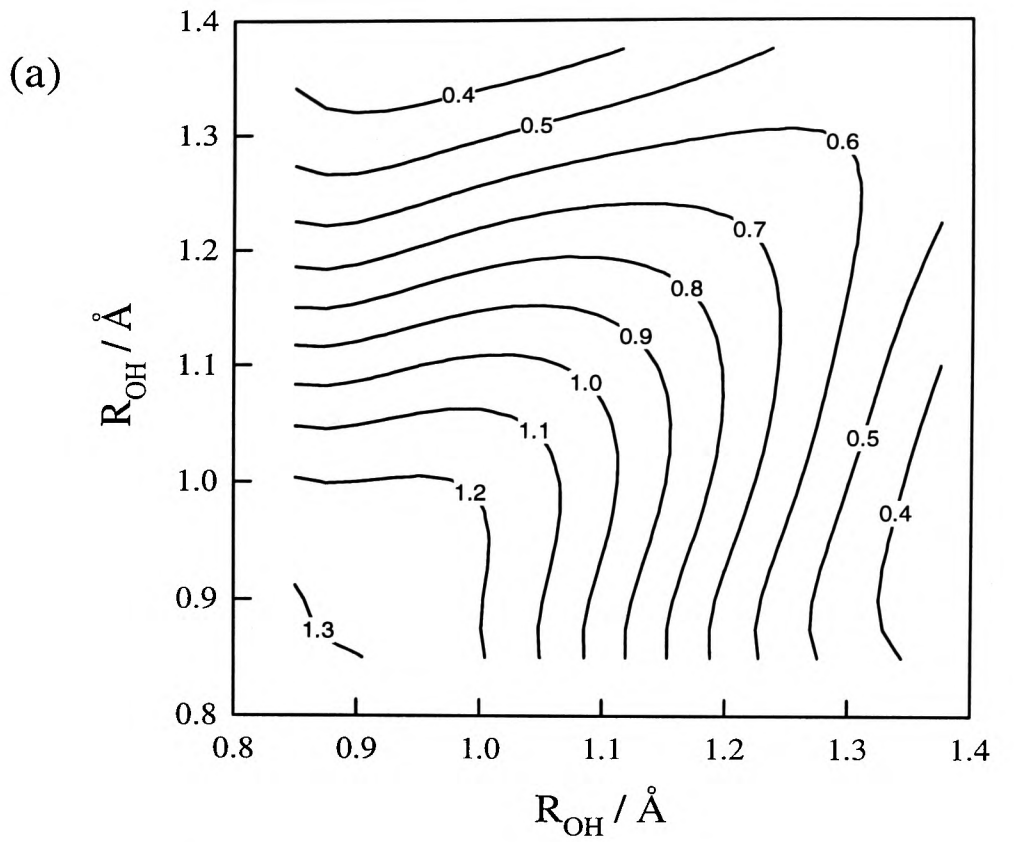

Figure 5.2 (a) A contour plot of the H_2O $\tilde{A}$–$\tilde{X}$ dipole moment function (in Debye) plotted against the two O–H bond lengths, R_{OH}. (b) A plot of the angular dependence of the dipole moment function with r = 0.958 Åand R = 0.958, 1.185 and 1.365 Å. Also shown is the ground state water total bending wavefunction for reference.

- Schinke and coworkers [259] showed that for $H_2O(\tilde{A})$ only the angular anisotropy (which indirectly leads to rotational-translational coupling) of the potential surface in the region directly above the ground state equilibrium geometry, for $\theta_e = 104.5°$, is important in determining the rotational state distribution of the OH photofragments. Although the surface is globally anisotropic [40, 230], $V(\tilde{A})$ has the same equilibrium bending angle as the ground state potential, $V(\tilde{X})$. Excitation from the $\tilde{X}$ state zero-point bending potential will therefore occur preferentially to the lowest $\tilde{A}$ state bending state. The anisotropy will be locally very weak in the excitation region [4] and no appreciable torque is exerted on the OH molecule during the dissociation [260].

4. The ground state radial wave function $\Phi^{J_i P_i}_{v'' j'' \lambda''}(R)$ is assumed to be independent of the vibrational quantum number v'' and removes the summation over this quantum number in equation 5.9. They are also assumed to be very sharply peaked at a value of R where excitation to the $\tilde{A}$ state surface preferentially occur from, R_x, and is replaced by a delta function:

$$\Phi^{J_i P_i}_{v'' j'' \lambda''}(R) \approx C^{J_i P_i}_{j'' \lambda''} \cdot \delta(R - R_x) \tag{5.14}$$

Similarly, the excited state radial wave function will lose their R dependence and

$$\Phi^{-}(R) \approx constant \tag{5.15}$$

- The full *ab initio* [40, 41] and Franck-Condon [34, 232] calculations for J = 0 of Schinke and coworkers were able to show that the rotation-bending motion of the ground state parent water molecule was primarily responsible for determining the rotational distribution of the OH photofragment. The two stretching degrees of freedom only account for the vibrational excitation of the OH and the coupling between the bending and stretching motions is very small. This is also consistent with the work of Child and Lawton [182] who found that the structure of the ground state local-mode stretching vibrational manifolds was insensitive to the number of quanta of bending vibration[5].

[4] Note that this only true for zero quanta of bending vibration excitation in the ground state parent molecule

[5] These calculations were for low parent angular momentum states

By fixing the **R** coordinate at one particular value (Schinke used the equilibrium value $R_e = 0.97\mathring{A}$, similar to Beswick and Gelbart [251]) adiabatically separates the stretching and bending motions, in the centre of mass frame.

It is also worth noting that the original theory of Balint-Kurti and Shapiro [254] is for an A-BC photofragmentation, not for an A-BA molecule. The expression for the $H_2O(\tilde{A}–\tilde{X})$ photofragmention **T** matrix, taken from equation 5.9, is not antisymmetrized with respect to the exchange of the H atoms [261, 262]. The significance of this will be discussed in section 5.7. Of course, there is no problem with regards to the isotopomer, HOD, as the symmetry is conveniently broken.

The expression for the photofragmentation **T** matrix is now greatly simplified and an expression for the relative probability of producing different OH Λ-doublet states, labelled by the quantum numbers ji, can be written as, (Eqn. (2) in Ref. [232])

$$\begin{aligned} P_{ji}^{J_i P_i} &= \sum_{v} \bar{\sigma}(Evji|E_i, J_i, P_i) \\ &\approx \sum_{jk\lambda} (2J+1)(2k+1)t_\lambda^2 \mid \sum_{j''\lambda''} C_{j''\lambda''}^{J_i P_i} \frac{1}{2(1+\delta_{\lambda 0})}\{[J-\lambda|J_i\lambda'](-1)^\lambda \\ &+ P_i(-1)^{J+J_i}[J\lambda|J_i\lambda']\}F_i(jk\lambda|j''\lambda'')|^2 \end{aligned} \tag{5.16}$$

[...|...] and F(...|...) (defined in equations (5) and (3) and (4) respectively of reference [232]) contain the angular momentum coupling terms arising from the proper treatment of the open shell nature of the photofragments (contained within $G_{k\lambda ji}^{JMP}(\gamma, \underline{\Omega})$). $C_{j''\lambda''}^{J_i P_i}$ are the expansion coefficients of the ground state wavefunction defined in equation 5.14. This expression is completely analogous to that obtained in the closed shell Franck-Condon model of Beswick and Gelbart [251]:

$$P_j^J = \sum_{\lambda} |C_{j''\lambda''}^{J_i P_i}|^2 \tag{5.17}$$

The OH rotational distributions, dependent on the coefficients $C_{j''\lambda''}^{J_i P_i}$, therefore simply reflect the bound state rotational and bending motions of the parent molecule. In the experiments presented here, the $\tilde{A}$ state is accessed at highly extended R_{H-OH} configurations where the anisotropy in the bending potential is significantly reduced from that at equilibrium. The bending potentials for both the $\tilde{A}$ and $\tilde{X}$ states at a selection of R values, shown in Figures 5.3, clearly display a substantial reduction in the anisotropy with R. However, the

similarity of the bending potentials for the two electronic states over the relevant R values does indicate that the Franck-Condon model, previously employed with both bond lengths set at equilibium [34, 232], is likely to be just as applicable in the present long wavelength experiments.

To simulate the OH rotational distributions observed in this study, equation 5.16 was applied, fixing r at its equilibrium value in free OH, $r = 0.97$ Å, and varying R typically from 0.958 to ≈ 1.4 Å.

The original calculations [122] were carried out using the modified version [228] of the Sorbie-Murrell [226] ground state potential. However, Jensen [229] has resently calculated a water potential function which has a more accurate asymptotic behaviour than the Sorbie-Murrell potential. Considering the long wavelength experiments presented here will preferentially sample this region of the surface, the Franck-Condon calulations have been repeated using the Jensen ground state potential function. Shown in Figure 5.4 are the calculated $OH(^2\Pi_{\frac{3}{2}})$ lambda doublet population distributions for H_2O J_{K_a,K_c} = (a) 0_{00} and (b) 4_{04}, using either the Jensen (left-hand side) or modified Sorbie-Murrell (right-hand side) ground state potential functions and fixing R, the Jacobi bond length, at two different values, 0.958 Å and 1.365 Å (r is fixed at 0.97 Å). At low values of R, for both low and high parent angular momentum states, there is no significant change in the distributions. At large values of R, especially for low initial parent angular momentum, noticable differences in the A″ population distribution are clearly evident. The A′ distributions appear to be relatively insensitive to the choice of potential.

By freezing the Jacobi coordinates R and r (as well as γ at γ_e), the Hamiltonian for the bound state parent molecule, given in equation 5.2, is reduced to that of a 'rigid bender': [258]

$$\hat{H} = \frac{\hat{l}^2}{2\mu R^2} + \frac{\hat{j}^2}{2\mu_{OH} r^2} + V(R, r, \gamma) \tag{5.18}$$

The rotational and bending motion of the ground electronic state water molecule is treated rigorously, including the centrifugal and Coriolis terms (the diagonal Hamiltonian matrix elements of $\hat{\mathbf{l}}^2$ and $\hat{\mathbf{j}}^2$ and the off-diagonal matrix elements of $\hat{\mathbf{l}}^2$ respectively [257]) which couple the overall rotation with the bending motion by mixing basis functions of the same and different projection quantum number λ respectively. Although the coupling between the

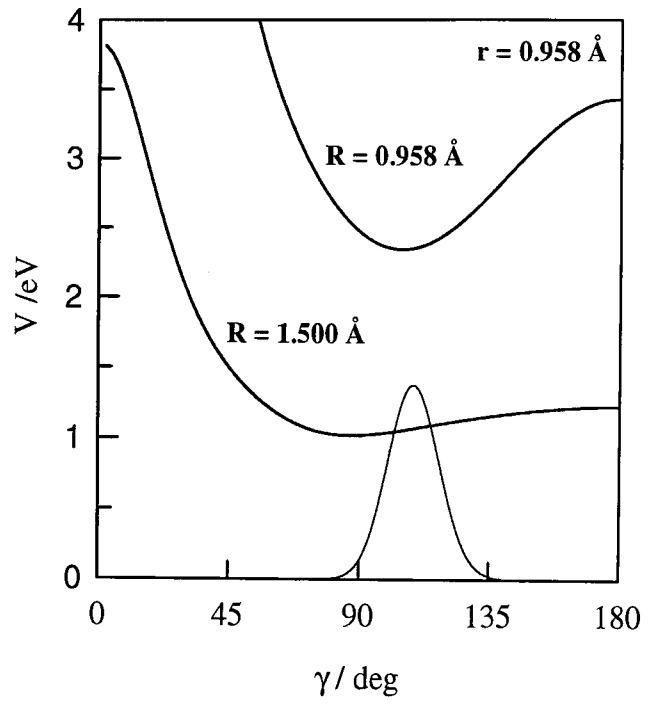

Figure 5.3 The bending potentials (as a function of γ) for the $\tilde{A}$ [230] (upper figure) and $\tilde{X}$ (lower figure) states of water [229] as a function of the H–OH Jacobi length, R. The length of r has been fixed at 0.97 Å

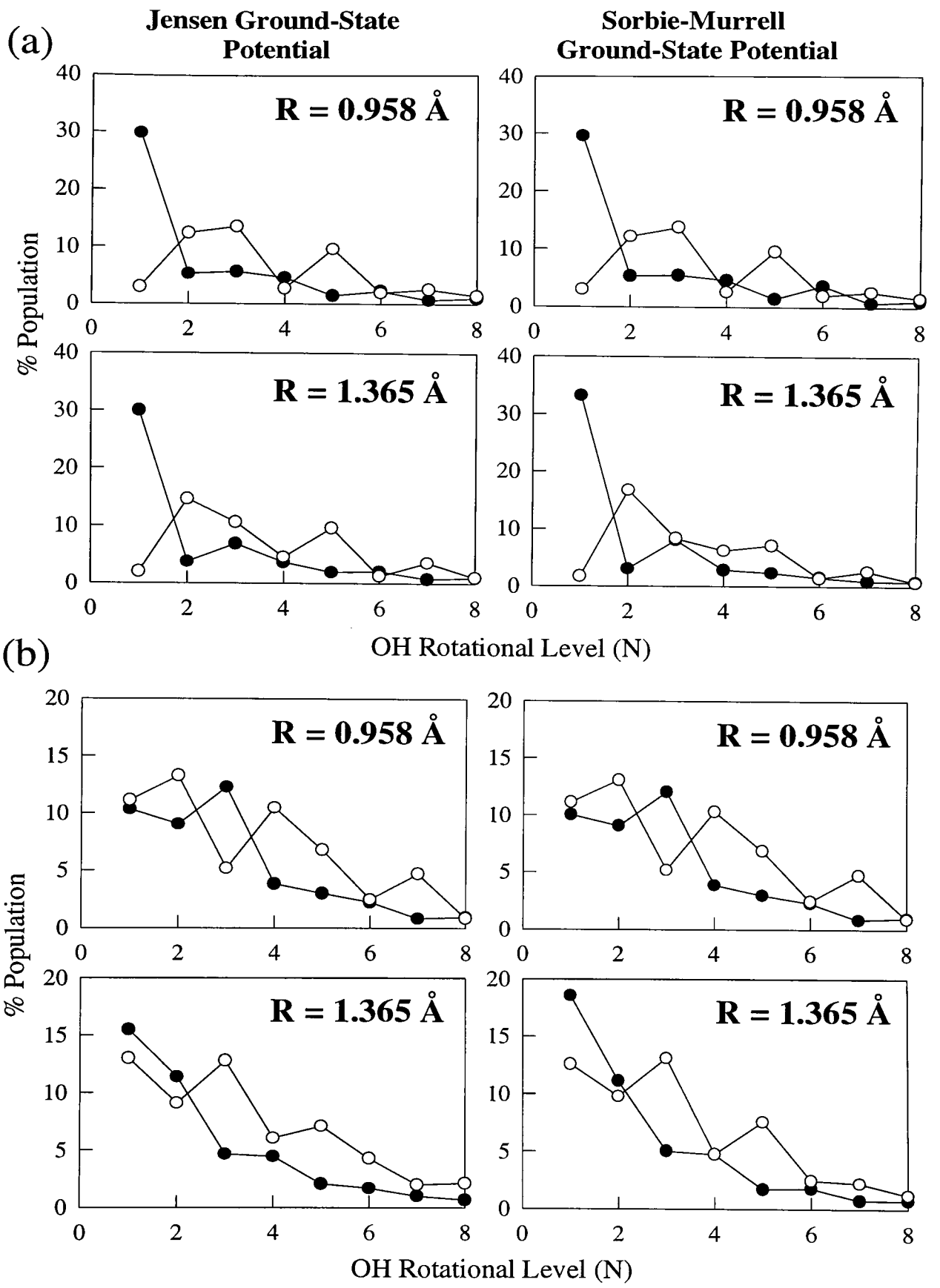

Figure 5.4 Franck-Condon calculated $OH(^2\Pi_{\frac{3}{2}})$ population distributions, for both lambda-doublets, A′ (•) and A″ (○), arising from the dissociation of H_2O $J_{K_a,K_c} = 0_{00}$ (a) and 4_{04} (b) using either the Jensen [229] (left hand side) or the modified [228] Sorbie-Murrell [226] ground state potential and fixing R, the Jacobi bond length, at 0.958 or 1.365 Å. r was fixed at 0.97 Å

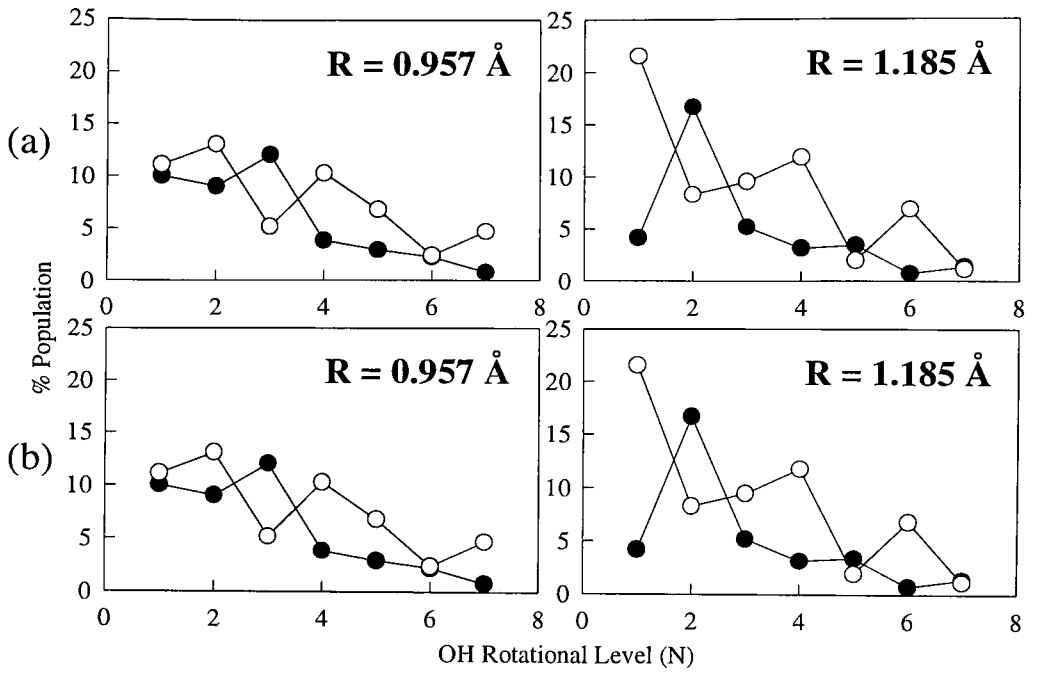

Figure 5.5 Comparison of the calculated photofragment rotational distributions at two different values of R obtained using the simple (a) and the full (b) Franck-Condon models decribed in the text. In the latter, the zero-point vibrational motion of the OH spectator bond is treated rigorously, while in the former model r is fixed at 0.97 Å. In both calculations the rotational state dissociated was $J_{K_a,K_c} = 4_{04}$

stretching and bending motions is very small, for high parent angular momentum, dynamical Coriolis coupling between these two degrees of freedom may well become important. By freezing R and r, the model cannot accomodate for this effect and likewise it cannot account for Fermi resonances between the stretching and bending levels [182].

It is worth noting that fixing the bond length of the OH moiety r at the value of free OH, is not an essential ingredient of the Franck-Condon model. By just freezing the R coordinate, the ground state Hamiltonian can be written as,

$$\begin{aligned} \hat{H} &= \frac{\hat{l}^2}{2\mu R^2} + \frac{\hat{j}^2}{2\mu_{OH} r^2} - \frac{\hbar^2}{2\mu}\left[\frac{1}{r^2}\frac{\partial}{\partial r}\left(r^2\frac{\partial}{\partial r}\right)\right] + V(R,r,\gamma) \\ &= \frac{\hat{l}^2}{2\mu R^2} + \hat{H}_{OH}(r) + [V(R,r,\gamma) - V_{OH}(\gamma)] \end{aligned} \tag{5.19}$$

in which $\hat{H}_{OH}(r)$ and $V_{OH}(\gamma)$ are the Hamiltonian and potential energy function for free OH, which is treated as a rigid-rotor harmonic oscillator.

Recalculating the coefficients $C_{J''\lambda''}^{J_i P_i}$ using this Hamiltonian (taking proper account of the zero-point vibrational motion along the r coordinate [258]) does not lead to significantly different OH photofragment distributions compared with those obtained from the much simpler, fixed r treatment. A comparison of the predictions from the two Franck-Condon models is shown in Figure 5.5 for two values of R, dissociating the same rotational state $J_{K_a,K_c} = 4_{04}$. The good agreement between the two calculated OH distributions is consistent with the previous finding [34] that those derived from the simpler treatment (using the Hamiltonian given in equation 5.18) are insensitive to the choice of r.

5.4 The 282 nm VMP of H_2O $|04\rangle^-$ and $|05\rangle^-$

5.4.1 OH photofragment rotational distributions

A selection of calculated photofragment $OH(^2\Pi_{\frac{3}{2}})$ lambda-doublet population distributions are shown in Figures 5.6–5.9, as functions of the dissociation coordinate R, for H_2O J_{K_a,K_c} = 0_{00} [Fig. 5.6] , 2_{02} [Fig. 5.7(a)], 3_{03} [Fig. 5.7(b)], 4_{04} [Fig. 5.8(a)], 5_{05} [Fig. 5.8(b)] and 5_{15} [Fig. 5.9]. Also included are the experimental distributions from this work and from the previous results of Andresen and coworkers [34], Crim and coworkers [201] and Rosenwaks and coworkers [165].

The first key feature of the calculations is that the experimentally observed insensitivity of the OH rotational distributions, arising from the dissociation of H_2O $J_{K_a,K_c} = 0_{00}$, to the initial ground state overtone level and the photolysis photon energy is mirrored by the corresponding Franck-Condon distributions and their insensitivity to the extension of R (see Figure 5.6). Although the agreement with the experimental distributions is only qualitative, the correct trends for both lambda-doublet distributions are predicted.

For H_2O $J > 0$ (Figures 5.7–5.9), the phase of oscillation and general shape of the experimental distributions is replicated, although the correct amplitude of the oscillations between the lambda-doublet populations are not reproduced in the simulations for some of the initial parent rotational states. More importantly, the differences in the lambda-doublet distributions from this and previous studies[6] can be seen in the R dependence of

[6]The present studies supply less available energy for disposal in the photofragments than the previous studies.

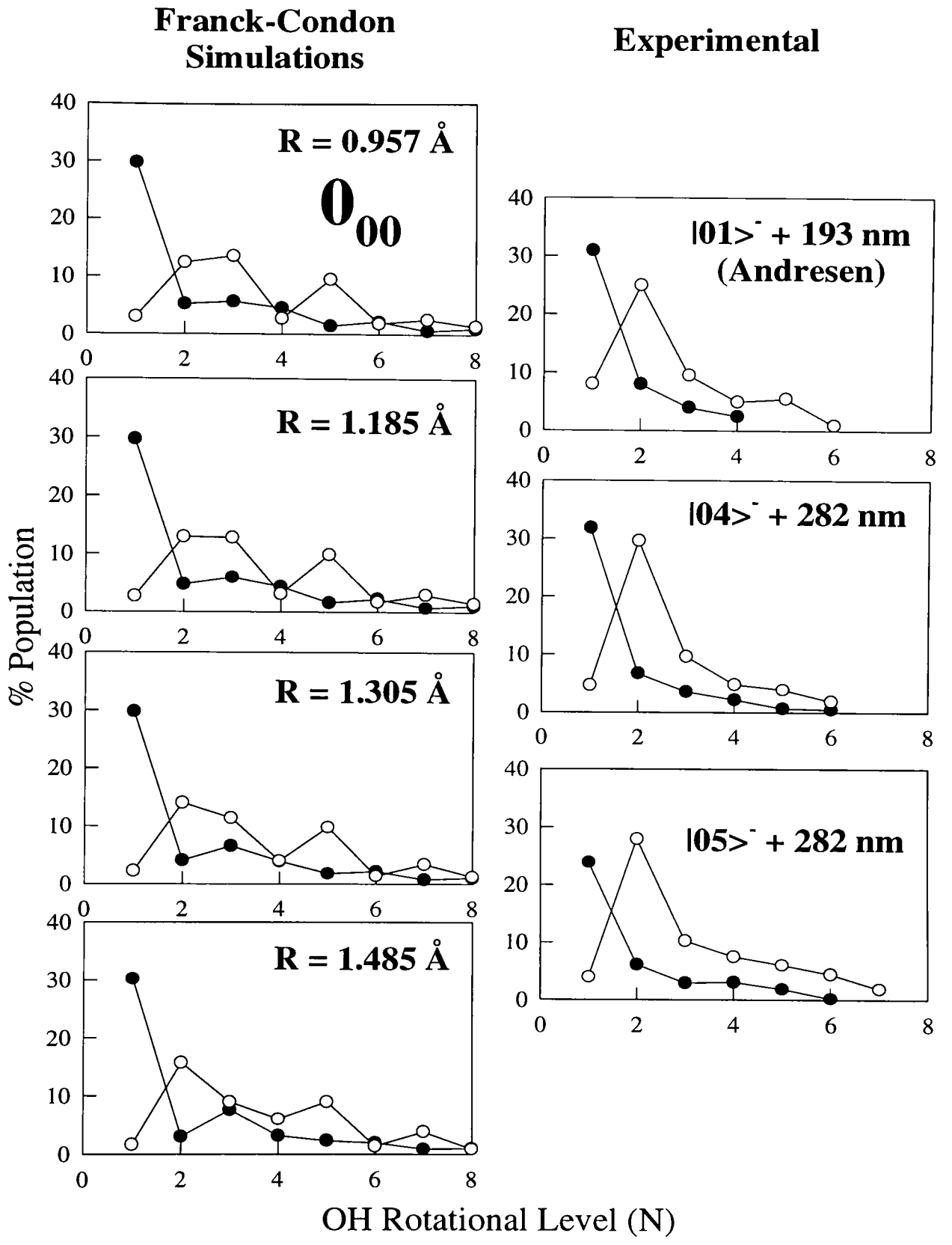

Figure 5.6 The Franck-Condon calculated $OH(^2\Pi_{\frac{3}{2}})$ rotational distributions (shown on the left) for both lambda-doublet states, A′ (•) and A″ (○), obtained at the R values indicated for $J_{K_a,K_c} = 0_{00}$. On the right-hand side are the experimental distributions obtained from this work and from the previous study of Andresen and coworkers [34].

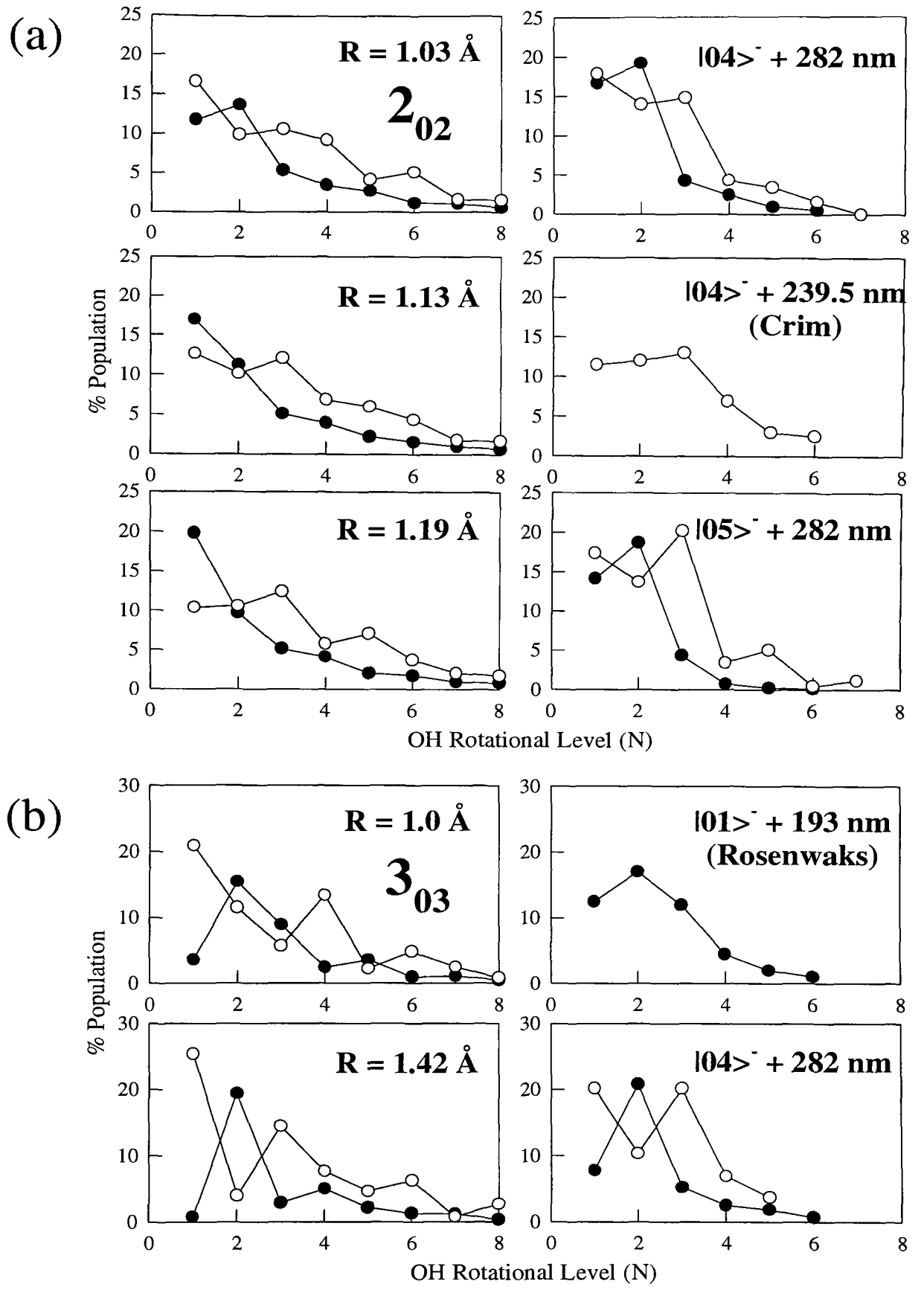

Figure 5.7 The Franck-Condon calculated OH($^2\Pi_{\frac{3}{2}}$) rotational distributions (shown on the left) for both lambda-doublet states, A′ (•) and A″ (○), obtained at the R values indicated for J_{K_a,K_c} = (a) 2_{02} and (b) 3_{03}. These are compared with the experimental distributions from this study and from the previous work of Crim and coworkers [201] and Rosenwaks and coworkers [165].

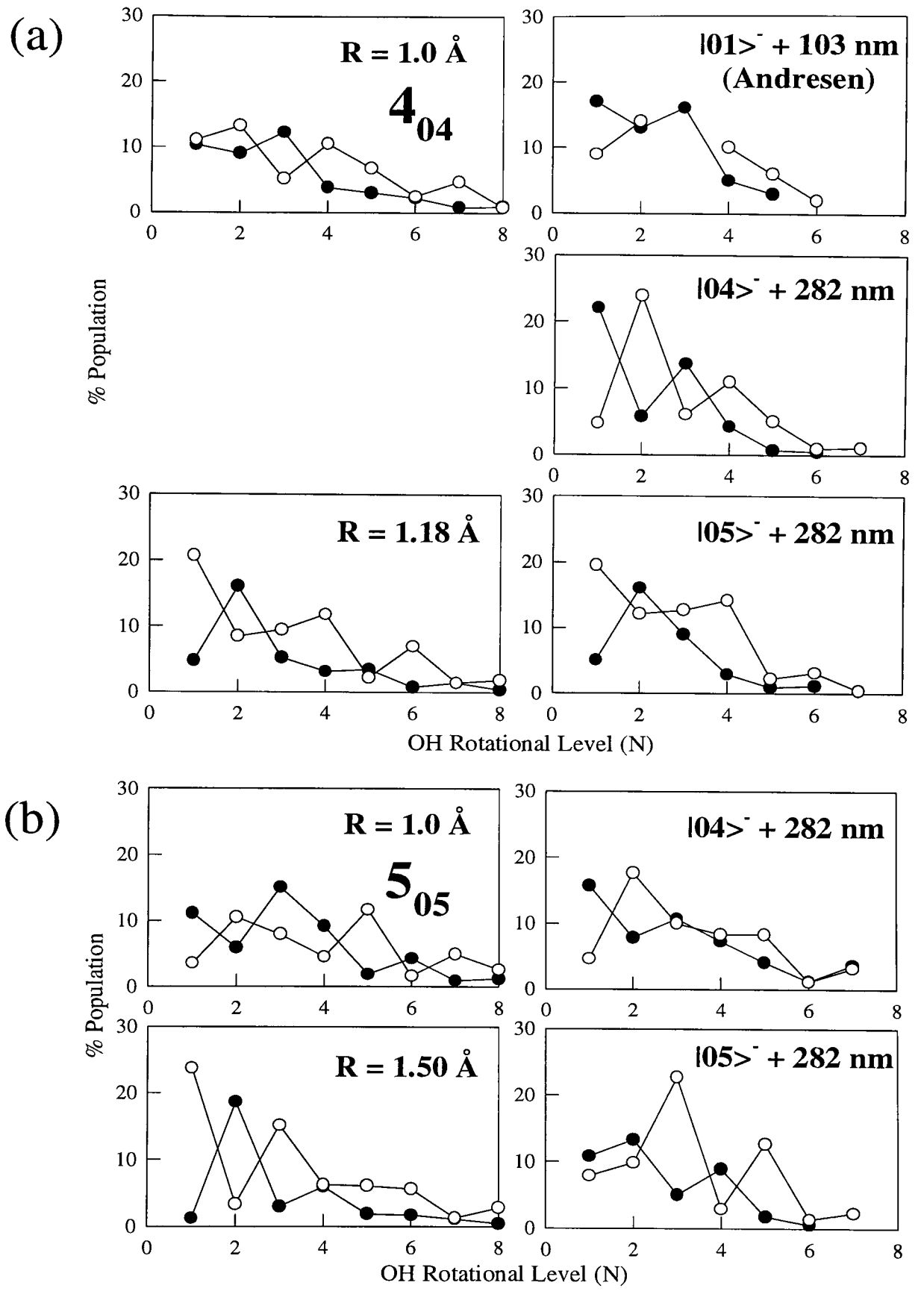

Figure 5.8 The Franck-Condon calculated $OH(^2\Pi_{\frac{3}{2}})$ rotational distributions (shown on the left) for both lambda-doublet states, A′ (•) and A″ (○), obtained at the R values indicated for J_{K_a,K_c} = (a) 4_{04} and (b) 5_{05}.

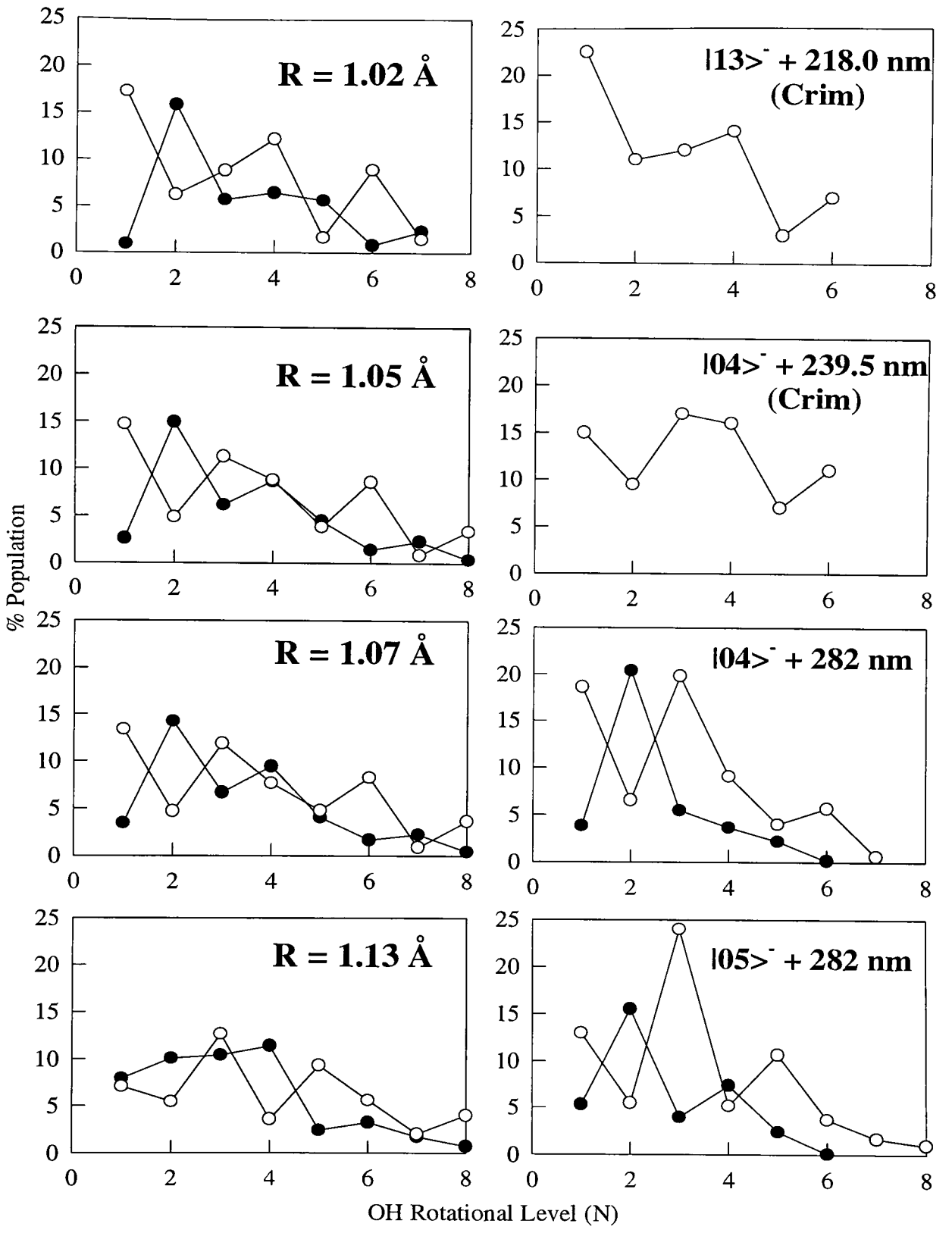

Figure 5.9 The Franck-Condon calculated $OH(^2\Pi_{\frac{3}{2}})$ rotational distributions (shown on the left) for both lambda-doublet states, A′ (•) and A″ (○), obtained at the R values indicated for $J_{K_a,K_c} = 5_{15}$. The calculated distributions are compared with the experimental data of obtained from this study and the previous work of Crim and coworkers [201].

the calculated distributions. In general, there is a qualitative correlation between experimental distributions generated *via* photolysis at decreasing total supplied energy, and those calculated employing increasing values of R.

Shown in Figure 5.10 are the calculated photofragment lambda-doublet distributions for H_2O $J_{K_a,K_c} = 0_{00}$ (a) and 4_{04} (b) for both spin-orbit states, $OH(^2\Pi_{\frac{3}{2}})$ (left-hand side) and $OH(^2\Pi_{\frac{3}{2}})$ (right-hand side), fixing R at 0.958 and 1.365 Å. This figure serves to illustrate that analogous to the experimental observation (see Chapters 3 and 4), there are small differences in the Franck-Condon-predicted oscillatory structure of the $^2\Pi_{\frac{3}{2}}$ and $^2\Pi_{\frac{1}{2}}$ lambda-doublet population distributions. These changes are more marked for the A′ lambda-doublet, which again is in accord with the experimental measurements; this is reiterated in Figures 5.11 and 5.12 in which the OH $^2\Pi_{\frac{1}{2}}$ population distributions from this study and the corresponding best-fit simulation are shown for H_2O $J_{K_a,K_c} = 2_{11}$ [Fig. 5.11(a)], 3_{13} [Fig. 5.11(b)], 4_{23} [Fig. 5.12(a)], 4_{22} [Fig. 5.12(b)] and 6_{06} [Fig. 5.12(c)]. The good agreement between the simulations and experiment for both the phase and amplitude of the oscillatory structure of each lambda-doublet and between the two lambda-doublets is clearly evident. Of particular note is that the values of R required to model the lambda-doublet population distribution in the $^2\Pi_{\frac{3}{2}}$ spin-orbit state are the same as those needed to simulate the $^2\Pi_{\frac{1}{2}}$ data. The inconsistency of the values of R required for different J_{H_2O}, will be discussed later in Section 5.7.

No OH $^2\Pi_{\frac{1}{2}}$ data from the previous experimental studies have been presented for the initial parent rotational states shown in Figures 5.11 and 5.12. However, OH $^2\Pi_{\frac{1}{2}}$ product distributions for $J_{H_2O} = 0_{00}$ [34], 4_{04} [34] and 3_{03} [165] have been published and a comparison with the data from this study (see Table 5.2) again shows that an increasing value of R is required for theory and experimment to be in agreement. The results of the calculations are further summarised in Tables 5.1(a) and 5.2 which show the approximate values of R for which experiment and theory are in reasonable accord. Shown in Table 5.2 are the H_2O rotational state-specific values of R; the reagent rotational state-averaged values are presented in Table 5.1(a). Both of these tables serve to highlight the trend that experiments conducted at lower photolysis photon energies or *via* higher intermediate overtone levels tend to yield OH distributions in better agreement with the Franck-Condon calculated distributions employing more extended values of R. Although some of the detailed structure in the calculated distributions is not in exact agreement with experimental results,

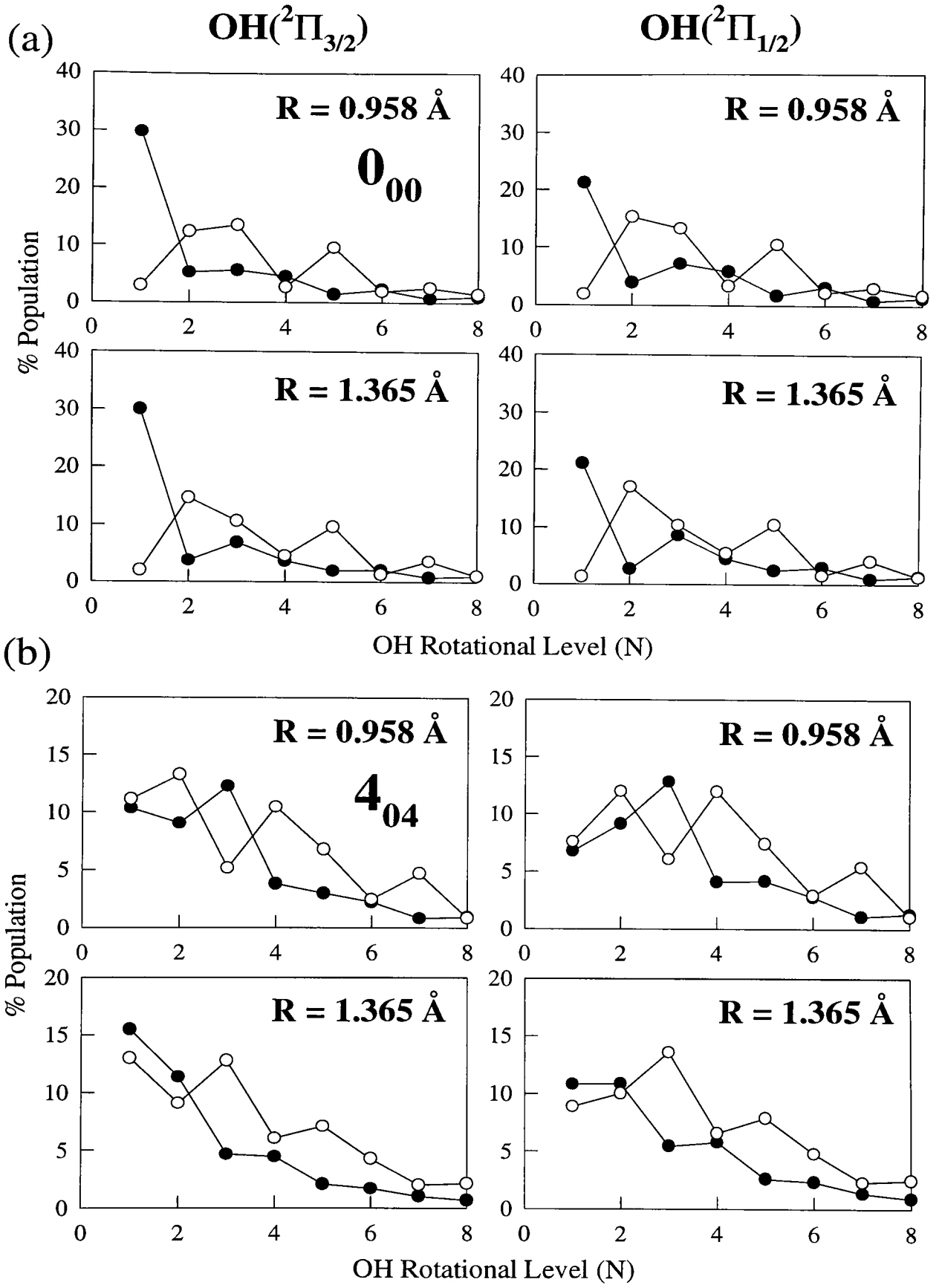

Figure 5.10 The calculated OH photofragment lambda-doublet distributions (• = A′, ∘ = A″), for H_2O $J_{K_a,K_c} = 0_{00}$ (a) and 4_{04} (b), fixing R at 0.958 and 1.365 Å, for both spin-orbit states OH($^2\Pi_{\frac{3}{2}}$) (left-hand side of the figure) and OH($^2\Pi_{\frac{3}{2}}$) (right-hand side). r was set at 0.97 Å throughout.

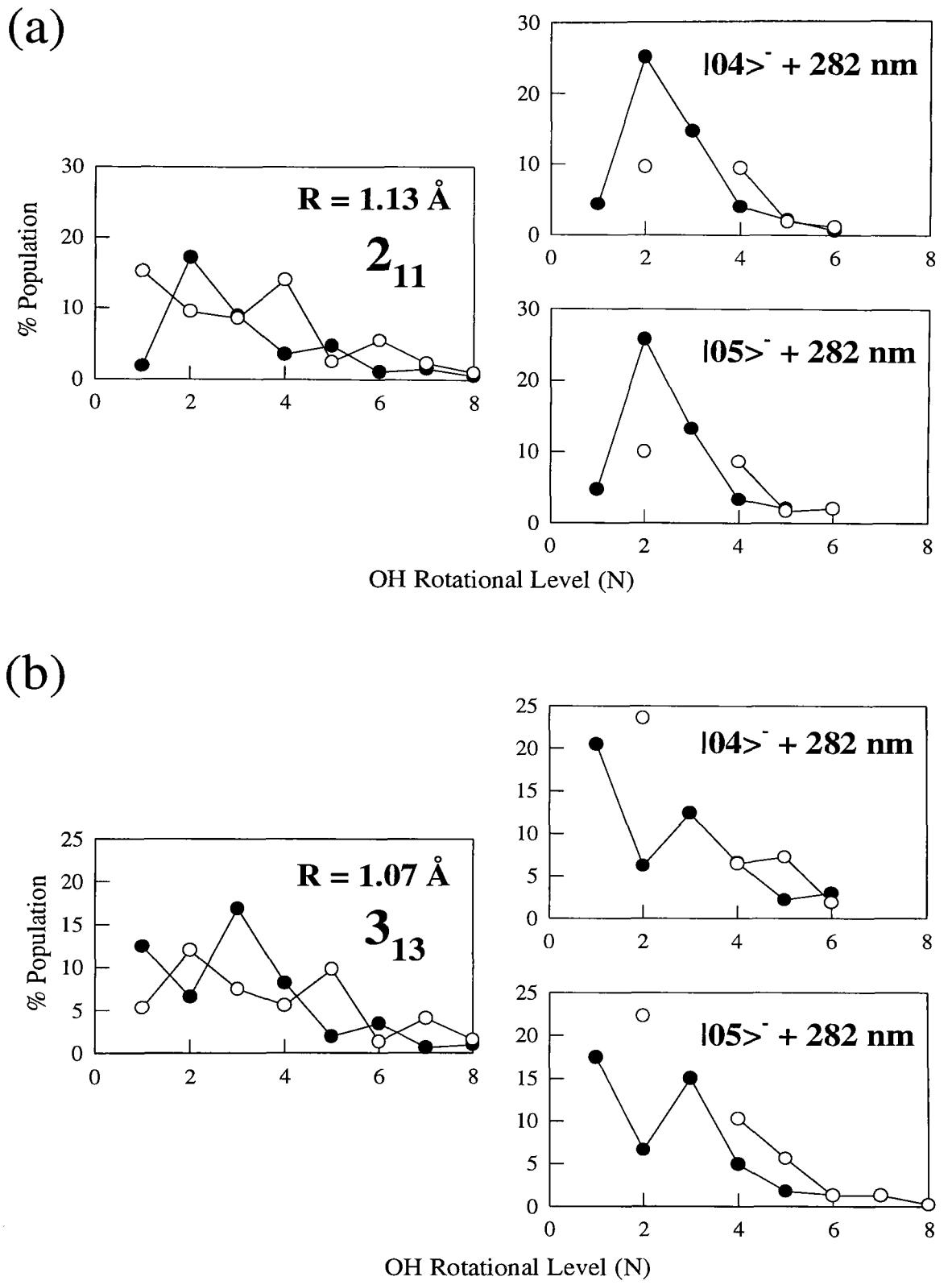

Figure 5.11 The Franck-Condon calculated $OH(^2H_{\frac{1}{2}})$ rotational distributions (shown on the left) for both lambda-doublet states, A′ (•) and A″ (○), obtained at the R values indicated for J_{K_a,K_c} = (a) 2_{11} and (b) 3_{13}. On the right-hand side are the experimental distributions obtained from the present experimental study. These have been placed adjacent to the calculated distributions with which they are in reasonable accord.

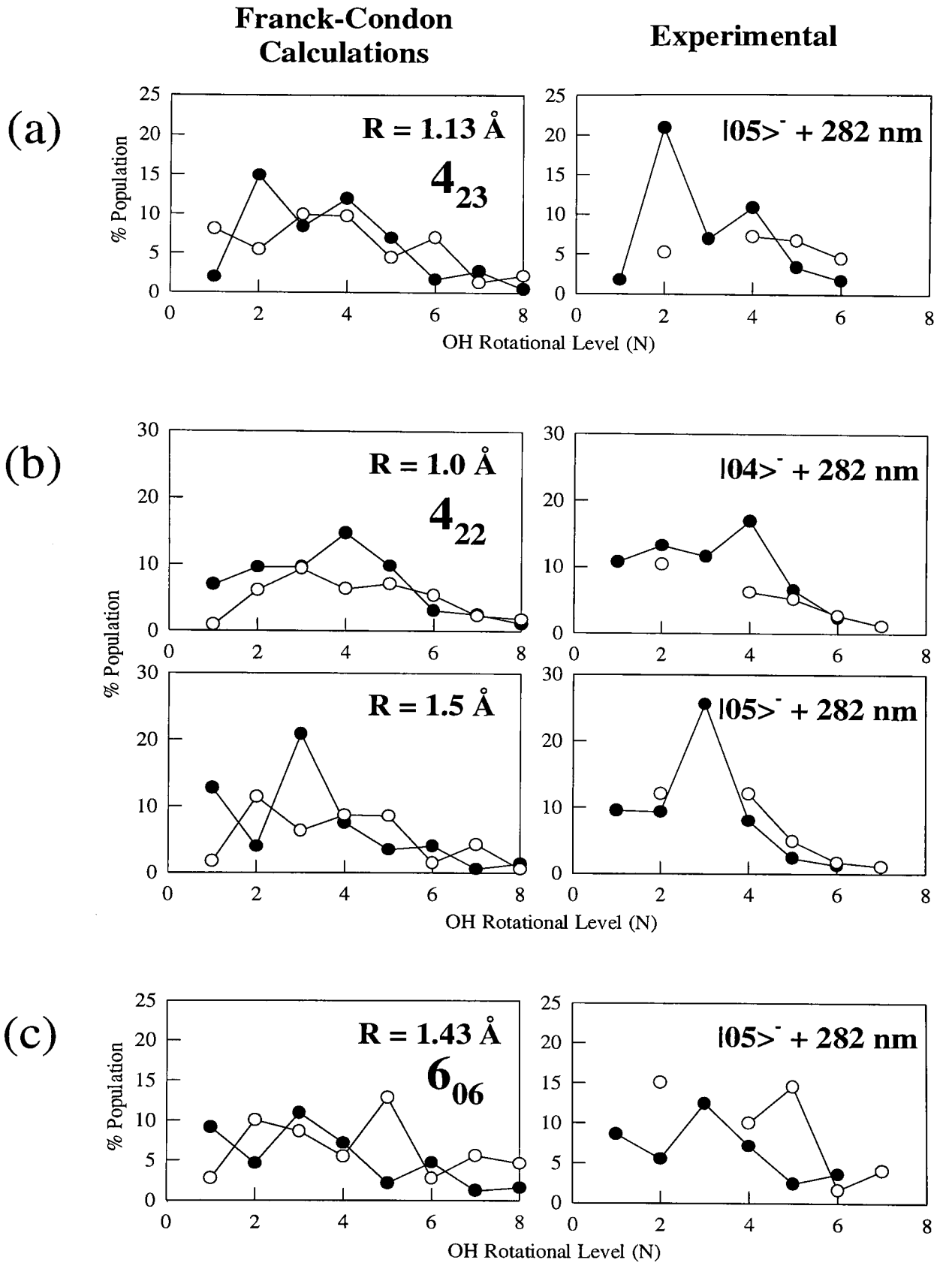

Figure 5.12 The Franck-Condon calculated OH($^2\Pi_{\frac{1}{2}}$) rotational distributions (shown on the left) for both lambda-doublet states, A′ (•) and A″ (○), obtained at the R values indicated for J_{K_a,K_c} = (a) 4_{23}, (b) 4_{22} and (c) 6_{06}. On the right-hand side are the experimental distributions obtained from the present experimental study. These have been placed adjacent to the calculated distributions with which they are in reasonable accord.

		H_2O State			
		$\|05\rangle^-$+282 nm	$\|04\rangle^-$+282 nm	$\|04\rangle^-$+240 nm	$\|01\rangle^-$+193 nm
(a)	$\langle R\rangle$ / Å	1.26 ± 0.10	1.11 ± 0.09	1.06 ± 0.06	1.05 ± 0.04
(b)	R_{EXP} / Å	~ 1.40 ± 0.05	~ 1.49 ± 0.05	~ 1.27 ± 0.05	~ 1.27 ± 0.05

Table 5.1 (a) The approximate average values of R, $\langle R\rangle$, for which the Franck-Condon model described in the text yields OH distributions in reasonable accord with experiment. The length r is fixed at its equilibrium value in free OH of 0.97$\mathring{A}$. (b) The energetically expected approximate values of R, R_{EXP}, were excitation to the $\tilde{A}$ state potential surface should preferentially occur from. The ground state potential of Jensen [229] and the excited state surface of Steammler and Palma [230] were used to make these estimates.

the qualitative trends are well reproduced by the model, and the overall level of agreement is comparable with that observed for the 193 nm photodissociation of $H_2O|01\rangle^-$ by Schinke and coworkers [34], who employed $r \approx R \approx 1.0$ Å.

However, what are surprising are the fluctuations in the values of R required in the calculations to be in agreement with the experimental results and also the generally lower (average) values than would be expected from purely energetic considerations (see Table 5.1(b)). For nearly all of the experimental studies, the average value of R necessary is consistently lower than expected by about 0.2 Å. However, although less energy is supplied for the 282 nm photolysis of $H_2O|04\rangle^-$ in the double-resonance step to the $\tilde{A}$ state than the other experiments, the average value of R is higher than that found necessary in the previous studies, but lower than is required to model the $|05\rangle^-$ data. According to the available potential energy surfaces, 282 nm excitation from the $|04\rangle^-$ overtone to the $\tilde{A}$ state should occur just past the classical turning point. This is certainly possible, as the tail in the absorption spectrum is attributed to tunnelling into this classically forbidden region [40, 41]. As the OH photofragment rotational distributions seem to be so sensitive to

H_2O State [a]	OH Level [b]	0_{00}	2_{02}	2_{11}	3_{03}	3_{13}	4_{04}	4_{23}	4_{22}	5_{05}	5_{15}	6_{06}	7_{17}
$\|05\rangle^-$ 282 nm	A′	1.3 ±0.2	1.07 ±0.03	1.19 ±0.1		1.13 ±0.05	1.19 ±0.07	1.49 ±0.05	1.13 ±0.06	1.48 ±0.05	1.13 ±0.1	1.19 ±0.05	1.3 ±0.1
$\|05\rangle^-$ 282 nm	A″	1.45 ±0.2	1.19 ±0.05	1.43 ±0.05		1.13 ±0.05	1.19 ±0.04	1.49 ±0.1	1.13 ±0.06	1.48 ±0.05	1.13 ±0.1	1.3 ±0.05	1.37 ±0.1
$\|04\rangle^-$ 282 nm	A′	1.1 ±0.2	1.03 ±0.03	1.07 ±0.1	1.43 ±0.05	1.07 ±0.05	1.00 ±0.07	1.02 ±0.1		1.02 ±0.05	1.02 ±0.1		
$\|04\rangle^-$ 282 nm	A″	1.4 ±0.2	1.13 ±0.05	d	1.43 ±0.05	1.07 ±0.05	1.00 ±0.05	1.00 ±0.1		1.02 ±0.05	1.10 ±0.1		
$\|04\rangle^-$ [c] 240 nm	A″		1.15 ±0.05	1.07 ±0.05		1.02 ±0.03	1.00 ±0.04				1.06 ±0.05		
$\|01\rangle^{\pm}$ [e] 193 nm	A′	1.00 ±0.2			1.00 ±0.1		1.00 ±0.04	1.00 ±0.05					
$\|01\rangle^{\pm}$ [e] 193 nm	A″	1.3 ±0.2			d		1.00 ±0.04						

[a] The intermediate vibrational state of the parent molecule and the dissociation wavelength.

[b] The lambda doublet level in the OH $^2\Pi_{\frac{3}{2}}$ and $^2\Pi_{\frac{3}{2}}$ state.

[c] OH population data taken from reference [201].

[d] This data could not be modelled well by the calculations.

[e] OH population data taken from references [34] and [165].

Table 5.2 The approximate values of R for which the Franck-Condon model described in the text yields OH distributions in reasonable accord with experimental results. The column headings refer to the J_{K_a,K_c} state selected in the parent water molecule. The length r is fixed at its equilibrium value in free OH of $0.97\mathring{A}$.

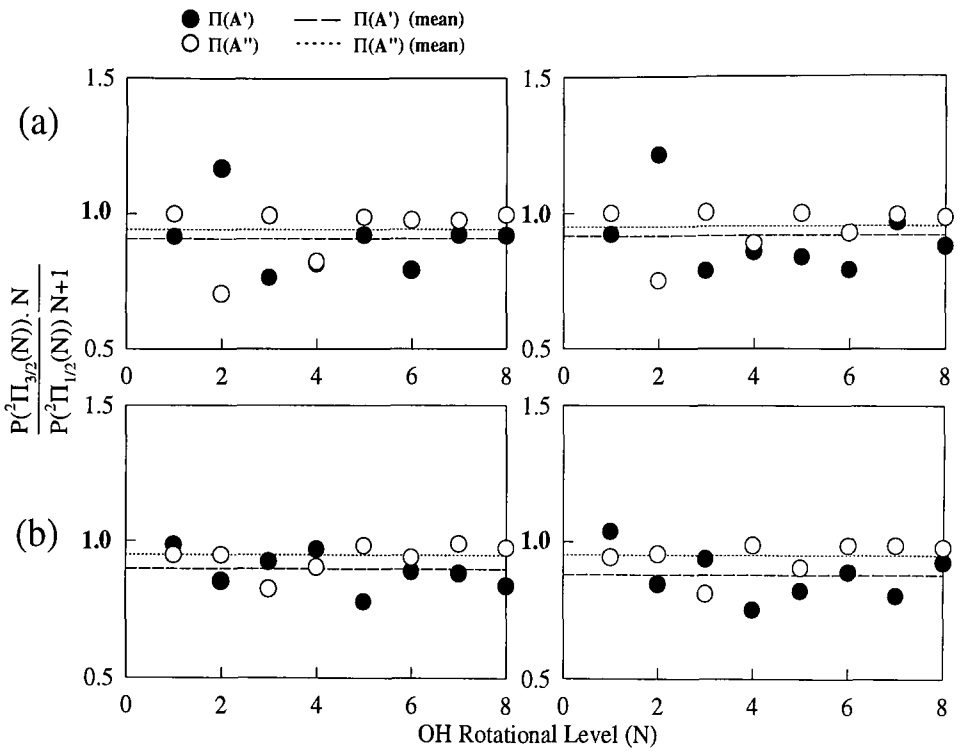

Figure 5.13 The ratio of the calculated population in rotational states in OH $^2\Pi_{\frac{1}{2}}(N)$ and $^2H_{\frac{3}{2}}(N)$ plotted as a function of N, for H_2O J_{K_a,K_c} = (a) 0_{00} and (b) 4_{04}, at the values of R where agreement with the 282 nm photodissociation of $H_2O|04\rangle^-$ and $|05\rangle^-$ experimental data could be obtained. The spin state populations for the A′ (•) and the A″ (◦) lambda-doublet levels and the corresponding mean distribution are shown.

the bound state parent rotational and bending motions, the non-classical behaviour of the water molecule in this region of the ground state potential may require a different treatment of the bound state parent molecule than is currently used to calculated the photofragment rotational distrubutions.

5.4.2 Preferential OH spin-orbit state populations

In Figure 5.13, the ratio of the calculated populations in the OH $^2\Pi_{\frac{3}{2}}(N)$ and $^2\Pi_{\frac{1}{2}}(N)$ spin-orbit states is plotted as a function of N, for H_2O J_{K_a,K_c} = (a) 0_{00} and (b) 4_{04}, at the values of R for which agreement with the data from the 282 nm photolysis of $H_2O|04\rangle^-$ and $|05\rangle^-$ was found. Using the calculated A″ lambda-doublet populations the Franck-Condon model predicts a spin statistical population as N increases. However, at low values of N, particularly for low initial parent angular momentum, the value of the ratio oscillates between one and less than one (0.7–0.9). At low values of N, the oscillatory behaviour

of the lambda-doublet populations is most prominent; the result is a mean distribution (averaged over N) of ~ 0.95, demonstrating a slight preference for the $^2\Pi_{\frac{1}{2}}$ spin-orbit state. In addition, increasing the value of R for which the calculated distribution is obtained seems to have very little effect on the overall picture.

However, if the calculated A′ population distributions are used, there is a small but clear deviation from a statistical distribution at both high an low values of N. At low N, and especially for low parent angular momentum states, there is an N-dependent preferred population of the spin-orbit states. In general, and especially at high values of N, there is a small calculated preference for the $^2\Pi_{\frac{1}{2}}$ spin-orbit state in the product OH of ~ 0.9 (averaged over N). This is, however, less than that observed experimentally for the VMP of $H_2O|04\rangle^-$ and $H_2O|05\rangle^-$ (shown in Figures 3.21 and 3.22, respectively). This will be discussed further in Section 5.7.

5.5 The 282 nm VMP of H_2O $|04\rangle|2\rangle^-$

Shown on the left-hand side of figure 5.14 are the Franck-Condon calculated OH $^2\Pi_{\frac{3}{2}}$ lambda-doublet distributions, fixing $r \approx R = 0.97$ Å, for $H_2O(k=2)$[7] J_{K_a,K_c} = (a) 2_{02}; (b) 2_{11}; (c) 4_{13}; (d) 4_{22}; (e) 4_{31}. Adjacent to these are the corresponding experimental distributions arising from the 282 nm photolysis of $H_2O|04\rangle|2\rangle^-$.

No qualitative agreement could be obtained between the experimental and calculated distributions at any value of R. However, fixing both bond lengths at their equilibrium value, the calculated distributions do bear some resemblance to the experimental results if they are shifted to the left by 3 values of N. This is consistent with the previous of work of Crim and Schinke and coworkers [224] who reported the OH rotational distribution arising from the 239.5 nm photolysis of $H_2O|03\rangle|2\rangle^-$ J = 0_{00}. The 'cooling' of the distribution was attributed to the anisotropy on the excited state surface that is experienced when bending motion in the parent molecule is excited. The value of R is however surprising considering that a much lower photolysis energy was used in this study; this will be discussed in Section 5.7.

[7] k refers to the number of quanta of bending vibration

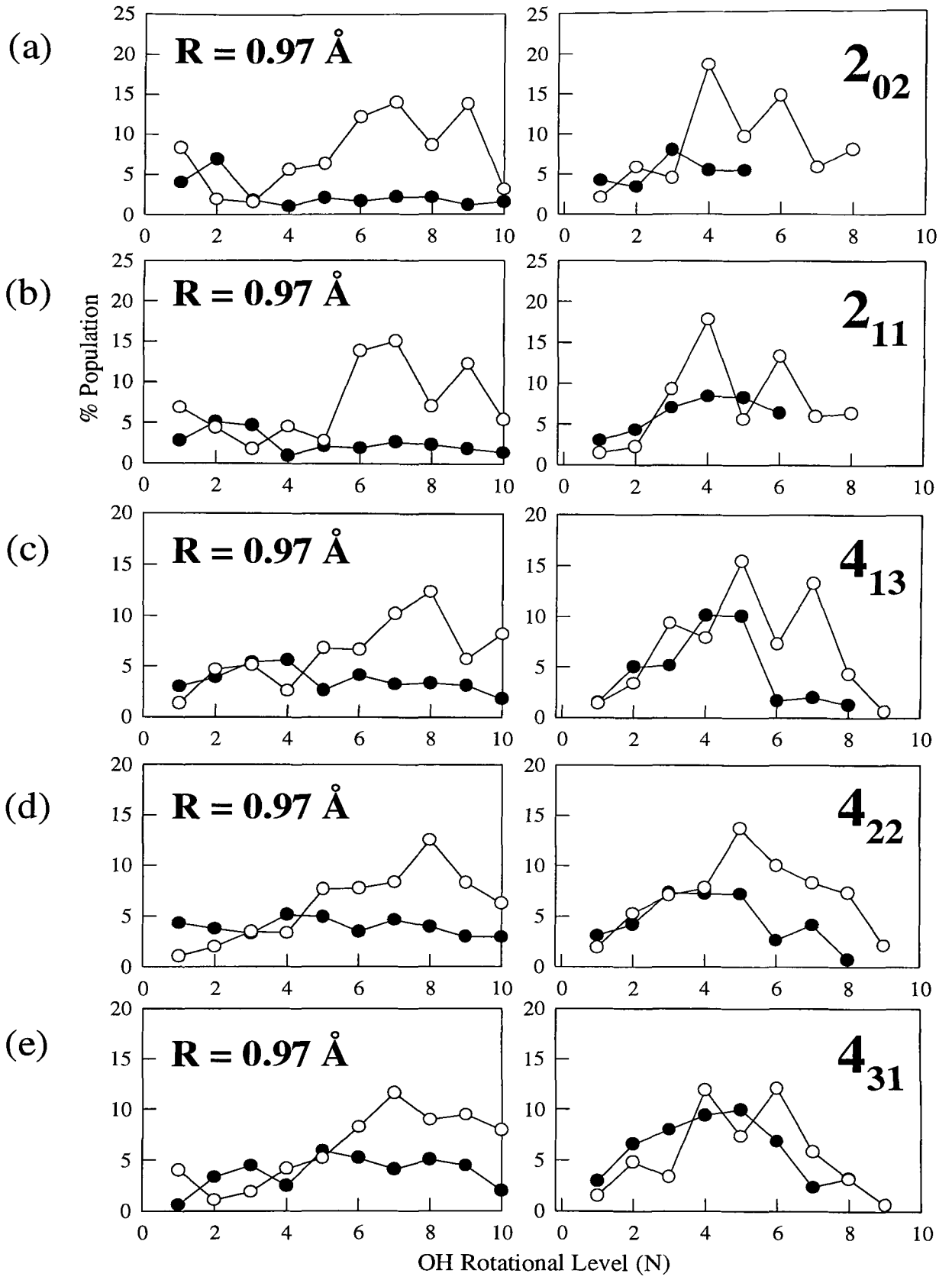

Figure 5.14 The Franck-Condon calculated OH $^2\Pi_{\frac{3}{2}}$ lambda-doublet (A′ (•) and A″ (○)) population distributions (left), fixing $r \approx R = 0.97$ Å, for $H_2O(k = 2)$ J_{K_a,K_c} = (a) 2_{02}; (b) 2_{11}; (c) 4_{13}; (d) 4_{22}; (e) 4_{31}. k refers to the number of quanta of bending vibration. Adjacent to these are the corresponding experimental distributions arising from the 282 nm photolysis of $H_2O|04\rangle|2\rangle^-$.

5.6 The 288 nm VMP of HOD(4,0,0) and (5,0,0)

Within the Born-Oppenheimer approximation, the HOD molecule will have the same ground and excited electronic state potential energy surfaces as its isotopomer HOH. The Jensen [229] H_2O ground state potential function was therefore used to perform Franck-Condon simulations of the 288 nm photodissociation of HOD(4,0,0) and (5,0,0).

5.6.1 OD photofragment rotational distributions

Shown on the left-hand side of Figure 5.15 are the Franck-Condon calculated OD $^2\Pi_{\frac{3}{2}}$ lambda-doublet population distributions for HOD $J_{K_a,K_c} = 4_{04}$, with increasing R. Shown on the right-hand side of the figure are the corresponding experimental distributions, from the photolysis of HOD($4\nu_{OH}$ & $5\nu_{OH}$) at 288 nm. A poor agreement with experiment can be obtained by fixing both bonds at their equilibrium value. For the other initial reagent rotational states that were employed (see tables 4.2 and 4.3 in Chapter 4), the same is also true but the agreement is not very good, with only the phase in the structure, for selected N values, being correctly predicted. These values R, where preferential excitation from the vibrational overtone to the $\tilde{A}$ state PES should occur are certainly very unrealistic, as the energetically expected values are similar to those given in Table 5.1 for the isoenergetic H_2O VMP study.

One effect of substituting a deuterium atom for a hydrogen atom in the water molecule is to shift the centre of mass further away from the oxygen atom. The exit-channel torque, imparted by the departing H atom on the rest of the molecule will therefore be larger (~ 1.9 times) for H–OD than for H–OH. Although this torque is neglected in the H_2O calculations because the centre of mass of the OH is so close to the O atom, it may well be that for HOD the small increase is sufficient to have an experimentally noticable effect on the OD fragment rotational motion.

5.6.2 Modified Franck-Condon model

The Franck-Condon model always yields the initial product angular momentum distribution inherent in the parent rotating-bending wave function. During the dissociation, this initial angular momentum distribution subsequently evolves under the influence of the excited PES

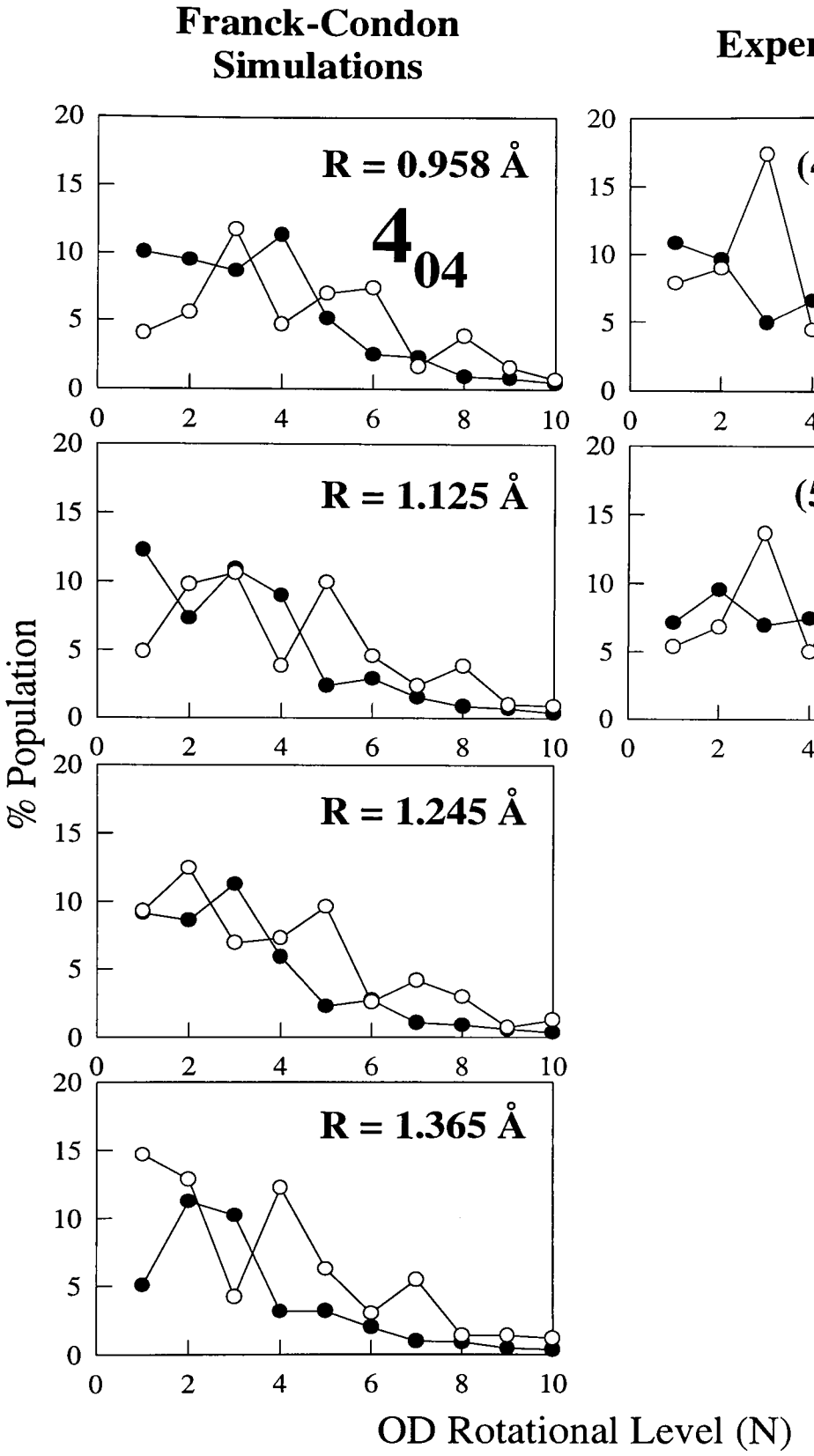

Figure 5.15 The Franck-Condon-calculated OD($^2\Pi_{\frac{3}{2}}$) rotational distributions (left) for both lambda-doublet states, A′ (•) and A″ (○), shown for increasing values of R, for HOD $J_{K_a,K_c} = 4_{04}$. On the right-hand side are the experimental distributions obtained from this study. These have been placed adjacent to the calculated distributions which provide the closest agreement with experiment

into the observed product rotational distributions. For a fast dissociation and a modest exit-channel torque, a final rotational distribution can still reflect some of the character of this initial distribution [263]–[265].

Reisler and coworkers [263]–[265], in an attempt to model the NO product rotational distributions arising from the photodissociation of ClNO *via* the T_1 state, developed a modified form of the semiclassical Franck-Condon model of Morse and Freed [145, 252] (for J = 0) which included an approximation for the effects of the small exit channel torque on the T_1 surface. This was treated in a time-dependent fashion (dissociation on the T_1 surface has been shown by Schinke and coworkers [266, 267] to be on a time scale of $\sim$ 600 fs) and the resulting change in the equilibrium bending angle during disscociation generates a time dependent, unidirectional angular momentum, $J_t(t)$, superimposed on the angular momenta that is derived from the parent bending motion. The application of the model to simulate the product rotational distributions and the details of the (closed-shell) Franck-Condon model that is used, is thoroughly discussed in references [41], [264] and [265] and only the key features will be mentioned here.

In a simplistic form, the semiclassical Franck-Condon model developed by Morse and Freed [145, 252] for an initially non-rotating parent molecules can be written as [263]

$$P_j^n \approx \left(|C_{+j}^n|^2 + |C_{-j}^n|^2\right) \; + \; interference\ terms \tag{5.20}$$

where n is the initial reagent quantum state. $|C_{+j}^n|^2$ and $|C_{-j}^n|^2$ are equivalent to the coefficients defined earlier in equation 5.14 and are defined as the Fourier transform of the parent rotating-bending wave function in the coordinate representation, in other words represents the wave function in the angular momentum representation [268]. This will be discussed in more detail in Section 5.7. Equation 5.20 can be interpreted as the bending motion of the dissociating excited parent molecule providing an equal source of clockwise (-j) and counter-clockwise (+j) rotation of the diatomic fragment (caused by the opening and the closing of the bending angle respectively). The interference of these two motions can be understood as the cause of the oscillatory structure in the OH rotational distributions [145, 252, 264, 265] (see also Section 5.7). This is shown schematically in Figure 5.16.

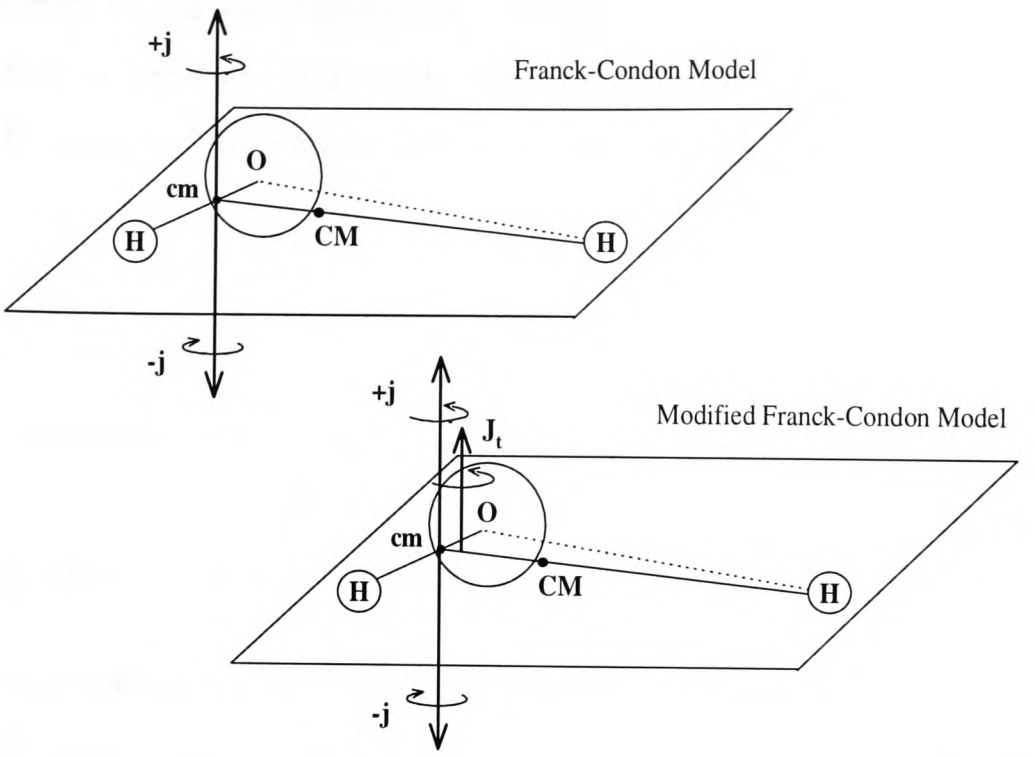

Figure 5.16 Pictorial representiation of the sources of angular momentum giving rise to the observed OH rotational excitation. The bending wavefunction of the parent H_2O is the source of equal clockwise and counterclockwise rotation, $\pm$j. The angular momentum J_t, generated by the torque imparted by the departing H atom, is unidirectional.

Including the additional angular momentum generated by the exit torque, calculated at the time T when the Franck-Condon expansion is carried out, Equation 5.20 can be written as [263]

$$P_j^n \approx F[j + J_t(T)] + F[-j + J_t(T)] \; + \; interference\ terms \tag{5.21}$$

and

$$F(x) = |C_x^n|^2 \tag{5.22}$$

A similar approach has been taken to modify the open shell Franck-Condon model of Balint-Kurti [233]. The measured dissociation time for H_2O on the $\tilde{A}$ state is between ~20 fs [212] and ~40 fs [166](c) and it is assumed that the torque maybe treated as being impulsive. Nearly all of the available energy in the two VMP processes, HOX(X=H or D) $(4\nu_{OH})$ and $(5\nu_{OH})$ + 282(8) nm (E_{AVL} $\approx$ 8000 cm^{-1} and 11000 cm^{-1} respectively) goes into

translational energy of the photofragments. From a simple classical argument, for HOD(J = 0) dissociating to produce OD + H, the linear angular momentum, l, generated by the departing H atom will be converted into rotational angular momentum, j', of the OD fragment:

$$\mu.v.b = \hbar.\sqrt{j'(j'+1)} \tag{5.23}$$

in which μ is the reduced mass of the parent, v is the relative speed of the photofragments calculated from the excess energy provided by the two-photon VMP excitation and b is the distance between the O atom and the centre of mass of the OD in the dissociating molecule.

For the HOD experiments presented here, initially exciting four and five quanta in the O–H stretch, the departing H atom will transfers $\sim$ 1.1 and 1.3 unit of rotational angular momentum, respectively, onto the rotating OD [8]. The modification to the Franck-Condon model will only allow an integral value of angular momentum to be 'added' to the rotating OD product. The additional momentum, J_t, was therefore defined as having a value of 1 and acts in a direction specified by the direction of the torque which decreases the bending angle. The adding of an additional angular momentum, acting in a counterclockwise direction will therefore have significant effect the structure of the product rotational distribution.

To modify the Balint-Kurti model, a new set of expansion coefficients $C_{j'\lambda}^{J_i P_i}$ were calculated from the original coefficients $C_{j\lambda}^{J_i P_i}$ (defined in equation 5.14) which are calculated from the bound state parent Hamiltonian, in which

$$j' = j + J_t \quad and \quad \lambda' = \lambda$$

using[249, 256]

$$C_{j'\lambda}^{J_i P_i} = \sum_j (j\lambda J_t 0|j'\lambda)\ C_{j\lambda}^{J_i P_i} \tag{5.24}$$

and (...|...) are Clebsch-Gordon coefficients. Inserting these new values into equation 5.16, which contain the remaining coupling terms needed to couple j' with s and l, the exit-torque modified OD photofragment lambda-doublet population distributions can be calculated. For parent J = 0, calculating the closed-shell OD rotational distribution using Equation 5.17

[8] Using a similar classical argument for the 282 nm photodissociation of $H_2O(4\nu_{OH})$ and $(5\nu_{OH})$, the torque which would generate an additional angular momentum of $\sim$ 0.8 and 0.9, respectively.

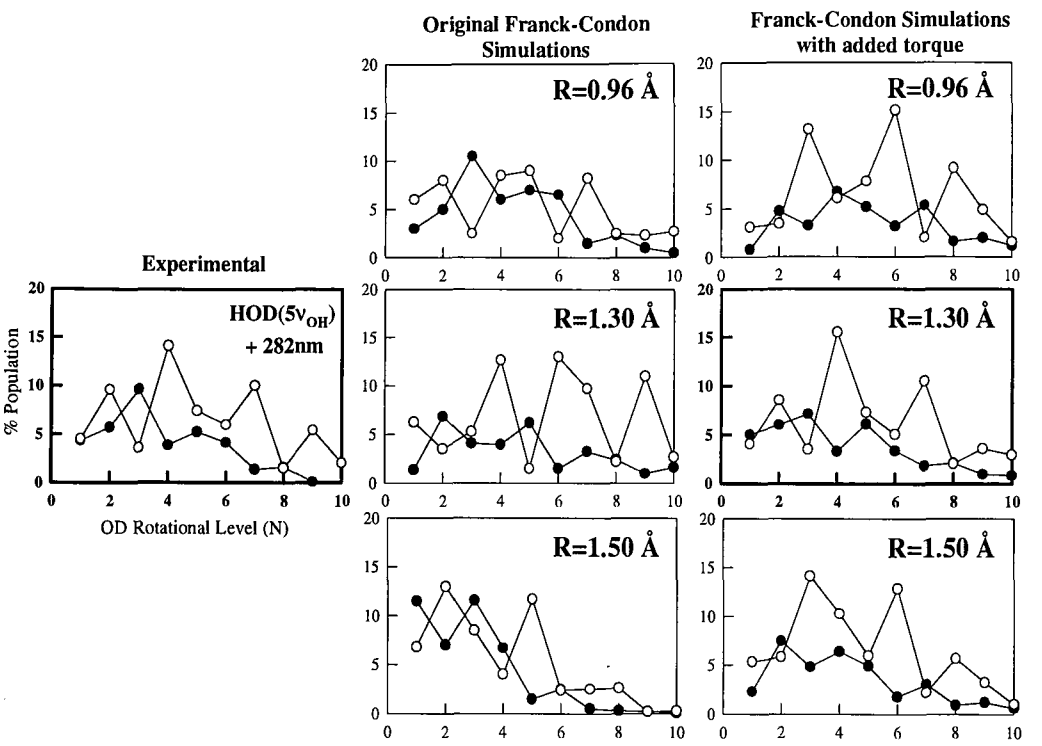

Figure 5.17 The calculated OD $^2\Pi_{\frac{3}{2}}$ population distribution, for both lambda-doublets A′ (•) and A″ (○), for HOD $J_{K_a,K_c} = 6_{06}$, as a function of R, using the original Franck-Condon model (middle) and the modified model (right) which includes an added impulsive torque. r was fixed at the equilibrium value of free OD. Also shown in the left of the figure is the corresponding experimental distribution, photolysis HOD($5\nu_{OH}$) at 288 nm.

and the new set of coefficients, the end result is completely equivalent to the work of Reisler and coworkers, employing Equation 5.21.

Shown on the left of Figure 5.17 is the experimental OD $^2\Pi_{\frac{3}{2}}$ lambda-doublet population distribution obtained by photolysing HOD(5,0,0) $J_{K_a,K_c} = 6_{06}$ at 288 nm. Also shown are the corresponding calculated distributions, for three values of R, using the original (middle) and the modified (right-hand side) Franck-Condon model. Comparing the two sets of calculated distributions, it is clear that the simulated torque has a marked effect on the oscillatory structure of the lambda-doublet populations. More importantly, good qualitative agreement with experiment is obtained at realistic values of R with the new model.

5.6.3 Modified Franck-Condon simulations of the OD photofragment rotational distributions

Shown on the left of Figure 5.18 are the calculated OD $^2\Pi_{\frac{3}{2}}$ rotational distributions for HOD J_{K_a,K_c} = (a) 3_{13}, (b) 4_{04} and (c) 5_{05}, at the values of R given; the corresponding experimental distributions obtained from the 288 nm photodissociation of HOD(4,0,0) are shown on the right. These were the only rotational states selected in the (4,0,0) overtone, and the calculated distributions that are shown provide the closest agreement with the experiment using the modified Franck-Condon model.

For $J_{K_a,K_c} = 3_{13}$, the fit is poor, especially for the A′ lambda-doublet, but for values of N greater than 3, the model qualitatively predicts the structure in each of the lambda-doublet distributions. The overall agreement is noticably improved by increasing the values of J. However, the calculated population for N = 1 and 2 in both lambda-doublet states appears to be consistently under-estimated by the model when compared with the experimental values; for higher values of N, the agreement is almost quantitative. The values of R that are required in the model compare very well with the energetically expected values (see Table 5.1(b)).

In Figure 5.19 the 'best fit' calculated OD$^2\Pi_{\frac{3}{2}}$ rotational distributions are compared with the corresponding experimental data obtained from the 288 nm photolysis of HOD(5,0,0) for the same three bound parent rotational states. Again, with increasing J, the agreement between experiment and theory improves, and for all values of N except 1 and 2, the agreement is qualitatively good. The model still appears to be unable to correctly predict the population in N = 1 and 2, particularily for the A′ lambda-doublet state.

The slight difference seen experimentally between the product distributions arising from HOD(4,0,0) $J_{K_a,K_c} = 5_{05}$ and HOD(5,0,0) $J_{K_a,K_c} = 5_{05}$ (see Figures 5.18(c) and 5.19(c)) are predicted by the model when a higher value of R is used for the lower overtone experiment. This conformed with what is expected on purely energetic grounds, and with what was seen in the H_2O VMP experiments. The remaining HOD($5\nu_{OH}$) + 288 nm experimental and their corresponding 'best-fit' (modified) Franck-Condon predicted OD $^2\Pi_{\frac{3}{2}}$ distributions for J_{K_a,K_c} = (a) 5_{15}, (b) 6_{06}, (c) 6_{16} and (d) 7_{07}, are shown in Figure 5.20.

Figure 5.21 compares the modified Franck-Condon predicted (a) OD $^2\Pi_{\frac{3}{2}}$ and (b) OD $^2\Pi_{\frac{1}{2}}$ lambda-doublet population distributions for HOD $J_{K_a,K_c} = 6_{06}$ at low and high values of

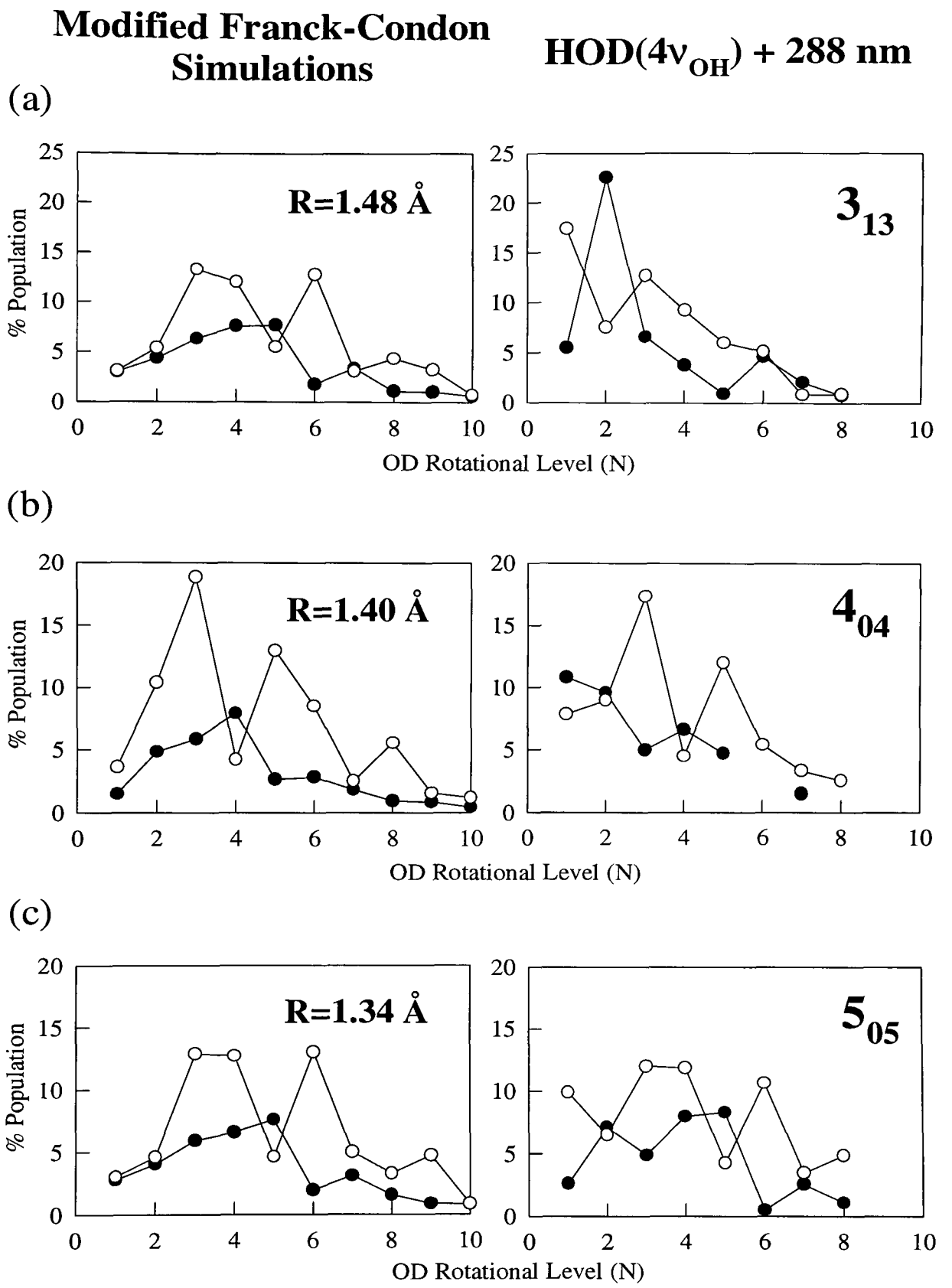

Figure 5.18 The modified Franck-Condon model calculated OD $^2\Pi_{\frac{3}{2}}$ rotational distributions (left) obtained at the values of R indicated for HOD J_{K_a,K_c} = (a) 3_{13}, (b) 4_{04} and (c) 5_{05}. On the right-hand side are the corresponding experimental distributions obtained in this work, photolysing HOD(4,0,0) at 288 nm.

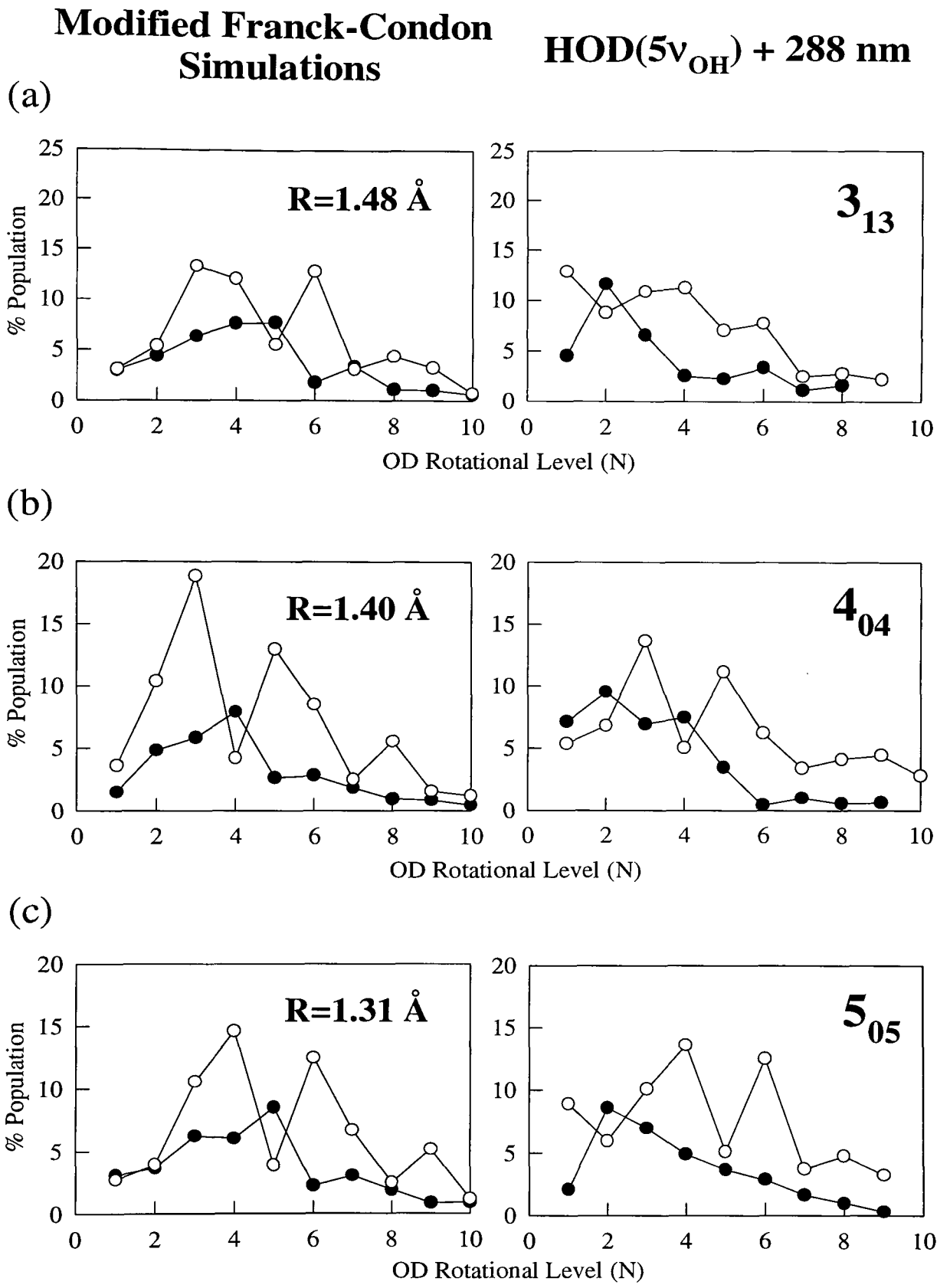

Figure 5.19 The modified Franck-Condon model calculated OD $^2\Pi_{\frac{3}{2}}$ rotational distributions (left) obtained at the values of R indicated for HOD J_{K_a,K_c} = (a) 3_{13}, (b) 4_{04} and (c) 5_{05}. On the right-hand side are the corresponding experimental distributions obtained in this work, photolysing HOD(5,0,0) at 288 nm.

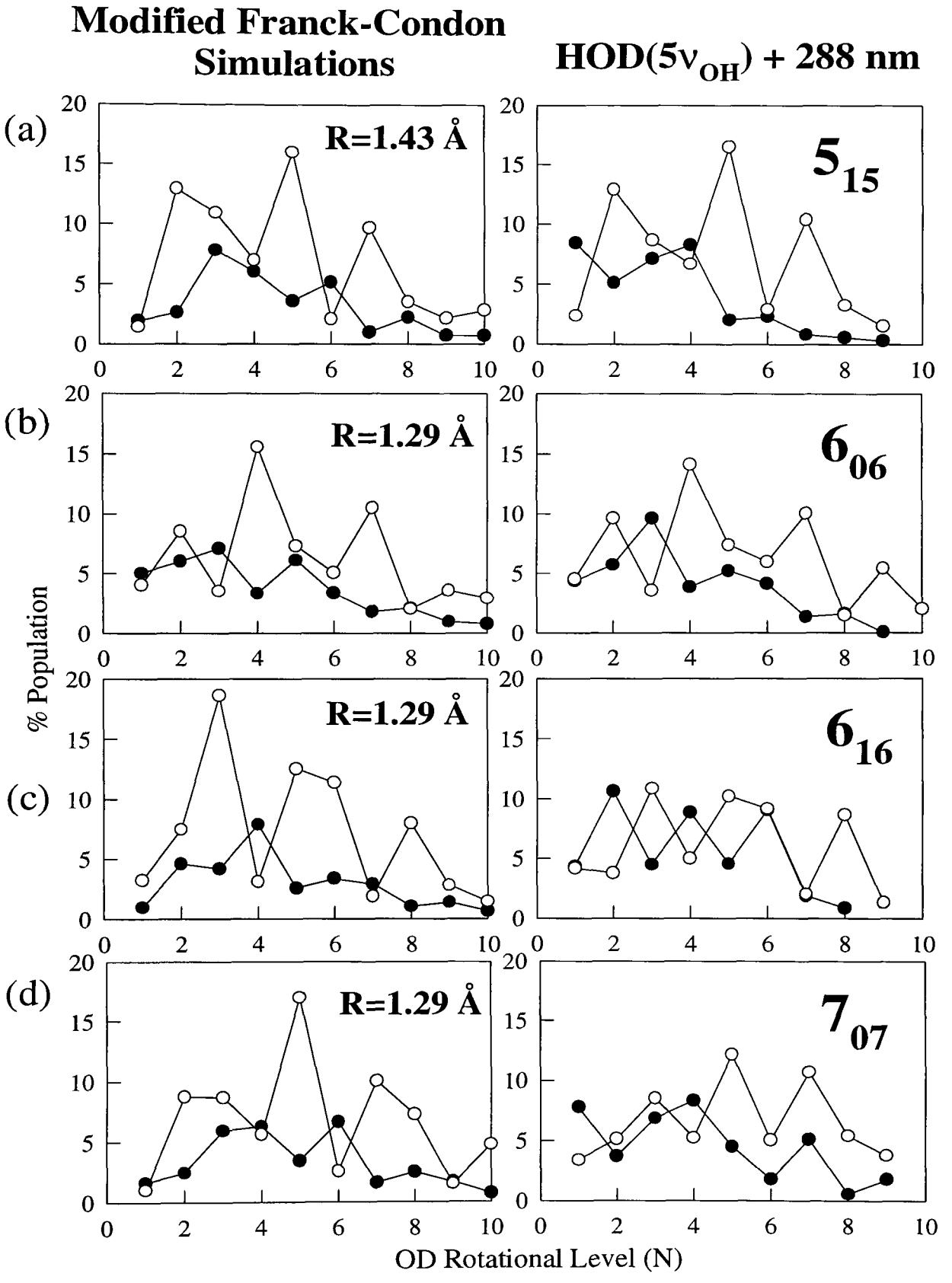

Figure 5.20 As in 5.19 but for HOD J_{K_a,K_c} = (a) 5_{15}, (b) 6_{06}, (c) 6_{16} and (d) 7_{07}.

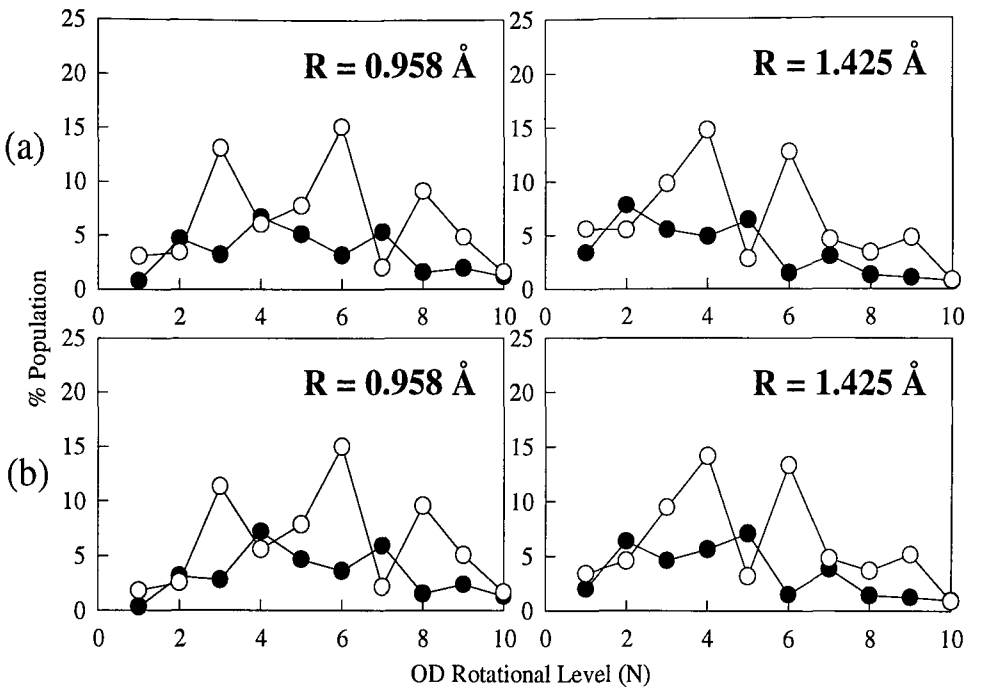

Figure 5.21 The modified Franck-Condon predicted OD $^2\Pi_{\frac{3}{2}}$ (a) and OD $^2\Pi_{\frac{1}{2}}$ (b) product lambda-doublet population distributions for HOD $J_{K_a,K_c} = 6_{06}$ at a low and a high value of R.

R. In agreement with experimental observations there are no real differences between the two (within the error margins). A comparison with the experimental OD $^2\Pi_{\frac{1}{2}}$ distributions for $J_{K_a,K_c} = 3_{03}$ and 5_{15} are shown in Figure 5.22. Allowing for the anomaly at N= 1 and 2, the same value of R required for the $^2H_{\frac{3}{2}}$ data was necessary to obtain a good fit, in line with the H_2O simulations.

These results are summarised in Table 5.3, showing the reagent state rotational state-specific and averaged approximate values of R at which experiment and theory are in reasonable accord. This table serves to highlight two key points: First, the results are consistent with the Franck-Condon simulations of the VMP of H_2O, in which experiments conducted at lower photolysis photon energies or *via* higher intermediate overtone levels tend to yield OD distributions in good agreement with those from the Franck-Condon calculations at more extended values of R. Second, the values of R given in the table appear sensible; the outer maximum of the HOD(5,0,0) vibrational wavefunction occurs at about $\sim$ 1.35 Å [241](b) and at about $\sim$ 1.3 Å for HOD(4,0,0). However, the $\tilde{A}$–$\tilde{X}$ transition moment function, which should be very similar to that in H_2O [41], decreases significantly with bond extension. 288

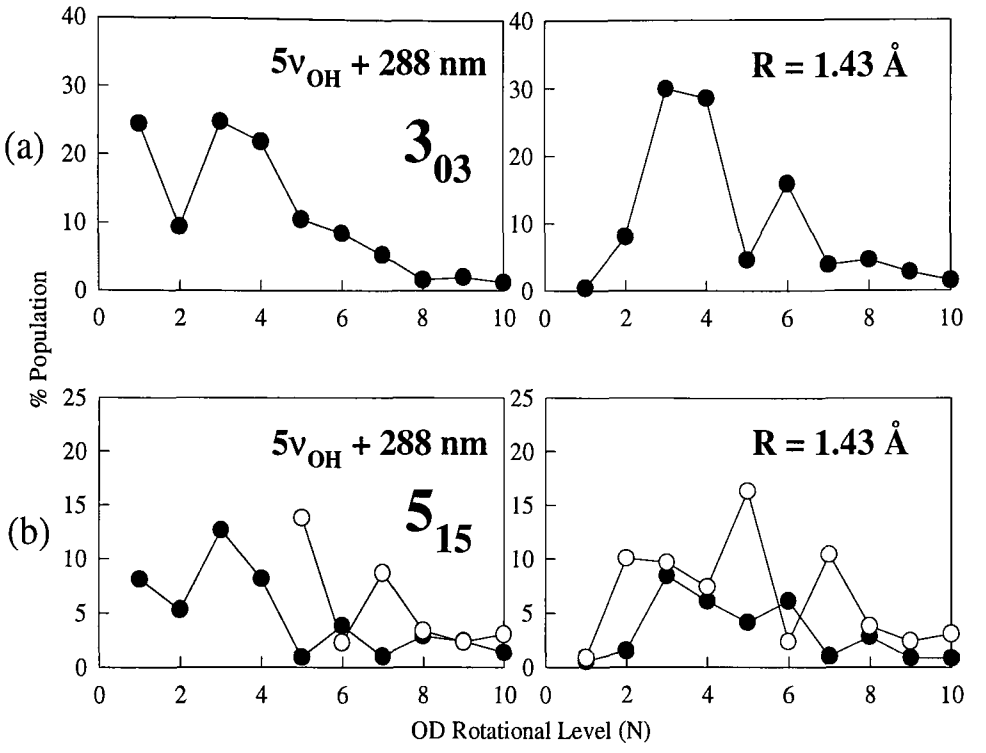

Figure 5.22 The modified Franck-Condon model calculated OD $^2\Pi_{\frac{1}{2}}$ rotational distributions (left) obtained at the values of R indicated for HOD J_{K_a,K_c} = (a) 3_{03} and (b) 5_{15}. Also shown are the corresponding experimental distributions obtained in this work, photolysing HOD(5,0,0) at 288 nm.

HOD State	Parent Rotational State J_{K_a,K_c}								$\langle R \rangle$ / Å
a	$\mathbf{3}_{03}$	$\mathbf{3}_{13}$	$\mathbf{4}_{04}$	$\mathbf{5}_{05}$	$\mathbf{5}_{15}$	$\mathbf{6}_{06}$	$\mathbf{6}_{16}$	$\mathbf{7}_{07}$	b
(4,0,0)		1.48	1.40		1.34				**~1.41**
+ 288 nm		±0.05	±0.05		±0.05				±0.05
(5,0,0)	1.43	1.48	1.40	1.43	1.31	1.29	1.29	1.29	**~1.36**
+ 288 nm	±0.05	±0.05	±0.05	±0.05	±0.05	±0.05	±0.05	±0.05	±0.05

[a]The intermediate vibrational state of the parent molecule and the dissociation wavelength.

[b]The average required value of R.

Table 5.3 The parent rotational state-specific and averaged approximate values of R required in the modified Franck-Condon model in order for experiment and theory to be in reasonable accord.

nm dissociation out of the (4,0,0) state, which energetically should occur preferentially from beyond the outer maxima ($R \sim 1.5\pm0.05$ Å), is therefore likely to occur at slightly smaller R configurations than anticipated. The average value required in the calculations was $\langle R \rangle = 1.41\pm0.05$ Å. 288 nm dissociation out of the (5,0,0) overtone however is expected (energetically) to occur preferentially very close to the outer maxima ($R \sim 1.4\pm0.05$ Å), which is relatively unaffected by the dipole moment function. The average value obtained was $\langle R \rangle = 1.36\pm0.05$ Å. Figure 5.23 shows contour plots of the square of the vibrational eigenstates HOD (4,0,0) and (5,0,0), plotted against the two stretching coordinates. The energetically expected values of R are indicated by the lines labelled b, and the average value arising from the simulations by the lines labelled a. The effect of the dipole moment function on the wave function has been shown by Schinke and coworkers [41] (for H_2O, but the effect will be similar for HOD) to squash the tail of the outer maximum to smaller values of R, but does not significantly shift the position of the outer maximum. This would qualitatively explain the values required in the simulations in order that theory and experiment are in accord and would also be consistent with the experimental observation that the VMP cross-section for HOD(5,0,0) + 288 nm, $\sigma^{VMP}_{(5\nu_{OH})}$, is approximately 20 times larger than that for HOD(4,0,0) + 288 nm, $\sigma^{VMP}_{(4\nu_{OH})}$.

5.6.4 Preferential OD spin-orbit state population

The ratio of the calculated population in the OD $^2\Pi_{\frac{3}{2}}(N)$ and $^2\Pi_{\frac{1}{2}}(N)$ spin-orbit states is plotted in figure 5.24 as a function of N, for HOD $J_{K_a,K_c} = 4_{04}$ (left) and 6_{06} (right) at the values of R for which agreement with the experimental data was found. Similar to the original Franck-Condon simulations of the VMP of H_2O, the A″ lambda-doublet calculations show a near spin statistical population of the two OD spin-orbit states. However, a slight preference for the $^2\Pi_{\frac{1}{2}}$ state is again seen when the A′ lambda-doublet states are considered. The errors in the measured distributions (shown in Figures 4.14 and 4.15) do however prevent a realistic experimental test of the model.

5.7 Discussion

The insensitivity of the H_2O $J_{K_a,K_c} = 0_{00}$ photofragment rotational distributions both to the intermediate stretching vibrational overtone level excited in the bound water molecule and to the photolysis photon energy is surprising, as is the analogous insensitivity predicted by

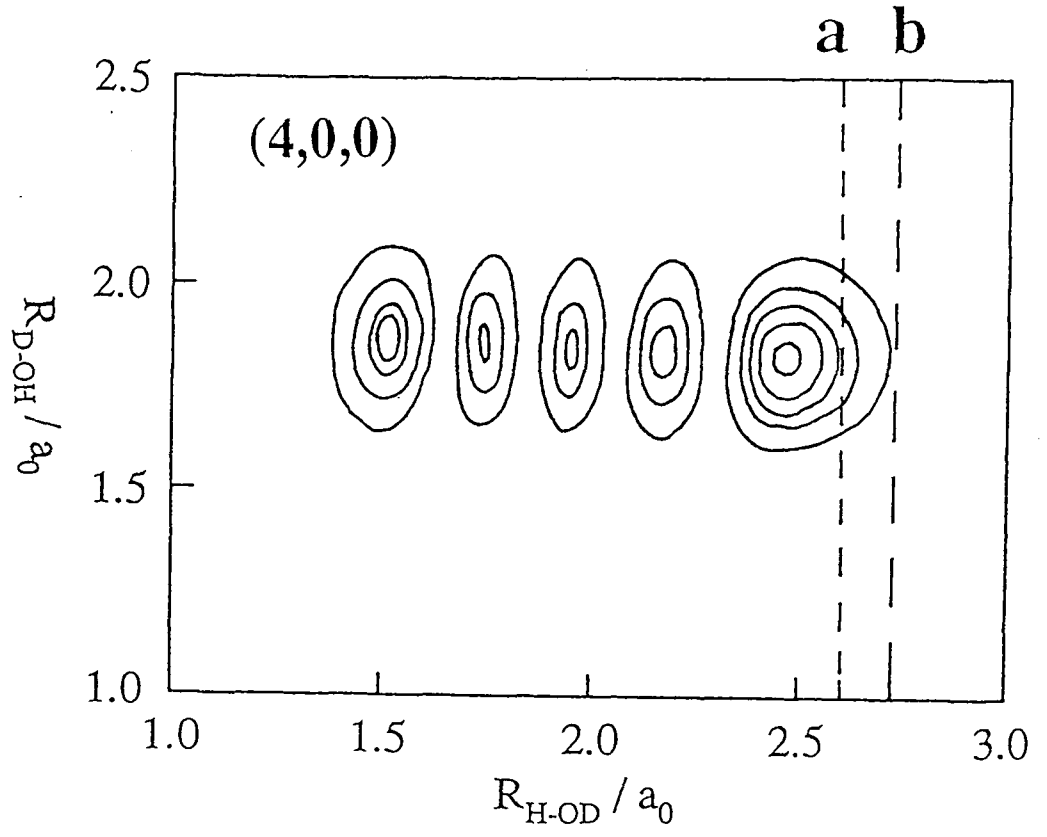

Figure 5.23 Contour plots of the square of the HOD(4,0,0) and (5,0,0) vibrational wavefunctions, plotted against the two stretching coordinates. The approximate average values of R for which excitation from the bound overtone state to the excited electronic state is (energetically) expected and predicted by the modified Franck-Condon model are indicated by the lines labelled **b** and **a** respectively.

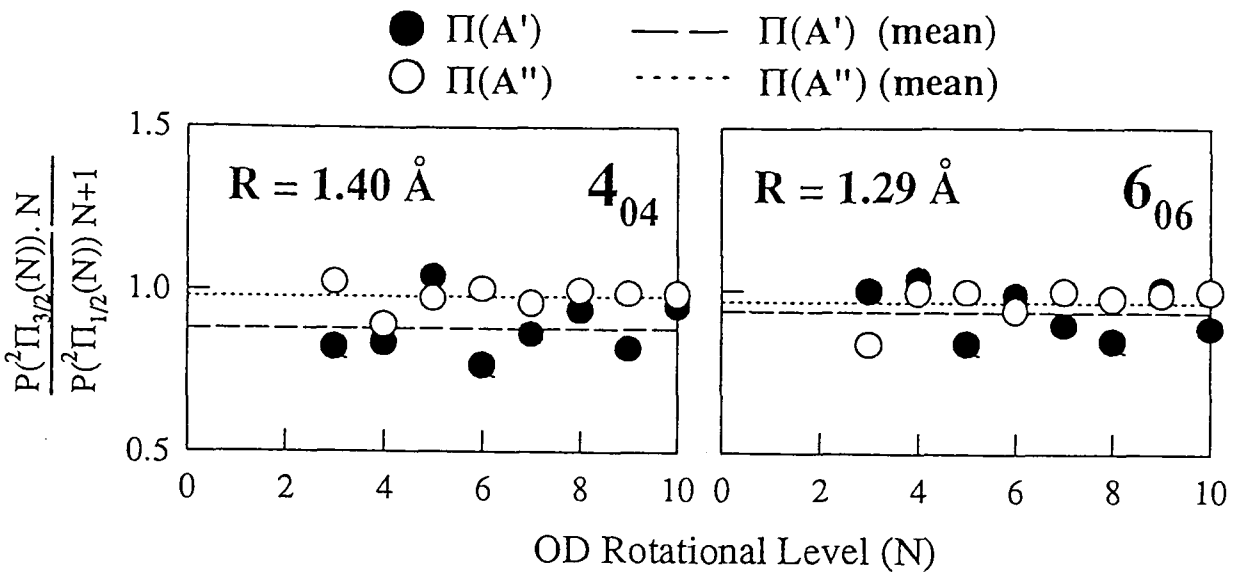

Figure 5.24 The ratio of the calculated population in rotational states in OD $^2\Pi_{\frac{1}{2}}$(N) and $^2\Pi_{\frac{3}{2}}$(N) plotted as a function of N, for HOD $J_{K_a,K_c} = 4_{04}$ (left) and 6_{06} (right), at the values of R for which agreement with the experimental data could be obtained. The spin state populations for the A′ (•) and the A″ (○) lambda-doublet levels and the corresponding mean distribution are also shown.

the Franck-Condon calculations described in section 5.4. The OH product rotational motion in this case will be purely dependent on the zero-point bending motion of the ground state parent molecule. Figure 5.3 clearly shows that the ground state bending potential changes significantly with bond extension, becoming more isotropic with increasing R.

This behaviour can be qualitatively rationalized [123] on the basis of the semiclassical expression for the photofragment distributions, P(j) (closed shell), from the Franck-Condon model of Morse and Freed [146, 254] which has recently been discussed in detail by Schinke and coworkers [41] and Reisler and coworkers [266, 267]. The inclusion of the electronic structure of the photofragments into the Franck-Condon model appears only to have the effect of dampening the rapid oscillations in P(j) once the latter have been averaged over the lambda-doublet levels [41, 34]. This is shown in Figure 5.25 where the Franck-Condon calculated OH rotational distributions for H_2O $J_{K_a,K_c} = 0_{00}$ are plotted for the situation

when the electronic structure of the OH molecule is either neglected or included within the model. The overall form of the rotational distributions, for parent J = 0 are clearly similar to those derived from the semiclassical closed shell expression [145, 252]

$$P(j) \propto \left[\bar{j}\gamma_e + (-1)^k \frac{\pi}{4}\right] . (H_k[\alpha\bar{j}]exp(-1/2\alpha^2\bar{j}^2))^2 \tag{5.25}$$

where k is the bending vibration quantum number,

$$\bar{j} = j + \frac{1}{2}$$

and γ_e is the equilibrium bond angle in water, 104.5°. The constant α in equation 5.25 is defined as

$$\alpha = \left[\frac{\hbar}{I\omega}\right]^{\frac{1}{2}} \tag{5.26}$$

where I is the effective moment of inertia for the bending motion,

$$I = \left[\frac{I}{\mu_{OH}r^2} + \frac{1}{\mu R^2}\right]^{-1} \tag{5.27}$$

and ω is the harmonic frequency of the bending vibration. The rotational distribution can be readily interpreted as arising from the combination of the two terms in equation 5.25. The second term represents half of the square of the harmonic oscillator bending wave function in momentum space, and determines the overall width and shape of the distribution. For intermediate states with zero quanta of bending vibration ($k = 0$), it has a simple Gaussian form of width proportional to $(I\omega)^{\frac{1}{2}}$. This is 'modulated' by the first term which gives rise to the rapid oscillatory structure in P(j) of period $\Delta j \approx \frac{\pi}{\gamma_e}$ for $\gamma < \frac{\pi}{2}$ and $\frac{\pi}{\pi-\gamma_e}$ for $\gamma_e > \frac{\pi}{2}$ [41, 145, 252, 264, 265]. As mentioned in section 5.6.2, the opening and closing bending motion gives rise to equal amounts of counterclockwise and clockwise rotation of the diatomic fragment whose interference gives rise to the oscillations.

The form of the photofragment distributions for H_2O J = 0 depends on two factors, the equilibrium bending angle γ_e and the width parameter α. The bending potentials shown in Figure 5.3 reveal that the equilibrium bond angle in the ground electronic state changes very little with bond extension, so the phase and amplitude of the rapid oscillations in P(j) will be insensitive to R and hence, within the framework of the Franck-Condon model, to the dissociation photon energy. The second factor, α, defined in Equation 5.26, is also

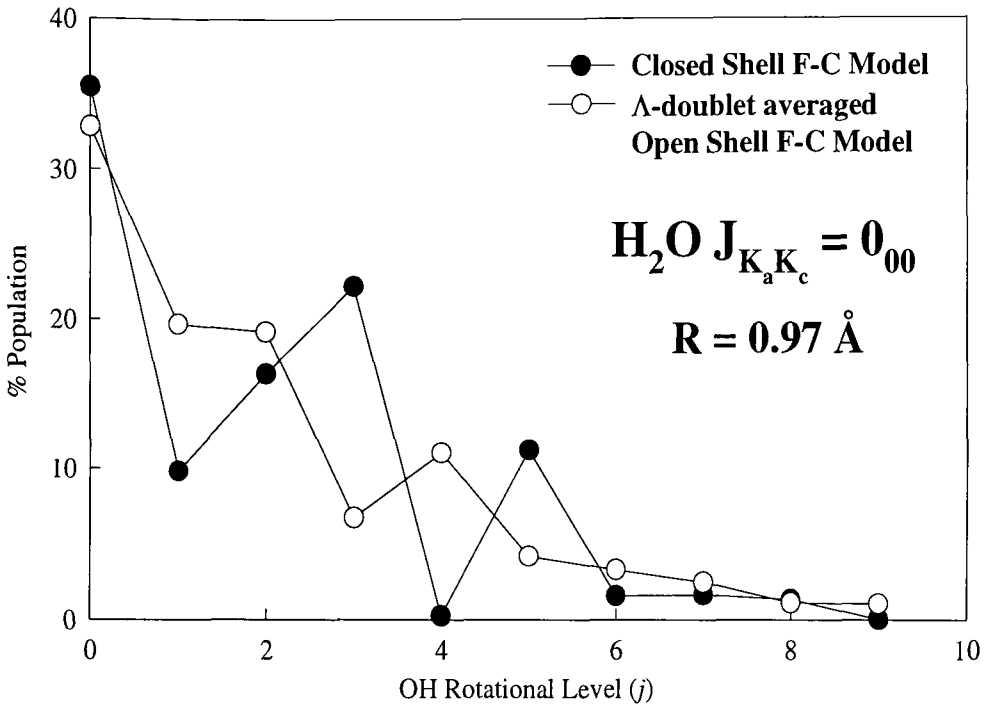

Figure 5.25 The closed shell (semiclassical) and lambda-doublet averaged open shell (neglecting and including the electronic structure of the photofragments) Franck-Condon model calculated OH rotational distribution for H_2O $J_{K_a,K_c} = 0_{00}$, fixing $r \approx R = 0.97$ Å.

insensitive to R in spite of the fact that the bending frequency on the Jensen potential decreases significantly with increasing R (see Figure 5.3). This is shown for $R = 0.97$–1.49 Å in Table 5.4. The variation in ω is almost exactly, but incidentally, balanced by the corresponding increase in the effective moment of inertia, I, with increasing R. The width in the photofragment distribution is therefore also invariant to the bond extension. This behaviour is probably peculiar to the $H_2O(\tilde{X})$ potential energy surface but may be observed for similar AB_2 molecules such as H_2S. The variation in the resulting OH photofragment rotational distributions with R for parent $J > 0$ can therefore not be attributed to the change in the bending potential shown in Figure 5.3. The Franck-Condon calculated OH $^2\Pi_{\frac{3}{2}}$ rotational distributions for H_2O $J_{K_a,K_c} = 4_{04}$, both freezing $V(\gamma)$ at its equilibrium value ($r \approx R = 0.96$ Å) and allowing $V(\gamma)$ to change with bond extension, are shown in Figure 5.26. The bending potential clearly has very little influence on the structure of the fragment rotational distribution arising from the excitation of zero quanta of bending vibration in the intermediate parent ground vibrational overtone state.

Dissociation of higher bending states of water ($k > 0$) is however likely to yield OH dis-

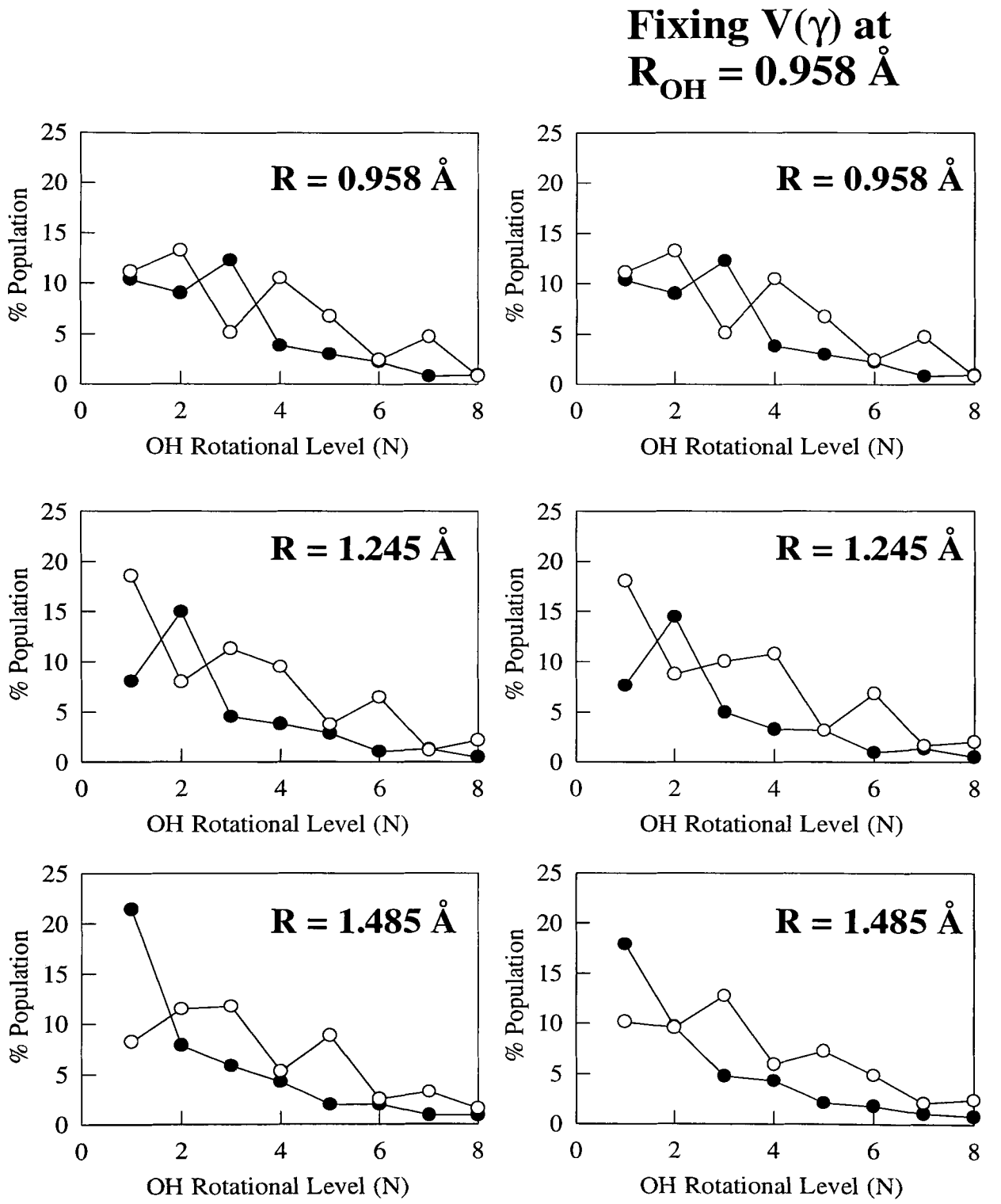

Figure 5.26 The Franck-Condon calculated OH $^2\Pi_{\frac{3}{2}}$ photofragment rotational distribtions for H_2O $J_{K_a,K_c} = 4_{04}$ both freezing V(γ) at its equilibrium value ($r \approx R = 0.96$ Å) (right) and allowing V(γ) to change with bond extension (left).

R (Å)	α	ω (cm^{-1})
0.97	1.00	1612
1.07	1.00	1476
1.19	1.02	1298
1.25	1.04	1205
1.37	1.09	1026
1.49	1.15	866

Table 5.4 The variation of the parameter α, defined in Equation 5.26, and the bending frequency, ω, with the Jacobi length, R. The OH bond length, r, was fixed at 0.97 Å and the values of α are relative to that at $R = 0.97$ Å.

tributions which are more sensitive to the slight changes in α shown in Table 5.4. This is confirmed by the closed shell Franck-Condon calculations for H_2O J=0, $k = 2$, in Figure 5.27, which demonstrates a significant cooling of the photofragment rotational distribution as R is increased, in spite of the minor change in α over the same range. However, the open shell Franck-Condon calculations performed for H_2O $J > 0$, $k = 2$, which did show a cooling of the rotational distribution with increasing R, were unable to reproduce the distributions observed experimentally. Using a value of $R \approx 0.97$ Å(which is very unrealistic) the calculated structures do bear some resemblance to the experimental distribution but are much hotter, shifted up by three values of N (Figure 5.14). This additional cooling of the fragment rotational excitation is reminiscent of the cooling of the photofragment distributions observed previously in the 239.5 nm photodissociation of the J = 0 states of $H_2O|03\rangle|1\rangle^-$ and $|03\rangle|2\rangle^-$ [224], which was ascribed to the influence of the much greater anisotropic regions of the $\tilde{A}$ state potential surface sampled when bending vibration is excited in the parent molecule.

The value of R ($\approx R_e$) employed in the model is however not consistent with the simulations of the VMP of H_2O(k = 0), where long wavelength dissociation has been shown to occur preferentially with extended values of R. In these configurations, the bending frequency is reduced (α is increased) and the fragment rotational distributions will be cooler than at $R = R_e$. The exit channel effects are undoubtedly the primary cause of the cooling of the

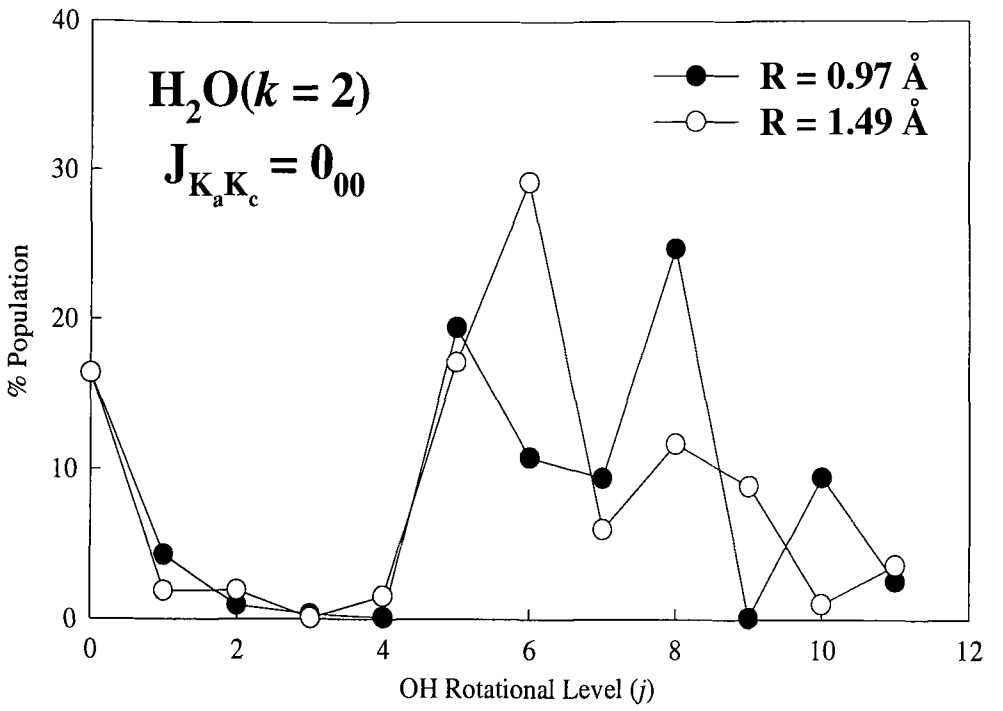

Figure 5.27 The closed shell Franck-Condon calculated OH rotational distributions arising from the dissociation of $H_2O(k = 2)$ J = 0 at R = 0.97 Å(•) and R = 1.49 Å(◦). Note the significant cooling of the distribution with increasing R.

OH distributions produced in the photolysis of H_2O stretch-bend vibrational state. Once this has been included in the theoretical model, by incorporating the $\tilde{A}$ state potential in the calculation, it can be expected (drawing an analogy with the result of the HOD simulation) that (energetically realistic) extended values of R will be needed in order to obtain agreement with the long wavelength experiments. The cooling in the experimental OH fragment rotational distributions may also reflect in part the preferential excitation from extended R configurations.

Insight into the origins of the more complex variations of the OH (and OD from the VMP of HOD) distributions with the intermediate rovibrational level and the dissociation photon energy can also be gained from an examination of the distributions predicted by the closed-shell Franck-Condon model. The calculated distributions for different H_2O J_{K_a,K_c} levels with zero quanta in the bending mode are found to take on a very simple form as the H–OH bond is stretched (Figure 5.28). As R is increased, the distributions arising from levels with $K_a = 0$ and $J > 0$ begin to peak at $j_{OH} = 0$ and become indistinguishable from the J = 0 distribution (see Figure 5.25), while those for K_a = 1,2, · · · show increasingly

prominent peaks at J_{OH} = 1,2, $\cdots$ respectively. Furthermore, as the rotational state of the parent is increased, larger values of R are required for these similarities to become evident.

This behaviour can be explained by the effect that changing R has on the inertial axes and on the Jacobi angle, γ, of the parent molecule. This is shown schematically for H_2O in Figure 5.29(a) and (b). At large values of R, the a-inertial axis lies nearly parallel with the vector **R** between H and OH, and γ is close to 90°. As a consequence, parent rotational motion about the a axis will be mapped directly onto product rotation, whereas rotation about the b and c axes will primarily be mapped onto orbital angular momentum of the departing fragments and will therefore have very little effect on the product rotations. The photofragment rotational distributions in the latter case primarily reflect the influence of the bending motion in the intermediate state and are not significantly influenced by the parent rotational motion.

This hypothesis is confirmed by the data shown in Figure 5.30 in which the square modulus of $\Psi_{\lambda}^{J_i P_i}(\gamma)$, the λ-dependent ground-state parent partial rotating-bending wave functions, are plotted against γ, the Jacobi bending angle, at large R (1.49 Å), for $J_{K_a,K_c} = 4_{22}$ and 4_{23}. $\Psi_{\lambda}^{J_i P_i}(\gamma)$ are defined as

$$\Psi_{\lambda}^{J_i P_i}(\gamma) = \sum_{j} C_{j\lambda}^{J_i P_i} \, . \, Y_{j\lambda}(\gamma, 0) \tag{5.28}$$

in which $C_{j\lambda}^{J_i P_i}$ are the expansion coefficients of the parent bound state wavefunction, defined in Equation 5.14, and λ is the helicity quantum number, the projection of J onto the **R**. At large R, for both $J_{K_a,K_c} = 4_{22}$ and 4_{23}, the rotational excitation of the OH photofragment is primarily caused by the rotational motion of the parent molecule about **R** transferring two units of parent rotational angular momentum onto the OH moiety. The a-inertial axis must therefore lie nearly parallel to **R** and $\lambda \approx K_a$.

Also shown in Figure 5.29 is the corresponding change in the direction of the a axis for HOD. The effect of increasing R is the same as in H_2O, but because of the shift in the centre of mass, R must be extended much further than in H_2O for the a axis to lie parallel to the R vector. Similarities in the OD closed shell rotational distributions for a given value of K_a, but different J, only become evident at much larger values of R.

This closed shell interpretation of the large R dependence of the calculated OH rotational distributions for H_2O J > 0 (and in part for the calculated OD distributions for HOD J > 0

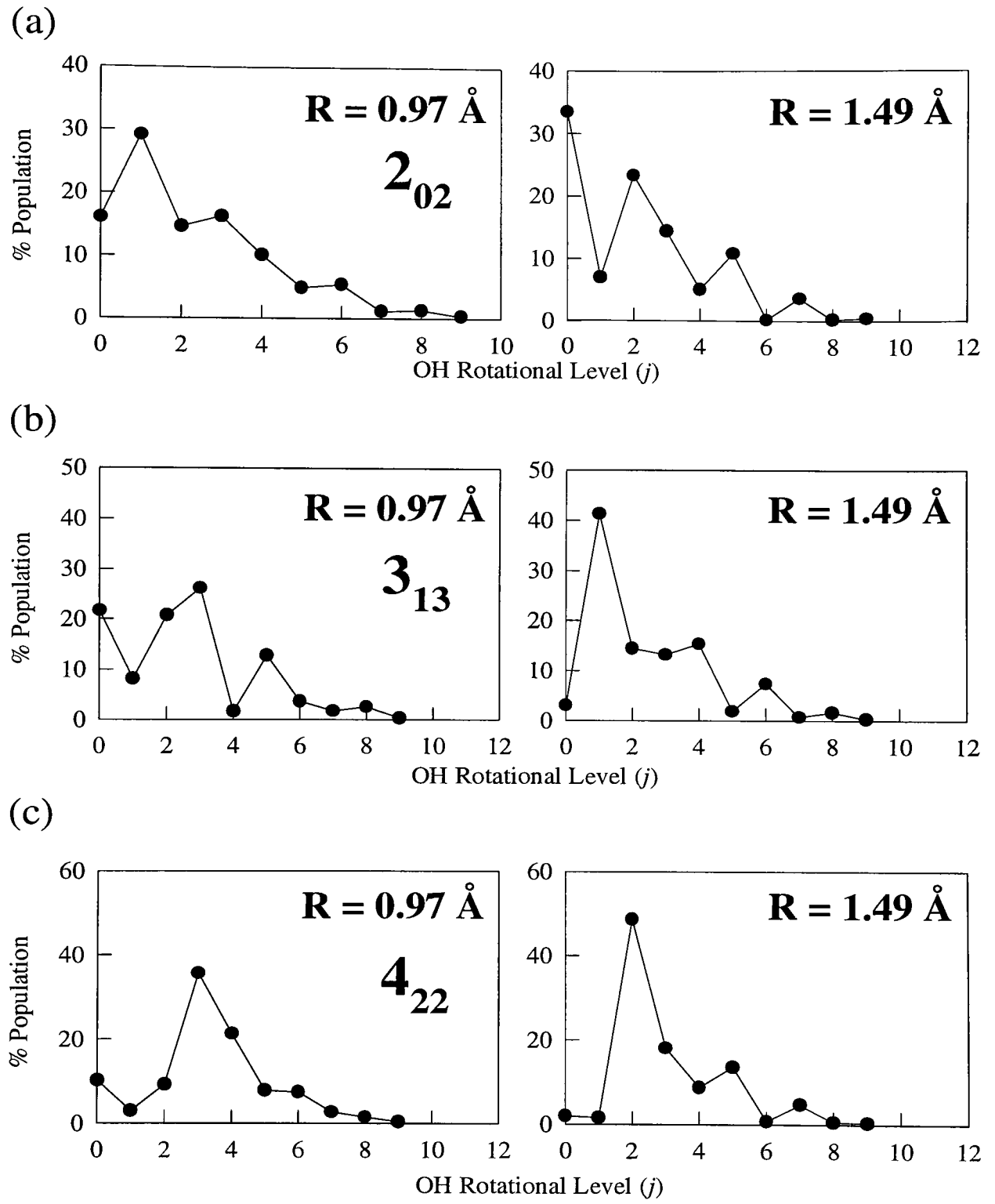

Figure 5.28 Closed shell Franck-Condon calculated OH rotational distributions for H_2O J_{K_a,K_c} = (a) 2_{02}, (b) 3_{13} and (c) 4_{22} at high and low values of R. Note that at high values of R, the distributions predominantly peak at $j_{OH} = K_a$.

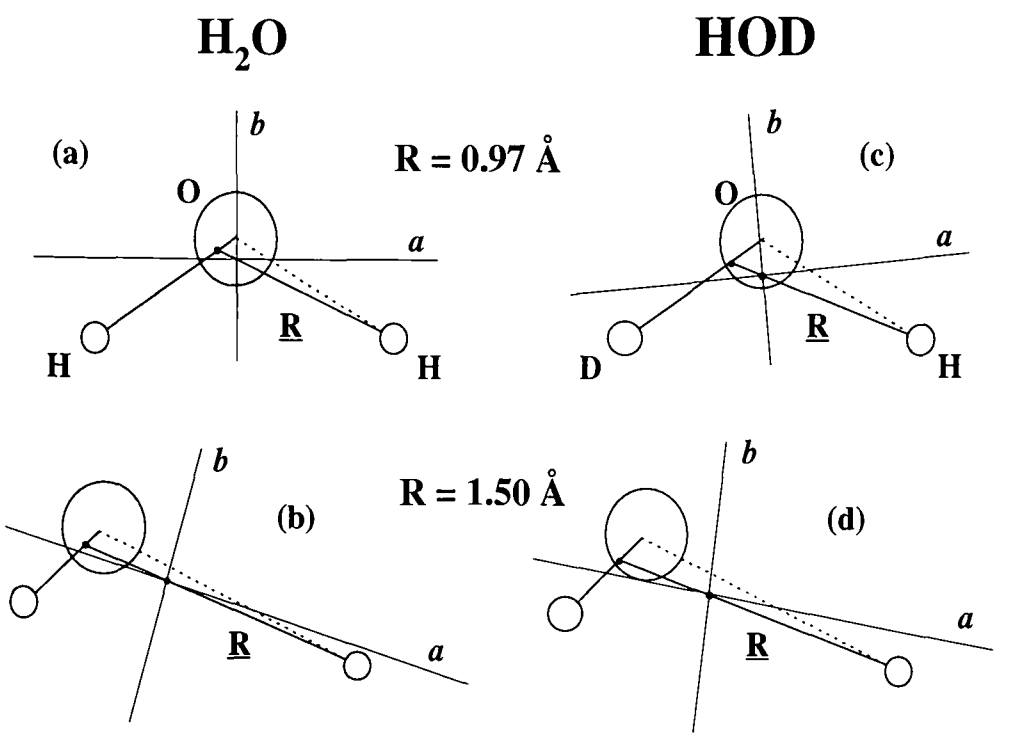

Figure 5.29 The change in the direction of the a inertial axis of the parent molecule, with respect to **R** connecting H and the OH(D) centre of mass, as R is increased for H_2O, (a) and (b), and HOD, (c) and(d).

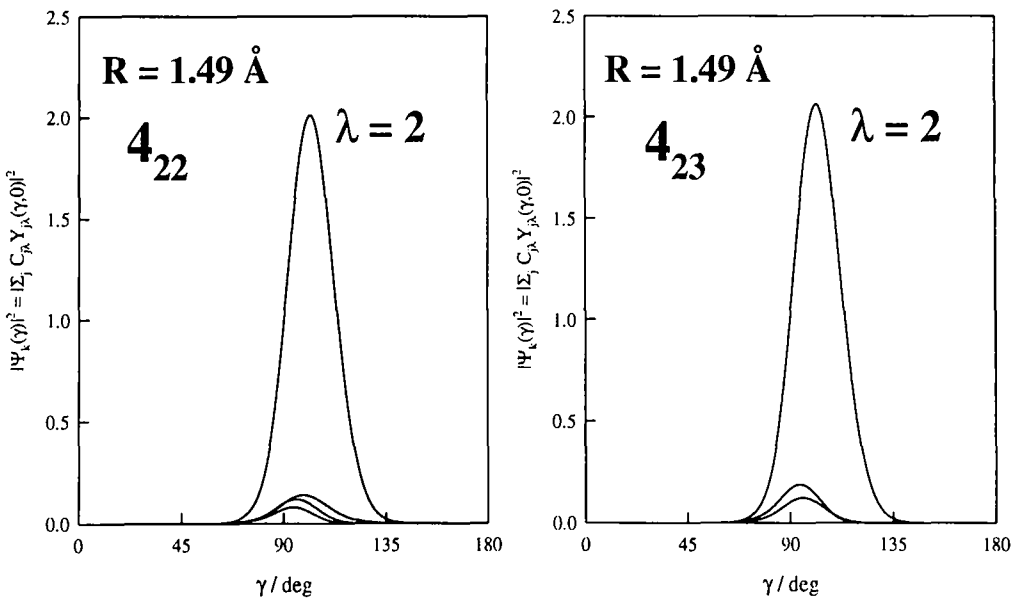

Figure 5.30 The square modulus of $\Psi_\lambda^{J_i P_i}(\gamma)$ the ground state H_2O partial (λ dependent) rotating-bending wave function, at $R = 1.49$ Å, for $J_{K_a,K_c} = 4_{22}$ (left) and 4_{23} (right). The $\lambda = 2$ component in each case has been labelled.

- see below) is supported by inspection of the Hamiltonian for the bound-state rotation-bending motion given in Equation 5.18:

$$\hat{H} = \frac{\hat{l}^2}{2\mu R^2} + \frac{\hat{j}^2}{2\mu_{OH} r^2} + V(R, r, \gamma) \tag{5.29}$$

for which the parity-adapted angular basis functions, given in Equations 5.4 and 5.5 are

$$Y_{j\lambda}^{J_i M_i P_i}(\gamma, \underline{\Omega}) = \frac{1}{\sqrt{2(1+\delta_{\lambda 0})}} [Y_{j\lambda}^{J_i M_i}(\gamma, \underline{\Omega}) + (-)^{J_i + P_i} Y_{j-\lambda}^{J_i M_i}(\gamma, \underline{\Omega})] \tag{5.30}$$

for which

$$Y_{j\lambda}^{J_i M_i}(\gamma, \underline{\Omega}) = \left(\frac{2J_i + 1}{4\pi}\right)^{\frac{1}{2}} Y_{j\lambda}(\gamma, 0)\ D_{\lambda M_i}^{J_i}(\underline{\Omega}) \tag{5.31}$$

The centrifugal and Coriolis coupling matrix elements arising from the $\hat{\mathbf{l}}^2$ diagonal and off-diagonal (same j, different λ) terms, respectively, in Equation 5.29, are given by [257]

$$< j\lambda JMP| \left(\frac{\hat{l}^2}{2\mu R^2}\right) |j\lambda JMP > = \frac{[J(J\ +\ 1)\ +\ j(j\ +\ 1)\ -\ 2\lambda^2]}{2\mu R^2} \tag{5.32}$$

and

$$< j\lambda \pm 1JMP| \left(\frac{\hat{l}^2}{2\mu R^2}\right) |j\lambda JMP > = < j\lambda JMP| \left(\frac{\hat{l}^2}{2\mu R^2}\right) |j\lambda \pm 1JMP >$$

$$= -\sqrt{1\ +\ \delta_{\lambda 0}}\ \frac{F_{\pm}(j, \lambda)\ F_{\pm}(J, \lambda)}{2\mu R^2} \tag{5.33}$$

for which

$$F_{\pm}(x, \lambda) = [x(x\ +\ 1) - \lambda(\lambda\ \pm\ 1)]^{\frac{1}{2}} \tag{5.34}$$

Both of these matrix elements depend upon $1/R^2$ and will therefore be switched off as R increases, leaving only the potential matrix elements[9], [257]

$$V_{j'\lambda', j\lambda}^{JMP} = \delta_{\lambda'\lambda}\ 2\Pi \int_0^{\Pi} Y_{j'\lambda'}(\gamma, 0)^* V(\gamma) Y_{j\lambda}(\gamma, 0)\ \sin\gamma\ d\gamma \tag{5.35}$$

(V(γ) is the interaction potential at a given value of r and R) and the matrix elements arising from $\hat{\mathbf{j}}^2$,

$$< j\lambda JMP| \left(\frac{\hat{j}^2}{2\mu_{OH} R^2}\right) |j\lambda JMP >= \frac{j(j\ +\ 1)}{2\mu_{OH} r^2} \tag{5.36}$$

[9] which are diagonal in λ [257]

Although both of these quantities are independent of J, the former depends upon λ, the component of J (and j) about **R**. As R increases, the overall rotational motion of the ground state water becomes more prolate-top in character, with $\lambda \simeq K_a$, and the sum over λ in the expansion of each bound state wave function (see Equations 5.3 and 5.16) reduces to a single term with $\lambda = \mathrm{K}_a$. At large values of R, all parent rotational states with $\mathrm{K}_a = 0$ will generate product rotational distributions similar to those for J = 0, which simply reflects the zero-point bending motion in the intermediate state prior to excitation to the $\tilde{\mathrm{A}}$ state. Similiarly, dissociation of states with $\mathrm{K}_a > 0$ will generate distributions similar to those for $\mathrm{K}_a = 0$, but shifted by the component of J about the a inertial axis, which lies approximately parallel to **R**. In both the closed shell and open shell calculations for H_2O (and HOD using the modified F-C model), the switch to the simple behaviour described occurs at rather modest values of R, particularly for low J: The $\mathrm{J}_{K_a,K_c} = 2_{02}$ OH distributions, for example, become very similar to those for $\mathrm{J}_{K_a,K_c} = 0_{00}$ at $R \approx 1.37$ Å and, even for $\mathrm{J}_{K_a,K_c} = 4_{04}$, the similarities are clearly evident at 1.5 Å (see Figure 5.31).

The modified Franck-Condon model simulation of the OD photofragment rotational distributions arising from the VMP of HOD provide additional insight into the factors which affect the product distributions and their variation with increasing R, (that is, with increasing OH stretching quanta in the intermediate overtone level and decreasing photon energy). Including the effect of the small torque applied by the departing H atom on the OD photofragment on the $\tilde{\mathrm{A}}$ state surface, the prediction of the modified Franck-Condon model was able to qualitatively simulate the experimental distributions, employing energetically realistic values of R for all of the initial HOD rotational states. This result may also provide an explanation for the values of R required in the original Franck-Condon model to simulate the OH distributions obtained in the VMP of H_2O from this and the previous studies [34, 165, 201], which are smaller than expected, and fluctuate over a considerable range ($\sim$ 0.2 Å). The Balint-Kurti Franck-Condon model was shown to (poorly) reproduce the experimental OD rotational distributions from the VMP of HOD (Section 5.6.2), using values of $R \sim 0.97$ Å , much smaller than those required in the H_2O simulations. The torque produced in HOD dissociation transfers approximately one unit of angular momentum onto the rotating OD fragment, whereas in HOH dissociation, it transfers the equivalent of approximately 0.7–0.8, which the modified Franck-Condon model cannot accommodate. This would suggest that the OH photofragment rotational distributions in the H_2O study are

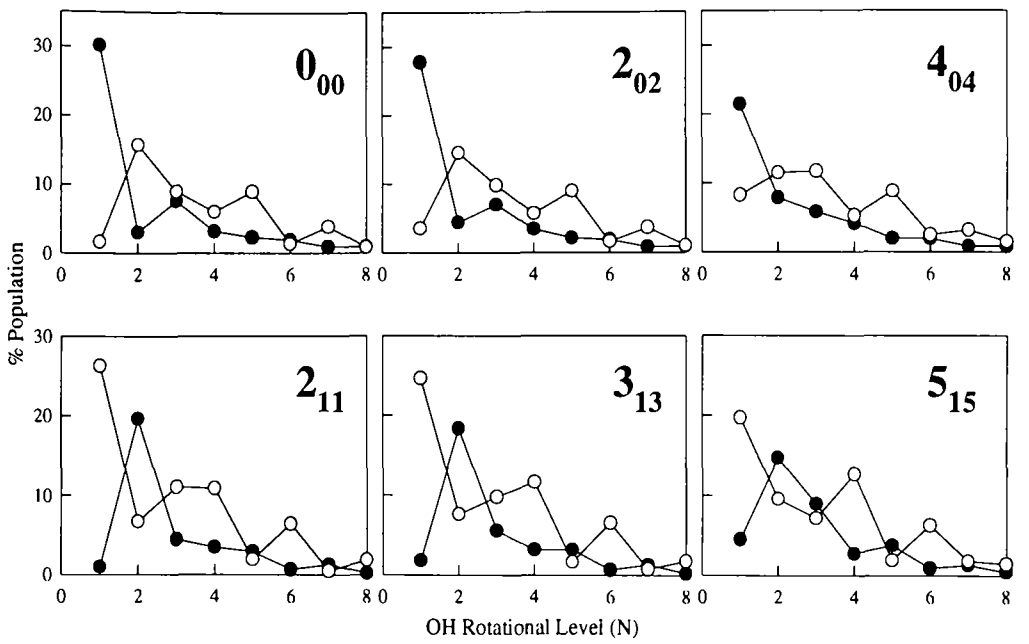

Figure 5.31 Calculated open shell photofragment rotational distributions arising from the dissociation of H_2O in the rotational levels shown and employing $R = 1.49$ Å. Note the similarity on the $K_a = 0$ (top) and $K_a = 1$ (bottom) distributions for different values of J (the change in the phase of the lambda-doublet population oscillations is due to the change in the parity of the parent rotational states, even (top) or odd (bottom)).

influenced by the impulsive torque exerted during the dissociation, but to a lesser extent than the OD fragment in HOD photolysis. It is also interesting to note that in addition to the modification of the oscillatory structure within the fragment lambda-doublet distribution, the impulsive torque causes a very slight 'cooling' of the overall rotational motion of the fragment, which is reflected in the rotational temperatures shown in Table 4.4.

In summary, the variation in the calculated photofragment rotational distributions with increasing R (and hence the analogous variations in the experimental OH distributions with decreasing photon energy and increasing OH stretching quanta in the intermediate overtone level), primarily reflect the switching off of the centrifugal and Coriolis coupling terms which depend on $1/R^2$ in the ground state rotation-bending Hamiltonian and the change in the rotational character of the water molecule from a highly asymmetric rotor at $R = R_e$ to a near prolate rotor at large R. The actual phase and oscillatory structure of the lambda-doublet population distributions, for a given value of R, is then determined by

these two factors and by an underlying influence of a small exit-channel torque imparted by the departing atomic fragment on the molecular moiety during the dissociation.

The calculated Franck-Condon distributions still do not quantitatively match the experimentally observed product rotational distributions, even when an approximation for the small exit-channel torque is included in the model. The correct trends have been predicted and assigned to some of the factors involved in the parent dynamics on both the ground and excited potential surfaces. The other likely factor is the crudity of the some of the approximations made in both the original and the modified Franck-Condon model. The OD photofragment rotational distributions calculated using the modified Franck-Condon model were consistently unable to model the experimental population distributions, in both lambda-doublet states, for N = 1 and 2. This was rather surprising considering that the model performed very well for N > 2. The additional angular momentum, J_t, transferred onto the OD molecule by the impulsive torque, was estimated at between ~ 1 and ~1.2 units of angular momentum (see Section 5.6.2). Fixing J_t at the value of 1 in the model, considering the sensitivity of the distributions to a small exit-torque, is therefore not a good approximation, and a 2- or 3-dimensional[10] calculation, including the excited state PES, is needed to fully account for this effect.

The need for a proper treatment of the excited electronic state is perhaps also illustrated in the experimentally observed preferential population of the OH $^2\Pi_{\frac{1}{2}}$ spin orbit states arising from the VMP of H_2O, but only for the A′ lambda-doublet. A preferential population of a fragment spin-orbit state reflects either the spin-orbit coupling in the fragments or a final state interaction [15, 26, 34, 54, 127, 269]. In the absence of a final state interaction, the experimentally observed spin-orbit population distributions should match those determined by a Franck-Condon model that takes a proper account of the electronic structure of the photofragments; in theory, the Balint-Kurti model [233] is an example. In practice, the Balint-Kurti model is successful in predicting the relative OH lambda-doublet population distributions and their dependence on R; however, the model underestimates the preference for the $^2\Pi_{\frac{1}{2}}$ spin-orbit state observed experimentally using the A′ lambda-doublet population distributions. Within the experimental error, a statistical OH spin-orbit population is observed and calculated if the A″ lambda-doublet distributions are used. This would suggest

[10]The present calculation is classed as being 1-dimensional, ignoring the excited state potential and freezing the vibrational coordinate, r.

that the problem does not lie in the angular momentum coupling scheme employed by Balint-Kurti, but with the influence of a final state interaction which is neglected in the (Balint-Kurti) Franck-Condon model.

The experimentally observed OH spin-orbit state distributions from the 157 nm [34, 212] and 193 nm [165] photodissociation of ground state H_2O indicate a near-statistical population if the A″ data is used, but a slight preference for the $^2\Pi_{\frac{3}{2}}$ spin state if the A′ data is used. Initially exciting one quantum of stretch into the water molecule prior to 193 nm photolysis [34, 165] (moving the Franck-Condon region on the excited PES further into the exit channel) indicates a near-statistical spin-orbit population distribution using both the A′ and A″ data. The VMP studies of H_2O presented in this thesis preferentially excite the state selected parent molecule even further into the exit channel. There appears to be an energy dependence on the relative population of the OH photofragment spin-orbit states which would be consistent with a spin-orbit interaction of the initially prepared singlet state with a nearly triplet state [11]. Ab-initio molecular electronic structure calculations certainly show that there is a triplet state with the same A″ symmetry as the prepared singlet state, which also correlates with the $H(^2S) + OH(^2\Pi)$ photofragments. The Balint-Kurti model only connects the (assumed isotropic) $^1A''$ state with the electronic wavefunctions of the photofragments. A more precise measurement of the energy (or R dependence) of the OH fragment spin-orbit distributions would therefore be very useful in clarifying this, as yet speculative, exit-channel electronic-state interaction.

The assumption that dissociation occurs at fixed values of R is also clearly not a realistic approximation. First, excitation is likely to occur from a narrow range of R values and a proper treatment of the R dependence of the bound state radial functions, $\Phi_{vj\lambda}^{J_i P_i}(R)$, can be included within the model. The good qualitative agreement found in the simulations would, however, suggest that this would only modify the calculated distributions very slightly and, once the effect of the exit torque is included, the fragment rotational distributions will be dependent on only a narrow range of R values, which will be the same for all intermediate parent angular momentum states (for a given intermediate vibrational state and photolysis energy). This approximation, as discussed in section 5.3, also neglects to consider dynamic Coriolis coupling and Fermi resonances between stretching and bending levels in the bound-

[11] Of course, depending on the R dependence of the strength of a singlet-triplet state spin-orbit coupling in the exit-channel, excitation from the ground state may occur directly into the triplet state or singlet state.

state water. The former might be expected to lead to a systematic deviation from the simple theory with increasing parent molecular rotational state. Over the range of J_{K_a,K_c} states selected, no such systematic behaviour is observed for H_2O and HOD. Examining the rotational spectra of the vibrational overtones excited in both H_2O and HOD (see Sections 3.2 and 4.2), there are no obvious signs of Fermi resonances occuring within the range of J_{K_a,K_c} selected in this study.

Alternatively, the origin of the discrepancies may lie in the neglected consideration of anti-symmetrization of the H_2O wave functions due to the equivalence of the two H atoms (see Section 5.3); this is of course not important in HOD dissociation. The intermediate bound H_2O overtone wave functions selected by this study and by Andresen and coworkers [34] and Crim and coworkers [201, 224] can be written in the local mode nomenclature [175] as

$$\Psi_{-}^{v} = \frac{1}{\sqrt{2}}(\Psi_{0v(1)} - \Psi_{v(2)0}) \tag{5.37}$$

in which $\Psi_{0v(1)}$ refers to the excitation of v quanta of stretching vibration in the O–H(1) bonds and 1 labels the H atom; $\Psi_{v(2)0}$ similarly refers to excitation of the O–H(2) bond. Taking into account the degeneracy of the dissociation channels, the photofragment wave functions can be written as the symmetric and antisymmetric combination of the individual channel-scattering wave functions (which are used in the Balint-Kurti/Shapiro formalism [254]):

$$\Psi_{\pm}^{f} = \frac{1}{\sqrt{2}}(\Psi_{H(1)+OH(2)} \pm \Psi_{H(2)+OH(1)}) \tag{5.38}$$

in which $\Psi_{H(1)+OH(2)}$ refers to the channel which breaks bond 1 to produce H(1) and OH(2). The measured cross-section is then given by

$$\begin{aligned} \sigma^{-} &\propto |\langle \Psi_{\pm}^{f} | \Psi_{-}^{v} \rangle|^2 \\ &= \frac{1}{4} |\langle \Psi_{H(1)+OH(2)} | \Psi_{0v(1)} \rangle - \langle \Psi_{H(1)+OH(2)} | \Psi_{v(2)0} \rangle \\ &\quad \mp \langle \Psi_{H(2)+OH(1)} | \Psi_{v(2)0} \rangle \pm \langle \Psi_{H(2)+OH(1)} | \Psi_{0v(1)} \rangle|^2 \end{aligned} \tag{5.39}$$

However, the two dissociation channels, producing H(1) and H(2) are equivalent and the photodissociation cross-section can be written as

$$\sigma^{-} \propto |\langle \Psi_{H(1)+OH(2)} | \Psi_{0v(1)} \rangle - \langle \Psi_{H(1)+OH(2)} | \Psi_{0v(2)} \rangle|^2 \tag{5.40}$$

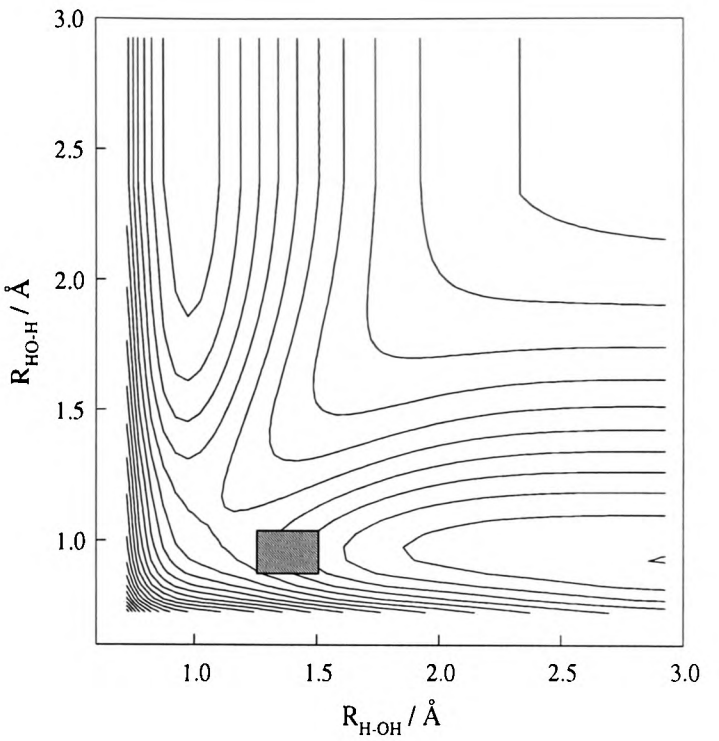

Figure 5.32 Contour plot of the $\tilde{A}$ state potential energy surface calculated by Steammler and Palma [230] at $\gamma = \gamma_e$. The shaded areas on the figure represent the regions of the surface that will be sampled by the VMP experiments presented in this thesis and in the previous studies of Andresen and coworkers [34], Crim and coworkers [201, 224] and Rosenwaks and coworkers [165].

The experiments of Rosenwaks and coworkers [165] excite a symmetric local mode state in the intermediate H_2O,

$$\Psi_+^v = \frac{1}{\sqrt{2}}(\Psi_{0v(1)} + \Psi_{v(2)0}) \tag{5.41}$$

and the photodissociation cross-section is therefore given by

$$\sigma^+ \propto |\langle \Psi_{H(1)+OH(2)} | \Psi_{0v(1)} \rangle + \langle \Psi_{H(1)+OH(2)} | \Psi_{0v(2)} \rangle|^2 \tag{5.42}$$

The first term in equations 5.39 and 5.42 is the overlap integral which is used in the Franck-Condon model to calculate the photofragmentation cross-section. The antisymmetrization of the H_2O wave functions therefore produces an additional interference term which arises when the O–H bond that is not vibrationally excited, is broken instead of the vibrationally excited bond. Terms will only be non-zero when the photolysis photon is of high enough energy to excite the ground state above the barrier for hydrogen exchange. For the experiments presented here, and for the previous studies, excitation into the $\tilde{A}$ state will occur

preferentially into the dissociation channel of the bond that is excited, at an energy well below the barrier (see Figure 5.32). The interference term is therefore likely to be negligible and the neglect of antisymmetrization will have little or no effect on the photofragment rotational distributions. This would have been confirmed if Rosenwaks and coworkers [165], photodissociating $H_2O|01\rangle^+$ at 193 nm, had reported an OH distribution arising from a parent J_{K_a,K_c} state which was selected by Andresen and coworkers [34], who photodissociated $H_2O|01\rangle^-$ with 193 nm radiation. Unfortunately this was not the case, but the overall level of agreement between the Franck-Condon calculations and the distributions from both experiments is comparable, suggesting that $\sigma^- = \sigma^+$.

5.8 Conclusions

H_2O molecules, rotational state selected in the $|04\rangle^-$, $|05\rangle^-$ and $|04\rangle|2\rangle^-$ stretching overtone levels, have been photodissociated at $\sim$ 282 nm *via* the $\tilde{A}$ state. The photofragment OH rotational distributions are found to vary with the number of quanta of OH stretch excited in the intermediate state, and in comparison with previous work on H_2O at higher photon energies [34, 201, 165], with the photodissociation wavelength. Model Franck-Condon calculations using the theory of Balint-Kurti [233] qualitatively reproduce the observed trends, provided that dissociation at the lower photon energies and *via* higher overtone excited intermediate states is assumed to occur preferentially at extended values of the H–OH distance, R. The calculations also suggest that the primary cause of the variation in the photofragment rotational distributions lies a the gradual change in the inertial properties of the bound state water molecule (rather than in the softening of the bending potential) as the H–OH bond is stretched.

In a second study, HOD molecules rotational state selected in the (4,0,0) and (5,0,0) OH stretching overtone levels have been photodissociated at $\sim$ 288 nm *via* the $\tilde{A}$ state. A branching ratio between the H + OD and D + OH dissociation channels is estimated to be $\Phi(OD)/\Phi(OH) > 20$, which compares well with the previous experimental study of Crim and coworkers [202, 203] and the theoretical work of Imre and coworkers [241]. The small shift in the centre of mass arising from the deuterium is shown to have a marked effect on the rotational distributions of the OD photofragments, which are more sensitive to the exit-torque applied by the departing H atom than are the OH distributions produced in

H_2O dissociation. Calculations using a modified Franck-Condon model, which includes an approximate exit-torque, are able to reproduce qualitatively the experimental distributions at values of R that are in agreement with those expected energetically, based on the current knowledge of the $\tilde{X}$ and $\tilde{A}$ potential energy surfaces. These calculations indicate that, in addition to being sensitive to the small changes in the ground state dynamics of the parent molecule, the OD photofragment rotational distributions (and to a lesser extent the OH distributions from the VMP of H_2O) are also sensitive to the small final-state interaction on the dissociative potential surface.

Finally, it is perhaps worth suggesting further areas of potential study using this 'benchmark' photodissociation system. A full 2- or 3-dimensional calculation of the photofragment rotational distributions will be valuable in helping to ascertain the origin of the more subtle differences found between the Franck-Condon calculated and the experimentally observed OH rotational distributions. The OH rotational distributions obtained in this and the previous study of Andresen and coworkers [34], photolysing $H_2O(n\nu_{OH})$ J=0, are not well reproduced by the Franck-Condon model of Balint-Kurti. This would strongly suggest that a better account of the potentials involved in the photodissociation dynamics is needed or that the treatment of the open-shell nature of the photofragments in the model [233] is inadequate. To use the experimental data as a test of either the potentials or the Balint-Kurti open shell formalism [233], then a full 2- or 3-dimensional is essential. An investigation into the puzzling discrepancy between full ab initio calculated [40] fragment vibrational distributions and the experimentally measured distributions [222, 223, 201] is also long overdue. The evidence to date suggests that the error lies in the widely used calculated $\tilde{A}$ state potential surface. The calculations of Schinke and coworkers [40] showed that the OH vibrational distribution was extremely sensitive to the surface. The experimental observation of less vibrational excitation than predicted would suggest that the barrier height on the $\tilde{A}$ state is too low, but adjusting this variable to correctly predict the vibrational distribution would ruin the excellent agreement with the experimental absorption spectrum. The discrepancy between the experimentally measured state-to-state HOD dissociation channel branching ratio and those predicted by theory also suggest that there is a problem with the barrier on the $\tilde{A}$ state. Selecting an intermediate O–H stretching overtone, the predicted [241] branching ratio dependence on the subsequent photolysis energy agrees very well with the measurements of Crim and coworkers [202] and with the present study [123]. However,

selecting an intermediate O–D stretching overtone, the photon energy dependence of the preferential OH + D production branching ratio differs from the experiment of Rosenwaks and coworkers [168].

Chapter 6 The Temperature probing of cool flames

This chapter is concerned with experiments carried out in Oxford and at Thornton Research Centre (TRC) using photoacoustic spectroscopy to measure the rotational temperature of water molecules contained within a stabilised cool flame produced in the autoignition of an hydrocarbon/air mixture. This technique was used with great success in the vibrational mediated photodissociation experiments presented previously; this chapter describes the evaluation of its sensitivity as a potential temperature probe, working under very different experimental conditions.

6.1 Introduction

The autoignition of hydrocarbon/air mixtures is a process of significance in several practical situations. It may constitute a hazard in the handling of fuels, it is essential for the operation of diesel engines, and by causing the phenomenon of 'knock', is a major constraint in the design of spark ignition engines and the fuels to use in them. The tendency of a given hydrocarbon fuel to 'knock' is measured by its octane number and, as it is advantageous for car engines to operate as close as possible to 'knocking' conditions, there has been a vast amount of research conducted into the prediction of the autoignition properties of a given fuel mixture within an engine. Much of the early research was concerned with the characterisation of the phenomenological aspects of autoignition - cool flame appearance, negative temperature coefficient regions (decreasing rate of reaction with increasing temperature), two-stage autoignitions, product formation at low temperatures - and primary kinetic schemes were built to reproduce the observed phenomena [270]–[272]. More recently, interest in hydocarbon oxidation studies has been revived, with the emphasis on modelling at high pressures to reflect engine-relevant conditions. Much of this work has been thoroughly reviewed over the past few years [273]–[276].

The chemical mechanism for the oxidation of hydrocarbons is complex [272, 277, 278] and in order to investigate engine 'knock', a model must reflect the fact that the end gases in

the combustion chamber pass through different distinct initial temperature regimes during their ignition process, and in each regime, different chemical reactions dominate the ignition reaction [279]. The low temperature regime (below about 700 K) is characterised by a two-stage ignition process ('mild' followed by 'strong' ignition [280]) and a linear increase of the reaction rate and ignition delay time with temperature. The kinetic processes at these temperatures are dominated by

$$RH + OH \rightarrow R + H_2O \tag{6.1}$$

$$R + O_2 \rightleftharpoons RO_2 \tag{6.2}$$

and the internal transfer of H atoms within the RO_2 radicals to produce peroxy olefin radicals,

$$RO_2 \rightleftharpoons QOOH \tag{6.3}$$

The subsequent reactions of the QOOH species lead to chain branching and acceleration of ignition, particularly through the production of OH radicals.

The second temperature regime is between 700–900 K, and is characterised by a transition from a two-stage to a one-stage ignition with increasing temperature and a negative temperature coefficient, caused by a transition from a low-temperature to a high-temperature kinetic mechanism [281]–[284]. The reactions of the HO_2 radical are particularly important here and the dominant chain branching sequence includes:

$$Fuel + HO_2 \rightleftharpoons Radical + H_2O_2$$

$$H_2O_2 \rightleftharpoons OH + OH \tag{6.4}$$

In the high temperature regime, above about 900 K, autoignition is only a single ignition process and the reaction rate linearly increases again with increasing temperature. Alkyl radicals quickly decompose at these temperatures and hydrogen atom chemistry is important, with chain branching primarily produced in the single step

$$H + O_2 \rightleftharpoons O + OH \tag{6.5}$$

The end gases produced in the combustion chamber of the engine are usually at temperatures as high as 1000 K before autoignition occurs. The reactions in the low temperature regime

are considerably slower than at higher temperatures, but because the end gases spend a considerable fraction of their preignition history at these relatively low temperatures, the reactions that take place earlier in the cycle play an important role in governing whether or not autoignition will occur, by generating heat and intermediate products. An accurate evaluation of the temperature and molecular product composition within cool flames at these low initial temperatures is therefore an important aid to the interpretation of the chemistry of auto-ignition processes under engine-relevant conditions.

During the past 15 years, effort have been made to develop laser-based measuring techniques as precise, time- and space-resolved, non-intrusive tools for the investigation of laboratory flames and practical combustion systems [161], [285]–[288]. Laser-induced fluorescence techniques have proved very attractive methods for the measurement of number densities of radical and atomic species at low concentrations and temperatures. In particular, LIF has the capability to be applied in a two-dimensional excitation and detection scheme to determine concentration and temperature fields in turbulent flow [289, 290]; however, the high pressure environments commonly encountered in flame studies restrict their accuracy and, therefore, their suitability for such measurements. Under these conditions, rapid quenching and relaxation processes compete with fluorescence and lead to perturbations of the spectral intensities, which are the signatures of temperature and composition. The ideal spectroscopic probe is clearly either one which has a short interrogation time compared with the time between collisions (which is typically > 10 ps) or one which is unaffected by the influence of quenching. Two such techniques which meet one of these requirements are

- Non-Linear Spectroscopy - SRS, CARS and LIGS and
- Photoacoustic Spectroscopy

6.1.1 Non-linear spectroscopy

In the last 5 years, spontaneous Raman scattering (SRS), Coherent Anti-Stokes Raman Scattering (CARS) and LIGS (laser-induced grating spectroscopy) have been found to be very useful techniques for measuring the temperature of flames [161, 285, 288]. The main advantage of SRS and CARS for application in combustion flames is the fact that the Raman signal is not influenced by quenching and in fact increases with pressure. It has also been shown that collisional quenching has little effect on the LIGS signal levels [291]. The scattering nature of the signal for all three techniques does however limit the accuracy

of their temperature measurements to clean, stable non-sooted flames. In addition, the relationship between the SRS, LIGS and CARS signal intensity and the determination of a population is often very complicated [121, 161, 286] and restricts the precision of a calculated temperature.

6.1.2 Photoacoustic spectroscopy

Photoacoustic spectroscopy is a highly sensitive and accurate method of recording rovibrational transitions in gas phase molecules and is frequently used in the detection of high overtone levels [8]. As mentioned in Section 2.3, this technique involves the thermal formation of pressure waves in the gas due to the absorption of laser radiation by the molecules; these waves are then detected with a microphone. The fact that the signal is formed on absorption of laser radiation means that the effect of any perturbation from rapid quenching and relaxation (within a cool flame) on the recorded rovibrational spectra will be negligible. Modelling these spectra will give a realistic value for the rotational temperature of the molecule in question.

6.2 Evaluation of photoacoustic detection under near-cool flame conditions

The usual conditions employed in photoacoustic detection require the gas of the molecule in question to be at a pressure equal to its vapour pressure under vacuum, in an enclosed environment, and the detector placed $\sim$ 5 mm from the focus of the laser beam passing through the gas. In the VMP study of H_2O presented in Chapter 3, this has been found to be sufficient to give a signal-to-noise ratio of at least $\sim$ 100:1 for the third stretching overtone. Within the laboratory cool flame apparatus (see Section 6.4), the experiments are carried out under atmospheric conditions. The microphone obviously cannot be placed too close to the flame, and because of the environment, there will be many heat (pressure) waves already present, in addition to the signal pressure wave. Nevertheless, this technique has an important attribute which proves to be very important under the proposed experimental conditions; it involves the use of pulsed laser radiation. In conjuction with a gated boxcar integrator for data collection, this means that only the pressure waves due to molecular absorption of the radiation are detected; any other 'interferences' can be gated out with minimal information loss.

Using the experimental setup described in Chapter 2, a portion of the third stretching vibrational overtone of water was recorded photoacoustically under three different conditions. These are shown in Figure 6.1. It should be noted that all of the spectra have been separately normalised to the most intense transition. The spectrum in Figure 6.1(a) was recorded under the usual experimental conditions, $\sim$ 17 Torr of H_2O (the vapour pressure), with the microphone $\sim$ 5 mm away from the laser beam. The boxcar integrator (Stanford Research System SR 250) gate width was set at a delay of 110 μs and a width of 15 μs (the maximum setting of the gate width with the boxcars used). The second spectrum, shown in Figure 6.1(b), was recorded under the same pressure conditions as Figure 6.1(a), but the detector was placed 50 mm away from the laser beam. This was estimated to be the closest distance at which a microphone could be placed next to a cool flame and remain operable close to room temperature conditions. The boxcar integrator gate width was kept at 15 μs but the delay was extended to 540 μs, reflecting the different arrival time of the pressure wave (see below). The only noticable effect of moving the detector away from the laser beam was to drop the signal level by a factor of about two.

The spectrum shown in Figure 6.1(c) was recorded under the same pressure and 'spatial' conditions expected in the cool flame experimental setup (see Section 6.4), keeping the detector 50 mm away from the laser beam and using a 2.6 % mixture of water in air, with a total pressure of 760 Torr. Under these pressure conditions, the signal wave ($\sim$ 20 kHz frequency [1]) was superimposed on a much larger waveform (an order of magnitude in ampitude) which was a superposition of various similar frequency waves ($\sim$ 0.1 kHz) produced by the vibration of equipment in the laboratory; this is shown schematically in Figure 6.2. By virtue of the much higher frequency of the signal, the noise was easily removed by the $>$ 10 kHz frequency filter built into the boxcar integrator. The net result of the increased noise level of photoacoustic detection under these pressure conditions was a small, constant shift in the baseline of the recorded spectrum. This is indicated in Figure 6.1(c) by an arrow where the major noise source (a rotary vacuum pump) was switched off for a few seconds. The signal level in Figure 6.1(c) was found to be four times smaller than signal under ideal conditions for photoacoustic detection (Figure 6.1(a)).

Preamplification of the noise filtered signal before gated collection should therefore produce

[1] The frequency and the modulated growth and decay of the waveform is probably a mechanical response of the detector to the signal pressure wave.

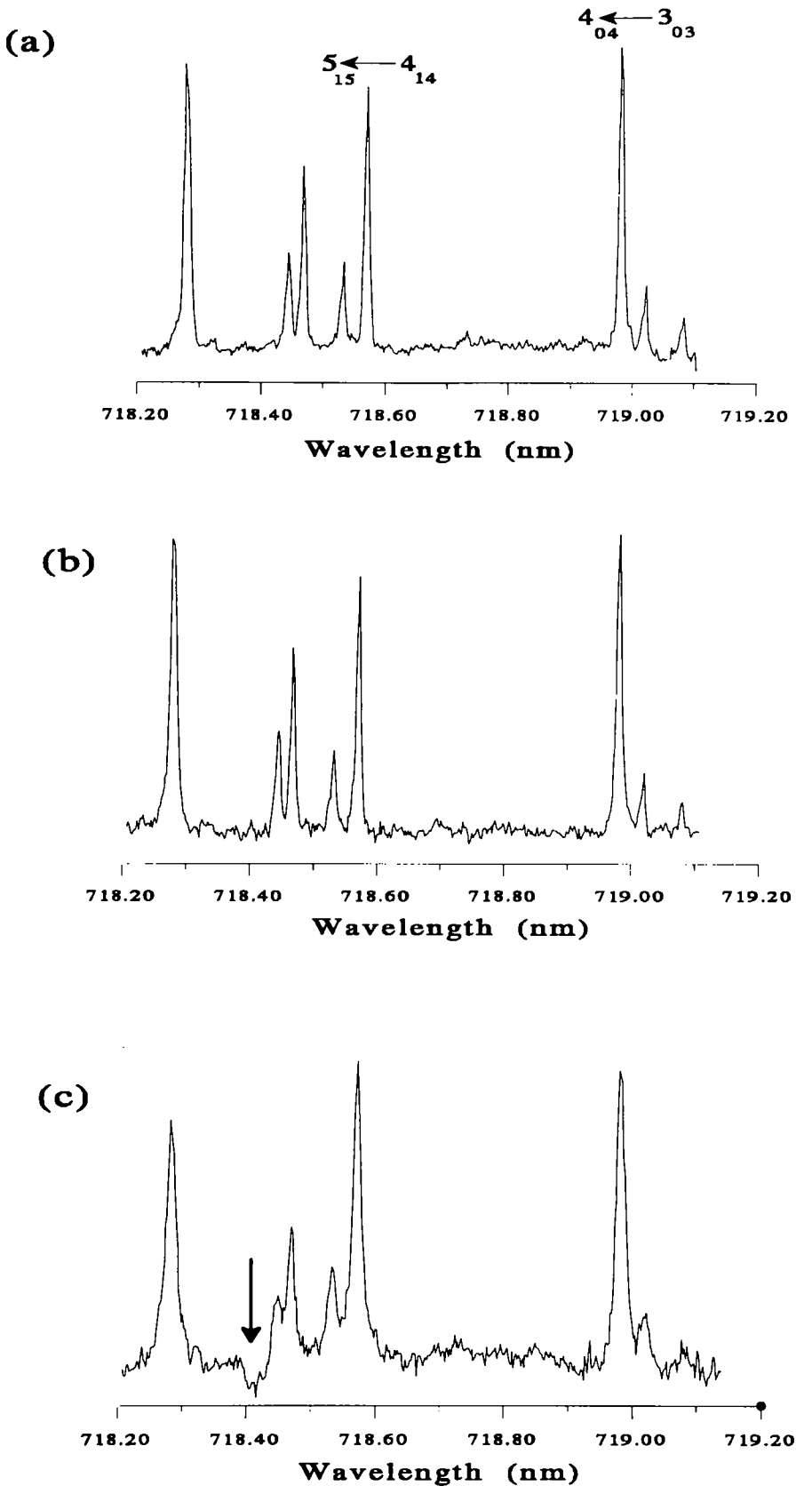

Figure 6.1 Photoacoustic spectra of a section of the third stretching vibrational overtone of water, recorded with:(a) $\sim$ 17 Torr of water, the detector $\sim$ 5 mm away from the laser beam and a 110 μs and 15 μs boxcar gate delay and width. (b) as (a) except with the detector $\sim$ 50 mm away from the laser beam and boxcar gate delay of 540 μs. (c) as (b) except with a 2 % mixture of water in air (760 Torr total pressure). All the spectra have been normalised separately so that the maximum peak height is one (arbitary units). The size of the signal in (a) is twice that in (b) and four times that in (c).

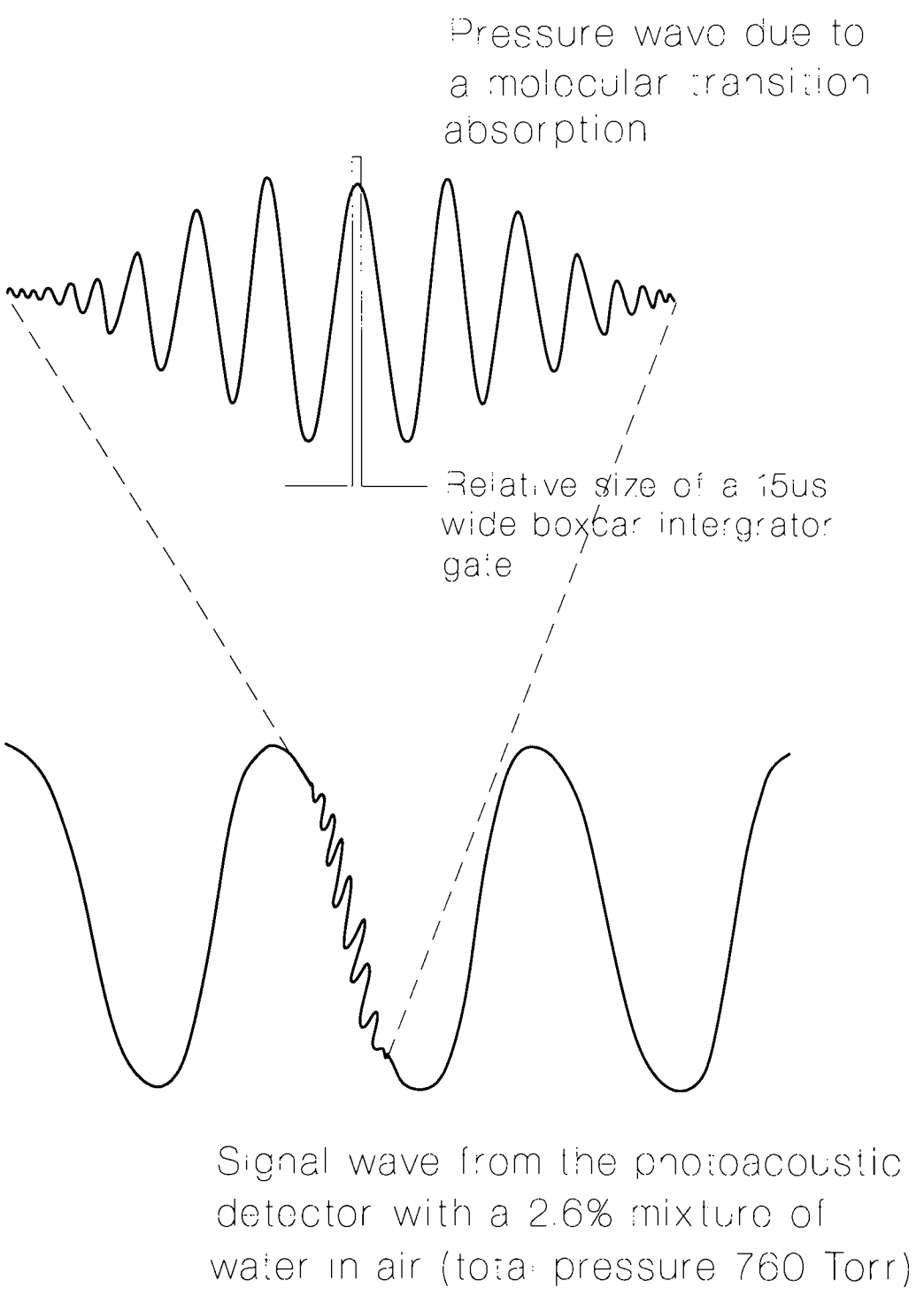

Figure 6.2 Schematic of the signal wave seen due to molecular absorption with only 20 Torr of water in the chamber (top), and then the same signal wave seen with a 2.6 % mixture of water in air (760 Torr total pressure) (bottom), now superimposed on a much larger waveform due to equipment vibrations in the laboratory. Also shown (top) is the relative position and width of the 15 μs boxcar integrator gate with respect to the (desired) signal wave throughout the three experiments in Figure 1. The frequency of the wave due to molecular absorption is $\sim$ 20 kHz and is an order of magnitude smaller (in amplitude) than the waveform due to laboratory 'noise', which had a frequency of $\sim$ 0.1 kHz.

a signal-to-noise ratio good enough for a precise determination of a rotational temperature. Another limitation on the signal-to-noise ratio may be the boxcar gate width used to collect the signal wave. Without modifying the boxcar, the maximum gate width which could be used was 15 μs, which could only cover a very small portion of the signal. Possible improvements in the signal detection will be discussed in Section 6.10.

It is clear from the spectrum shown in Figure 6.1(c) that, operating the photoacoustic detector at atmospheric pressure also increases the linewidth of the transitions and causes partial overlap of some of the transitions within the resolution of the laser radiation ($\sim$ 0.2 cm^{-1}). This would make integrated line area measurements of individual rotational states difficult and limit the accuracy of a calculated rotational temperature based on these measurements. However, this collision induced additional line-broadening is very well characterised and arises because of the pressure dependence of the transition probability (due to an increase in the probabilitity of collision-induced depopulation) resulting in a corresponding pressure-dependent linewidth which is proportional to the pressure of the gas [99]. The pressure-broadened linewidth for a given molecule can be accurately calculated using a variety of methods [292]–[297] which essentially differ only in the treatment of the interaction potential between the molecule and its perturber. The N_2 and air-broadened room-temperature linewidths of water vapour rotational transitions are well documented [298, 299]. Much detailed experimental and theoretical work has also been carried out investigating the temperature dependence of pressure-broadened linewidths over a wide range of water rotational transitions (J = 1–14) between 80–1000 K by gases such as O_2 and N_2 [298, 299]. At temperatures above $\sim$ 150 K; the measured pressure broadened linewidth, γ(T), at a temperature T, has been shown to be accurately reproduced by a power law expression developed by Benedict and Kaplan [300],

$$\gamma(T) = \gamma(T_0) \cdot \left(\frac{T_0}{T}\right)^n \tag{6.6}$$

in which $\gamma(T_0)$ is the linewidth, at the same pressure, but at the reference temperature T_0(300 K). The temperature dependence of the linewidth is contained within the value of the exponent n. This has been determined for a wide range of rotational transitions in water [299] and varies between $\sim$0.59 and $\sim$0.75. For spectrally resolved transitions, it is therefore possible to predict the rotational temperature of the molecule with precision, by measuring the linewidth at two different temperatures, but at the same pressure (for example within a

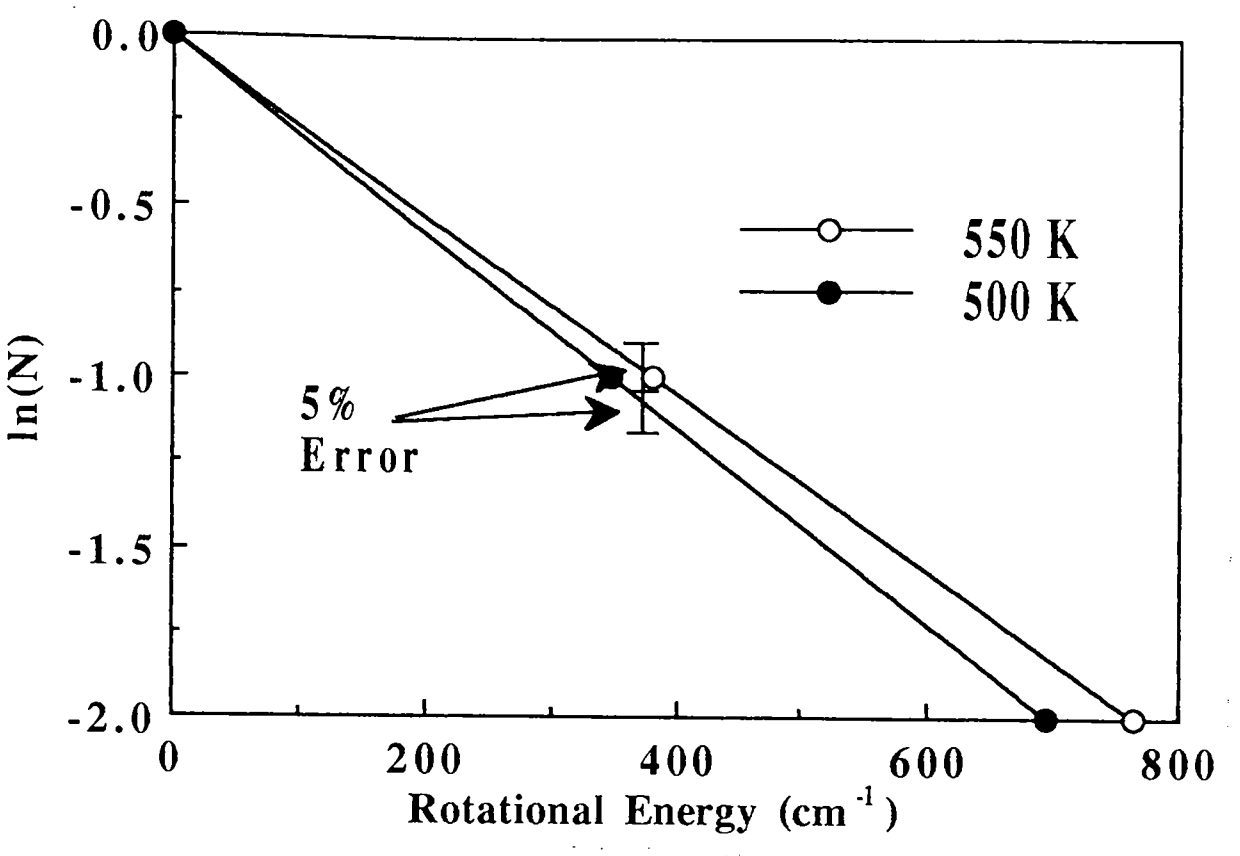

Figure 6.3 A Boltzmann plot, ln (relative rotational population) *vs.* rotational energy, for a Rotational Temperature of 500K and 550K. With an error in intensity measurements of 5%, rotational transition with a rotational energy greater than $\sim$ 380 cm^{-1} can be used to calculate a rotational temperature with an error of 10%.

cool flame and at room temperature, both at atmospheric pressure). Such a measurement would complement the corresponding integrated line area measurements of the rotational temperature.

The spectrum in Figure 6.1(c) was recorded at 300 K and at atmospheric pressure. With the apparatus at TRC (see section 6.4), the cool flame temperature, at the same pressure, is expected to between $\sim$ 500 K and 700 K. It is clear from equation 6.6 that there will be a reduction in the linewidth, at this temperature, of $\sim$ 0.7 compared with that in Figure 6.1(c). The degree of overlap is likely to be similar to that seen in Figures 6.1(a) and 6.1(b), whose linewidths are approximately half that in 6.1(c). Spectral overlap under cool flame conditions can therefore be expected to be of little consequence, even with the current laser resultion of $\sim$ 0.2 cm^{-1}. If bandwidth narrowed radiation is used, this of course increases the precision of the measured integrated areas and linewidths.

	Transition	500 K Relative Intensity	550 K Relative Intensity	Percentage Difference
1	$8_{0,8} \leftarrow 7_{0,7}$ $8_{1,8} \leftarrow 7_{1,7}$ $6_{3,5} \leftarrow 5_{3,2}$	1.490	1.573	5.3%
2	$5_{2,3} \leftarrow 4_{2,2}$	1.127	1.066	5.4%
3	$5_{1,4} \leftarrow 4_{1,3}$	1.331	1.260	5.3%
4	$4_{1,3} \leftarrow 3_{1,2}$ $5_{2,4} \leftarrow 4_{2,3}$	2.368	2.230	5.7%
5	$5_{0,5} \leftarrow 4_{0,4}$	1.976	1.865	5.6%
6	$5_{1,5} \leftarrow 4_{1,4}$	1.585	1.495	5.7%
7	$4_{0,4} \leftarrow 3_{0,3}$ $4_{2,3} \leftarrow 3_{2,2}$	1.689	1.580	6.4%
8	$3_{1,2} \leftarrow 2_{1,1}$	1.274	1.156	9.3%
9	$4_{1,4} \leftarrow 3_{1,3}$	1.547	1.445	6.6%

Table 6.1 The relative intensities of water rotational transitions with an energy greater than ~380 cm^{-1} for rotational temperatures of 500 K and 550 K. Also shown for each transition is the corresponding percentage change of the line intensity at 550 K with respect to the intensity at 500 K.

6.3 Sensitivity analysis - simulation of the rovibrational spectra of water at 500 K and 550 K

Whether photoacoustic spectroscopy can be of benefit to cool flame temperature measurements depends on the sensitivity of the rovibrational spectra to different rotational temperatures within the error margin of the experiment. In order to try to answer this question, simulations of the third stretching vibrational overtone ($|04\rangle^-$) of H_2O were carried out at 500 K and 550 K. This particular overtone level was chosen for the ease of detection of this band using excimer pumped dye lasers, which were to be used in the cool flame experiment. The absorption cross-section drops rapidly with increasing overtone level, and if a lower vibrational level is required (a larger signal is needed) then a different laser system

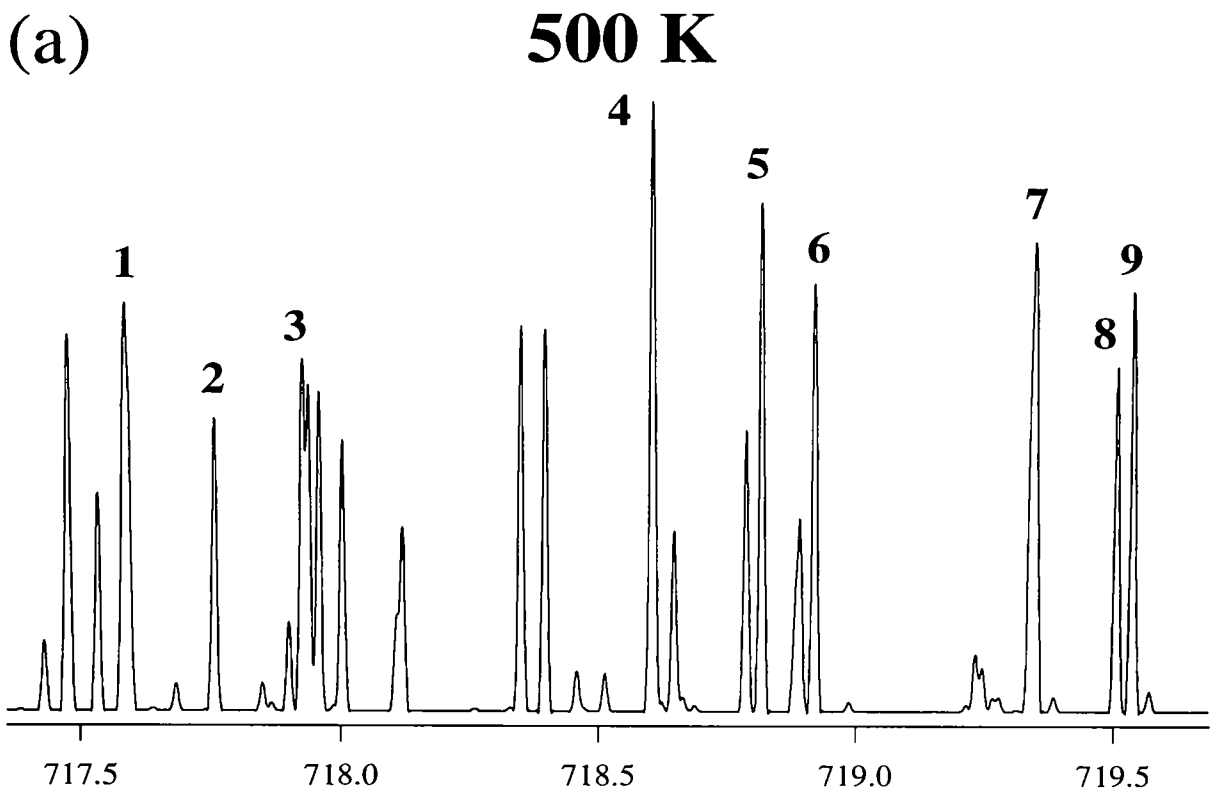

Figure 6.4 Simulation of the third stretching vibration overtone of water at a rotational temperature of (a) 500 K and (b) 550 K. Only transitions with a rotational energy greater than 380 cm^{-1} have been shown, and those of importance (see the text) have been numerically labelled (in (a)) and assigned (in (b)) using the nomenclature that has been used throughout this thesis. The intensity of the calculated transitions are normalised against $6_{25} \leftarrow 5_{24}$ in both spectra.

would probably have to be used. The two temperatures, 500 and 550 K fall approximately within the range expected for a cool flame produced within the low initial fuel temperature region (~400 K), 550K lying at the upper limit of a 10 % error in 500 K. If the spectra corresponding to these values can be distinguished, then the temperature of the cool flame could be probed with a maximium error of 10 %, which is more than satisfactory.

Boltzmann plots for H_2O rotational temperatures of 500 K and 550 K are shown in Figure 6.3. Assuming a 5 % experimental error in measuring the intensity of a rotational transition (taking this value from the signal-to-noise ratio of the spectrum shown in Figure 6.1(c)), using transitions to a rotational state with an energy greater than $\sim$ 380 cm^{-1} (as shown in Figure 6.3) will give a minimum 10 % error in the calculated rotational temperature (*i.e* 500±50 K). This can be seen more clearly in Figure 6.4 and Table 6.1. Figure 6.4 shows a segment of the simulated rovibrational spectra for $H_2O|04\rangle^-$ within the region that complies with the rotational state energy requirement discussed ($>$ 380 cm^{-1}), calculated for rotational temperatures of 500 K and 550 K. The intensity of the transitions labelled in Figure 6.4(b) (corresponding to a temperature of 550 K) are found to differ by at least 5 % (the assumed experimental error) of the intensity of the corresponding transition calculated at 500 K (shown in Figure 6.4(a)). The results are summarised in Table 6.1. If an experimental signal-to-noise ratio of $\sim$ 20:1 (a $\sim$ 5 % error) can be obtained, these calculations show that the measurement of a cool flame temperature from a simulation of the rovibrational spectrum of water present in the flame is sensitive within the desired precision of ± 10 %.

6.4 Stabilised cool flames

The experimental set up at TRC used during the photoacoustic measurements is shown schematically in Figure 6.5. The procedure for producing the stabilised cool flame has been described in more detail elsewhere [301] and only the main features will be presented here. A schematic of the flat cool flame burner is shown in Figure 6.6. Premixed vaporised fuel and N_2 and O_2 enriched air were rapidly heated by passing them through an electrically heated sintered metal fibre sheet to a temperature of between 200 and 400 °C. A stabilised cool flame could then be produced, at atmospheric pressure, further downstream, and its blue luminescence could be seen above the burner plate. The gases were then cooled by passing them through a water cooled sintered plate and pumped away by an air ejector.

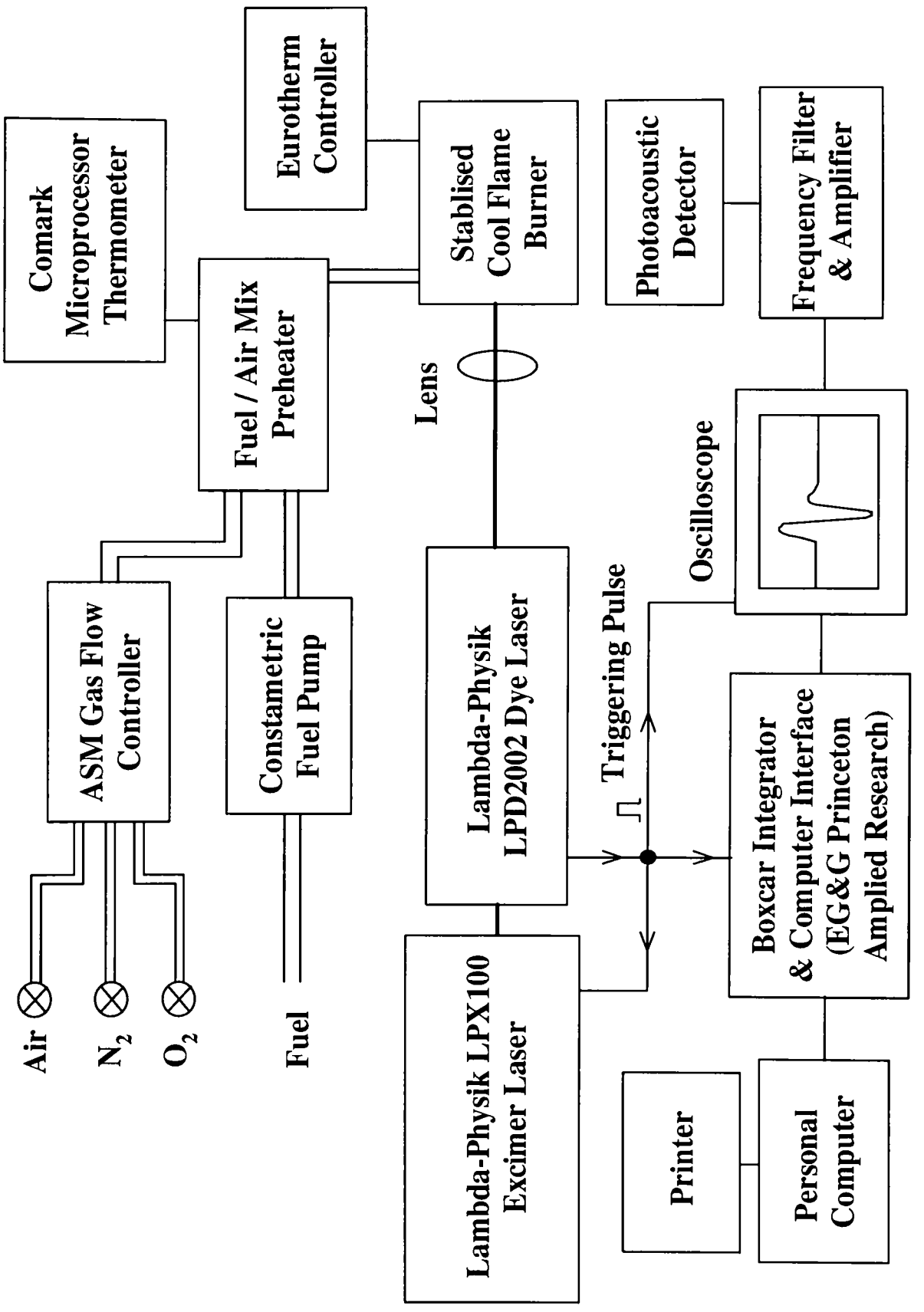

Figure 6.5 Schematic of the Experimental Apparatus used in the photoacoustic detection of $H_2O|04\rangle^-$ within a stabilised cool flame.

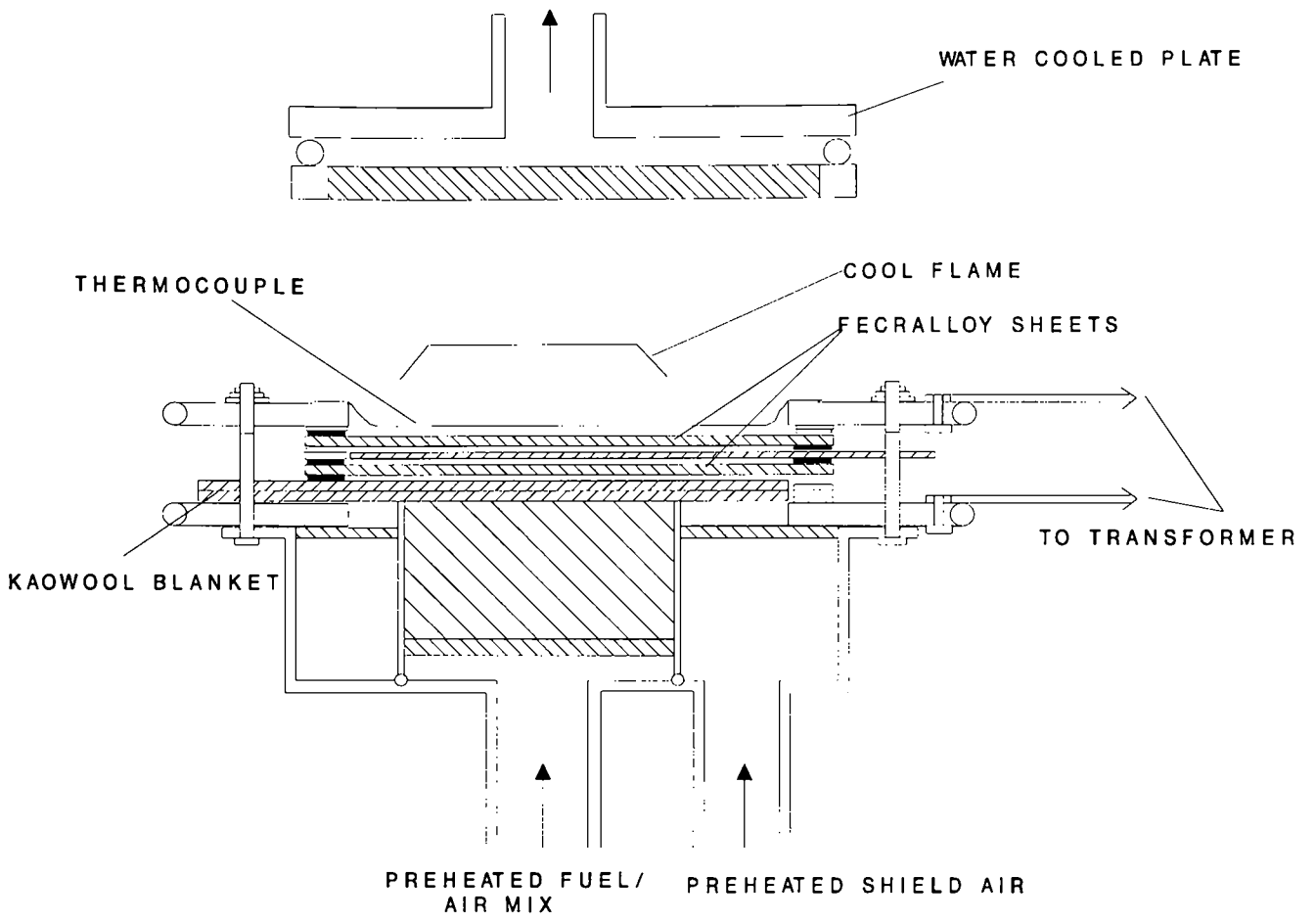

Figure 6.6 The stabilised flat cool flame burner [301].

The reactant gas temperature above the burner surface was measured by a 50 μm Type K thermocouple which controlled the electrical heat input.

Previous work showed that n-Pentane produced a very stable cool flame, making this an ideal starting fuel. Initially, the fuel was pumped (Constametric Fuel Pump) into the apparatus with a flow rate of $\sim$ 5 ml/min, with an air/N_2/O_2 mixture (flow rates of 44, 12 and 2.5 ml/min respectively) flowing through, regulated by an Advanced Semiconductor Materials (ASM) gas flow controller. The gas/fuel mix was preheated to $\sim$ 100 °C before passing onto the burner plates. Setting the burner temperature to $\sim$ 200 °C[2] was sufficient to produce the cool flame, which stabilised at a thermocouple temperature reading of $\sim$ 480 °C.

In later experiments, it was found necessary to remove the separate N_2 flow and increase the air flow to 56 ml/min. The major source of noise in the photoacoustic measurements was the gas flow; more specifically, the N_2 flow. Removing this flow reduced the noise

[2]There is about a 50 % error in the temperature measurement of the thermocouple.

level considerably. Under these conditions, a cool flame could be maintained, but stabilised temperature readings from the thermocouples on the top plate and on the burner plate were never obtained. It should be noted, however, that even with no cool flame and with the fuel air/O_2 flowing, the temperature reading was unstable. Whether this implies that these readings were unrealistic and the temperature stability of the cool flame was good is unclear.

As a further modification, water was pumped through with the fuel, using a EYELA Micro Tube Pump, to increase the water content in the cool flame region. The water absorption signal detected in the presence of a cool flame was, surprisingly, present even when the fuel and gas flows were turned off. Investigation revealed that the signal being detected was due to water in the air and the signal was larger in the cool flame apparatus because of the higher humidity caused by the burner. The higher the water concentration, the bigger the photoacoustic signal, and pumping water through with the fuel increased the signal by a factor of ~ 5. Increasing the water concentration within the cool flame is of course unrealistic and was only intended to help set up the photoacoustic detection apparatus.

With the separate water pump on its lowest flow speed, releasing one drop every 10 seconds, a cool flame could only be maintained for about one hour. Condensed water dropping from the top plate of the burner was found to gather on the bottom plate and eventually cause the flame to become unstable and disappear. The effect of having water pumped through with the fuel on the cool flame (ignoring the effect of the condensation) appeared, on observation, to be fairly minimal. The problem of the water condensing and causing the flame to eventually go out could not be avoided with the present experimental set up.

n-Heptane was briefly used in later experiments to see if this fuel would produce more water in its cool flame. Unfortunately, although a cool flame could be produced, it rapidly became very unstable and no real comparison of the two fuels could be attempted.

6.5 Laser calibration and operation

As shown in Figure 6.5, a XeCl Excimer Laser (Lambda-Physik LPX100) was used to produce the 308 nm radiation which then pumped a Dye Laser (Lambda-Physik FL2002). To produce the near-IR radiation necessary for exciting the $H_2O|04\rangle^-$ stretching overtone

Transition $J''_{K_a,K_c} \leftarrow J'_{K_a,K_c}$	Wavelength (nm)
$4_{04} \leftarrow 3_{03}$	719.495
$5_{15} \leftarrow 4_{14}$	719.091
$4_{23} \leftarrow 3_{22}$	719.050
$4_{22} \leftarrow 3_{21}$	718.983
$5_{05} \leftarrow 4_{04}$	718.962
$4_{13} \leftarrow 3_{12}/4_{32} \leftarrow 3_{31}$	718.800
$6_{25} \leftarrow 5_{24}$	718.085
$5_{14} \leftarrow 4_{13}$	718.105

Table 6.2 Line positions of some of the rotational transitions of the 3rd stretch overtone of water taken from the dye laser.

state (715-730 nm), Rhodamin 700 (Lambda-Physik LC7000) was used in the dye laser. By optimising the excimer laser and running at 22kV and 15 Hz, a peak power of $\sim$ 200mJ/pulse was obtained. This was sufficient to give a peak output from the dye laser of $\sim$ 30mJ/pulse and appeared to give the best signal-to-noise ratios. For pulsed radiation, the size of the photoacoustic signal is proportional to the laser intensity, making the optimisation of the laser power critical for these experiments. To help optimise the conditions necessary for detection of signals from a cool flame, it was necessary to know the calibration of the grating on the dye laser in order to set the laser wavelength at the peak of a water rotational line in the overtone. Using the preheater used in the cool flame apparatus, a steady flow of steam was set up and a spectrum of the 3rd overtone recorded to give the necessary line positions, which are given in Table 6.2 for some of the key transitions (see Section 6.3). During the experiments, the 4_{13} rotational line was used to help set up the rest of the detection equipment, as this was the most intense transition.

6.6 Frequency filter

It was shown in Section 6.2 that the primary limitation of the success of this technique under atmospheric pressure conditions was the noise pressure waves produced in the laboratory environment. In an attempt to remove this background noise and to preamplify the

remaining signal wave, a frequency filter was built, with a fast, high gain amplifier built into it. The filter was intially set at > 10 kHz, with a 6 dB/octave roll-off.

Within the cool flame apparatus at TRC, the low frequency noise superimposed on the photoacoustic signal wave from equipment in the laboratory was successfully removed with the filter. Unfortunately, the gas flow necessary for cool flame production introduced high frequency noise (8-12 kHz), which was orders of magnitude bigger than any signal from water absorption. Increasing the filter's cut-off frequency in stages towards the frequency of the signal waveform caused the noise level to drop considerably. It was found that setting the frequency filter to > 20 kHz gave the lowest noise level and the maximum signal transmittance. Increasing the filter to > 25 kHz which, according to the oscilloscope was very close to the frequency of the signal ($\sim$ 26 kHz), the noise level was minimal, but the signal level also dropped significantly. Throughout the cool flame experiments, the filter was set at > 20 kHz as the best compromise. However, the noise waves were so intense that the cut-off of the frequency filter was not sharp enough to completely remove the noise waves, even though the frequency range of the noise was below the nominal cut-off. The signal from the filter was averaged over n = 50–100 laser shots per grating setting on a boxcar integrator and averager (EG & G Princeton Amplified Research) before being transferred to a PC for collection. A gate width of $\sim$15 μs was used throughout these experiments.

6.7 Direct photoacoustic detection

With the noise levels inherently present in the system, maximising the signal was essential if a good signal-to-noise ratio was be obtained. If the standard method of photoacoustic detection was to be used (pointing the face of the microphone directly at the laser beam) it was important to determine the temperature close to the cool flame. Moving a thermocouple towards the flame, in the same position of which the microphone would be mounted, the temperature profile shown in Figure 6.7 was obtained. Within the design specifications of the microphone (Knowles Electronics CF Series), the closest it could be placed to the edge of the flame was $\sim$ 15 mm.

Positioning the laser beam at the edge of the cool flame, 15 mm away from the detector, the best $H_2O|04\rangle^-$ signal-to-noise ratio obtained, even employing the frequency filter described above and optimising the laser power and the data collection, was only $\sim$ 2:1. Moving

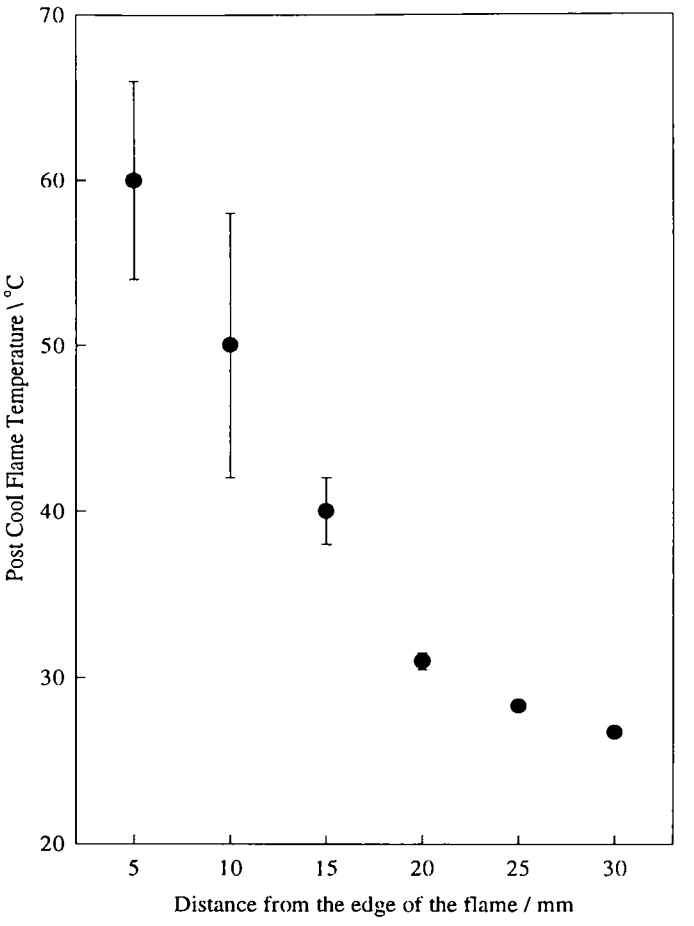

Figure 6.7 Temperature profile obtained by moving a thermocouple (in the same position as the photoacoustic detector) towards the flame. The distances given along the x-axis are from the edge of the flame, itself 10 mm from the centre of the flame.

the laser beam focus to the centre of the flame, even for the stronger water transitions, no signal (within the noise level) was detected. Artificially introducing more water into the flame, the signal-to-noise at the edge of the flame increased to $\sim$ 4:1, and a small signal could just be detected at the centre of the flame. The signal levels obtained with direct photoacoustic detection were still too small to gain any useful information, even with the extra water present in the flame.

6.8 Indirect photoacoustic detection - signal enhancement with a parabolic mirror

The signal wave is (to a good approximation) radially emitted from the focus of the laser beam, and the microphone, which has a small surface area, is a relatively large distance away from the signal point source. The majority of the signal (in the direction of the detector) is therefore not utilised. Increasing the cone of acceptance of the microphone, while still

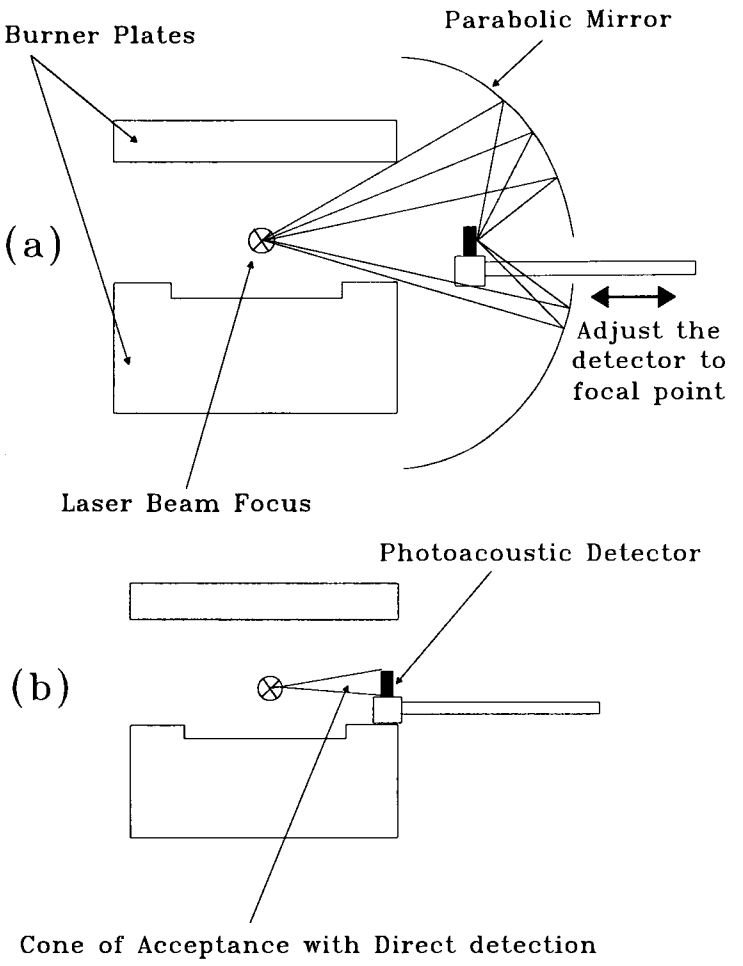

Figure 6.8 Arrangement of a parabolic mirror and the detector next to the flame apparatus (shown in (a)) increased the cone of acceptance of the detector by orders of magnitude compared with direct detection (shown in (b)). This increased the signal-to-noise level by at least an order of magnitude.

keeping its small size to decrease the noise level detected, was the next step taken in the experiments.

By placing a parabolic mirror close to the cool flame and the microphone at its focus, it was possible to increase the effective cone of acceptance (of the photoacoutic signal) of the detector by an orders of magnitude (see Figure 6.8). Moving the microphone back and forth between the flame and the back edge of the mirror, the focal point could easily be found from the size of the water signal seen on an oscilloscope. The focal point was found to be $\sim$ 15 mm from the back of the mirror, depending on whether the focus of the laser beam was at the edge or at the centre of the flame. This meant that the microphone was well away from the flame, removing any temperature restrictions and reducing the noise level. The signal was at least an order of magnitude bigger than the best signal that could be

obtained with direct detection.

With the laser beam focus at the very edge of the water enhanced cool flame, a signal-to-noise ratio of $\sim$ 20:1 was obtained, producing a spectrum of high enough quality for analysis. Moving the laser beam into the flame, the signal was found to drop off rapidly, giving a signal-to-noise ratio of $\sim$ 3:1 at the centre of the flame; the two spectra are shown in Figure 6.9. Comparing the two spectra, probing the edge and the centre of the flame, shows that the rotational temperature of the water at the centre is noticably higher than at the edge. This can be seen in the different intensity ratio and the additional transitions indicated by the black arrows in the bottom plot. On inspection of the burner plate, condensed water dropping down from the top plate was gathering around the edges of the plate. This would explain the high signal (*i.e.* high concentration) of water found at the edge of the flame and also the lower temperature, as the temperature of the burner was much lower than the (approximate) temperature of the cool flame. As mentioned previously, artificially increasing the water concentration in the cool flame was only intended to help set up the photoacoustic detection system, and the spectra shown in Figure 6.9 are only intended to demonstrate the noise problems encountered within the experimental set-up. Removing the additional water from the cool flame, a signal could be detected, but with a signal-to-noise ratio of only $\sim$ 1:1.

6.9 Summary of the experimental results

- The $H_2O|04>^-$ photoacoustic signal detected within the cool flame was, surprisingly, produced by water molecules in the air and not by water produced in the cool flame chemistry. Flowing water through the fuel-pump increased the photoacoustic signal considerably. However, this caused the cool flame to go out after about an hour because of excessive water build-up on the burner plates.
- The use of a mirror arrangement enhanced the signal level further, as well as reducing the noise level slightly and enabling the microphone to be placed away from the flame, allowing its operation at room temperature.
- High frequency noise produced by the gas flow through the apparatus could only be partially removed with the frequency filter used. This proved to be the only limiting factor to the success of the experiments.
- The size of the signal at the centre of the cool flame (without the additional water)

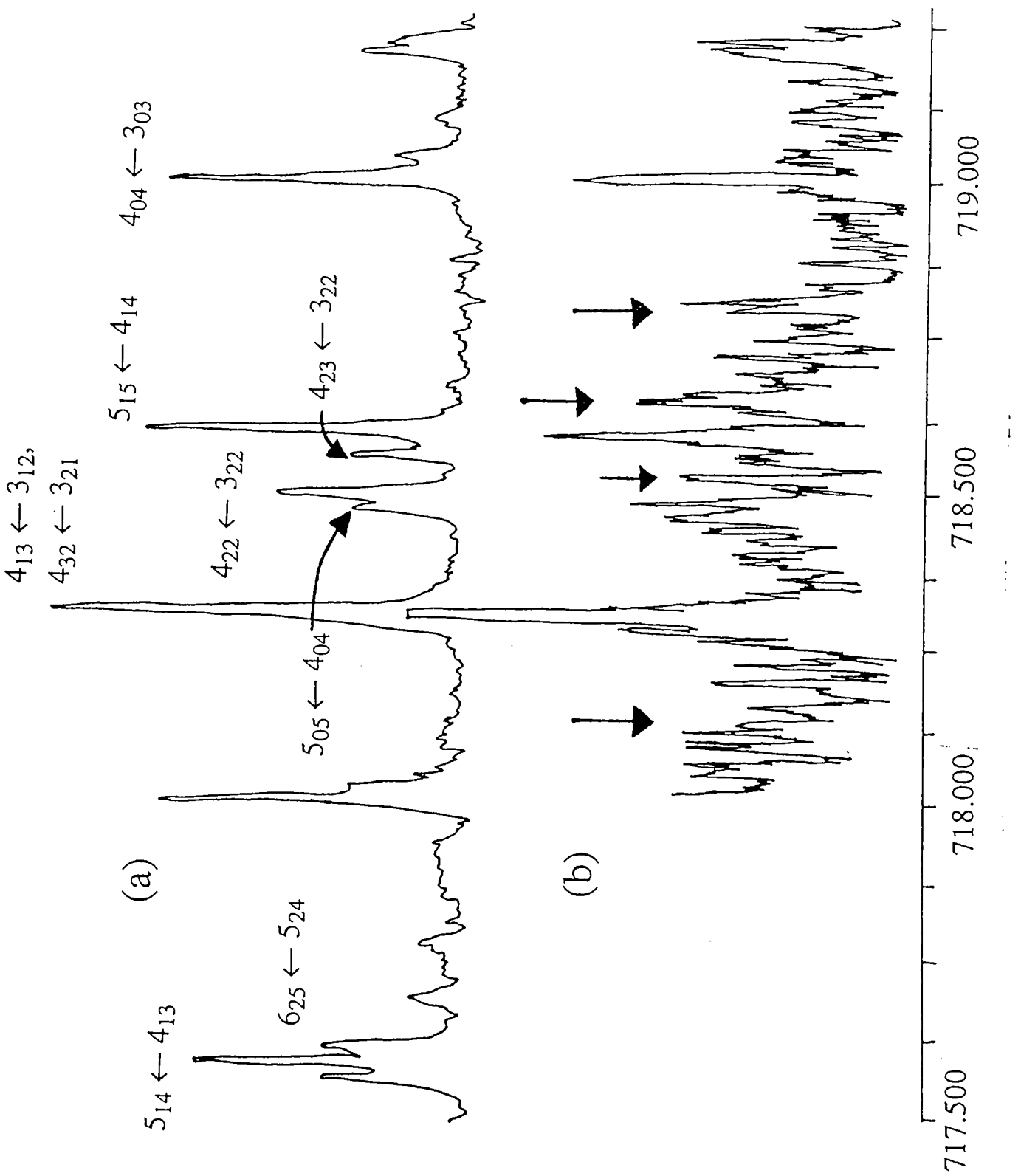

Figure 6.9 Photoacoustic spectra taken with a n-Pentane cool flame, with optimal signal production and detection: (a) at the very edge of the flame. (b) at the centre of the flame. Indicated in (b) are additional features not present in (a) showing a higher rotational temperature at the centre than at the edge of the flame. This can be explained by condensed water gathering at the edges of the burner plate and then evaporating.

was about 40 mV, well within the sensitivity of the boxcar integrator and averager used for data collection, but the noise level was too high for an accurate temperature measurement.

6.10 Discussion and conclusion

It has been demonstrated that photoacoustic spectroscopy has the potential of probing the temperature of molecules within a cool flame, and its sensitivity is only limited by the noise produced in the experimental environment. The present method of extracting the signal wave, using a cut-off frequency filter, is clearly limited by the roll-off of the filter. For the experiments presented in this chapter the filter was built with a 6 dB/octave roll-off. According to the oscilloscope used in the experiment, the signal wave had a frequency of ~26 kHz and the noise ranged between 8 and 15 kHz[3]. Setting the cut-off frequency at 20 kHz, the percentage transmittance at 10 kHz would therefore be 25 %. Considering the intensity of the noise wave is many orders of magnitude greater intensity than the signal intensity, it is not surprising that the frequency filter available during the experiments was inadequate for this system. To date, the best roll-off for a commercially available frequency filter is 24 dB/octave, which would drop the transmittance at 10 kHz (for a 20 kHz cut-off frequency) to 0.4 %. Another improvement would be to use a band-pass filter rather than a cut-off (low-pass) filter and only transmit the signal frequency (± the 24 dB/octave roll-off). This would be more effective at reducing the possible percentage transmittance of the filter within the frequency range of the noise.

As mentioned in Section 6.2, under the present gated collection of the signal waveform, the 15 μs gate width covers only a small fraction of the total wave. The boxcar integrator can be easily modified to produce a gate width large enough to allow an integration over the whole of the signal ($\sim$ 500 μs), but the signal wave would have to squared because of its oscillatory nature (switching between a positive and negative voltage). However, this would only be advantageous if the noise was effectively filtered out.

An alternative to gated detection in the time domain is to perform a Fourier transform on the signal and to collect the signal from one particular frequency component. In these

[3]These values have not been calibrated and may not be the true frequencies, but their magnitudes relative to the signal frequency will be correct.

experiments, there did not appear to be any noise with the same frequency as the signal, and this should be a 'noise-free' way of data collection. The only limitiation is the speed at which a Fourier transform could be carried out with the laser repetition rate that was used. This is determined by the number of points in the time domain that the transform integral is performed over [302]. With a suitable point selection and the available Fourier transform computer software, this may be a very useful alternative for the data collection.

References

[1] R. N. Zare, *Mol. Photochem.*, 1972, **4**, 1.

[2] J. P. Simons in Special Periodical Report: Gas Kinetics and Energy Transfer, Eds. P. G. Ashmore, R. J. Donovan, Royal Society of Chemistry, London, 1977, Vol 2, p 58.

[3] W. M. Gelbart, *Ann. Rev. Phys. Chem.*, 1977, **28**, 323.

[4] H. Okabe, *Photochemistry of Small Molecules*, (John Wiley and Sons, New York, 1978).

[5] S. R. Leone, in *Dynamics of Excited State*, Ed. K. P. Lawley, *Adv. Chem. Phys.*, 1982, **50**, 255.

[6] M. Shapiro, R. Bersohn, *Ann. Rev. Phys. Chem.*, 1982, **33**, 409;

[7] J. P. Simons, *J. Phys. Chem.*, 1984, **88**, 1287.

[8] F. F. Crim, *Ann. Rev. Phys. Chem.*, 1984, **35**, 657.

[9] G. G. Balint-Kurti, M. Shapiro, *Adv. Chem. Phys.*, 1985, **60**, 403.

[10] H. Reisler, C. Wittig, *Ann. Rev. Phys. Chem.*, 1986, **37**, 307.

[11] J. P. Simons, *J. Phys. Chem.*, 1987, **91**, 5378.

[12] P. L. Houston *J. Phys. Chem.*, 1987, **91**, 5388.

[13] R. Bersohn, *Molecular Photodissociation Dynamics*, Eds M. N. R. Ashfold, J. E. Baggott (Royal Society of Chemistry, London, 1987), Chapter 1.

[14] A. M. Wodtke, Y. T. Lee, *Molecular Photodissociation Dynamics*, Eds M. N. R. Ashfold, J. E. Baggott (Royal Society of Chemistry, London, 1987), Chapter 2.

[15] P. Andresen, R. Schinke, *Molecular Photodissociation Dynamics*, Eds M. N. R. Ashfold, J. E. Baggott (Royal Society of Chemistry, London, 1987), Chapter 3.

[16] M. P. Docker, A. Hodgson, J. P. Simons, *Molecular Photodissociation Dynamics*, Eds M. N. R. Ashfold, J. E. Baggott (Royal Society of Chemistry, London, 1987), Chapter 4.

[17] R. Schinke, *Ann. Rev. Phys. Chem.*, 1989, **40**, 375.

[18] G. E. Hall, P. L. Houston, *Ann. Rev. Phys. Chem.*, 1989, **40**, 375.

[19] P. L. Houston, *Acc. Chem. Res.*, 1989, **22**, 309.

[20] R. N. Dixon, *Acc. Chem. Res.*, 1991, **24**, 16.

[21] M. N. R. Ashfold, I. R. Lambert, D. H. Mordaunt, G. P. Morley, C. M. Western, *J. Phys. Chem.*, 1992, **96**, 2938.

[22] W. H. Green Jr., C. B. Moore, W. F. Polik, *Ann. Rev. Phys. Chem.*, 1992, **43**, 591.

[23] F. F. Crim, *Ann. Rev. Phys. Chem.*, 1993, 44, 397.

[24] S. R. Leone, S. A. Rogers, *Applied Spectroscopy*, 1993, **47**, 1430.

[25] J. R. Huber, R. Schinke, *J. Phys. Chem.*, 1993, **97**, 3463.

[26] R. Schinke, *Photodissociation Dynamics*, (Cambridge University Press, Cambridge, 1993).

[27] R. N. Dixon, *Chem. Soc. Rev.*, 1994, **23**, 375.

[28] R. J. Gordon, G. E. Hall, *Adv. Chem. Phys.*, in press.

[29] N. Y. Turro, *Modern Molecular Photochemistry*, (Benjamin, Menlo Park, 1978).

[30] R. N. Wayne, *Principles and Applications of Photochemistry*, (Oxford University Press, Oxford, 1988).

[31] R. D. Levine, R. B. Bernstein, *Molecular Reaction Dynamics and Chemical Reactivity*, (Oxford University Press, Oxford, 1987).

[32] (a) D. J. Kligler, D. J. Pummer, W. K. Bischel, C. K. Rhodes, *J. Chem. Phys.*, 1978, **69**, 4652; (b) W. K. Bischel, J. Bokor, J. Dallarosa, C. K. Rhodes, *J. Chem. Phys.*, 1979, **70**, 5593.

[33] (a) P. F. Zittel, D. D. Little, *J. Chem. Phys.*, 1979, **71**, 713; (b) *Chem. Phys.*, 1981, **63**, 227; (c) *J. Chem. Phys.*, 1980, **72**, 5900

[34] (a) P. Andresen, V. Beushausen, D. Häusler, H. W. Lülf, E. W. Rothe, *J. Chem. Phys.*, 1985, **83**, 1429; (b) D. Häusler, P. Andresen, R. Schinke, *ibid.*, 1987, **87**, 3949.

[35] R. Cotting, V. Engel, J. R. Huber, *J. Chem. Phys.*, 1994, **100**, 1040.

[36] A. Ogai, C. X. W. Qian, H. Reisler, *J. Chem. Phys.*, 1990, **93**, 1107.

[37] R. Schinke, M. Nonella, H. U. Suter, J. R. Huber, *J. Chem. Phys.*, 1990, **93**, 1098.

[38] A. Untsch, K. Weide, R. Schinke, *J. Chem. Phys.*, 1991, **95**, 6496.

[39] H. Y. Wang, W. S. Felps, S. P. McGlynn, *J. Chem. Phys.*, 1977, **67**, 2614.

[40] (a) R. Schinke, V. Engel, V. Steammler, *Chem. Phys. Lett.*, 1985, **116**, 165; (b) *J. Chem. Phys.*, 1988, **88**, 129.

[41] K. Weide, S. Hennig, R. Schinke, *J. Chem. Phys.*, 1989, **91**, 7630.

[42] G. Herzberg, *Electronic Spectra of Polyatomic Molecules*, (Van Nostrand, New York, 1966).

[43] R. N. Dixon, K. B. Jones, M. Noble, S. Carter, *Mol. Phys.*, 1981, **42**, 455.

[44] R. N. Dixon, C. A. Rosser, *Chem. Phys. Lett.*, 1984, **108**, 125.

[45] R. N. Dixon, M. Noble, C. A. Taylor, M. Delhoume, *Faraday Disc. Roy. Soc. Chem.*, 1981, **71**, 125.

[46] (a) M. N. R. Ashfold, J. M. Bayley, R. N. Dixon, *Chem. Phys.*, 1984, **84**, 35; (b) M. N. R. Ashfold, J. M. Bayley, R. N. Dixon, J. D. Prince, *Ber. Bungenges. Phys. Chem.*, 1985, **89**, 254.

[47] M. N. R. Ashfold, *Mol. Phys.*, 1986, **58**, 1.

[48] H. H. Kuge, K. Kleinermanns, *J. Chem. Phys.*, 1989, **90**, 46.

[49] S. W. Novicki, R. Vasudev, *J. Chem. Phys.*, 1991, **95**, 7269.

[50] (a) R. N. Dixon, H. Rieley, *J. Chem. Phys.*, 1989, **91**,2308; (b) *Chem. Phys.*, 1989, **137**, 307.

[51] R. Vasudev, S. J. Wategaonkar, S. W. Novicki, J. H. Shan, *ACS Symposium Series*, 1992, **502**, 279.

[52] S. Hennig, A. Untch, R. Schinke, M. Nonella, J. R. Huber, *Chem. Phys.*, 1989, **129**, 93.

[53] H. U. Suter, J. R. Huber, *Chem. Phys. Lett.*, 1989, **155**, 203.

[54] O. B. d'Azy, F. Lahmani, C. Lardeux, D. Solgadi, *Chem. Phys.*, 1985, **94**, 247.

[55] (a) A. Untch, K. Weide, R. Schinke, *Chem. Phys. Lett.*, 1991, **180**, 265; (b) A. Untch, R. Schinke, R. Cotting, J. R. Huber, *J. Chem. Phys.*, 1993, **99**, 9553.

[56] E. Kodes, M. Rosslein, J. R. Huber, *Chem. Phys. Lett.*, 1993, **209**, 275.

[57] S. A. Reid, J. T. Brandon, H. Reisler, *Chem. Phys. Lett.*, 1993, **209**, 22.

[58] M. S. Child, *Molecular Collision Theory*, (Academic Press, London, 1974), Chapter 4.

[59] U. Fanu, A. R. P. Rao, *Atomic Collisions and Spectra*, (Academic Press, Orlando, 1986), Chapter 8.

[60] (a) D. C. Clary, C. M. Lovejoy, S. V. O'Neil, D. J. Nesbitt, *Phys. Rev. Lett.*, 1988, **61**, 1576; (b) D. J. Nesbitt, C. M. Lovejoy, T. G. Lindeman, S. V. O'Neil, D. C. Clary, *J. Chem. Phys.*, 1989, **91**, 722.

[61] C. M. Lovejoy, D. J. Nesbitt, *J. Chem. Phys.*, 1990, *93*, 5387.

[62] (a) M. I. Lester, R. W. Randall, L. C. Giancarlo, S. E. Choi, *J. Chem. Phys.*, 1993, **99**, 6211; (b) *Faraday Discuss. Chem. Soc.*, 1994, **97**, 365.

[63] (a) M. T. Berry, R. A. Loomis, L. C. Giancarlo, M. I. Lester, *J. Chem. Phys.*, 1992, **96**, 7890; (b) W. H. Green Jr., M. I. Lester, *J. Chem. Phys.*, 1992, **96**, 2573; (c) M. T. Berry, M. R. Brustein, M. I. Lester, C. Chakravarty, D. C. Clary, *Chem. Phys. Lett.*, 1991, **178**, 301.

[64] D. W. MacArthur, K. B. Butterfield, D. A. Clarke, J. B. Donahue, P. A. M. Gram, H. C. Bryant, C. J. Harvey, W. W. Smith, G. Comtet, *Phys. Rev. A - General Physics*, 1985, **32**, 1921.

[65] M. Cortes, F. Martin, *Phys. Rev. A*, 1993, **48**, 1227.

[66] Y. K. Ho, *Phys. Rev. A*, 1995, **52**, 375.

[67] Y. Zhou, C. D. Lin, *Phys. Rev. Lett.*, 1995, **75**, 2296.

[68] (a) Y. K. Ho, A. K. Bhatia, *Phys. Rev. A*, 1992, **45**, 6268; (b) *ibid.* 1993, **48**, 264; (c) *ibid.* 1994, **50**, 2155.

[69] D. G. Imre, J. L. Kinsey, A. Sinha, J. Krenos, *J. Phys. Chem.*, 1984, **88**, 3956.

[70] H. J. Foth, J. C. Polyani, H. H. Telle, *J. Chem. Phys.*, 1982, **86**, 5027.

[71] (a) E. J. Heller, *Acc. Chem. Phys.*, 1981, **14**, 368; (b) E. J. Heller in *Potential Energy Surfaces and Dynamics Calculations*, ed. D. G. Truhlar, (Plenum Press, New York, 1981).

[72] S. O. Williams, D. G. Imre, *J. Chem. Phys.*, 1988, **92**, 6636.

[73] R. J. Sension, R. J. Brudzynski, B. S. Hudson, *Phys. Rev. Lett.*, 1988, **61**, 694.

[74] R. J. Sension, R. J. Brudzynski, B. S. Hudson, J. Zhang, D. G. Imre, *Chem. Phys.*, 1990, **141**, 393.

[75] L. J. Butler, *Chem. Phys. Lett.*, 1991, **182**, 393.

[76] M. von Dirke, B. Heumann, R. Schinke, R. J. Sension, B. S. Hudson, *J. Chem. Phys.*, 1993, **99**, 1050.

[77] R. J. Brudzynski, R. J. Sension, B. S. Hudson, *Chem. Phys. Lett.*, 1990, **165**, 487.

[78] K. Lao, M. D. Person, P. Xayariboun, L. J. Butler, *J. Chem. Phys.*, 1990, **92**, 823.

[79] (a) M. D. Person, K. Q. Lao, B. J. Ecklohm, L. J. Butler, *J. Chem. Phys.*, 1989, **91**, 812; (b) P. W. Browning, E. Jensen, G. C. G. Waschwsky, M. R. Tate, L. J. Butler, *J. Chem. Phys.*, 1994, **101**, 5652.

[80] L. C. Lee, X. Wang, M. Suto, *J. Chem. Phys.*, 1987, **86**, 4353.

[81] (a) K. Weide, V. Staemmler, R. Schinke, *J. Chem. Phys.*, 1990, **93**, 861; (b) B. Heumann, R. Düren, R. Schinke, *Chem. Phys. Lett.*, 1991, **180**, 583; (c) B. Heumann, K. Weide, R. Düren, R. Schinke, *J. Chem. Phys.*, 1993, **98**, 5508; B. Heumann, R. Schinke, *J. Chem. Phys.*, 1994, **101**, 7488.

[82] G. Theodorakopoulos, I. D. Petsalakis, *Chem. Phys. Lett.*, 1991, **178**, 475.

[83] (a) R. N. Dixon, C. C. Maston, G. G. Balint-Kurti, *J. Chem. Phys.*, 1990, **93**, 6520; (b) G. G. Balint-Kurti, *Faraday Discuss. Chem. Soc.*, 1991, **91**, 123.

[84] A. Gedanken, M. D. Rowe, *Chem. Phys. Lett.*, 1975, **34**, 39.

[85] (a) S. L. Baughcum, S. R. Leone, *J. Chem. Phys.*, 1980, **72**, 6531; (b) H. W. Hermann, S. R. Leone, *ibid.*, 1982, **76**, 4759 and 4766.

[86] T. Suzuki, H. Kanamori, E. Hirota, *J. Chem.Phys.*, 1991, **94**, 6607.

[87] R. A. Hertz, J. A. Syage, *J. Chem. Phys.*, 1994, **100**, 9265.

[88] M. Dzvonik, S. Yang, R. Bersohn, *J. Chem. Phys.*, 1974, **61**, 4409.

[89] (a) R. K. Sparks, K. Shobatake, L. R. Carlson, Y. T. Lee, *J. Chem. Phys.*, 1981, **75**, 3838; (b) T. K. Minton, P. Felder, R. J. Brudzynski, Y. T. Lee, *J. Chem. Phys.*, 1984, **81**, 1759.

[90] G. N. A. van Veen, T. Baller, A. E. de Vries, N. J. A. van Veen, *Chem. Phys.*, 1984, **87**, 405.

[91] Q.-X. Xu, K.-H. Jung, R. B. Bernstein, *J. Chem. Phys.*, 1988, **89**, 2099.

[92] (a) D. W. Chandler, P. L. Houston, *J. Chem. Phys.*, 1987, **87**, 1445; (b) R. O. Loo, G. E. Hall, H.-P. Haerri, P. L. Houston, *J. Chem. Phys.*, 1988, **92**, 5; (c) G. E. Hall, R. O. Loo, H. P. Harri, N. Sivakumar, G. K. Chawla, P. L. Houston, D. W. Chandler, J. W. Hepburn, I. Burak, *Ber. Bunsenges. Phys. Chem.*, 1988, **92**, 281.

[93] D. W. Chandler, J. W. Thoman, M. H. M. Janssen, D. H. Parker, *Chem. Phys. Lett.*, 1989, **156**, 151.

[94] (a) C. A. Taatjes, M. H. M. Janssen, S. Stolte, *Chem. Phys. Lett.*, 1993, **203**, 363; (b) J. W. G. Mastenbroek, C. A. Taatjes, K. Nauta, M. H. M. Janssen, S. Stolte, *J. Phys. Chem.*, 1995, **99**, 4360.

[95] P. G. Wang, L. D. Ziegler, *J. Phys. Chem.*, 1993, **97**, 3139.

[96] H. Guo, G. C. Schatz, *J. Chem. Phys.*, 1990, **93**, 393.

[97] (a) K. F. Freed, M. R. Wedlock, *J. Chem. Phys.*, 1991, **95**, 7275; (b) M. R. Wedlock, E. Jensen, L. J. Butler, K. F. Freed, *J. Phys. Chem.*, 1991, **95**, 8096; (c) R. A. Harris, M. R. Wedlock, L. J. Butler, K. F. Freed, *J. Chem. Phys.*, 1992, **96**, 2437.

[98] *Atomic and Molecular Beam Methods*, ed. G. Scoles, (Oxford University Press, New York, 1988 and 1992), Vol. 1 and 2.

[99] W. Demtröder, *Laser Spectroscopy* (Springer-Verlag, Berlin Heidelberg, 1988).

[100] P. Felder, *Chimia*, 1994, **48**, 43.

[101] R. Uberna, R. D. Hinchliffe, J. I. Cline, *J. Chem. Phys.*, 1995, **103**, 7934.

[102] (a) D. P. Baldwin, M. A. Buntine, D. W. Chandler, *J. Chem. Phys.*, 1990, **93**, 6578; W. P. Hess, D. W. Chandler, J. W. Thowman Jr. *Chem. Phys.*, 1992, **183**, 5843.

[103] D. P. Baldwin, M. A. Buntine, D. W. Chandler, *J. Chem. Phys.*, 1992, **96**, 5843.

[104] A. J. R. Heck, D. W. Chandler, *Ann. Rev. Phys. Chem.*, 1995, **46**, 335.

[105] (a) T. Sukuki, V. P. Hradil, S. A. Hewitt, P. L. Houston, B. J. Whitaker, *Chem. Phys. Lett.*, 1991, **187**, 257; (b) *J. Chem. Phys.*, 1993, **99**, 4455.

[106] A. G. Suits, R. L. Miller, L. S. Bontuyan, P. L. Houston, *Chem. Soc. Faraday Trans.*, 1993, **89**, 1443.

[107] (a) K. Tonokura, T. Suzuki, *Chem. Phys. Lett.*, 1993, **224**, 1; (b) T. Suzuki, K. Tonokura, L. S. Bontuyan, N. Hashimoto, *J. Phys. Chem.*, 1994, **98**, 13447.

[108] T. Sato, T. Kinugawa,T. Arikawa, M. Kawasaki, *Chem. Phys.*, 1992, **165**, 173.

[109] See references 32 and 43-49 in Reference [21].

[110] (a) J. Segall, Y. Wen, R. Singer, M. Dulligan, C. Wittig, *J. Chem. Phys.*, 1993, **99**, 6600; (b) Y. Wen, J. Segall, M. Dulligan, C. Wittig, *J. Chem. Phys.*, 1994, **101**, 5655; (c) J. Zhang, M. Dulligan, J. Segall, Y. Wen, C. Wittig, *J. Phys. Chem.*, 1995, **99**, 13680.

[111] (a) G. P. Morley, I. R. Lambert, M. N. R. Ashfold, K. N. Rosser, C. M. Western, *J. Chem. Phys.*, 1992, **97**, 3157; (b) D. H. Morduant, I. R. Lambert, D. H. Morduant,

S. H. S. Wilson, M. N. R. Ashfold, R. N. Dixon, C. M. Western, L. Schnieder, K. H. Welge, *J. Chem. Phys.*, 1993, **98**, 2054; (c) G. P. Morley, I. R. Lambert, D. H. Morduant, S. H. S. Wilson, M. N. R. Ashfold, R. N. Dixon, C. M. Western, *J. Chem. Soc. Faraday Trans.*, 1993, **89**, 3865; (d) S. H. S. Wilson, M. N. R. Ashfold, R. N. Dixon, *J. Chem. Phys.*, 1994, **101**, 7538.

[112] M. Drabbels, C. G. Morgan, D. S. McGuire, A. M. Wodtke, *J. Chem. Phys.*, 1995, **102**, 611.

[113] M. H. M. Janssen, D. H. Parker, G. O. Sitz, S. Stolte, D. W. Chandler, *J. Chem. Phys.*, 1991, **95**, 8007.

[114] (a) K.-H. Gericke, A. U. Grunewald, S. Klee, F. J. Comes, *J. Chem. Phys.*, 1988, **88**, 6255; (b) K.-H. Gericke H. G. Gläser, C. Maul, F. J. Comes, *J. Chem. Phys.*, 1990, **92**, 411; (c) *J. Chem. Soc. Faraday Trans. 2*, 1989, **85**, 1297.

[115] K.-H. Gericke, *Phys. Rev. Lett.*, 1988, **60**, 561;

[116] A. Ticktin, J. R. Huber, *Chem. Phys. Lett.*, 1989, **156**, 372.

[117] D. C. Dayton, K. W. Jueles, R. E. Miller, *J. Chem. Phys.*, 1989, **90**, 2631.

[118] (a) T. J. Butenhoff, K. L. Cartelon, M. C. Chuang, C. B. Moore, *J. Chem. Soc. Faraday Trans. 2*, 1989, **85**, 1155; (b) T. J. Butenhoff, K. L. Cartelon, C. B. Moore, *J. Chem. Phys.*, 1990, **92**, 377.

[119] M. Brouard, M. T. Martinez, J. O'Mahony, *Mol. Phys.*, 1990, **71**, 1021.

[120] R. N. Dixon, J. Nightingale, C. M. Western, X. Yang, *Chem. Phys. Lett.*, 1988, **151**, 328.

[121] J. J. Valentini, in *Laser Spectroscopy and its Applications*, Opt. Eng., Vol. 11, eds. L. J. Radziensky, R. W. Solarz, J. A. Paisner, (Marcel Dekker, New York, 1987), p. 507.

[122] M. Brouard, S. R. Langford, D. E. Manolopoulos, *J. Chem. Phys.*, 1994, *101*, 7458.

[123] M. Brouard, S. R. Langford, G. A. J. Markillie, in preparation.

[124] V. Engel, V. Steammler, R. L. Vander Wal, F. F. Crim, R. J. Sension, B. Hudson, P. Andresen, S. Hennig, K. Weide, R. Schinke, *J. Phys. Chem.*, 1992, **96**, 3201.

[125] R. Schinke, *J. Chem. Phys.*, 1986, **85**, 5049.

[126] R. Schinke, V. Engel, *Faraday Discuss. Chem. Soc.*, 1986, **82**, 111.

[127] (a) R. Vasudev, R. N. Zare, R. N. Dixon, *Chem. Phys. Lett.*, 1983, **96**, 399; (b) *J. Chem. Phys.*, 1984, **80**, 4863;

[128] J. H. Shan, S. J. Wategaonkar, R. Vasudev, *Chem. Phys. Lett.*, 1989, **158**, 317.

[129] J. H. Shan, R. Vasudev, *Chem. Phys. Lett.*, 1987, **141**, 472.

[130] J. H. Shan, V. Vorsa, S. J. Wategaonkar, R. Vasudev, *J. Chem. Phys.*, 1989, **90**, 5493.

[131] G. W. King, D. Moule, *Can. J. Chem.*, 1962, **40**, 2057.

[132] F. Flouquet, J. A. Horsley, *J. Chem. Phys.*, 1974, **60**, 3767.

[133] J. N. Murrell, S. Carter, I. M. Mills, M. A. Guest, *Mol. Phys.*, 1981, **42**, 605.

[134] (a) G. Theodorakopoulos, C. A. Nicolaides, R. J. Buenker, S. D. Peyerinhoff, *Chem. Phys. Lett.*, 1982, **89**, 164; (b) G. Theodorakopoulos, I. D. Petsalakis, R. J. Buenker, S. D. Peyerimoff, *Chem. Phys. Lett.*, 1984, **105**, 253; (c) G. Theodorakolpoulos, I. D. Petsalakis, R. J. Buenker, *Chem. Phys.*, 1985, **96**, 217.

[135] D. M. Hirst, M. S. Child, *Mol. Phys.*, 1992, **77**, 463.

[136] T. Carrington, *J. Chem. Phys.*, 1964, **41**, 2012.

[137] (a) J. P. Simons, A. J. Smith, R. N. Dixon, *J. Chem. Soc. Faraday Trans. 2*, 1984, **80**, 1489; (b) A. Hodgson, J. P. Simons, M. N. R. Ashfold, J. M. Bayley, R. N. Dixon, *Chem. Phys. Lett.*, 1984, **107**, 1; (c) *Mol. Phys.*, 1985, **54**, 351; (d) A. Hodgson, J. P. Simons, R. N. Dixon, in *Photophysics and Photochemistry Above 6 eV*, ed. F. Lahmani (Elsevier, Amsterdam, 1985), p. 505.

[138] N. Shafizadeh, J. Rostas, J. L. Lemaire, F. Rostas, *Chem. Phys. Lett.*, 1988, **152**, 75.

[139] (a) C. G. Atkins, R. G. Briggs, J. B. Halpern, G. Hancock, *Chem. Phys. Lett.*, 1988, **152**, 81; (b) *J. Chem. Soc. Faraday Trans. 2*, 1989.

[140] H. J. Krautwald, L. Schnieder, K. H. Welge, M. N. R. Ashfold, *Faraday Discuss. Chem. Soc.*, 1986, **82**, 193.

[141] D. H. Morduant, M. N. R. Ashfold, R. N. Dixon, *J. Chem. Phys.*, 1994, **100**, 7360.

[142] K. Weide, R. Schinke, *J. Chem. Phys.*, 1989, **90**, 7150.

[143] R. N. Dixon, *Mol. Phys.*, 1985, **85**, 333.

[144] R. N. Dixon, *J. Chem. Phys.*, 1995, **102**, 301.

[145] K. F. Freed, Y. B. Band, *Excited States*, edited by F. C. Lim (Academic Press, New York, 1977), Vol 3.

[146] (a) J. P. Simons, P. W. Tasker, *Mol. Phys.*, 1973, **26**, 1267; (b) *Mol. Phys.*, 1974, **27**, 1691.

[147] J. Solomon, *J. Chem. Phys.*, 1967, **47**, 889.

[148] G. E. Busch, K. E. Wilson, *J. Chem. Phys.*, 1972, **56**, 3638.

[149] J. P. Simons, *Faraday Discuss. Chem. Soc.*, 1991. **91**, 366.

[150] J.-X. Wang, Ph.D. Thesis, University of Nottingham, 1992.

[151] M. Brouard, J.-X. Wang, *J. Chem. Soc. Faraday Trans.*, 1992, **88**, 3511.

[152] (a) X. Luo, P. T. Rieger, D. S. Perry, T. R. Rizzo, *J. Chem. Phys.*, 1988, **89**, 4448; (b) X. Luo, T. R. Rizzo, *J. Chem. Phys.*, 1991, **94**, 889; (c) *J. Chem. Phys.*, 1992, **96**, 5129; (d) X. Luo, P. R. Fleming, T. R. Rizzo, *J. Chem. Phys.*, 1992, **96**, 5659.

[153] P. R. Fleming, M. Li, T. R. Rizzo, *J. Chem. Phys.*, 1991, **95**, 865.

[154] P. R. Fleming, M. Li, T. R. Rizzo, *J. Chem. Phys.*, 1991, **94**, 2425.

[155] O. V. Boyarkin, T. R. Rizzo, *J. Chem. Phys.*, 1995, **103**, 1985; O. V. Boyarkin, T. R. Rizzo, R. D. F. Seltte, *Ber. Bunsenges. Phys. Chem.*, 1995, **99**, 504.

[156] C. E. Hamilton, J. L. Kinsey, J. L. Field, *Ann. Rev. Phys. Chem.*, 1986, **37**, 493.

[157] Y. S. Choi, P. Teal, C. B. Moore, *J. Opt. Soc. America B- Opt. Phys.*, 1990, **7**, 1829.

[158] F. J. Northrup, T. J. Sears, *Ann. Rev. Phys. Chem.*, 1992, **43**, 127.

[159] X. Yang, J. M. Price, J. A. Mack, C. G. Morgan, C. A. Rogaski, D. McGuire, E. H. Kim, A. Wodtke, *J. Chem. Phys.*, 1993, **97**, 3944.

[160] (a) D. W. Neyer, X. Luo, P. L. Houston, I. Burak, *J. Chem. Phys.*, 1992, **97**, 9036; (b) *ibid.*, 1993, **98**, 5095; (c) *ibid.* 1995, **102**, 1645.

[161] G. Hall, B. J. Whitaker, *J. Chem. Soc. Faraday Trans.*, 1994, **90**, 1.

[162] M. A. Buntine, D. W. Chandler, C. C. Hayden, *J. Chem. Phys.*, 1995, **102**, 2718.

[163] J. S. Keller, T. Dowd, R. Fauseit, L. Miller, C. Schehr, proceedings of the *Conference on the Dynamics of Molecular Collisions*, Asilomar, July 1995.

[164] T. J. Butenhoff, E. A. Rohling, *J. Chem. Phys.*, 1992, **97**, 5460.

[165] D. David, A. Strugano, I. Bar, S. Rosenwaks, *J. Chem. Phys.*, 1993, **98**, 409.

[166] (a) D. David, I. Bar, S. Rosenwaks, *J. Phys. Chem.*, 1993, **97**, 11571; (b) *J. Chem. Phys.*, 1993, **99**, 4218; (c) . *Chem. Phys.*, 1994, **187**, 21.

[167] (a) I. Bar, Y. Cohen, D. David, T. Arusi-Parpar, S. Rosenwaks, J. J. Valentini, *J. Chem. Phys.*, 1989, **90**, 6807; (b) *ibid*, 1990, **93**, 2146; (c) *ibid*, 1991, **95**, 3341; (d) *J. de Physique IV*, 1991, **C7-1**, 651.

[168] Y. Cohen, I. Bar, S. Rosenwaks, *J. Chem. Phys.*, 1995, **102**, 3612.

[169] J. Wolfrum, *Faraday Disc. Chem. Soc.*, 1987, **84**, 191.

[170] (a) U. Gaubatz, P. Rudecki, S. Sclumann, K. Bergmann, *Phys. Rev. A*, 1989, **40**, 6741; (b) K. Bergmann, S. Sciemann, A. Kuhn, S. Steuerwald, *Phys. Rev. Lett.*, 1993, **71**, 3637.

[171] C. A. Taajes, M. H. M. Janssen, S. Stolte, *Chem. Phys. Lett.*, 1993, **203**, 363.

[172] D. Y. Kim, N. Brandstaer, L. Pipers, T. Garner, D. Baugh, *J. Phys. Chem.*, 1995, **99**, 4364.

[173] B. R. Henry, W. Seibrand, *J. Chem. Phys.*, 1968, **49**, 5369.

[174] E. B. Wilson, J. C. Decius, P. C. Cross, *Molecular Vibrations*, (McGraw-Hill, New York, 1955).

[175] (a) M. S. Child, L. Halonen, *Adv. Chem. Phys.*, 1984, **57**, 1; (b) M. S. Child, *Acc. Chem. Res.*, 1985, **18**, 45.

[176] L. Halonen, *J. Phys. Chem.*, 1989, **93**, 3386.

[177] B. R. Henry, H. G. Kjaergaard, B. Niefer, B. J. Schattka, D. M. Turnbull, *Can. J. Appl. Specrosc.*, 1993, **38**, 42.

[178] (a) G. M. Schmid, S. L. Coy, R. W. Field, R. J. Silbey, *Chem. Phys. Lett.*, 1994, **219**, 331; (b) *J. Chem. Phys.*, 1994, **101**, 869.

[179] T. Lukka, L. Halonen, *J. Chem. Phys.*, 1994, **101**, 8380.

[180] P. R. Stannard, M. L. Elert, W. M. Gelbart, *J. Chem. Phys.*, 1981, **74**, 6050.

[181] O. S. Mortensen, B. R. Henry, A. Mohamadi, *J. Chem. Phys.*, 1981, **75**, 4800.

[182] (a) M. S. Child, R. T. Lawton, *Chem. Phys. Lett.*, 1982, **87**, 217; (b) *J. Chem. Soc. Faraday Trans.* 1981, **71**, 273.

[183] R. T. Lawton, M. S. Child, *Mol. Phys.*, 1979, **37**, 1799.

[184] R. T. Lawton, M. S. Child, *Mol. Phys.*, 1980, **40**, 733.

[185] E. J. Heller, *Acc. Chem. Res.*, 1981, **14**, 368.

[186] K. K. Lehmann, *J. Chem. Phys.*, 1983, **79**, 1098.

[187] M. Kellman, *J. Chem. Phys.*, 1985, **83**, 3842.

[188] Discussion on Intramolecular Kinetics, *Faraday Disc. Chem. Soc.*, 1983, **75**, 1–432.

[189] Symposium on Potential Energy Surfaces, Unimolecular Processes and Spectroscopy, *J. Chem. Soc. Faraday Trans II*, 1988 **84**(9).

[190] (a) P. M. Felker, A. H. Zewail, *J. Chem. Phys.*, 1985, **82**, 2961; (b) *ibid.*, 1985, **82**, 2975; (c) *ibid.*, 1985, **82**, 2994.

[191] K. K. Lehmann, G. Scoles, B. H. Pole, *Ann. Rev. Phys. Chem.*, 1994, **45**, 241 and references therein.

[192] M. Brouard, R. Mabbs, *Chem. Phys. Lett.*, 1993, **204**, 543.

[193] (a) T. R. Rizzo, C. C. Hayden, F. F. Crim, *Faraday Disc. Chem. Soc.*, 1983, **75**, 223; (b) *J. Chem. Phys.*, 1984, **81**, 4501; (c) H. R. Dubal, F. F. Crim, *J. Chem. Phys.*,

1985, **83**, 3863; (d) T. M. Tichich, T. R. Rizzo, H. R. Dubal, F. F. Crim, *J. Chem. Phys.*, 1986, **84**, 1508.

[194] P. J. Robinson, K. A. Holbrook, *Unimolecular Reactions*, (Wiley, London, 1972).

[195] P. Pechukas, J. C. Light, C. Rankin, *J. Chem. Phys.*, 1966, **44**, 794.

[196] M. Quack, J. Troe, *Ber. Bunsenges. Phys. Chem.*, 1974, **78**, 240.

[197] J.-Y. Mandin, J.-P. Chevillard, C. Camy-Peyret, J.-M. Flaud, J. W. Brault, *J. Mol. Spectrosc.*, 1986, **116**, 167.

[198] C. Camy-Peyret, J.-M. Flaud, J.-Y. Mandin, J.-P. Chevillard, J. Brault, D. A. Ramsay, M. Vervloet, J. Chauville, *J. Mol. Spectrosc.*, 1985, **113**, 208.

[199] (a) J. J. Barrett, M. J. Berry, *Appl. Phys. Lett.*, 1979, **34**, 144; (b) K. V. Reddy, F. F. Heller, M. J. Berry, *J. Chem. Phys.*, 1982, **76**, 2814.

[200] (a) P. Vujković Cvijin, D. A. Gilmore, M. A. Leugers, G. H. Atkinson, *Anal. Chem.*, 1987, **59**, 300; (b) P. Vujković Cvijin, D. A. Gilmore, G. H. Atkinson, *Appl. Specrosc.*, 1988, **42**, 770.

[201] (a) R. Vander Wal, F. F. Crim, *J. Phys. Chem.*, 1989, **93**, 5331; (b) R. Vander Wal, J. L. Scott, F. F. Crim, *J. Chem. Phys.*, 1991, **94**, 1859.

[202] R. L. Vander Wal, J. L. Scott, F. F. Crim, *J. Chem. Phys.*, 1990, **92**, 803.

[203] R. L. Vander Wal, J. L. Scott, F. F. Crim, K. Weide, R. Schinke, *J. Chem. Phys.*, 1991, **94**, 3548.

[204] G. H. Dieke, H. M. Crosswhite, *J. Quant. Spectrosc. Radiat. Transfer*, 1962, **2**, 97.

[205] (a) A. Oura, *Low Temp. Sci. Series A, Physical Sciences*, 1951, **6**, 41; (b) M. A. Clyne, J. A. Coxon, A. R. Woon Fat, *J. Mol. Spec.*, 1973, **46**, 146.

[206] R. A. Sutherland, R. A. Anderson, *J. Chem. Phys.*, 1973, **58**, 1226.

[207] D. R. Yarkony, *J. Chem. Phys.*, 1992, **97**, 1838.

[208] T. Bergeman, P. Erman, Z. Haratym, M. Larsson, *Phys. Scr.*, 1981, **23**, 45.

[209] M. H. Alexander, P. J. Dagdigian, *J. Chem. Phys.*, 1984, **80**, 4325.

[210] G. Herzberg, *Spectra of Diatomic Molecules*, (Van Nostrand, New York, 1950).

[211] J. L. Kinsey, *J. Chem. Phys.*, 1984, **81**, 6410.

[212] (a) P. Andresen, E. W. Rothe, *J. Chem. Phys.*, 1983, **78**, 989; (b) P. Andresen, G. S. Ondrey, B. Titze, E. W. Rothe, *J. Chem. Phys.*, 1984, **80**, 2548.

[213] P. Andresen, E. W. Rothe, *J. Chem. Phys.*, 1985, **82**, 3634.

[214] M. H. Alexander, P. Andresen, R. Bacis, R. Bersohn, F. J. Comes, P. J. Dagdigian, R. N. Dixon, G. W. Flynn, K.-H. Gericke, E. R. Grant, B. J. Howard, J. R. Huber, D. S. King, J. L. Kinsey, K. Kleinermanns, K. Kuchitsu, A. C. Luntz, A. J. McCaffery, B. Pouilly, H. Reisler, S. Rosenwaks, E. W. Rothe, M. Shapiro, J. P. Simons, R. Vasudev, J. R. Wiesenfeld, C. Wittig, R. N. Zare, *J. Chem. Phys.*, 1982, **89**, 1749.

[215] R. Altkorn, R. N. Zare, *Ann. Rev. Phys. Chem.*, 1984, **35**, 265.

[216] J. F. Cordova, C. T. Rettner, J. L. Kinsey, *J. Chem. Phys.*, 1981, **75**, 2742.

[217] I. L. Chidsey, D. R. Crosley, *J. Quant. Spectrosc. Radiat. Transfer*, 1980, **23**, 182.

[218] W. L. Dimpfl, J. L. Kinsey, *J. Quant. Spectrosc. Radiat. Transfer*, 1979, **21**, 233.

[219] C. H. Greene, R. N. Zare, *Ann. Rev. Phys. Chem.*, 1982, **33**, 119.

[220] C. H. Greene, R. N. Zare, *J. Chem. Phys.*, 1983, **78**, 6741.

[221] A. U. Grunewald, K.-H. Gericke, F. J. Comes, *Chem. Phys. Lett.*, 1987, **133**, 501.

[222] (a) K. Mikulecky, K.-H. Gericke, F. J. Comes, *Chem. Phys. Lett*, 1991, **182**, 290; (b) *Ber. Bunsenges. Phys. Chem.*, 1991, **95**, 927.

[223] D. David, I. Bar, S. Rosenwaks (unpublished)

[224] R. Schinke, R. L. Vander Wal, J. L. Scott, F. F. Crim, *J. Chem. Phys.*, 1991, **94**, 283.

[225] (a) D. F. Plusqueliic, O. Votava, D. J. Nesbitt, *J. Chem . Phys.*, 1994, **101**, 6356; (b) in press.

[226] (a) K. S. Sorbie, J. N. Murrell, *Mol. Phys.*, 1975, **29**, 1387; (b) *ibid.*, 1976, **31**, 905.

[227] (a) J. R. Reimers, R. O. Watts, *Mol. Phys.*, 1984, **52**, 357; (b) D. F. Coker, J. R. Reimers, R. O. Watts, *J. Chem. Phys.*, 1985, **82**, 3554; (c) *ibid.*, 1987, **91**, 2513.

[228] M. J. Redmon, G. C. Schatz, *Chem. Phys.*, 1981, **54**, 365.

[229] (a) P. Jensen, *J. Mol. Spectrosc.*, 1988, **128**, 478; (b) *ibid.*, 1989, **133**, 438; (c) P. Jensen, S. A. Tashkun, Vl. G. Tyuterev, *ibid.*, 1994, **168**, 271.

[230] V. Steammler, A. Palma, *Chem. Phys.*, 1985, **93**, 63.

[231] J. M. Bowman, A. Wierzbicki, J. Zuriga, *Chem. Phys. Lett.*, 1988, **150**, 269.

[232] R. Schinke, V. Engel, P. Andresen, D. Häusler, G. G. Balint-Kurti, *Phys. Rev. Lett.*, 1985, **55**, 1180.

[233] G. G. Balint-Kurti, *J. Chem. Phys*, 1986, **84**, 4443.

[234] K. Kühl, R. Schinke, *Chem. Phys. Lett*, 1989, **158**, 81.

[235] H. Guo, J. N. Murrell, *J. Chem. Soc. Faraday Trans. 2*, 1988, **84**, 949.

[236] H.-T. Wang, W. S. Felp, S. P. McGlynn, *J. Chem. Phys.*, 1977, **67**, 2614.

[237] G. Herzberg, *Infrared and Raman Spectra*, (Van Nostrand, New York 1945).

[238] W. Bauman, R. Mecke, *Z. Phys.*, 1933, **81**, 455.

[239] F. Freudenberg, R. Mecke, *Z. Phys.*, 1933, **81**, 465.

[240] R. Schinke, V. Engel, *J. Chem. Phys.*, 1988, **88**, 6831.

[241] (a) D. G. Imre, J. Zhang, *Chem. Phys. Lett.*, 1988, **149**, 233; (b) J. Zhang, D. G. Imre, J. H. Frederick, *J. Phys. Chem.*, 1989, **93**, 6831; (c) D. G. Imre, J. Zhang, *Chem. Phys.*, 1989, **139**, 89.

[242] M. J. Davis, E. J. Heller, *J. Chem. Phys.*, 1981, **75**, 246.

[243] N. Shafer, S. Satyapal, R. Bersohn, *J. Chem. Phys.*, 1989, **90**, 6807.

[244] (a) R. J. Sension, R. J. Brudzynski, B. S. Hudson, *Phys. Rev. Lett.*, 1988, **61**, 694; (b) R. J. Sension, R. J. Brudzynski, B. S. Hudson, J. Zhang, D. G. Imre, *Chem. Phys.*, 1990, **141**, 393.

[245] F. C. De Lucia, R. L. Cook, P. Helminger, W. Gordy, *J. Chem. Phys.*, 1971, **55**, 5334.

[246] W. S. Benedict, N. Gailar, E. K. Plyler, *J. Chem. Phys.*, 1956, **24**, 1139.

[247] D. David, A. Strugano, I. Bar, S. Rosenwaks, *Appl. Spectrosc.*, 1992, **46**, 1149.

[248] (a) N. Papineau, C. Camy-Peyret, J. M. Flaud, G. Guelachvili, *J. Mol. Spectrosc.*, 1982, **92**, 451; (b) A. Perrin, C. Camy-Peyret, J. M. Flaud, *Can. J. Phys.*, 1986, **64**, 736.

[249] R. N. Zare, *Angular Momentum - Understanding Spatial Aspects in Chemistry and Physics* (John Wiley and Sons, New York and London, 1987).

[250] H. C. Allen Jr., P. C. Cross, *Molecular Vib-Rotors*, (John Wiley and Sons, New York and London, 1963).

[251] J. A. Beswick, G. M. Gelbart, *J. Phys. Chem.*, 1980, **84**, 3148.

[252] (a) M. D. Morse, K. F. Freed, Y. B. Band, *J. Chem. Phys.*, 1979, **70**, 3604; (b) M. D. Morse, K. F. Freed, *Chem. Phys. Lett.*, 1980, **74**, 49; (c) *J. Chem. Phys.*, 1981, **74**, 4395; (d) *ibid*, 1983, **78**, 6045.

[253] M. Shapiro, H. Kaplan, *J. Chem . Phys.*, 1979, **71**, 2182.

[254] (a) G. G. Balint-Kurti, M. Shapiro, *Chem. Phys.*, 1981, **61**, 137; (b) *ibid.* 1982, **72**, 456.

[255] J. R. Taylor, *Scattering Theory*, (New York, John Wiley and Sons, 1972).

[256] A.R. Edmonds, *Angular Momentum in Quantum Mechanics*, (Princeton University, Princeton, 1974).

[257] R. T. Pack, *J. Chem. Phys.*, 1974, **60**, 1974.

[258] M. Shapiro, G. G. Balint-Kurti, *J. Chem. Phys.*, 1979, **71**, 1461.

[259] R. Schinke, V. Engel, V. Staemmler, *J. Chem. Phys.*, 1985, **83**, 4522.

[260] (a) R. Schinke, *J. Chem. Phys.*, 1986, **85**, 5049; (b) R. Schinke, V. Engel, *Faraday Discuss. Chem. Soc*, 1986, **82**, 111.

[261] E. Segev, M. Shapiro, *J. Chem. Phys.*, 1982, **77**, 5604.

[262] A. Kuppermann, G. C. Schatz, M. Baer, *J. Chem. Phys.*, 1976, **65**, 4596.

[263] C. X. W. Qian, A. Ogai, L. Iwata, H. Reisler, *J. Chem. Phys.*, 1990, **92**, 4296.

[264] C. X. W. Qian, A. Ogai, J. Brandon, Y. Y. Bai, H. Reisler, *J. Phys. Chem.*, 1991, **95**, 6763.

[265] C. X. W. Qian, H. Reisler, *Advances in Molecular Vibrations and Collision Dynamics*, Ed. J. M. Bowman (JAI Press Inc., London, 1992).

[266] J. R. Huber, R. Schinke, *J. Phys. Chem.*, 1993, **97**, 3463.

[267] D. Sölter, H. J. Werner, M. von Dirke, A. Untsch, R. Schinke, *J. Chem. Phys.*, 1992, **97**, 3357.

[268] L. D. Landau, E. M. Lifshitz, *Quantum Mechanics*, (Pergamon, Oxford, 1977).

[269] (a) M. H. Alexander, P. J. Dagdigian, H.-J. Werner, *J. Chem. Phys.*, 1988, **89**, 1388; (b) *Faraday Discuss. Chem. Soc.*, 1991, **91**, 319.

[270] D. Downs, A. D. Walsh, R. W. Weeler, *Phil. Trans. Roy. Soc. Lond. A*, 1951, **243**, 463.

[271] V. Ya Shtern, *The Gas-Phase Oxidation of Hydrocarbons*, (Pergamon, Oxford, 1964).

[272] R. T. Pollard, *Comprehensive Chemical Kinetics*, Eds. C. H. Bamford and C. F. H. Tipper (Elsevier, New York, 1977), vol. 17, pp 249–367.

[273] P. G. Lignola, E. Reverchon, *Prog. Ener. Combust. Sci.*, 1987, **13**, 75.

[274] J. F. Griffith, S. K. Scott, *Prog. Ener. Combust. Sci.*, 1987, **13**, 161.

[275] T. A. Litzinger, *Prog. Ener. Combust. Sci.*, 1990, **16**, 155.

[276] C. K. Westbrook, *Chemistry and Industry*, 1992, **15**, 562.

[277] L. J. Kirsch, C. P. Quinn, *J. Chem. Phys.*, 1985, **82**, 459.

[278] (a) D. L. Baulch, C. J. Cobos, R. A. Cox, P. Frank, G. Hayman, T. Just, J. A. Kerr, T. Murrels, M. J. Pilling, J. Troe, R. W. Walker, J. Warnatz, *J. Phys. Chem. Ref. Data*, 1992, **21**, 411; (b) *ibid.* 1994, **98**, 59; (c) *ibid.* 1994, bf 23, 847; (d) *ibid.* 1995, **24**, 1609.

[279] C. K. Westbrook, W. J. Pitz, SAE paper SAE872107, 1987.

[280] A. K. Oppenheim, *Phil. Trans. Roy. Soc. Lond. A*, 1985, **315**, 471.

[281] M. P. Halstead, L. J. Kirsch, C. P. Quinn, *Combust. Flame*, 1977, **30**, 161.

[282] C. K. Westbrook, J. Warnatz, W. J. Pitz, *Twenty-second Symposium (International) on Combustion*, The Combustion Institute, Pittsburgh, 1988, pp. 893.

[283] C. Chevalier, W. Pitz, J. Warnatz, C. K. Westbrook, *Twenty-fourth Symposium (International) on Combustion*, The Combustution Institute, Pittsburgh, 1992.

[284] U. C. Müller, N. Peters, A. Linan, *Twenty-fourth Symposium (International) on Combustion*, The Combustution Institute, Pittsburgh, 1992.

[285] A. C. Eckbreth, in: *Laser Diagnostics for Combustion, Temperature and Species*, eds. A. K. Gupta and D. G. Lilley, (Abacus Press, Cambridge, 1988), Energy and Engineering Series, Vol. 7.

[286] D. A. Greenhalgh, in: *Advances in Non-Linear Spectroscopy*, eds. R. J. H. Clark, R. E. Hester, (John Wiley and Sons, New York, 1988), pp. 193.

[287] N. M. Laurendeau, *Prog. Ener. Combust. Sci*, 1988, **14**, 147.

[288] W. Stricker, W. Meier, in: *Trends in Applied Spectroscopy*, ed. by The Council of Scientific Research Integration, Research Trends, Trivandrum, India, 1993.

[289] R. K. Hanson, J. M. Seitzman, P. H. Paul, *Appl. Phys. B - Photophys. Laser Chem.*, 1990, **50**, 441.

[290] K. McManus, B. Yip, S. Candel, *Exptl. Therm. Fluid Sci.*, 1995, **10**, 1995.

[291] T. Dreier, D. J. Rakestraw, *Opt. Lett.*, 1990, **15**, 72.

[292] (a) P. W. Anderson, *Phys. Rev.*, 1949, **76**, 657; (b) *ibid.*, 1950, **80**, 511.

[293] C. J. Tsao, B. Curnutte Jr., *J. Quant. Spectrosc. Radiat. Transfer*, 1962, **2**, 41.

[294] M. Berard, P. Lallemand, *J. Quant. Spectrosc. Radiat. Transfer*, 1978, **19**, 387.

[295] D. Robert, J. Bonamy, *J. Phys. (Paris)*, 1979, **40**, 923.

[296] R. P. Leavitt, D. Korff, *J. Chem. Phys.*, 1981, **74**, 2180.

[297] J. P. Looney, R. M. Herman, *J. Quant. Spectrosc. Radiat. Transfer*, 1987, **37**, 547.

[298] (a) L. S. Rothaman, R. R. Gamache, R. H. Tipping, C. P. Rinsland, M. A. H. Smith, D. C. Benner, V. M. Devi, J. M. Flaud, C. Camy-Peyret, A. Perrin, A. Goldman, S. T. Massie, L. R. Brown, R. A. Toth, *J. Quant. Spectrosc. Radiat. Transfer*, 1992, **48**, 469; (b) *Scientist*, 1994, **8**, 17.

[299] R. R. Gamache, J. M. Hartmann, L. Rosenmann, *J. Quant. Spectrosc. Radiat. Transfer*, 1994, **52**, 481.

[300] W. S. Bendedict, L. D. Kaplan, *J. Chem. Phys.*, 1959, **30**, 388.

[301] C. Morley, *Twenty-second Symposium (International) on Combustion*, The Combustion Institute, Pittsburgh, 1988, p911.

[302] P. A. Lynn, *An introduction to the Analysis and Processing of Signals*, (The MacMillan Press Ltd, London 1983).